University of Cyprus

Department of Electrical and Computer Engineering

Wireless Information and Power Transfer for Next-Generation Mobile Networks: A System Level Perspective

Yuan Guo

A Dissertation

Submitted in Partial Fulfillment of the

Requirements for the Degree of

Doctor of Philosophy

at the University of Cyprus

Jan., 2024

Yuan Guo

© Yuan Guo, 2024

Yuan Guo

APPROVAL PAGE

Yuan Guo

Wireless Information and Power Transfer for Next-Generation Mobile Networks: A System Level Perspective

The present Doctorate Dissertation was submitted in partial fulfillment of the requirements for the Degree of Doctor of Philosophy in the Department of Electrical and Computer Engineering, and was approved on Jan.19, 2024 by the members of the Examination Committee.

Committee Chair _____
Dr. Georgios Ellinas

Research Supervisor _____
Dr. Ioannis Krikidis

Committee Member _____
Dr. Themistoklis Charalambous

Committee Member _____
Dr. Emad Alsusa

Committee Member _____
Dr. Constantinos B. Papadias

Yuan Guo

DECLARATION OF DOCTORAL CANDIDATE

The present doctoral dissertation was submitted in partial fulfillment of the requirements for the degree of Doctor of Philosophy of the University of Cyprus. It is a product of original work of my own, unless otherwise mentioned through references, notes, or any other statements.

..... [Full Name of Doctoral Candidate]

..... [Signature]

Yuan Guo

Abstract

Over the past two decades, wireless communication networks have experienced an exponential rise in mobile users (MUs), leading to the widespread deployment of advanced technologies such as base stations (BSs), sensors, and various access points to ensure uninterrupted data services and support extremely high data rates. Despite these advancements, a significant challenge has emerged: the limited battery life of MUs, which substantially impacts network performance, highlighting the urgent need for innovative power solutions. In this context, simultaneous wireless information and power transfer (SWIPT) emerges as a pivotal technology, particularly suited for the emerging era of sixth-generation (6G) wireless networks. 6G networks are anticipated to operate seamlessly across diverse scenarios, encompassing both urban and remote areas, and are designed to cater to the needs of both static and high-mobility users while integrating terrestrial and non-terrestrial infrastructures for comprehensive global coverage. The extensive range of applications and environments in 6G underscores the crucial role of SWIPT, with its dual functionality in energy harvesting and data transmission. However, effectively integrating SWIPT into 6G networks is challenging, necessitating innovative approaches to enhance its performance within the complex and diverse environment of 6G infrastructures. Towards this direction, this PhD dissertation introduces a groundbreaking analytical framework based on stochastic geometry to comprehensively evaluate the performance of wireless information and power transfer in 6G networks. This framework includes the development of novel techniques/schemes designed to enhance the efficiency of SWIPT across diverse scenarios within the 6G network environment.

Firstly, in Chapter 3, we investigate the small- and large-scale SWIPT-enabled cellular networks. In specific, we develop a novel low-complexity threshold-based pair switching (TbPS) technique and a traffic load-based sleeping (TLbS) technique

Yuan Guo

for infinite- and finite-area network deployments, respectively, focusing on the interference management and illustrating the trade-off between information and power transfer. Motivated by the interference correlation issue discussed in Chapter 3 and aiming to further enhance the SWIPT performance, Chapter 4 delves into an investigation of the performance of a linear minimum mean square error (MMSE) receiver with the successive interference cancellation (SIC) technique within the context of SWIPT-enabled cellular networks.

In Chapter 5, we focus on the SWIPT-enabled cellular networks with high-mobility MUs. A novel coverage area-based CoMP (CA-CoMP) scheme is proposed to reduce the handover rate and enhance the overall SWIPT performance of high-mobility MUs. Further, in Chapter 6, we delve into the exploration of a SWIPT-assisted vehicular network. Utilizing SWIPT technology, battery-operated road-side sensors simultaneously receive control information and harvest energy from cellular BSs, subsequently using the harvested energy to spread data to vehicles.

In Chapter 7 and Chapter 8, we expand our exploration into the domains of non-terrestrial networks. In specific, Chapter 7 investigates the multi-tier low Earth orbit (LEO) satellite networks in the context of three association schemes. In Chapter 8, we study the feasibility of space-based solar power (SSP) system with LEO satellites.

Throughout this PhD dissertation, we employ tools from stochastic geometry that enable the evaluation of fundamental network performance metrics, including coverage probability, handover rate, data rate, and the amount of harvested energy. The established analyal framework facilitates the derivation of closed-form expressions, providing a quick and convenient methodology to assess system performance, and offering valuable insights into the impact of key system parameters on the performance of SWIPT-enabled 6G networks.

Yuan Guo

Περίληψη

Κατά τις δύο τελευταίες δεκαετίες, τα ασύρματα δίκτυα επικοινωνίας έχουν βιώσει μια εκθετική αύξηση στους κινητούς χρήστες (MUs), οδηγώντας στην εκτεταμένη ενσωμάτωση προηγμένων τεχνολογιών όπως οι σταθμοί βάσεις (BSs), αισθητήρες και διάφορα σημεία πρόσβασης υπεύθυνα για την αδιάλειπτη εξασφάλιση δεδομένων και την υποστήριξη εξαιρετικά υψηλών ταχυτήτων. Παρά τις προόδους αυτές, έχει προκύψει ένα σημαντικό πρόβλημα: η περιορισμένη διάρκεια ζωής της μπαταρίας των MUs, η οποία επηρεάζει σημαντικά την απόδοση του δικτύου, τονίζοντας την επείγουσα ανάγκη για καινοτόμες λύσεις ενέργειας. Σε αυτό το πλαίσιο, η ταυτόχρονη ασύρματη μετάδοση πληροφοριών και ενέργειας (SWIPT) αναδεικνύεται ως μια καθοριστική τεχνολογία, ιδιαίτερα κατάλληλη για την επερχόμενη εποχή των δικτύων ασύρματης επικοινωνίας έκτης γενιάς (6G). Τα δίκτυα 6G αναμένεται να λειτουργούν απρόσκοπτα σε διάφορα σενάρια, καλύπτοντας τόσο αστικές όσο και απομακρυσμένες περιοχές, και είναι σχεδιασμένα για να ικανοποιούν τις ανάγκες τόσο των στατικών όσο και των χρηστών υψηλής κινητικότητας, ενώ ενσωματώνουν επίγειες και μη επίγειες υποδομές για παγκόσμια κάλυψη. Η πληθώρα εφαρμογών των 6G δικτύων υπογραμμίζει τον κρίσιμο ρόλο της τεχνολογίας SWIPT, με τη διπλή λειτουργικότητα στη συλλογή ενέργειας και τη μετάδοση δεδομένων. Ωστόσο, η αποτελεσματική ένταξη της τεχνολογίας SWIPT στα δίκτυα 6G αποτελεί πρόκληση, απαιτώντας καινοτόμες προσεγγίσεις για την ενίσχυση της απόδοσής της εντός του περίπλοκου και διαφορετικού περιβάλλοντος των υποδομών. Προς αυτή την κατεύθυνση, αυτή η διδακτορική διατριβή παρουσιάζει ένα καινοτόμο αναλυτικό πλαίσιο βασισμένο στη στοχαστική γεωμετρία για την ολοκληρωμένη αξιολόγηση της απόδοσης της ασύρματης μετάδοσης πληροφοριών και ενέργειας στα δίκτυα 6G. Αυτό το πλαίσιο περιλαμβάνει την ανάπτυξη νέων τεχνικών/σχημάτων σχεδιασμένων για την ενίσχυση της αποδοτικότητας του SWIPT σε διάφορα σενάρια εντός του περιβάλλοντος δικτύου 6G.

Καταρχάς, στο Κεφάλαιο 3, διερευνούμε τα μικρής και μεγάλης κλίμακας δίκτυα κυψελωτής επικοινωνίας που επιτρέπουν την τεχνολογία SWIPT. Συγκεκριμένα, αναπτύσσου-

Yuan Guo

με μια νέα τεχνική εναλλαγής ζεύγους βασισμένη σε κατώφλι χαμηλής πολυπλοκότητας (TbPS) και μια τεχνική ύπνου βασισμένη στο φορτίο κίνησης (TLbS) για την ανάπτυξη δικτύων μη πεπερασμένης και πεπερασμένης περιοχής, αντίστοιχα, επικεντρώνοντας στη διαχείριση της παρεμβολής και απεικονίζοντας τον συμβιβασμό μεταξύ της μεταφοράς πληροφοριών και ενέργειας. Με κίνητρο το ζήτημα της συσχέτισης παρεμβολής που συζητείται στο Κεφάλαιο 3 και με στόχο την περαιτέρω βελτίωση της απόδοσης της τεχνολογίας SWIPT, το Κεφάλαιο 4 εμβαθύνει σε μια διερεύνηση της απόδοσης ενός γραμμικού δέκτη ελάχιστου μέσου τετραγωνικού σφάλματος (MMSE) με την τεχνική διαδοχικής ακύρωσης παρεμβολής (SIC) στο πλαίσιο των κυψελωτών δικτύων επικοινωνίας που επιτρέπουν την τεχνολογίαSWIPT.

Στο Κεφάλαιο 5, επικεντρωνόμαστε στα κυψελωτά δίκτυα επικοινωνίας που επιτρέπουν την τεχνολογία SWIPT με χρήστες υψηλής κινητικότητας. Προτείνεται ένα νέο σχήμα CA-CoMP για τη μείωση του ρυθμού ηανδοερ και τη βελτίωση της συνολικής απόδοσης της τεχνολογίας SWIPT για χρήστες υψηλής κινητικότητας. Επιπλέον, στο Κεφάλαιο 6, εμβαθύνουμε στην εξερεύνηση ενός δικτύου οχημάτων που υποστηρίζεται από την τεχνολογία SWIPT. Χρησιμοποιώντας την τεχνολογία SWIPT, οι αισθητήρες που είναι τοποθετημένη στη πλευρά του δρόμου και λειτουργούν με μπαταρία, λαμβάνουν ταυτόχρονα πληροφορίες ελέγχου και συλλέγουν ενέργεια από τους κυψελωτούς σταθμούς βάσης, χρησιμοποιώντας στη συνέχεια την συλλεγμένη ενέργεια για τη διάδοση δεδομένων στα οχήματα.

Στο Κεφάλαιο 7 και στο Κεφάλαιο 8, επεκτείνουμε την εξερεύνησή μας στους τομείς των μη επίγειων δικτύων. Ειδικότερα, το Κεφάλαιο 7 διερευνά τα πολυεπίπεδα δίκτυα δορυφόρων χαμηλής τροχιάς της Γης (LEO) στο πλαίσιο τριών σχημάτων συσχέτισης. Στο Κεφάλαιο 8, μελετάμε την εφικτότητα του συστήματος ηλιακής ενέργειας διαστήματος (SSP) με δορυφόρους LEO.

Σε όλη αυτή τη διδακτορική διατριβή, χρησιμοποιούμε εργαλεία από τη στοχαστική γεωμετρία που επιτρέπουν την αξιολόγηση των θεμελιωδών μετρικών απόδοσης δικτύου, συμπεριλαμβανομένων της πιθανότητας κάλυψης, του ρυθμού ηανδοερ, της ταχύτητας δεδομένων και της ποσότητας της συλλεγμένης ενέργειας. Το καθιερωμένο αναλυτικό πλαίσιο διευκολύνει την παραγωγή εκφράσεων σε κλειστή μορφή, παρέχοντας μια γρήγορη και βολική μεθοδολογία για την αξιολόγηση της απόδοσης του συστήματος και προσφέροντας πολύτιμες πληροφορίες σχετικά με τον αντίκτυπο των κύριων παραμέτρων του συστήματος στην απόδοση των δικτύων 6G που επιτρέπουν την τεχνολογία SWIPT.

Yuan Guo

Acknowledgments

This research was conducted from 2019 to 2024 at the IRIDA Research Centre for Communication Technologies, within the Department of Electrical and Computer Engineering at the University of Cyprus. The four and a half years spent in the Ph.D. program have been a remarkable and transformative period in my life. I wish to extend my heartfelt gratitude to the numerous individuals who offered their assistance and support throughout this journey.

First and foremost, my heartfelt thanks go to my family—my parents and my sister. Their endless love, patience, and encouragement have been the bedrock of my resilience and perseverance. In moments of doubt and challenge, their belief in my abilities fueled my determination to press forward. Their sacrifices have not gone unnoticed, and I am eternally grateful for their unconditional support.

I am exceptionally thankful to Prof. Ioannis Krikidis for his mentorship, expertise, and insightful guidance. His dedication to academic excellence and his thoughtful feedback have been instrumental in shaping both the direction and success of my research. His encouragement and support have significantly contributed to my personal and academic development. Working under his guidance has been a truly enriching experience, for which I am deeply grateful.

I would also like to extend my heartfelt thanks to Dr. Christodoulos Skouroumounis, whose assistance has been invaluable not only in my research endeavors but also in navigating the challenges of daily life during my Ph.D. studies. His generosity, mentorship, and the practical advice have greatly eased my journey, and I am profoundly thankful for his kindness and support.

My sincere appreciation goes to the European Union for their financial support, which has been critical in facilitating my research and academic progress. This funding has allowed me to dedicate myself fully to my studies, making a significant difference in my Ph.D. journey.

Yuan Guo

I acknowledge my own efforts and perseverance throughout this demanding process. This Ph.D. thesis represents not just an academic achievement but a period of immense personal growth and self-discovery. The challenges faced and the knowledge gained have been invaluable, and I am proud of the work I have accomplished.

Lastly, I must also express my sincere gratitude to my friends and colleagues who have been there for me throughout this journey. Mr. Elio Faddoul, Mr. Triantafyllos Mavrovoltsos, Mr. Duan Wei, Mr. Zhao Jinqiang, Miss Li Yujie, Miss Li Jin, Mr. Liu Jie, Mr. Ma Rui, Mr. Guo Long, Mrs. Zhang Shuhua, Mrs. Filitsa Charalambous, Mr. Andreas Nicolaides, Miss Maria Demetropoulou, Dr. Nizar Khalfet, Dr. Priyadarshi Mukherjee, Dr. Zhang Kangkang, Dr. Huang Jiahao, Dr. Costas Psomas, Dr. Elena Demarchou, Dr. Christos Efrem, Dr. Kapila W.S. Palitharathna - your friendship, camaraderie, and unwavering support have been my comfort and encouragement during the highs and lows of my Ph.D. studies. Whether it was a much-needed break, a listening ear, or critical feedback, you all played an essential role in this process. Your presence and support have been a constant source of strength and motivation, for which I am incredibly thankful.

In closing, this journey has been a testament to the power of collective support, encouragement, and academic collaboration. I am profoundly grateful to each and every one of you who has contributed to my Ph.D. journey, whether mentioned here by name or not. Your impact has been immeasurable, and I cherish the bonds we have formed along the way.

Yuan Guo

In loving memory of my grandfather, Mr. Guo Xing.

Yuan Guo

List of Abbreviations

1G	First-**G**eneration
2G	Second-**G**eneration
3G	Third-**G**eneration
4G	Fourth-**G**eneration
5G	Fifth-**G**eneration
6G	Sixth-**G**eneration
AS	**A**ntenna **S**wiching
BPP	**B**inomial **P**oint **P**rocess
BS	**B**ase **S**tation
CA-CoMP	**C**overage **A**rea-based **Co**ordinated **M**ulti-**P**oint
cdf	**C**umulative **D**istribution **F**unction
CoMP	**Co**ordinated **M**ulti-**P**oint
CSI	**C**hannel **S**tate **I**nformation
DC	**D**irect **C**urrent
EH	**E**nergy **H**arvesting
gRA	**G**round **R**ectenn**a**
gUE	**G**round **U**ser **E**quipment
ID	**I**nformation **D**ecoding
IRS	**I**ntelligent **R**eflecting **S**urface
ISAC	**I**ntegrated **S**ensing **a**nd **C**ommunications
IoT	**I**nternet-**o**f-**T**highs
LEO	**L**ow **E**arth **O**rbit
LoS	**L**ine-**o**f-**S**ight
MGF	**M**oment **G**enerating **F**unction
MIMO	**M**ultiple **I**nput **M**ultiple **O**utput
MMSE	Mimum **M**ean **S**quare **E**rror

Yuan Guo

mmWave	**m**illi**m**eter-**wave**
MRC	**M**aximum **R**atio **C**ombing
MU	**M**obile **U**ser
NLoS	**N**on-**L**ine-**o**f-**S**ight
NOMA	**N**on-**O**rthogonal-**M**ultiple-**A**ccess
OFDM	**O**rthogonal **F**requency **D**ivision **M**ultiplexing
pdf	**P**robability **D**ensity **F**unction
PGFL	**P**robability **G**enerating **F**unctiona**l**
PLP	**P**oisson **L**ine **P**rocess
PP	**P**oint **P**rocess
PPP	**Poisson P**oint **P**rocess
PS	**P**ower **S**plitting
RF	**R**adio **F**requency
RWP	**R**andom **W**ay**p**oint
SIC	**S**uccessive **I**nterference **C**ancellation
SIMO	**S**ingle **I**nput **S**ingle **O**utput
SINR	**S**ignal-to-**I**nterference-plus-**N**oise **R**atio
SIR	**S**ignal-to-**I**nterference **R**atio
SR	**S**hadowed-**R**ician
SSB	**S**ynchronization **S**ignal **B**lock
SSP	**S**pace **S**olar **P**ower
SWIPT	**S**imultaneous **W**ireless **I**nformation and **P**ower **T**ransfer
TbPS	**T**hreshold-**b**ased **P**air **S**witching
TLbS	**T**raffic **L**oad-**b**ased **S**leeping
TS	**T**ime **S**witching
WIPT	**W**ireless **I**nformation and **P**ower **T**ransfer
WPT	**W**ireless **P**ower **T**ransfer

Yuan Guo

Publications

Journal publications

1. **Y. Guo**, C. Skouroumounis and I. Krikidis, "On User Association in Large-Scale Heterogeneous LEO Satellite Network," submitted in *IEEE Transactions on Aerospace and Electronic Systems* (second round of review).

2. **Y. Guo**, C. Skouroumounis and I. Krikidis, "A Coverage Area-Based CoMP Technique for SWIPT-Enabled Mobile Networks," *IEEE Transactions on Green Communications and Networking*, vol. 7, no. 4, pp. 1807-1822, Dec. 2023

3. **Y. Guo**, C. Skouroumounis and I. Krikidis, "Joint Information and Energy Transfer of SWIPT-Enabled Mobile Users in Wireless Networks," *IEEE Transactions on Green Communications and Networking*, vol. 6, no. 2, pp. 1141-1156, Jun. 2022.

Conferences publications

1. **Y. Guo**, E. Faddoul, C. Skouroumounis and I. Krikidis, "LEO Satellite-based Space Solar Power Systems," in *Proceedings of IEEE International Conference on Acoustics, Speech, and Signal Processing Workshop*, Rhodes Island, Greece, Jun. 2023.

2. **Y. Guo**, C. Skouroumounis and I. Krikidis, "Large-scale Heterogeneous Ultra-dense LEO Satellite-based Cellular Networks," in *Proceedings of IEEE International Conference on Communications*,, Rome, Italy, May 2023.

3. **Y. Guo**, C. Skouroumounis and I. Krikidis, "A Linear MMSE Receiver for SWIPT-enabled Wireless Networks," in *Proceedings of IEEE Vehicular Technology Conference*, London, United Kingdom, Sep. 2022, pp. 1-6.

Yuan Guo

4. **Y. Guo**, C. Skouroumounis and I. Krikidis, "A Linear MMSE Receiver for Multi-Antenna SWIPT-enabled Wireless Networks," in *Proceedings of IEEE International Conference on Communications,* Seoul, Korea, May 2022, pp. 3166-3171.

5. **Y. Guo**, C. Skouroumounis and I. Krikidis, "A Coverage Area-Based Cooperation Technique for SWIPT- Enabled Systems with Mobility," in *Proceedings of IEEE Global Communications Conference*, Madrid, Spain, Dec. 2021, pp. 1-6.

6. **Y. Guo**, C. Skouroumounis and I. Krikidis, "Threshold-Based Pair Switching Scheme in SWIPT-Enabled Wireless Downlink System," in *Proceedings of IEEE Vehicular Technology Conference*, Helsinki, Finland, Apr. 2021, pp. 1-7.

7. E. Faddoul, **Y. Guo**, G. M. Kraidy, C. Psomas, and I. Krikidis, "Correlation Mitigation Schemes for Index-Modulated Fluid Antenna Systems," in *Proceedings of IEEE Global Communications Conference*, Kuala Lumpur, Malaysia, Dec. 2023.

8. **Y. Guo**, E. Faddoul, C. Skouroumounis, and I. Krikidis, "Simultaneous wireless information and power transfer-assisted vehicular networks," in progress.

9. E. Faddoul, **Y. Guo**, C. Skouroumounis, and I. Krikidis, "Temperature-modulated channel for SWIPT," *IEEE Wireless Communications Letters*, early access.

Yuan Guo

Contents

Yuan Guo

Yuan Guo

Yuan Guo

Yuan Guo

List of Figures

Yuan Guo

Yuan Guo

Yuan Guo

Chapter 1

Introduction

Wireless communications has witnessed a remarkable evolution from the introduction of first-generation (1G) to the advent of fifth-generation (5G) networks. At the inception of 1G in 1980s, analog cellular networks laid the foundation for mobile telephony, enabling basic voice communication on a limited scale. The subsequent arrival of second-generation (2G) networks brought about the digital revolution, allowing for the transmission of not only voice but also short text messages. With the third-generation (3G) networks, the world experienced a significant leap forward as mobile internet access became a reality, enabling users to browse the web, send emails, and enjoy multimedia content on their devices. The introduction of fourth-generation (4G) networks marked a turning point in wireless communications, offering faster data transfer speeds, enhanced capacity, and improved network reliability, which paved the way for the widespread adoption of video streaming, online gaming, and other bandwidth-intensive applications. Now, with the massive deployments of 5G networks, we are entering an era of unprecedented connectivity and technological advancement. 5G achieves ultra-high speeds, extremely low latency, and massive device connectivity, opening up new possibilities for autonomous vehicles, smart cities, Internet-of-Things (IoT) devices, and virtual reality experiences. Beyond data transmission, the wireless domain is now venturing into the realm of energy transfer. From wireless charging of mobile devices to powering remote or inaccessible devices such as implanted medical devices, wireless power transfer (WPT) introduces an entirely new dimension to the wireless revolution. The imminent arrival of sixth-generation (6G) networks is expected to integrate WPT as a key feature, fueled by the need to sustain the countless interconnected devices in

Yuan Guo

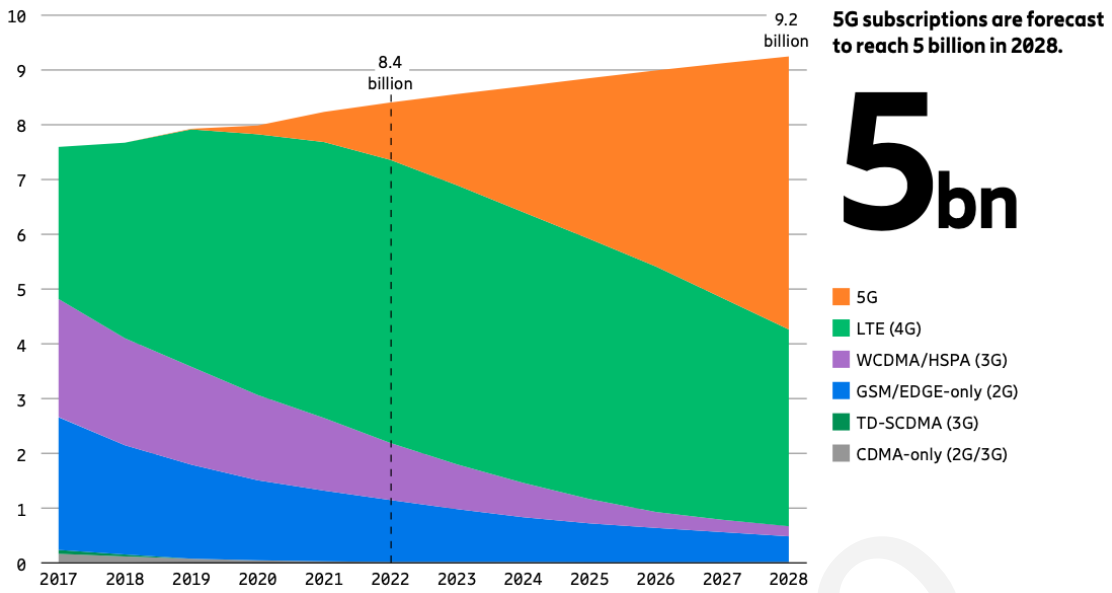

Figure 1.1: Mobile subscriptions (Source: Ericsson)

our increasingly digital world.

1.1 Motivation

Over the past two decades, cellular networks have experienced extraordinary growth in the number of mobile subscribers. According to the latest Ericsson mobility report [1], 5G subscriptions are forecast to reach 5 billion in 2028 (see Figure 1.1), while the total number of connected wireless devices is expected to reach almost 30 billion. This remarkable surge is predominantly driven by the rapid expansion of IoT devices, which are contributing significantly to the rise in global connectivity [2]. The proliferation of IoT devices offers numerous benefits, including enhanced efficiency, productivity, and convenience in various sectors such as healthcare, agriculture, manufacturing, and home automation. Additionally, the broad adoption of IoT devices supports the development of smart cities and infrastructure, enabling real-time monitoring, predictive maintenance, and data-driven decision making, significantly improving the quality of life and promoting sustainable development [3–5].

The unprecedented increase in IoT devices introduces substantial pressure on network infrastructures due to the surge in data traffic, and this, in turn, poses significant challenges in terms of ensuring adequate network capacity, data transfer rates, and energy efficiency. Although 5G technology has made significant advancements in accommodating the burgeoning IoT ecosystem, the anticipated volume of

Yuan Guo

future connections, coupled with their sophisticated requirements, calls for the development of a more advanced technological solution. This necessitates the inception of 6G of wireless communication technology. 6G promises to revolutionize the way we connect, not just in urban centers but across varied landscapes and scenarios [4–6]. In urban areas, 6G will enable dense networks to manage the increasing data traffic efficiently, while in remote regions, it aims to bridge the digital divide through enhanced connectivity options, including satellite integration [7]. Moreover, 6G will be instrumental in vehicular networks, supporting high-mobility scenarios crucial for the future of autonomous and connected vehicles [8,9]. Therefore, a key distinguishing feature of 6G is its versatility in supporting highly diverse scenarios, making it a quintessential technology for an increasingly interconnected and mobile world.

As we venture into the era of 6G, with its capability to support an unprecedented range of scenarios, the issue of energy consumption and management comes to the forefront [10]. The escalating data rates and the increasing number of mobile devices in 6G networks inevitably lead to a substantial rise in energy consumption [11]. Moreover, the operational lifetime of these battery-operated mobile devices is a pivotal factor affecting network reliability and efficiency. Therefore, ensuring sustainable energy supplies and utilizing energy-efficient communication techniques is critical for maintaining uninterrupted operation and enhancing device longevity, which is essential in the varied environments 6G aims to serve [12]. Conventional methods like frequent battery replacement or energy extraction from natural resources are often unpredictable, unstable, costly, and sometimes unfeasible, especially in less accessible or highly dynamic environments. In light of these challenges, the integration of wireless power transfer technologies within 6G infrastructures emerges as a compelling solution. Specifically, the co-design of information and energy signals via simultaneous wireless information and power transfer (SWIPT) stands out. SWIPT uniquely combines the transmission of data and energy in a single process, offering a solution to the growing energy demands of wireless networks. It facilitates continuous operation of low-power devices, eliminates the need for physical charging connections, and reduces maintenance and infrastructure costs. This approach is particularly synergistic with 6G's vision of ubiquitous, reliable, and efficient connectivity across a wide range of scenarios, from densely populated urban centers to remote areas, and even in high-mobility contexts such

Yuan Guo

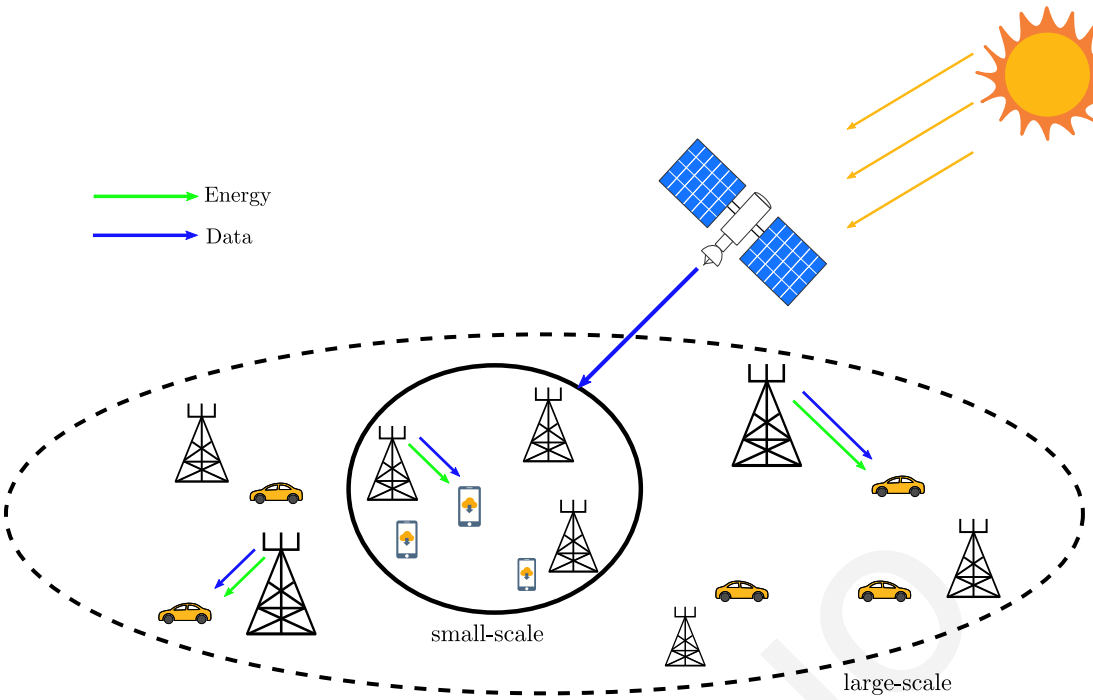

Figure 1.2: System diagram

as vehicular networks [11–15]. Hence, the adoption of SWIPT in 6G networks marks a crucial step towards achieving energy-efficient, uninterrupted wireless communication, essential for the diverse and demanding scenarios envisioned in the next generation of mobile connectivity.

1.2 Thesis outline and contributions

This thesis provides insights into the implementation of wireless information and power transfer techniques in 6G mobile networks, with the special focus on SWIPT technology, where an overall system diagram is illustrated in Figure 1.2. Additionally, multiple techniques are proposed to enhance the performance of both information and power transfer, such as advanced signal processing, network optimization, interference and mobility management, as well as user association techniques. The primary focus lies in the system-level analysis of SWIPT-enabled 6G networks in various scenarios, such as finite- and infinite-area networks, vehicular networks, high-mobility environments, etc. By leveraging tools from stochastic geometry, we establish analytical frameworks that incorporate key features of these cellular networks. Furthermore, we have conducted a thorough comparison of our proposed techniques against the latest state-of-the-art schemes, showcasing the significant ad-

Yuan Guo

vancements. The outline of this thesis, together with the publications supporting our contributions, is as follows, where the research focus of each chapter is also summarized in 1.1, and a road-map of the thesis is shown in Figure 1.3.

Table 1.1: Research focus in each chapter

Chapter	3	4	5	6	7	8
WPT	✓	✓	✓	✓	-	✓
Mobility	✓	-	✓	✓	-	-
System-level analysis	✓	✓	✓	✓	✓	-
Non-terrestrial networks	-	-	-	-	✓	✓

In Chapter 2, we provide preliminaries so that the concepts of this thesis are comprehensible. In particular, we introduce the concepts of SWIPT, focusing on the fundamental principle of integrating SWIPT into cellular networks. Moreover, we introduce state-of-the-art models for the analysis of the SWIPT-enabled mobile networks, while several technical designing challenges are discussed. The second part of the chapter focuses on the analysis of these networks with the aid of stochastic geometry, providing key results and important assumptions that are adopted throughout this thesis.

Firstly, in Chapter 3 and Chapter 4, we mainly focus on the interference management and mitigation techniques. In specific, in Chapter 3, we investigate SWIPT-enabled next-generation cellular networks under two types of network typologies, namely, the small- and large-scale cellular networks. We propose a low complexity antenna pair switching technique for SWIPT in the context of large-scale cellular networks, by taking into account the interference correlation between multiple receiver's antennas. Additionally, in order to alleviate the inter-cell interference and energy consumption, a novel cell sleeping technique is proposed in the context of small-scale finite-area network. Furthermore, in Chapter 4, by aiming to further enhance the SWIPT performance and to address the interference correlation issue discussed in Chapter 3, we investigate the performance of a linear minimum mean square error (MMSE) receiver with a successive interference cancellation (SIC) technique in the context of SWIPT-enabled cellular networks. Our results show that all aforementioned techniques can effectively improve the SWIPT performance. The content of these two chapters is based on the materials in:

Yuan Guo

- Y. Guo, C. Skouroumounis and I. Krikidis, "A Linear MMSE Receiver for SWIPT-enabled Wireless Networks," in *Proceedings of IEEE Vehicular Technology Conference,* London, United Kingdom, Sep. 2022, pp. 1-6.

- Y. Guo, C. Skouroumounis and I. Krikidis, "Joint Information and Energy Transfer of SWIPT-Enabled Mobile Users in Wireless Networks," *IEEE Transactions on Green Communications and Networking*, vol. 6, no. 2, pp. 1141-1156, Jun. 2022.

- Y. Guo, C. Skouroumounis and I. Krikidis, "A Linear MMSE Receiver for Multi-Antenna SWIPT-enabled Wireless Networks," in *Proceedings of IEEE International Conference on Communications*, Seoul, Korea, May 2022, pp. 3166-3171.

- Y. Guo, C. Skouroumounis and I. Krikidis, "Threshold-Based Pair Switching Scheme in SWIPT-Enabled Wireless Downlink System," in *Proceedings of IEEE Vehicular Technology Conference*, Helsinki, Finland, Apr. 2021, pp. 1-7.

Then, in Chapter 5 and Chapter 6, we study the mobility management schemes and explore the performance of SWIPT-assisted vehicular networks. More specifically, in Chapter 5, we study the SWIPT technology with the employment of coordinated multi-point (CoMP) transmission, in the context of a novel coverage area-based base stations (BSs) selection scheme. The proposed technique aims at reducing the handover rate for high-mobility users and enhancing the SWIPT performance. Our results show that the CA-CoMP scheme offers significant gains over conventional CoMP schemes, in terms of SWIPT performance. Furthermore, in Chapter 6, we investigate a SWIPT-enabled vehicular network. By utilizing SWIPT technology, battery-operated road-side sensors simultaneously receive control information and harvest energy from cellular BSs, subsequently using the harvested energy to spread data to vehicles. We demonstrate the optimal values of multiple system parameters that offer the highest downlink performance. These chapters include the materials in:

- Y. Guo, C. Skouroumounis and I. Krikidis, "A Coverage Area-Based CoMP Technique for SWIPT-Enabled Mobile Networks," *IEEE Transactions on Green Communications and Networking*, vol. 7, no. 4, pp. 1807-1822, Dec. 2023

- Y. Guo, C. Skouroumounis and I. Krikidis, "A Coverage Area-Based Cooperation Technique for SWIPT- Enabled Systems with Mobility," in *Proceedings of*

Yuan Guo

IEEE Global Communications Conference, Madrid, Spain, Dec. 2021, pp. 1-6.

- Y. Guo, E. Faddoul, C. Skouroumounis, and I. Krikidis, "Simultaneous wireless information and power transfer-assisted vehicular networks," in progress.

Moreover, in Chapter 7 and Chapter 8, we investigate the wireless information and power transfer (WIPT) performance of low Earth orbit (LEO) satellite-based networks. Specifically, we take into account the heterogeneous nature of real-world LEO satellite networks and propose three association schemes for the LEO satellite-based cellular networks. Moreover, we explore the flexibility of LEO satellite-based space solar power (SSP) system. These two chapters are based on the materials in:

- Y. Guo, C. Skouroumounis and I. Krikidis, "Large-scale Heterogeneous Ultra-dense LEO Satellite-based Cellular Networks," in *Proceedings of IEEE International Conference on Communications,* Rome, Italy, May 2023.

- Y. Guo, E. Faddoul, C. Skouroumounis and I. Krikidis, "LEO Satellite-based Space Solar Power Systems," in *Proceedings of IEEE International Conference on Acoustics, Speech, and Signal Processing Workshop*, Rhodes Island, Greece, Jun. 2023.

- Y. Guo, C. Skouroumounis, S. Chatzinotas and I. Krikidis, "On User Association in Large-Scale Heterogeneous LEO Satellite Network," submitted in *IEEE Transactions on Aerospace and Electronic Systems*.

Finally, in Chapter 9, we conclude the thesis with a summary of the main contributions and a discussion on potential directions for future work, such as SWIPT-assisted integrated sensing and communications (ISAC) systems for vehicular networks, as well as the integration of SWIPT into non-terrestrial networks.

Yuan Guo

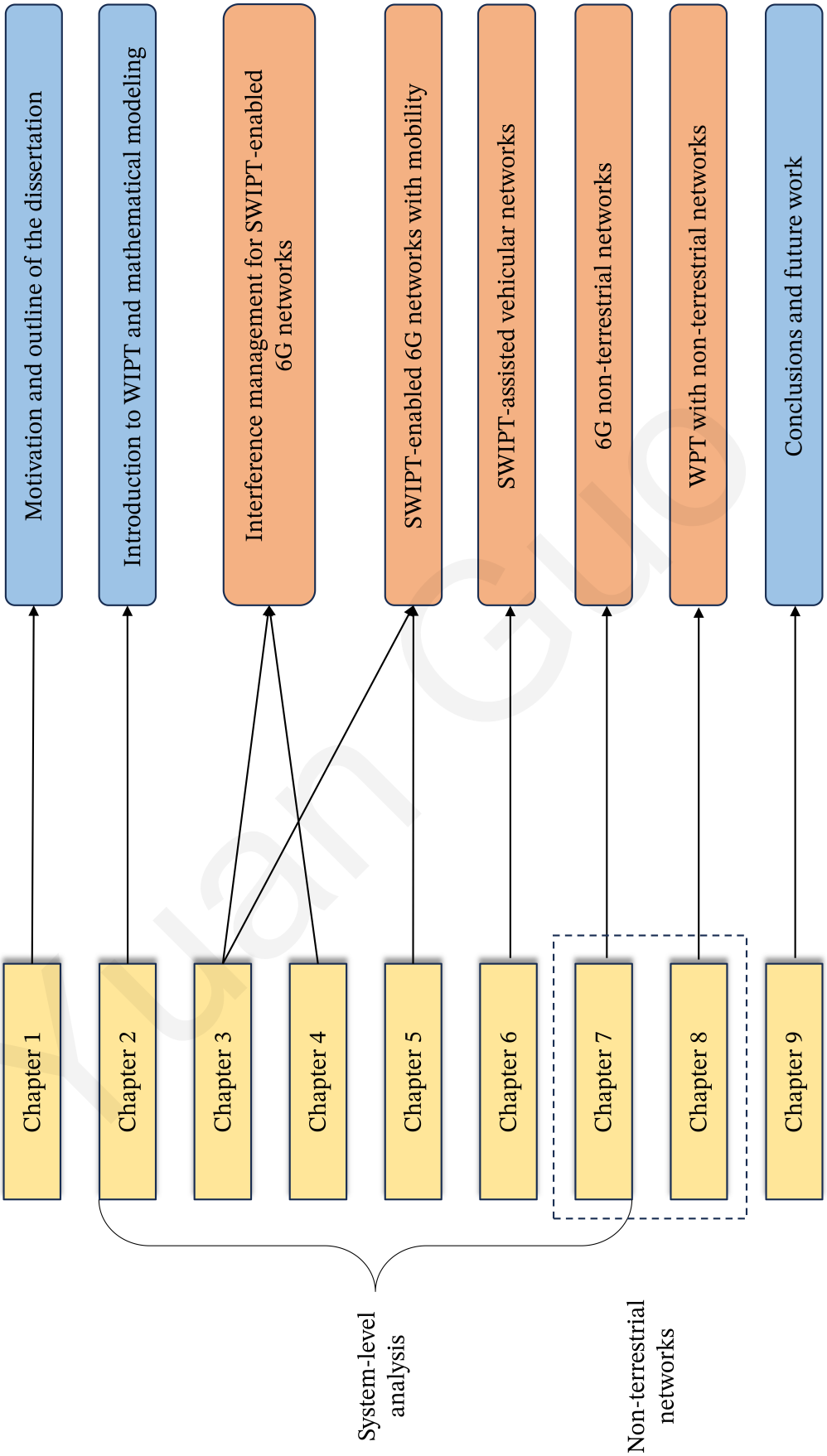

Figure 1.3: Road-map of the thesis.

Chapter 2

Background

SWIPT appears as a promising and attractive technology for 6G wireless networks, which are largely characterized by the massive connectivity of lower-power IoT devices. SWIPT enables the dual use of radio frequency (RF) signals to simultaneous convey information and energy to the end-users, acting as a sustainable solution to the energy challenges of battery-powered IoT devices [11]. In this chapter, we delve into an extensive overview of the fundamental principles of SWIPT. Moreover, we highlight several challenges of integrating SWIPT in 6G networks along with the potential solutions. Finally, we introduce the mathematical preliminaries for the system-level analysis of SWIPT-enabled mobile networks, along with the baseline system model for this thesis.

2.1 Wireless power transfer

In recent years, there has been a lot of interest in integrating WPT technologies into conventional communication networks. On the one hand, the extensive deployment of low-power, battery-operated IoT devices necessitates the implementation of innovative sustainable power supply methods. In this context, WPT emerges as an ideal solution to address such energy challenges. On the other hand, the inherent capability of WPT to utilize RF signals renders it naturally compatible with wireless communication networks [11,13,14]. The fundamental principle of WPT is based on the concept of electromagnetic fields, where electrical energy can be converted into electromagnetic waves that propagate through space. By leveraging different techniques, WPT enables devices to receive and harvest energy from dedicated sources

Yuan Guo

or even ambient wireless transmitters in the environment [16–18]. Transferring electromagnetic power wirelessly encompasses a wide range of techniques, which can be largely classified into three distinct cases [13]:

- **Near field power transfer**: by employing inductive, capacitive, or resonant coupling, electromagnetic power is transferred wirelessly over short distances of up to one meter (sub-wavelength). This technique has been widely utilized for the practical applications, such as wireless charging pads for smartphones, tablets, smartwatches, etc.

- **Far field directive power beaming**: by deploying directive antennas and/or antenna arrays to generate highly-directional power beam, electromagnetic power is conveyed at distances of up to several meters in indoor and outdoor environments. With the massive deployments of multiple-antenna wireless systems, such technique has attracted a lot of interest from both academia and industry, while the initial prototypes and testing platforms have been created.

- **Far field, low-power, ambient RF power collection**: receivers harvest power transmitted from random ambient transmitters, such as BSs, WiFi routers, mobile devices, etc. It has several unique benefits such as the low cost of deployment and compatibility with existing communication systems.

It is clearly evident that each method unfolds its unique advantages and corresponding challenges. In specific, near field power transfer, while notably efficient, is fundamentally restricted by distance, limiting its potential for applications that necessitate longer reach. Contrarily, far field directive power beaming widens its coverage significantly, stretching to several meters. However, it is inherently limited by the requirement for a highly focused, directional power beam. These factors spotlight the appeal of the third method: *far field, low-power, ambient RF power collection*. By leveraging power from random public transmitters, this method offers an ingenious solution that blends effortlessly with the existing wireless communication network. Therefore, we mainly focus on the *far field, low-power, ambient RF power collection* scenario throughout this thesis.

Yuan Guo

2.1.1 Simultaneous wireless information and power transfer

SWIPT takes the concept of WIPT one step further by allowing the concurrent transmission of data and power over the same channel, which enables significant gains in terms of spectral efficiency, time delay, energy consumption and interference management by superposing information and power transfer [13,14,19–23]. The SWIPT technology is typically operated through three main schemes as illustrated in Figure 2.1, namely, time switching (TS), power splitting (PS) and antenna switching (AS), of which the implementation procedures are summarized as following [13,14,19]

- **TS scheme**: the receiver switches in the time domain between information decoding (ID) and energy harvesting (EH). In this case, signal splitting is performed in the time domain. The TS technique allows for a simple hardware implementation at the receiver but requires accurate time synchronization and information/energy scheduling.

- **PS scheme**: PS scheme achieves SWIPT by splitting the received signal into two streams of different power levels using a PS component; one signal stream is converted to baseband for ID purpose, while the other one is directed to the rectenna for EH. The PS scheme leads to higher receiver complexity compared to TS due to the extra PS component; while it achieves instantaneous SWIPT, as the signal received in one time slot is used for both ID and EH. It is more suitable for applications with critical information/energy or delay constraints.

- **AS scheme**: AS scheme dynamically switches each antenna element between decoding/rectifying to achieve SWIPT in the antenna domain. More specifically, a receiver divides the receiving antennas into two groups where one group is used for ID and the other group for EH [13,14]. Owing to the massive deployments of multiple-antenna systems, AS becomes a promising technique for enhancing both ID and EH performance of SWIPT-enabled communication networks.

In order to achieve SWIPT, a typical receiver includes a receiver antenna or antenna array, a matching network, a RF to direct current (RF-to-DC) converter or rectifier, a power management unit, the energy storage unit, as well as a communication module [13,24]. Among these blocks/units, the RF-to-DC converter or rectifier is

Yuan Guo

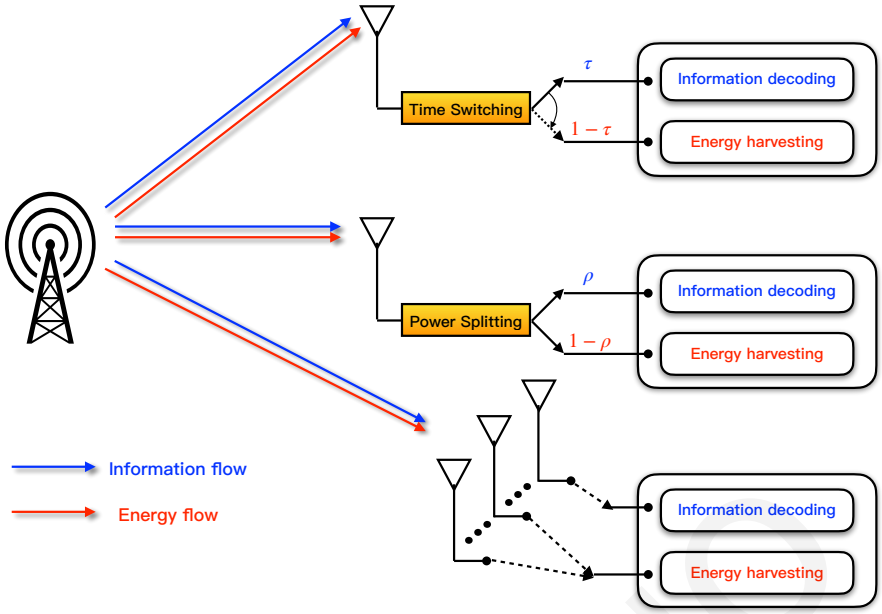

Figure 2.1: Illustrations for TS, PS, and AS schemes.

the most critical component, which poses significant challenges on both circuit design and theoretical modelling. The analytical model for the RF-to-DC converter is introduced later in the chapter.

2.1.2 Design challenges for SWIPT-enabled 6G networks

Integrating SWIPT into upcoming 6G networks presents an immense potential to meet the dual needs of information processing and energy conservation for the burgeoning population of low-power IoT devices. However, this integration introduces a complex set of design challenges that must be thoroughly examined, understood, and tactfully resolved to guarantee optimal system performance, seamless deployment, and long-term viability. By taking into account the unique features of 6G networks, such as ultra-dense deployments, multiple-antenna devices and high-mobility end-users, and satellite-based non-terrestrial networks, etc., we summarize four main concerns of this thesis for deploying SWIPT technology, as follows

- **Spatial modelling**: as aforementioned, *far field, low-power, ambient RF power collection* is regarded as the most promising solution for integrating SWIPT in the modern wireless communication networks, owing to its unique benefits, such as low-cost deployment and high-compatibility with existing communication systems. On the one hand, the ultra-dense deployments of wireless

transmitters (e.g. BSs) and end-users (e.g. IoT devices) in 5G/6G networks, produce rich RF signals in the environment, which boost the EH performance of SWIPT-enabled devices. On the other hand, the densification of cellular networks and users poses significant challenges on network spatial modelling and analysis. To address such challenges, *stochastic geometry* is extensively used for modelling the large-scale networks [19, 25–31], where the main idea is modelling the locations of network nodes as Point Process (PP). Although stochastic geometry tools have been utilized in large-scale cellular networks for over three decades, their application in the context of SWIPT-enabled networks still lacks comprehensive development and in-depth analysis.

- **Multiple-antenna system**: with the widespread application of multi-antenna technology, the field of communication networks has seen significant advancements in terms of data rates, reliability, and coverage [3, 14, 32–37]. Despite these benefits, integrating multiple-antenna systems into SWIPT-enabled networks presents a host of unique challenges. Among the most prominent issues is the complexity involved in simultaneously managing the dual functions of ID and EH in a multi-antenna context. The design and implementation of robust and efficient AS mechanisms become exponentially more challenging as the number of antennas increases. These systems also require advanced signal processing techniques to handle the high dimensionality of multi-antenna systems, which can significantly increase the computational burden and often leads to intractability for theoretical analysis. Hence, developing efficient and low-complexity AS techniques to manage dual-functionality of SWIPT for satisfying various ID and EH requirements of IoT devices, and establishing a tractable framework for theoretical analysis, form an essential cornerstone of current research efforts.

- **Mobility**: the ultra-densification of BSs, coupled with the rise in user mobility propelled by modern advancements in transportation systems, has led to a significant increase in the user handover rates, making mobility issues ever more critical. Furthermore, 5G and 6G networks rely heavily on beamforming techniques to achieve network coverage, which amplifies the impact of mobility, i.e. high user mobility necessitates frequent beam switching, introducing another layer of complexity to network management [27, 38–40]. Addressing

Yuan Guo

these multifaceted challenges begins with developing precise mobility models. These models are instrumental in understanding the impact of increasing mobility on SWIPT-enabled networks, thus laying a critical groundwork for formulating effective management strategies. Moreover, the crafting of innovative mobility management solutions, complemented with advanced cell association and handover schemes, is crucial for streamlining the signalling costs, efficiently managing uneven traffic or user distribution, and ultimately enhancing the performance of SWIPT-enabled networks.

- **WIPT with satellite networks**: as we transition from 5G to 6G, satellite communication networks are anticipated to play a pivotal role in realizing the vision of a fully connected and intelligent world. Satellite communications can significantly contribute to achieving the goals of 6G by providing seamless global coverage and enhanced connectivity in remote, rural, and underserved areas, as well as reinforcing the resilience of communication networks in disaster-stricken regions [41–43]. Moreover, satellite-based energy transmission platform, i.e. SSP system, is a potential candidate that addresses the global energy challenges (e.g. high dependence on fossil fuels, climate change, limited energy access, and infrastructure needs) [44–47]. Despite the promising capabilities, designing a satellite-based system for WIPT is a complex and challenging task, demanding significant technological breakthroughs and careful harmonization of a wide range of intricate factors.

2.1.3 Related work

In this section, a comprehensive overview of SWIPT in the context of large-scale networks is presented. We introduce the state-of-the-art spatial modeling tools, highlight the open questions of SWIPT-enabled multiple-antenna system, and give several examples from the literature related to mobility and handover issues in 5G/6G mobile networks. Further, we provide an overview of LEO satellite-based communication networks and SSP system. For convenience, we summarize the main state-of-the-art literature and our unique contributions of this dissertation in Figure 2.2.

The SWIPT technology in the context of large-scale networks has been widely-investigated in the literature, which is typically categorised as *system-level analy-*

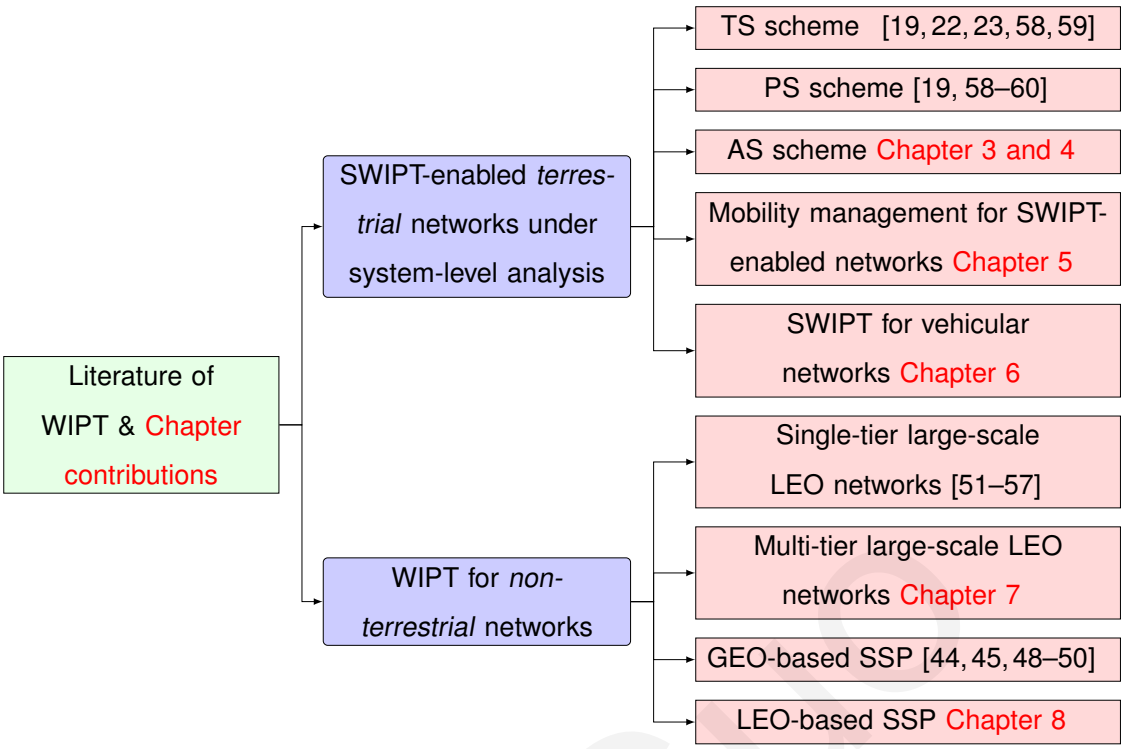

Figure 2.2: State-of-the-art literature and chapter contributions overview

sis [11]. The authors in [61] proposed a stochastic geometry-based framework for the analysis of SWIPT-enabled multiple-input multiple-output (MIMO) systems, and the trade-off between the data rate and the harvested energy was illustrated. In [19], the authors investigated the simultaneously joint ID and EH performance under TS and PS schemes, and the optimal partitioning parameters to achieve maximum joint ID and EH performance were demonstrated. The authors in [20] examine the trade-off between information rate and energy harvested in SWIPT-enabled networks, assessing the impact of obstacles and studying the stochastic behaviour of signal attenuation and multi-user interference. In [21], application of SWIPT in networks employing cooperative non-orthogonal multiple access (NOMA) is investigated with imperfect channel state information (CSI). Furthermore, the authors in [22] study the SWIPT with the employment of cell-free massive technologies in a network with randomly placed access points, by proposing a new energy storing scheme and by exploring the trade-off between EH and data rate, while the results suggest allocating more power to energy users can boost overall EH performance without significantly affecting other users. The authors in [23] explore the use of SIC technique in the context of SWIPT in a bipolar ad hoc network, and demonstrate that SIC could lead to considerable energy gains and, under certain scenarios, the

Yuan Guo

average harvested energy could reach its maximum limit. In [62], the idea of SWIPT in intelligent reflecting surface (IRS)-assisted cellular networks was explored, highlighting that the IRSs can promote the compensation of high RF signal attenuation over long distance and hence create efficient energy harvesting/charging zones in their vicinity. Most of the above work focuses on SWIPT-enabled networks that are based on protocols with either PS or TS schemes. Nevertheless, the strict synchronization constraint for the TS approach and the demand of the adequate PS circuit for the PS scheme, increase the complexity and cost of the required hardware [63]. AS scheme, on the other hand, is a promising low-complexity alternative approach which is overlooked from the current literature. Furthermore, even though SWIPT technology is well-investigated in the literature, most of the exiting works assume a simplistic linear EH model [13, 14, 19]. Nevertheless, in practice, the conversion process is a highly non-linear function and its impact on the network performance is not well studied [64–66]. In particular, by taking into account the non-linear nature of the rectification process, the authors in [64] propose a non-linear EH model capturing the dynamics of the RF energy conversion process for different input power levels, where the amount of the harvested energy is modelled based on a parametric logistic function. Furthermore, an alternative non-linear EH model is proposed in [65, 66], where the random noise in the detection and conversion of the actual harvested energy is considered, offering tractability for system-level analysis in wireless-powered networks.

The enormous amount of wireless connections that will host 6G mobile networks, leads to an unprecedented increase of inter-cell interference, which compromises the ID performance of the end-users. For the SWIPT-enabled multi-antenna receivers, the interference observed across different antenna elements is spatially correlated [61] [67]. While it has been long recognized that the correlated fading reduces the performance gain of multi-antenna communication systems, the concept of interference correlation has been overlooked until recently. Such spatial correlation of interference power affects the diversity gain of the system, especially in high path-loss environments [67]. In [68], the authors dealt with the interference correlation issues of the multiple-antenna users and characterized the performance of a maximum ratio combining (MRC) in the presence of spatially-correlated interference across antennas. In [69], the authors characterized the spatiotemporal interference correlation as well as the joint coverage probability at two spatial lo-

Yuan Guo

cations in a cellular network and showed that the interference correlation and the joint coverage probability decrease with the increase of the users' speed. By taking into consideration the interference impact, the linear MMSE receiver is indicated to achieve a maximum output signal-to-interference-plus-noise ratio (SINR) [35, 36]. The authors in [36] derive the exact distribution for the output SINR of an ideal linear MMSE receiver, where multiple interferers and Rayleigh fading channel are considered. This work is further extended in [35], by considering a random number of interferers, illustrating the optimal network density that offers the highest network spatial throughput. Although the performance of the MMSE receiver has been extensively studied, the co-design of SWIPT and MMSE is overlooked from the literature.

Mobility of wireless nodes is another key issue that has a fundamental impact on the performance of 5G/6G wireless networks [4–6, 26–29, 38–40, 70]. In general, mobility leads to the uneven traffic/users distribution under certain scenarios, increases cell handover rate/signalling cost, and poses significant challenges on beam management [26–28, 38]. In order to efficiently manage mobility, it is crucial to have a tractable and accurate theoretical mobility model that enables a comprehensive understanding of the behavior exhibited by diverse mobile users. Since it is difficult to obtain actual movement patterns, a common approach is to use synthetic mobility models which resemble the behaviour of actual mobile devices. Over the past decade, several research efforts have been carried out on characterizing the performance of a variety of wireless networks under several standard mobility models [71–73]. Due to its generality and tractability, the most commonly used mobility model is the random waypoint (RWP) model [73–75]. A detailed analytical framework of the spatial node distribution generated by the RWP model was first investigated in the context of ad hoc networks in [73]. The authors in [74] investigated two key parameters in the mobile networks, namely, handover rate and sojourn time, based on the RWP model with infinite network area. Moreover, the RWP model was utilised to characterize the performance for an infinite drone cellular network in [75]. In the context of small cells, where the coverage area is finite due to the high path-loss experienced by the RF signals [76], it has been noticed in [77, 78], that the spatial distribution of the nodes that move according to the RWP model is non-uniform. Nevertheless, the majority of existing analytical results assumes uniform/homogeneous spatial deployments. Therefore, an analytical framework is

Yuan Guo

required, which takes into account the occurred non-uniform deployment of network nodes due to their mobility in finite areas. In [77], several geometries of finite network areas, e.g. circular, square, hexagon areas, were investigated based on the RWP model, while it has been proven that the employment of RWP-based mobility model results in the concentration of the nodes around the center of the area. Similarly, the authors in [78] demonstrated that in the finite area mobile networks, the mean interference at the center under the RWP model was much higher than the interference at the border of the network area.

As mentioned before in this chapter, mobility not only results in uneven traffic distribution under certain scenarios, but also leads to increasing signalling cost and complexity of handover. 5G/6G networks, with the ultra-dense nature, are composed of a larger number of small cells. In such networks, handover executions occur more frequently since a user crosses more cells along it's trajectory and moves inside each cell for a limited time. In this case, the handover cost increases significantly and becomes crucial for a mobile users' performance in terms of the average throughput. Furthermore, due to the immense deployment of IoT applications in 6G networks, the unprecedented increment of the interference becomes a crucial factor, jeopardizing the ID performance of the end-users. Motivated by this, the CoMP transmission technique is proposed to enhance the link reliability of the mobile networks, by improving the intended received signal strength and by mitigating the multi-user interference [28, 29, 79]. On the one hand, it has been shown that the CoMP technique can effectively enhance the system performance. In particular, the authors in [79] demonstrate the aforementioned behaviour by investigating the CoMP technique in a downlink heterogeneous cellular network and revealing the significant gain achieved in terms of coverage probability. On the other hand, the multi-connection of a user with multiple BSs generally leads to more frequent handovers, alleviating the network performance due to the heavy signalling cost [28,29]. Specifically, the authors in [28] study the CoMP technique in the context of user-centric cooperation networks, where analytical expressions for the handover rate are derived, revealing that the handover rate is greatly increased by the CoMP operation. By aiming to decrease the handover rate, the authors in [29] propose a movement-aware CoMP handover scheme that exploits the trajectory and the cell dwell time of the users, to ensure a lower inter-cell handover rate. Nevertheless, the severe signalling overhead required by the cooperative techniques makes such

Yuan Guo

approaches impractical for users with scarce power resources, thus motivating the investigation of energy-efficient low-complexity techniques. Furthermore, to unlock the full potential of 6G communication networks, multiple-antenna techniques such as transmit beamforming, are essential solutions to enhance the link reliability and improve the data rate. Despite their many advantages, these techniques pose several new challenges for 6G mobile networks, such as heavy handover signalling cost [38]. Specifically, in addition to the inter-cell handover, another type of handover, namely beam reselection or *intra-cell* handover should be taken into account [27,38]. More specifically, the authors in [27,38] study the beam management based on stochastic geometry, where a closed-form expression for the beam reselection rate is analytically derived and the optimal number of beams that ensures maximum spectral efficiency is demonstrated. By taking into consideration both the inter- and intra-cell handover, the authors in [70] propose an evolutionary game theory-based approach to solve the problem of access model selection, aiming at improving the spectral efficiency in sub-6 GHz/millimetre-wave cellular networks. Moreover, the authors in [40] propose a velocity-based cell association technique in the context of multi-tier cellular networks, aiming to reduce the beam reselection overheads and improve the data rate, by associating users with different network tiers according to their velocities. Recently, the authors in [39] study the beam management in the context of vehicular communication networks, providing analytical expressions for the average number of beam switching and handover events.

Owing to the unique benefits of LEO satellites, such as minimal latency, superior spatial flexibility, and low-cost deployment, the employment of LEO satellites has emerged as an attractive solution for 6G networks [80, 81]. Over the past few years, approximately 4,700 LEO satellites have been successfully launched by various companies, including SpaceX, Amazon, and OneWeb, with the goal of providing satellite-based cellular services [51,52]. However, the proliferation of LEO satellites and mega constellations pose significant challenges on network modelling, design and analysis, necessitating the employment of sophisticated mathematical tools that accurately capture the characteristics of large-scale LEO satellite networks. Recently, tools from the field of stochastic geometry have been leveraged to analyze the performance of large-scale LEO satellite-based communication systems, highlighting its effectiveness as a powerful and tractable mathematical tool for assessing the impact of key parameters on network performance [51, 55, 57, 82, 83]. Specif-

Yuan Guo

ically, the authors in [51] study the performance of large-scale LEO satellite communication networks, illustrating the impact of satellites' density and constellation altitude on the coverage and communication latency. Moreover, the authors in [55] investigate the coverage performance of LEO satellite networks, by assuming that the satellite spatial deployment follows a homogeneous Poisson PP (PPP), where a novel path-loss model is introduced for the satellite communication networks. This work is further extended in [57], where the optimal satellite altitude for attaining the highest coverage probability is numerically investigated. Furthermore, the authors in [82] study the downlink performance of LEO satellite-based networks by modelling the spatial deployments of LEO satellites according to a homogeneous binomial point process (BPP) and by proposing an iterative algorithm to maximize the transmission rate and system throughput. The authors in [83] employ stochastic geometry to analyze uplink performance of large-scale LEO satellite networks, demonstrating the optimal LEO satellite density for achieving the maximum ergodic capacity. Additionally, the authors in [54] adopt a non-homogeneous PPP to model a massive LEO network and demonstrate the optimum altitude of LEO satellites as well as number of orthogonal frequency channels for achieving the highest network throughput. Nevertheless, these studies highlight the capability of stochastic geometry in modelling large-scale LEO satellite-based networks, under the assumption that all LEO satellites are deployed at the same altitude, opposed to real-world LEO satellite-based networks that exhibit significant heterogeneity [51,52,81].

2.2 Mathematical modeling

In this section, we will initially introduce some mathematical preliminaries from the stochastic geometry theory that are widely used in the literature, mainly focusing on the spatial modeling of the cellular networks. Moreover, we provide the baseline system model for this thesis, such that extensions to this model are highlighted in the following chapters as needed.

2.2.1 Introduction to point process

As previously discussed in this chapter, the stochastic geometry approach is a powerful mathematical framework that recently gained momentum as the only available

Yuan Guo

tool that provides a rigorous approach to model, analyze and design the current cellular networks [25, 30, 31]. A wireless communication network can be viewed as a collection of nodes located within a certain area, each capable of acting as either a transmitter or receiver of signals. At any given moment, several nodes may broadcast simultaneously, each transmits signals to their own specific receiver. As a result, apart from its own intended signal, a receiver also receives signals from the other active transmitters, i.e. interference. Hence, the SINR is a random variable that strongly depends on the network geometry and significantly varies from one receiver to another and from one time instant to another. Therefore, the spatial configuration of the nodes is crucial to the network efficiency as it directly affect the SINR at each receiver. To this end, stochastic geometry tools provide a natural way to define and calculate the macroscopic properties of such networks by averaging over all potential network topologies and weighting them by the probability of their occurrence. More specifically, stochastic geometry involves treating such networks as snapshots of a stationary random model in the entire Euclidean plane or space, and analysing them in a probabilistic way. [30]. The most basic stationary random models studied in the stochastic geometry are the multidimensional PPs, which can be depicted as a random collection of points in the d-dimensional space, describing the deployment of the network's nodes [25]. Probabilistic analysis of these PPs provides a way to estimate spatial averages that tend to reflect key dependencies in network performance characteristics (connectivity, stability, capacity, etc.) as a function of a relatively small number of parameters. Importantly, the empirical validation of our stochastic geometry-based model against actual network deployments has underscored its accuracy and reliability in reflecting real-world conditions. This validation not only reinforces the model's utility in capturing the complex dynamics of wireless communication networks but also highlights its crucial role in guiding the strategic planning, development, and optimization of scalable, heterogeneous networks, aligning closely with industry requirements and the practical challenges of deploying next-generation wireless infrastructures.

A PP can be described in statistical terms by defining the space of possible outcomes and then specifying the probabilities of different events. Let $\mathfrak{N}$ be the set of all point patterns in the d-dimensional Euclidean space $\mathbb{R}^d$, such that any point pattern $\Phi \in \mathfrak{N}$ is (i) finite, i.e. any bounded subset $B \subset \mathbb{R}^d$ contains only a finite number of points, and (ii) simple, i.e. $x \neq y$ for any $x, y \in \Phi$. We use the nota-

tion $N(B)$, to denote the number of points of the pattern Φ in the subset B, which is given by $N(B) = \sum_{i=1}^{\infty} \mathbb{1}(x_i \in B)$, where $\mathbb{1}(X)$ is an indicator function that is equal to $\mathbb{1}(X) = 1$ if X is true, otherwise $\mathbb{1}(X) = 0$. Finally, let $\mathcal{N}$ be the smallest sigma algebra and $(\Omega, \mathcal{F}, \mathbb{P})$ be a probability space, where Ω denotes the sample space, $\mathcal{F}$ is the set of the events and $\mathbb{P}$ corresponds to the mapping, which assigns probabilities to the events. Based on the aforementioned notation, we first give a formal definition of a PP.

Definition 2.1 (Point Process). *A PP $\Phi = \{x_1, x_2, \cdots\} \subset \mathbb{R}^d$ is a measurable mapping from a probability space $(\Omega, \mathcal{F}, \mathbb{P})$ to $(\mathfrak{N}, \mathcal{N})$, i.e.*

$$\Phi : \Omega \to \mathfrak{N}. \tag{2.1}$$

The average number of the random variables $x_i \in \Phi$ included in a subset $B \subset \mathbb{R}^d$, represents the intensity measure of the PP, and is defined as follows.

Definition 2.2 (Intensity Measure). *The intensity measure Λ of a PP Φ is defined as*

$$\Lambda(B) = \mathbb{E}\left[N(B)\right], \quad \forall B \subset \mathbb{R}^d, \tag{2.2}$$

and if Φ is stationary, the density of the PP Φ, is given by

$$\lambda = \frac{\mathbb{E}\left[N(B)\right]}{|B|},$$

where $|B|$ represents the area of $B \subset \mathbb{R}^d$, which contains only a finite number of points.

In the context of stochastic geometry, there are several basic yet important PPs, however, the most well-studied and most widely used PP is the PPP. Its importance mainly results from its convenient properties as a mathematical model as well as being mathematically interesting [26–28, 30, 31]. In the following sections, we introduce the formal definitions of the PPP, which is extensively used in this thesis.

Definition 2.3 (Poisson Point Process). *A PPP $\Phi = \{x_1, x_2, \cdots\} \subset \mathbb{R}^d$ with intensity measure Λ is a PP such that:*

- *$\forall B \subset \mathbb{R}^d$, $N(B)$ has a Poisson distribution with mean $\Lambda(B)$. If Λ admits a density λ, we may write*

$$\mathbb{P}(N(B) = k) = \exp\left(-\int_B \lambda(x)dx\right) \frac{\left(\int_B \lambda(x)dx\right)^k}{k!}, \tag{2.3}$$

  where $\lambda(x)$ denotes the density function of the PPP.

Yuan Guo

- *If $B_1, B_2, \cdots, B_m$ are disjoint bounded subregions of the underlying space, then the number of the points in each bounded subregion, i.e. $N(B_1), N(B_2), \cdots, N(B_m)$, will be completely independent to all the others. In other words, there is a lack of interaction between the different regions and the points in general, which motivates the PPP being sometimes called a "completely" random process.*

Five commonly used properties for analyzing the achieved performance of the cellular networks are provided as follows.

Definition 2.4 (Slivnyak theorem)**.** *A PPP Φ preserves its original distribution under the reduced Palm distribution, which means*

$$\mathbb{P}^{!}_{x_0}(E) = \mathbb{P}(\Phi \in E),$$

if the PP Φ is Poisson distributed.

An alternative view of the Slivnyak theorem is that the property observed by a typical point x_0 of the PPP Φ, is the same as that observed by x in $\Phi \cup \{x\}$, which means

$$\mathbb{P}(\Phi \in E | x_0 \in \Phi) = \mathbb{P}(\Phi + \delta_x \in E),$$

where δ_x is the Dirac measure at x.

Definition 2.5 (Campbell's Theorem)**.** *A PPP Φ with density $\lambda(x)$ and $f(x) : \mathbb{R}^d \mapsto \mathbb{R}$. Then,*

$$\mathbb{E}\left[\sum_{x\in\Phi} f(x)\right] = \int_{\mathbb{R}^d} \lambda(x) f(x) dx.$$

The Campbell's theorem is useful for computing the average interference power in large-scale cellular networks.

Definition 2.6 (Laplace Functional)**.** *For any non-negative function $f(x)$ on $\mathbb{R}^d$, the Laplace functional of a PPP Φ with intensity measure $\Lambda(x)$ is defined as*

$$\mathbb{E}\left[\exp\left(-\int_{\mathbb{R}^d} f(x)\Phi(dx)\right)\right] = \exp\left(-\int_{\mathbb{R}^d} \left(1 - \exp\left(-f(x)\right)\right) \Lambda(dx)\right).$$

In the context of wireless communications, the non-negative measurable function $f(x)$, represents the aggregate interference observed at a receiver. Laplace functional is a key transformation in the wireless network modelling and analysis with the stochastic geometry. This is because by using the Laplcae functional, the aggregate interference distribution can be uniquely defined.

Yuan Guo

Definition 2.7 (Probability Generating Functional (PGFL)). *The PGFL of a PPP Φ with intensity measure $\Lambda(x)$, is equal to*

$$\mathcal{Q}[u] = \exp\left[-\int_{\mathbb{R}^d} (1 - u(x))\, \Lambda(dx)\right],$$

where $u(x) : \mathbb{R}^d \to [0, \infty]$ is a real value function. If the PPP is stationary, then the PGFL, can be re-written as

$$\mathcal{Q}[u] = \exp\left[-\lambda \int_{\mathbb{R}^d} (1 - u(x))\, dx\right].$$

It is particularly useful to evaluate the Laplace functional of the sum $\sum_{x\in\Phi} f(x)$ using the PGFL as

$$\mathbb{E}\left[\exp\left(-\sum_{x\in\Phi} f(x)\right)\right] = \mathbb{E}\left[\prod_{x\in\Phi} \exp\left(-f(x)\right)\right] = \mathcal{Q}\left[\exp(-f(x))\right],$$

which typically appears in the analysis of the aggregate interference.

Definition 2.8 (Thinning). *Let $g : \mathbb{R}^d \to [0, 1]$ be a thinning function and apply it to a stationary PPP Φ by deleting each point x with probability $1 - g(x)$, independently of all the other points. This thinning procedure generates an inhomogeneous PPP Φ' with density that is equal to*

$$\lambda'(x) = \lambda g(x). \tag{2.4}$$

The thinning transformation is the process of removing certain points from a PP, usually according to a probabilistic rule $g : \mathbb{R}^d \to [0, 1]$. If the removal event is independent for all points, the thinning transformation is called *independent*.

In the rest of this chapter, we introduce the baseline system model that is adopted throughout the thesis, with slight modifications that are detailed in each chapter according to the considered network setup.

2.2.2 Network model

The network is studied from a large-scale point of view using stochastic geometry. For the *terrestrial networks*, we consider a single-tier bi-dimensional wireless cellular network, where all network's nodes are confined on a circular region $\mathcal{A}$ with radius $R \in (0, \infty)$. The locations of the BSs are modelled as a homogeneous PPP, $\Phi_{\mathrm{B}} = \{x_i \in \mathcal{A}\}$ with spatial density λ_b and unit transmit power, where x_i denotes the spatial coordinates of the i-th node. In addition, the locations of the mobile users (MUs) follow an arbitrary independent point process Φ_u with spatial density λ_u,

where $\lambda_u \gg \lambda_b$. For the satellite-based *non-terrestrial networks*, we consider a multi-tier constellation setup, where LEO satellites are deployed at K different spherical surfaces concentric with the Earth, of altitudes H_k above the mean sea level, with $H_k < H_{k+1},\ 1 \leq k \leq K-1$. Within each tier constellation, the LEO satellites' locations are assumed to be distributed according to the homogeneous PPP Φ_k with intensity λ_k. In addition, we consider that each tier constellation consists of N_k LEO satellites, and thus λ_k can be approximated as $\lambda_k \approx \frac{N_k}{4\pi(R_\oplus+H_k)^2}$, where $R_\oplus$ is the Earth radius; while Φ_i and Φ_j for $i \neq j$ are assumed to be independent [55, 57, 82]. Furthermore, we assume that the locations of ground user equipments (gUEs) follow a uniform distribution.

2.2.3 Channel model

All wireless signals are assumed to experience both large-scale path loss effects and small-scale fading [67]. For the large-scale path loss between a receiver at X and a transmitter at Y, we assume an unbounded singular path loss model, where the path loss only depends on the spatial distance between X and Y, and is given by $L(X,Y) = \|X-Y\|^\alpha$, where $\alpha > 2$ is the path loss exponent [30,31,67]. Regarding the small-scale fading in the terrestrial networks, we adopt the Rayleigh fading model, where different links are assumed to be independent and identically distributed [19,58]. Hence, the channel power gain follows an exponential distribution with unit mean, i.e. $h \sim \exp(1)$. For the non-terrestrial networks, we adopt a practical and well-known shadowed-Rician (SR) fading model for each link, which is typically a Rician fading channel with fluctuating line-of-sight (LoS) components [82]. Let $h_{i,j}$ denote the channel power gain of the link between the typical gUE and the i-th LEO satellite that belongs in the j-th tier. Then, the probability density function (pdf) and the cumulative distribution function (cdf) of the channel power gain are given by

$$f_h(x) = \left(\frac{2bm}{2bm+\Omega}\right)^m \frac{\exp(-\frac{1}{2b}x)}{2b}\ {}_1F_1\left(m;1;\frac{\Omega}{2b\,(2bm+\Omega)}x\right), \tag{2.5}$$

and

$$F_h(x) = \left(\frac{2bm}{2bm+\Omega}\right)^m \sum_{z=0}^{\infty} \frac{(m)_z}{z!\Gamma(z+1)} \left(\frac{\Omega}{2bm+\Omega}\right)^z \gamma\left(z+1,\frac{1}{2b}x\right), \tag{2.6}$$

respectively, where Ω and $2b$ are the average power for the LoS and the multi-path components, respectively, and m is the fading parameters based on the Nakagami-

m fading channels [84]. Finally, all wireless links exhibit additive white Gaussian noise.

2.2.4 Mobility model

The process representing the RWP-based movement of a MU within an area $\mathcal{A} \in \mathbb{R}^2$ can be described as follows. Initially, each MU is placed at the point P_1 chosen from the uniform distribution $\Phi_u \in \mathcal{A}$. Then, each MU uniformly chooses a destination (also called waypoint) P_2 in the region $\mathcal{A}$ and moves towards it with randomly selected speed i.e., $v \in [v_{\min}, v_{\max}]$, which remains constant during that movement. A new direction and speed are chosen only after the MU reaches the destination. For a long running time of the movement process, a stationary distribution, also known as *steady-state distribution*, is achieved [73]. It is important to mention here that, the uniform movement of MUs within an infinite-area network deployment leads to a uniform MUs' steady-state distribution, and hence, the performance of infinite-area networks deployments does not affected by the users' mobility process. Contrary, in the finite-area network deployments, the MUs bounce back when they reach the boundary, aiming the number of MUs in $\mathcal{A}$ to remain constant, i.e. $|\lambda_u \mathcal{A}|$ [73]. Hence, an MU starting near the boundaries of the network area clearly finds more destination waypoints in directions toward the center of the area than toward the border. As time passes and the MUs perform a number of movement periods, the spatial distribution of the MUs becomes more and more non-uniform.

2.2.5 SWIPT model

We take into account TS, PS and AS schemes for achieving the SWIPT capability. More specifically, by employing TS, each available time duration/slot is split into two parts, and a receiver allocates a fraction $\tau \in [0, 1]$ of the time for ID, while it harvests energy for the remaining time. Additionally, PS scheme achieves SWIPT by splitting the received signal into two streams of different power levels with a splitting ratio $\rho \in [0, 1]$; a fraction ρ of the received power is converted to baseband for ID purpose, while the remaining power is directed to the rectenna for EH. Finally, by using AS scheme, a receiver divides the receiving antennas into two groups where one group is used for ID and the other group for EH.

Although the theoretical circuit analysis for the behaviours of RF-to-DC con-

verter/rectifier is still an open question due to the implementation of non-linear components (i.e. diode), in this thesis, we mainly focus on two types of models, namely, the linear and non-linear EH models, which accurately capture the practical EH performance for most scenarios, and enables the tractability for the analytical study [11,13,14,65,66]. Without loss of generality, consider that the power of incoming signals that are directed to the RF-to-DC converter is P_{RF} (dBW). The output DC power is given by

$$P_{\mathrm{DC}} = \begin{cases} \eta P_{\mathrm{RF}}, & \text{linear EH}, \\ \eta \frac{\nu}{1+F} P_{\mathrm{RF}}, & \text{non-linear EH}, \end{cases} \tag{2.7}$$

where η is constant that represents of the RF-to-DC efficiency; F is an exponential random variable with mean ζ, which is used to capture the random noise in the detection and conversion of the actual harvested energy, $\nu = (\zeta e^{\zeta} \int_{-\zeta}^{\infty} e^{-t}/t \mathrm{d}t)^{-1}$.

Yuan Guo

Chapter 3

SWIPT-enabled mobile users in infinite- and finite-area cellular networks

In this chapter, we propose a low complexity threshold-based pair switching (TbPS) technique for SWIPT in the context of large-scale cellular networks. Under the TbPS technique, a subset of MU's antennas is allocated for ID, only when their post-combiner signal-to-interference ratio (SIR), exceeds a certain threshold, while the remaining antennas are allocated for EH. Contrary to traditional approaches which assume the existence of either uncorrelated or fully correlated interference, our proposed technique takes into consideration the interference correlation between nearby antennas. In order to further alleviate the inter-cell interference and energy consumption, we propose a traffic load-based sleeping (TLbS) technique in the context of finite-area network deployments, where lightly-loaded cells switch into sleep mode. By leveraging tools from stochastic geometry, we derive analytical expressions for the ID, EH as well as joint ID and EH success probability of MUs based on the proposed techniques.

3.1 Motivation and contributions

The performance of SWIPT-enabled MUs, that exhibit spatial interference correlation, in the context of 6G mobile networks, is overlooked from the literature. Hence, the aim of this work is to fill this gap by modelling and analyzing such networks

Yuan Guo

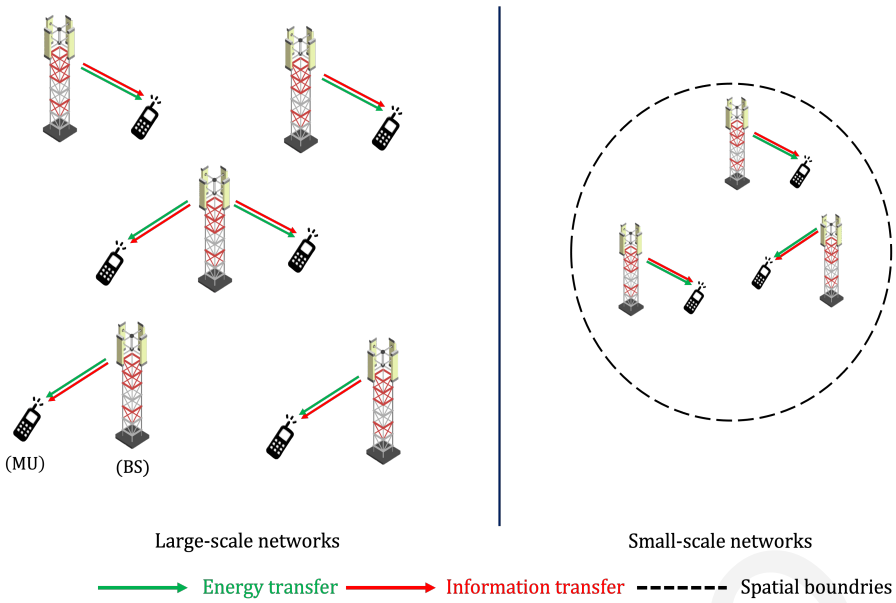

Figure 3.1: Large-scale and small-scale mobile networks.

and by providing new analytical results for the network performance in a stochastic geometry framework. Specifically, the main contributions of this paper are summarized as follows:

- We develop a mathematical framework based on stochastic geometry, which comprises the modelling of SWIPT-enabled MUs in the context of cellular networks. The developed framework takes into account the existence of spatially correlated interference between the users' antenna elements, and the ability of users to move within the network area based on a RWP model. Moreover, the performance of the considered system is assessed under two different network topologies as shown in Fig. 3.1, i.e. large-scale and small-scale networks, which cover an infinite and a finite area, respectively.

- In the infinite area scenario, i.e. large-scale outdoor environment, a novel antenna pairs switching scheme is proposed for cellular networks, aiming at facilitating the MUs' allocation either for ID or for EH. In particular, based on the proposed scheme, the receiver antenna elements are divided into pairs, and a subset of antenna pairs is allocated for ID, only when their post-combiner SIR is beyond a certain threshold, while the remaining pairs are allocated for EH. In addition, the interference power within each pair of antenna elements are assumed to be fully-correlated and for the different pairs, interference observed are assumed to be independent.

Yuan Guo

- In the finite area scenario, i.e. the indoor environment or small cells, we evaluate the performance of SWIPT-enabled MUs, in the context of a novel sleeping mechanism. Specifically, our proposed approach switches off cells in a probabilistic way based on their traffic load, which is non-uniform spatially distributed due to the MUs' mobility, aiming the joint optimization of users' throughput and EH performance. To guarantee the quality-of-service, the users of sleeping BSs are offloaded to active neighbouring BSs.

- Analytical expressions for the success probability of ID and EH, as well as for the joint success probability, i.e. ID and EH, are derived for the considered network deployments. Moreover, under specific practical assumptions, closed-form expressions for the Laplace transform of the received interference are derived. These closed-form expressions provide a quick and convenient methodology of evaluating the system's performance and obtaining insights into how key parameters affect the performance. Moreover, the optimal design parameters related to our proposed two techniques are illustrated, that maximise the joint ID and EH ability of MUs.

- Finally, our numerical and simulated results show that, by properly selecting the parameters, i.e. SIR and traffic load thresholds based on the network deployment, the proposed two techniques outperform the conventional techniques, e.g. traditional antenna switching and non-sleeping schemes, in the context of ID and EH success probabilities of SWIPT-enabled MUs..

3.2 System model

Recall that, we consider a bi-dimensional cellular network according to a homogeneous PPP. We consider the case where all BSs are equipped with a single transmit antenna [67]. The mobility of MUs are modelled by a RWP model. Moreover, we assume that all BSs have a continuous power supply, while all MUs are battery-operated. Specifically, we assume that each MU has SWIPT capabilities and thus it can decode the information and also harvest energy from the received signal simultaneously. We consider that the EH process is accomplished by using either our proposed TbPS technique (see Section 3.3.1) or the conventional PS receiver architecture (introduced in Section 2.2.5); while a linear EH model is considered.

3.3 SWIPT with threshold-based pair switching technique

In this section, we propose a TbPS technique in the context of infinite-area cellular networks, where the multi-antenna MUs employ a MRC technique in the presence of spatial interference correlation. In particular, we evaluate the ability of a MU to successfully decode the received signal and harvest sufficient energy. Based on the proposed low-complexity TbPS technique, analytical expressions for the ID, EH, and joint ID and EH success probability are derived by using tools from stochastic geometry. Without loss of generality, based on the Slivnyak's theorem, we perform our analysis for the typical MU, which is located at the origin [25,30], but the results hold for all users of the network.

3.3.1 Threshold-based pair switching scheme

Even though the channels between the BSs and each antenna element of a MU are assumed to be independent with each other, the received interference across different antenna elements is neither independent nor identical [61, 67]. More precisely, the interference terms observed at the different antennas are partially correlated random variables due to the common locations of the interfering BSs [67]. Therefore, as shown in Fig. 3.2, motivated by the extremely narrow spacing between adjacent antenna elements of a MU, we divide the set of antenna elements into η pairs of two adjacent antenna elements, i.e. $\eta = \mathcal{N}/2$, where $\mathcal{N}$ is the number of antennas of a MU. Such approach could capture the interference correlation between adjacent antenna elements and keep the tractability for the analytical framework. In particular, we assume that the observed interference between each antenna element of a pair is fully-correlated, while the intended received signal and interference between pairs are regarded uncorrelated. Then, based on the AS protocol [13], our proposed scheme allocates a subset of paired antenna elements, i.e. ν pairs, for ID purpose and the remaining $(\eta - \nu)$ pairs, for EH.

Let $\mathcal{S}_k$ and $\mathcal{I}_k$ denote the power of the intended signal and observed interference at the k-th antenna element of a MU, respectively, where $k = \{1, \cdots, \mathcal{N}\}$. Due to the full-correlation of the interference within each antenna pair, the interference across antennas in each pair is identical, i.e. $\mathcal{I}_k = \mathcal{I}_{k+1} = \mathcal{I}_n$ where $k = 2n - 1$ and

Yuan Guo

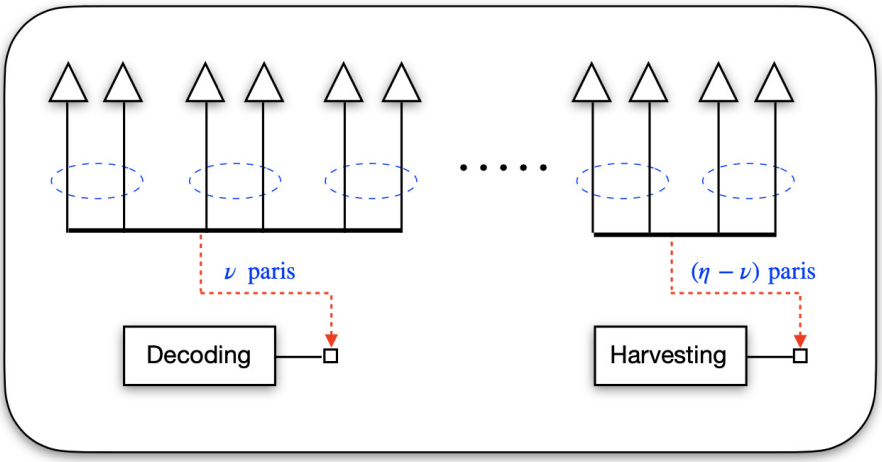

Figure 3.2: An $\mathcal{N}$-antenna TbPS receiver with η pair of antennas, where ν pairs of antennas are connected to decoding circuit and $(\eta - \nu)$ pairs of antennas to harvesting circuit.

$n = \{1, \cdots, \eta\}$. Thus, based on the MRC technique, the SIR of the n-th antenna pair of the typical MU, is given by [1]

$$\Gamma_n = \frac{\mathcal{S}_{2n-1} + \mathcal{S}_{2n}}{\mathcal{I}_n} = \frac{(h_{2n-1,o} + h_{2n,o})\, L^{-1}(x_o)}{\sum_{x_i \in \Phi_B^{\setminus o}} h_{n,i} L^{-1}(x_i)}. \tag{3.1}$$

Regarding the selection of the number of antenna pairs, ν, we develop a threshold-based approach based on the MRC [85]. Let Γ_ν denote the post-combiner SIR for the MRC at the receiver when ν pairs of antenna elements are selected, which is equal to $\Gamma_\nu = \sum_{j=1}^{\nu} \Xi_n$, where Ξ_n is given by the expression (3.1). Based on the TbPS scheme, the number of antenna pairs, ν, is selected so that the post-combiner SIR at the receiver exceeds a certain predefined threshold γ_{th} (dB). Starting from the single-pair case, the TbPS scheme gradually raises the number of selected pairs aiming to satisfy the aforementioned condition. The previous actions are repeated until Γ_ν is greater than the threshold γ_{th}. It should be noted that, in order to maintain the minimum harvested energy power, at least one pair is allocated for EH, i.e. for the case $\Gamma_{\eta-1} \leq \gamma_{th}$, $\eta - 1$ pairs are allocated for ID and the remaining one pair is allocated for EH. It is worth mentioning that, the proposed TbPS is a low-complexity antenna selection scheme, since the CSI is only required to be estimated at a fraction of the antenna elements. More specifically, once the post-combiner SIR reaches

[1] Since the large-scale networks with infinite area are regarded as interference-limited due to the high-level multi-cell interference power, the additive thermal noise is neglected [25, 67].

the threshold γ_{th}, then no more CSI is needed for the remaining antenna elements, where the number of antennas that require CSI, i.e. c, is bounded within the interval $2 \leq c \leq \mathcal{N} - 4$.

3.3.2 Information decoding success probability with TbPS scheme

Initially, we assess the conditional cdf of Ξ_n, i.e. $\mathbb{P}[\Xi_n < \mathrm{Y}|x_o]$, where Y is the decoding threshold, which is useful for evaluating the ID, EH, and the joint ID and EH success probability. The following lemma evaluates the conditional cdf of the SIR at the n-th antenna pair of the typical MU.

Lemma 3.1. *The conditional cdf for the SIR of the n-th antenna pair of the typical MU, i.e. Ξ_n is given by*

$$\mathfrak{F}(\mathrm{Y}|x_o) = 1 - \mathcal{L}_{\mathcal{I}_n}(s) + s\frac{\partial \mathcal{L}_{\mathcal{I}_n}(s)}{\partial s},$$

where $s = \mathrm{Y}L(x_o)$, $\mathcal{L}_{\mathcal{I}_n}(s)$ and $\partial\mathcal{L}_{\mathcal{I}_n}(s)/\partial s$ are the Laplace transform and the derivative of the Laplace transform of the interference observed at the n-th antenna pair, which are given by

$$\mathcal{L}_{\mathcal{I}_n}(s) = \exp\left(-\frac{2\pi\lambda_b s r_o^{2-\alpha}\, {}_2F_1\left(1, \frac{\alpha-2}{\alpha}; 2-\frac{2}{\alpha}; -s r_o^{-\alpha}\right)}{\alpha - 2}\right), \tag{3.2}$$

and

$$\frac{\partial \mathcal{L}_{\mathcal{I}_n}(s)}{\partial s} = \frac{2\mathcal{L}_{\mathcal{I}_n}(s)\pi r_o^2 \lambda_b \left(2 - \alpha - 2(1 + s r_o^{-\alpha})\, {}_2F_1\left(1, \frac{\alpha-2}{\alpha}; 2-\frac{2}{\alpha}; -s r_o^{-\alpha}\right)\right)}{(r_o^\alpha + s)(\alpha - 2)\alpha}, \tag{3.3}$$

r_o is the distance from the typical MU to its serving BS, i.e. $r_o = \|x_o\|$.

Proof. Based on the expression (3.1), the conditional cdf of SIR_n, can be expressed as

$$\mathfrak{F}(\mathrm{Y}|x_o) = \mathbb{P}\left[\Xi_n \leq \mathrm{Y}|x_o\right] = \mathbb{P}\left[h_{2n-1,o} + h_{2n,o} \leq L(x_o)\mathcal{I}_n \mathrm{Y}\right] = \mathbb{E}\left[\gamma\left(2, s\mathcal{I}_n\right)\right], \tag{3.4}$$

where $s = \mathrm{Y}L(x_o)$, and (3.4) follows from the fact that the sum of two exponential random variables follows the Gamma distribution [68]. Then, based on the moment generating function and $\gamma(x,y) = \Gamma(x) - (x-1)!e^{-y}\sum_{k=0}^{y-1}\frac{y^k}{k!}$, the final expression can be derived, where

$$\mathcal{L}_{\mathcal{I}_n}(s) = \mathbb{E}\left[\exp\left(-\sum\nolimits_{x_i \in \Phi_{\mathrm{B}}^{\setminus 0}} \frac{h_{n,i}s}{L(x_i)}\right)\right] = \exp\left(2\pi\lambda_b \int_{r_o}^{\infty} \left(\phi(x,s) - 1\right) x \mathrm{d}x\right), \tag{3.5}$$

where (3.5) is obtained from the PGFL of PPPs [25] and $\phi(x,s)$ is

$$\phi(x,s) = \mathbb{E}_h\left[\exp\left(-\frac{h_{n,i}s}{L(x)}\right)\right] = \frac{1}{1 + sL^{-1}(x)}.$$

Therefore, by evaluating the integral and derivative, the expressions in Lemma 3.1 can be derived. □

The following Remark investigates a special case of Lemma 3.1, where $\alpha = 4$, which is a common practical value for path-loss exponent in outdoor urban environments, where the closed-form expressions of the Laplace transform and the derivative of the Laplace transform of the interference are obtained.

Remark 3.1. *For the special case $\alpha = 4$, the Laplace transform and the derivative of the Laplace transform of the interference observed at the n-th antenna pair can be simplified as*

$$\mathcal{L}_{\mathcal{I}_n}(s) = \exp\left(-\pi\sqrt{s}\lambda_b \tan^{-1}\left(r_o^{-2}\sqrt{s}\right)\right),$$

and

$$\frac{\partial \mathcal{L}_{\mathcal{I}_n}(s)}{\partial s} = -\frac{\mathcal{L}_{\mathcal{I}_n}(s)\pi\lambda_b}{2}\left(\frac{r_o^2}{r_o^4+s} + \frac{\tan^{-1}\left(r_o^{-2}\sqrt{s}\right)}{\sqrt{s}}\right),$$

where $\tan^{-1}(\cdot)$ *is the inverse of the tangent function.*

Based on the adopted association scheme, i.e. each MU communicates with its closest BS at x_o, the complementary cumulative distribution function of the distance r_o between a MU and its serving BS, is given by $\mathbb{P}[r_o > r] = \exp(-\pi\lambda_b r^2)$, and the pdf of the distance r_o, i.e. $f_r(r) = \frac{\mathrm{d}}{\mathrm{d}r}\left(1 - \mathbb{P}[r_o > r]\right)$, is given by [67]

$$f_r(r) = 2\pi\lambda_b r \exp(-\pi\lambda_b r^2). \tag{3.6}$$

Then, we focus on the evaluation of the ID success probability in the context of our proposed TbPS scheme, which can be formulated as

$$\begin{aligned}\mathcal{F}_{\mathrm{ID}}(\chi,\gamma_{th}) =& \mathbb{P}\left[\Gamma_1 \geq \chi \;\&\; \Gamma_1 \geq \gamma_{th}\right] + \sum_{v=2}^{\eta-2}\mathbb{P}\left[\Gamma_v \geq \chi \;\&\; \Gamma_{v-1} < \gamma_{th} < \Gamma_v\right] \\ &+ \mathbb{P}\left[\Gamma_{\eta-1} \geq \chi \;\&\; \Gamma_{\eta-2} < \gamma_{th}\right],\end{aligned}$$

where χ (dB) is the decoding threshold.

It should be noted that, the proposed TbPS scheme is applicable for any MUs, of which the number of antenna elements is not less than four, i.e. at least one antenna pair is allocated for ID and one pair for EH. In addition, in order to achieve the adaptive and dynamic allocation of antenna pairs based on the instantaneous signal quality, i.e. SIR, the minimum number of antenna elements required at MUs is six. Hence, in this work we consider the scenario where $\mathcal{N} = 6$, for the sake of simplicity. The aforementioned scenario holds for practical wireless devices that are typically

Yuan Guo

equipped with a small number of antenna elements, due to space limitations and complexity constrains, e.g. smartphones, WiFi routers [30, 68]. For this special case, the following proposition characterizes the resulting performance in terms of ID success probability.

Proposition 3.1. *For the special case where MUs are equipped with six antenna elements, i.e. $\mathcal{N} = 6$, the ID success probability, $\mathcal{F}_{\mathrm{ID}}(\chi, \gamma_{th})$, is given by*

$$\mathcal{F}_{\mathrm{ID}}(\chi, \gamma_{th}) = \int_0^{\infty} \mathcal{J}_{\mathrm{ID}}(\chi, \gamma_{th}, r) f_r(r) \mathrm{d}r,$$

where

$$\begin{aligned}\mathcal{J}_{\mathrm{ID}}(\chi, \gamma_{th}, r) =& 1 - \bar{\mathcal{H}}(\chi - \gamma_{th}) \int_0^{\chi} \mathfrak{F}(\chi - y|r) f(y|r) \mathrm{d}y \\ &- \mathcal{H}(\chi - \gamma_{th}) \Big(\mathfrak{F}(\chi|r) - \mathfrak{F}(\gamma_{th}|r) + \mathfrak{F}(\chi - \gamma_{th}|r) \mathfrak{F}(\gamma_{th}|r) \\ &+ \int_{\chi - \gamma_{th}}^{\chi} \mathfrak{F}(\chi - y|r) f(y|r) \mathrm{d}y \Big), \end{aligned} \tag{3.7}$$

$\mathfrak{F}(\mathrm{Y}|x_o)$ is the conditional cdf of Ξ_n, which is given in Lemma 3.1, $f(\mathrm{Y}|x_o)$ is the conditional pdf of the Ξ_n and can be calculated as $f(\mathrm{Y}|x_o) = \partial \mathfrak{F}(\mathrm{Y}|x_o)/\partial \mathrm{Y}$, and $f_r(r)$ is the pdf of the distance from the typical MU to its serving BS, which is given by (3.6).

Proof. For the special case where $\mathcal{N} = 6$, the ID success probability, can be formulated as

$$\mathcal{F}_{\mathrm{ID}}(\chi, \gamma_{th}) = 1 - \mathbb{P}[\Xi_1 < \chi,\ \Xi_1 \geq \gamma_{th}] - \mathbb{P}[\Xi_1 + \Xi_2 < \chi,\ \Xi_1 < \gamma_{th}]. \tag{3.8}$$

For the scenario where $\gamma_{th} < \chi$, the above expression can be re-written as

$$\begin{aligned}\mathcal{F}_{\mathrm{ID}}(\chi, \gamma_{th}) =& 1 - \mathbb{P}\left[\gamma_{th} \leq \Xi_1 < \chi\right] - \mathbb{P}\left[\Xi_1 < \chi\ - \Xi_2 | \chi\ - \Xi_2 \leq \gamma_{th}\right] \\ &- \mathbb{P}\left[\Xi_1 < \gamma_{th} | \gamma_{th} \leq \chi\ - \Xi_2\right], \end{aligned} \tag{3.9}$$

while for $\gamma_{th} \geq \chi$, is given by

$$\mathcal{F}_{\mathrm{ID}}(\chi, \gamma_{th}) = 1 - \mathbb{P}\left[\Xi_1 < \chi\ - \Xi_2\ \&\ \Xi_1 \leq \gamma_{th}\right] = 1 - \mathbb{P}\left[\Xi_1 < \chi\ - \Xi_2\right]. \tag{3.10}$$

Then, by using the cdf of Ξ_n, which is derived in Lemma 3.1, the final expression for $\mathcal{F}_{\mathrm{ID}}(\chi, \gamma_{th})$ can be derived. □

Yuan Guo

3.3.3 Energy harvesting success probability with TbPS scheme

The success probability of EH accounts for the ability of a MU to effectively harvest certain amount of RF energy, which is above a predefined reliability threshold $\mathcal{Q}$ (dBm) based on the practical applications. Similar to [19], we consider a linear energy harvesting model for tractability purposes [86]. Such linear energy harvesting model captures the linear regime of the rectenna, while approximating the other operation regimes in a simple way. Therefore, the proposed mathematical framework also serves as a useful guideline for more practical nonlinear EH models [87]. Specifically, the harvested energy is defined as the aggregate received signal power multiplied with the conversion efficiency ζ of the energy harvester. In addition, in order to derive compact and informative expressions for the EH success probability, the aggregate interference power harvested by the energy harvester is approximated by the mean interference power, denoted as $\bar{\mathcal{I}}$. The accuracy of the above-mentioned approximation is illustrated in the numerical results in Section 3.5. Therefore, the mean interference power is given by [25]

$$\bar{\mathcal{I}} \triangleq \mathbb{E}_{h,\Phi_{\mathrm{B}}}\left[\sum\nolimits_{x_i\in\Phi_{\mathrm{B}}^{\setminus o}} h_{k,i}L(x_i)^{-1}\right] = \frac{2\pi\lambda_b r_o^{2-\alpha}}{\alpha-2}.$$

Then, based on the number of selected pairs, ν, the EH success probability achieved by the TbPS scheme, can be formulated as

$$\begin{aligned}\mathcal{F}_{\mathrm{EH}}(\mathcal{Q},\gamma_{th}) =& \mathbb{P}[\Gamma_1 \geq \gamma_{th}]\mathbb{P}\left[\zeta\left(\sum\nolimits_{j=1}^{\eta}\mathcal{S}_{2j-1}+\mathcal{S}_{2j}+2\bar{\mathcal{I}}\right)\geq\mathcal{Q}\right]\\ &+\sum\nolimits_{v=2}^{\eta-2}\mathbb{P}[\Gamma_{v-1}<\gamma_{th}<\Gamma_v]\mathbb{P}\left[\zeta\left(\sum\nolimits_{j=v+1}^{\eta}\mathcal{S}_{2j-1}+\mathcal{S}_{2j}+2\bar{\mathcal{I}}\right)\geq\mathcal{Q}\right]\\ &+\mathbb{P}\left[\Gamma_{\eta-2}<\gamma_{th}\right]\mathbb{P}\left[\zeta\left(\mathcal{S}_{2\eta-1}+\mathcal{S}_{2\eta}+2\bar{\mathcal{I}}\right)\geq\mathcal{Q}\right],\end{aligned}$$

where $\mathcal{Q}$ is the reliability threshold. For the special case where $\mathcal{N}=6$, the following proposition characterizes the resulting performance in terms of EH success probability.

Proposition 3.2. *For the special case where MUs are equipped with six antenna elements, i.e. $\mathcal{N}=6$, the EH success probability, $\mathcal{F}_{\mathrm{EH}}(\mathcal{Q},\gamma_{th})$, is given by*

$$\mathcal{F}_{\mathrm{EH}}(\mathcal{Q},\gamma_{th}) = \int_0^{\infty}\mathcal{J}_{\mathrm{EH}}(\mathcal{Q},\gamma_{th},r)f_r(r)\mathrm{d}r, \tag{3.11}$$

where

$$\mathcal{J}_{\mathrm{EH}}(\mathcal{Q},\gamma_{th},r_o) = \bar{\mathfrak{F}}(\gamma_{th}|r_o)\mathfrak{H}_2(\mathcal{Q}|r_o)+\mathfrak{F}(\gamma_{th}|r_o)\mathfrak{H}_1(\mathcal{Q}|r_o),$$

$$\mathfrak{H}_1(\mathcal{Q}|r_o) = \Gamma\left(2, \ell(r_o, 2)\right) \mathcal{H}\big(r_o - \gamma(1)\big) + \bar{\mathcal{H}}\big(r_o - \gamma(1)\big),$$
$$\mathfrak{H}_2(\mathcal{Q}|r_o) = \frac{\Gamma\left(4, \ell(r_o, 4)\right)}{\Gamma(4)} \mathcal{H}\big(r_o - \gamma(2)\big) + \bar{\mathcal{H}}\big(r_o - \gamma(2)\big),$$

$\bar{\mathfrak{F}}(\cdot) = 1 - \mathfrak{F}(\cdot)$, $\ell(x, y) = L(x)(\bar{\mathcal{Q}} - y\bar{\mathcal{I}})$, $\bar{\mathcal{Q}} = \mathcal{Q}/\zeta$, $\gamma(y) = \left(\frac{4y\pi\lambda_b}{\bar{\mathcal{Q}}(\alpha-2)}\right)^{\frac{1}{\alpha-2}}$.

Proof. For the considered scenario, i.e. $\mathcal{N} = 6$, the TbPS scheme either assigns a single or two pairs of antenna elements for energy harvesting, based on the number of antenna elements that is seleted for the ID part of the system. For the case where the TbPS scheme assigns two antenna pairs for ID, i.e. $\nu = 2$, then a single pair is allocated for EH. In this case, the EH success probability can be calculated as

$$\mathfrak{H}_1(\mathcal{Q}|x_o) = \mathbb{P}[S_k + S_{k+1} + 2\bar{\mathcal{I}} \geq \bar{\mathcal{Q}}|x_o],$$

where $\bar{\mathcal{Q}} = \mathcal{Q}/\zeta$. Similar with the proof of Lemma 3.1, for the case where $\bar{\mathcal{I}} < \bar{\mathcal{Q}}/2$, we have the condition that $\|x_o\| \geq \left(4\pi\lambda_b(\alpha-2)^{-1}/\bar{\mathcal{Q}}\right)^{1/(\alpha-2)}$ and hence,

$$\begin{aligned} \mathfrak{H}_1(\mathcal{Q}|x_o) &= \mathbb{P}\left[S_k + S_{k+1} \geq \bar{\mathcal{Q}} - 2\bar{\mathcal{I}}|x_o\right] \\ &= \Gamma\left(2, L(x_o)(\bar{\mathcal{Q}} - 2\bar{\mathcal{I}})\right), \end{aligned} \tag{3.12}$$

where (3.12) is from the same methodology of (a) in Lemma 3.1. Furthermore, for the case, where $2\bar{\mathcal{I}} \geq \bar{\mathcal{Q}}$, we have $\|x_o\| \leq \left(4\pi\lambda_b(\alpha-2)^{-1}/\bar{\mathcal{Q}}\right)^{1/(\alpha-2)}$ and $\mathfrak{H}_1(\mathcal{Q}|x_o) = 1$. Hence, the final expression of $\mathfrak{H}_1(\mathcal{Q}|x_o)$ is derived. For the case where two pairs of antenna elements are used for EH, the EH success probability can be calculated as

$$\mathfrak{H}_2(\mathcal{Q}|x_o) = \mathbb{P}\left[\sum_{j=0}^{3} S_{k+j} + 4\bar{\mathcal{I}} \geq \bar{\mathcal{Q}}|x_o\right].$$

The proof of $\mathfrak{H}_2(\mathcal{Q}|x_o)$ follows similar methodology, and hence it is ommitted due to space limitations. Finally, by multiplying the probability of ν and following the similar methodology used in proof of Proposition 3.1, the Proposition 3.2 is proven.

□

3.3.4 Joint information decoding and energy harvesting success probability with TbPS scheme

In this section, we address the trade-off between the ID and the EH in the context of the TbPS scheme, by evaluating the joint ID and EH success probability [19]. In particular, the joint ID and EH success probability, $\mathcal{F}_{\text{ID\&EH}}(\chi, \mathcal{Q}, \gamma_{th})$, refers to the

Yuan Guo

capability of a MU to achieve both the ID and EH threshold simultaneously. Hence, $\mathcal{F}_{\text{ID\&EH}}(\chi, \mathcal{Q}, \gamma_{th})$ can be evaluated as

$$\begin{aligned}\mathcal{F}_{\text{ID\&EH}}(\chi, \mathcal{Q}, \gamma_{th}) &= \mathbb{P}[\Gamma_1 \geq \chi \& \Gamma_1 \geq \gamma_{th}]\mathbb{P}\left[\sum_{j=1}^{\eta} \mathcal{S}_{2j-1} + \mathcal{S}_{2j} + 2\bar{\mathcal{I}} \geq \bar{\mathcal{Q}}\right] \\ &+ \sum_{v=2}^{\eta-2} \mathbb{P}[\Gamma_v \geq \chi \& \Gamma_{v-1} < \gamma_{th} < \Gamma_v] \times \mathbb{P}\left[\sum_{j=v+1}^{\eta} \mathcal{S}_{2j-1} + \mathcal{S}_{2j} + 2\bar{\mathcal{I}} \geq \bar{\mathcal{Q}}\right] \\ &+ \mathbb{P}\left[\Gamma_{\eta-1} \geq \chi \& \Gamma_{\eta-2} < \gamma_{th}\right] \mathbb{P}\left[\mathcal{S}_{2\eta-1} + \mathcal{S}_{2\eta} + 2\bar{\mathcal{I}} \geq \bar{\mathcal{Q}}\right]. \end{aligned} \tag{3.13}$$

In the following proposition, we evaluate the joint ID and EH success probability for the special case with $\mathcal{N} = 6$ antennas.

Proposition 3.3. *For the special case where MUs are equipped with six antenna elements, i.e. $\mathcal{N} = 6$, the joint ID and EH success probability is given by*

$$\mathcal{F}_{\text{ID\&EH}}(\chi, \mathcal{Q}, \gamma_{th}) = \int_0^{\infty} \mathcal{J}_{\text{ID\&EH}}(\chi, \mathcal{Q}, \gamma_{th}, r) f_r(r) \mathrm{d}r,$$

where

$$\begin{aligned}&\mathcal{J}_{\text{ID\&EH}}(\chi, \mathcal{Q}, \gamma_{th}, r) \\ =&\mathcal{H}(\chi - \gamma_{th})\left(\mathfrak{H}_2(\mathcal{Q}|r)\bar{\mathfrak{F}}(\chi|r) + \mathfrak{H}(\mathcal{Q}|r)\mathfrak{F}(\gamma_{th}|r) \times \int_0^{\gamma_{th}} \mathfrak{F}(\chi - y|r) f(y|r) \mathrm{d}y\right) \\ &+ \bar{\mathcal{H}}(\chi - \gamma_{th})\Bigg(\mathfrak{H}_2(\mathcal{Q}|r)\bar{\mathfrak{F}}(\gamma_{th}|r) + \mathfrak{H}_1(\mathcal{Q}|r)\mathfrak{F}(\gamma_{th}|r) \\ &\qquad \times \left(1 - \mathfrak{H}_1(\mathcal{Q}|r)\right) \int_0^{\chi} \mathfrak{F}(\chi - y|r) f(y|r) \mathrm{d}y\Bigg), \end{aligned} \tag{3.14}$$

where $\bar{\mathfrak{F}}(\cdot) = 1 - \mathfrak{F}(\cdot)$, $\mathfrak{H}_1(\cdot)$ and $\mathfrak{H}_2(\cdot)$ are derived in Proposition 3.2.

Proof. The proof follows the similar methodology with the Proposition 3.1 and Proposition 3.2, and hence is omitted. □

3.4 Cell sleeping mechanism in SWIPT-enabled mobile networks

In order to provide a general and universal insight on the SWIPT-enabled mobile networks, we now focus our attention on another type of the wireless network, i.e. the finite-area network deployment, such as small cells and indoor environment. In such scenario, the mobility of MUs based on RWP model results in a non-uniform distribution of MUs, which subsequently leads to the significantly different

network performance compared to the large-scale infinite area networks [78]. Therefore, we now investigate the additional achieved gains on the network performance, by exploiting the ability of BSs to perform an interference resource management approach, namely sleeping technique, based on its traffic load. More specifically, the main idea of the TLbS mechanism is to switch off idle or lightly-loaded BSs in order to reduce the aggregate interference and power consumption, triggering a non-trivial trade-off between ID and EH success probability. On the one hand, the observed interference is characterized as the main degradation factor in conventional networks, while on the other hand, it can be viewed as a useful aggregate energy signal that could be exploited for the harvesting purposes of IoT devices. Hence, by exploiting our proposed technique, the overall balance of the counter-posed effects introduced by the aggregate interference on finite-area cellular networks can be addressed.

3.4.1 Traffic load-based cell sleeping mechanism

The steady-state distribution of the MUs' locations within a finite-area network, i.e. $|\mathcal{A}| < \infty$, is a non-uniform distribution. Specifically, the intensity function of the steady-state distribution, is given by [73, 78]

$$\lambda_u(r) \triangleq \lambda_u^{\infty}(r) = 2\lambda_u \left(1 - \frac{r^2}{R^2}\right), \tag{3.15}$$

where r represents the distance from a MU to the center of the considered region $\mathcal{A}$ and λ_u is the initial density of MUs.

Since the steady-state distribution of the MUs' locations is no longer uniform on the considered circular disk area, i.e. MUs are more likely to be present around the centre; in the meantime, the density of the MUs near the border areas has dropped significantly. The TLbS mechanism dynamically determines the state of the BSs, i.e. either active or in sleeping mode, based on traffic load-based policy. Specifically, we consider a BS as active, if and only if, the number of MUs n in its coverage region is larger than N; otherwise, we consider that this particular BS is switched into the sleeping mode. In order to guarantee the communications quality, the users of sleeping BSs are offload to active neighbouring BSs. It should be noted that, the TLbS mechanism is also of low-complexity for the MUs devices; more specifically, the switching between active and sleeping modes is operated by the BSs, based on

the number of MUs located within the coverage area of each BS. In the modern wireless networks, the BSs can obtain the MUs' location information through positioning reference signals [88]. Then, based on the proposed TLbS mechanism, the distribution of the active BSs is characterized in the following lemma.

Lemma 3.2. *Based on the proposed* TLbS *mechanism, the location of the active BSs follows an non-homogeneous PPP* $\tilde{\Phi}_{\mathrm{B}}$ *with intensity function* $\tilde{\lambda}_b(r)$*, which is given by*

$$\tilde{\lambda}_b(r) = \lambda_b \delta(r), \tag{3.16}$$

where $\delta(r)$ *represents the active probability of a BS at distance* r *and is given by*

$$\delta(r) = 1 - \sum_{k=0}^{N-1} \frac{\lambda_u(r)^k \Omega^K \gamma\left[K+k, \pi(R^2\lambda_u(r)+\Omega)\right]}{\beta(r)^k k! \gamma[K, \pi\Omega](R^2\beta(r))^K}, \tag{3.17}$$

where r *is the distance from a network node to the center of the considered region* $\mathcal{A}$*,* $\Omega = KR^2\lambda_b$*,* $\beta(r) = \lambda_u(r) + K\lambda_b$*,* $\lambda_u(r)$ *is the intensity function of the MUs given in* (3.15)*, and* $K = 3.575$ [89].

Proof. Based on the proposed TLbS mechanism, the active probability $\delta(r)$ of a BS, of which coverage area is $\mathcal{C}$, is the probability that there are at least N MUs within its coverage region, which can be formulated as

$$\begin{aligned}
\delta(r) &= \mathbb{P}\{n \geq N\} \\
&= 1 - \mathbb{P}\{n=0\} - \mathbb{P}\{n=1\} - \cdots - \mathbb{P}\{n=N-1\} \\
&\overset{(a)}{=} 1 - \mathbb{E}_{\mathcal{C}}\Big[\exp(-\lambda_u(r)\mathcal{C}) + \lambda_u(r)\mathcal{C}\exp(-\lambda_u(r)\mathcal{C}) \\
&\quad + \cdots + \frac{(\lambda_u(r)\mathcal{C})^{N-1}}{(N-1)!}\exp(-\lambda_u(r)\mathcal{C})\Big] \\
&= \mathbb{E}_{\mathcal{C}}\left[1 - \textstyle\sum_{k=0}^{N-1} \frac{(\lambda_u(r)\mathcal{C})^k}{k!}\exp\left(-\lambda_u(r)\mathcal{C}\right)\right],
\end{aligned}$$

where (a) is from the probability mass function of Poisson distribution, and $\mathcal{C}$ is a random variable representing the coverage area of a Voronoi cell supported by the considered BS at distance r and its pdf is given by [89]

$$f_{\mathcal{C}}(x) = \lambda_b^K \frac{K^K}{\Gamma[K] - \Gamma[K, K\pi R^2\lambda_b]} x^{K-1}\exp(-K\lambda_b x).$$

Hence, the expression for $\delta(r)$ can be obtained by solving the following integral,

$$\delta(r) = \int_0^{\pi R^2} f_{\mathcal{C}}(x)\left(1 - \sum_{k=0}^{N-1}\frac{(\lambda_u(r)x)^k}{k!}\exp\left(-\lambda_u(r)x\right)\right)\mathrm{d}x.$$

Therefore, the resulting intensity function $\tilde{\lambda}_b(r)$ in Lemma 3.2 is derived. □

Yuan Guo

3.4.2 Information decoding success probability with TLbS mechanism

In this section, we investigate the ability of a MU to successfully decode the received signal power, i.e. the ID success probability. In order to maintain the complexity at a lower level, we assume that all MUs are equipped with single antenna element and perform ID and EH based on a power splitting approach [13]. As previously mentioned, the MUs' movement and the TLbS technique, causing the existence of non-uniform spatial distribution of the MU and the active BS, respectively. Without loss of generality, we focus our analysis on a general MU with distance d from the origin, where $0 \leq d \leq R$. The scenarios where $d = 0$ and $d = R$ refer to the case where MUs are located at the center and the edge of the network area $\mathcal{A}$, respectively. Then, based on the power splitting approach, the ID success probability of a general MU with distance d to the origin, is defined as [19, 58]

$$\mathcal{G}_{\mathrm{ID}}(\chi, d) \triangleq \mathbb{P}\left[\frac{\mathcal{S}}{\mathcal{I} + \sigma_N^2 + \sigma_C^2} \geq \chi\right], \tag{3.18}$$

where σ_N^2 is the thermal noise power, σ_C^2 accounts for the noise introduced during the conversion from radio frequency to baseband. Since, power splitting approach is considered, $\sigma_C^2 = \sigma_{cov}^2/(1-\rho)$, ρ is the power splitting parameter; $\mathcal{S}$ is the intended received signal power from the serving BS, $\mathcal{I}$ is the aggregate interference observed at the MU, and χ (dB) is the ID threshold.

We first assess the conditional cdf of the aggregate interference observed at a general MU, i.e. $\mathbb{P}[\mathcal{I} \leq \mathcal{X}|r_o]$, which is useful for evaluating the considered performance metrics. The following lemma characterizes the conditional cdf of the aggregate interference.

Lemma 3.3. *The conditional cdf of the aggregate interference observed at a MU is given by* [19]

$$\mathsf{F}_{\mathcal{I}}(\mathcal{X}, r_o) = \frac{1}{2} - \frac{1}{\pi}\int_0^{\infty} \frac{\mathrm{Im}\{\exp(-jt\mathcal{X})\psi(t, r_o)\}}{t}\mathrm{d}t, \tag{3.19}$$

where $j = \sqrt{-1}$, $\mathrm{Im}\{\cdot\}$ *is imaginary operator and* $\psi(t, r_o)$ *is the characteristic function of interference* $\mathcal{I}$*, which is given by*

$$\psi(t, r_o) = \exp\left(-2\int_0^{\mathcal{A}}\int_{r_o}^{d\cos(\theta)+\sqrt{R^2-d^2\sin(\theta)^2}} \left(1 - \frac{1}{1-jtz^{-\alpha}}\right) z\tilde{\lambda}_b(z)\mathrm{d}z\mathrm{d}\theta\right) \tag{3.20}$$

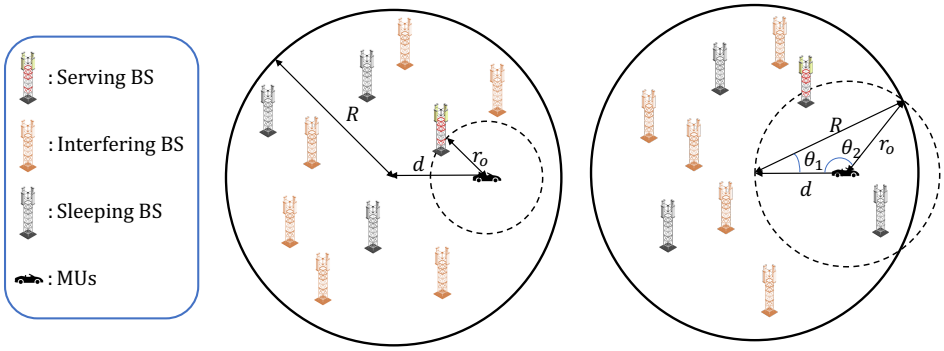

Figure 3.3: Simplified topology of the TLbS mechanism. The figure illustrates both the cases where the serving BS is close or far away from a MU, i.e. $r_o \leq R - d$ (left) and $r_o > R - d$ (right).

and

$$A = \begin{cases} \pi, & r_o \leq R - d, \\ \arccos\left(\dfrac{d^2 + r_o^2 - R^2}{2dr_o}\right), & r_o \geq R - d. \end{cases} \tag{3.21}$$

Proof. Based on the Gil-Pelaez inversion theorem, the conditional cdf of interference $\mathcal{I}$ in (3.19) can be derived from its characteristic function [58]. The calculation of characteristic function is just following the definition, i.e.

$$\begin{aligned} \psi(t, r_o) &= \mathbb{E}\left[\exp\left(jt\sum\nolimits_{i\in\tilde{\Phi}_B^{\setminus 0}} h_i r_i^{-\alpha}\right)\right] \\ &\overset{(a)}{=} \exp\left(-2\int_0^{\mathcal{A}}\int_{r_o}^{\mathcal{Z}}\left(1 - \frac{1}{1 - jtz^{-\alpha}}\right) z\tilde{\lambda}_b(z)\mathrm{d}z\mathrm{d}\theta\right), \end{aligned} \tag{3.22}$$

where $\mathcal{Z} = d\cos(\theta) + \sqrt{R^2 - d^2\sin(\theta)^2}$, and (a) is from the PGFL of PPPs [25]. In addition, the upper limits of the integral in (3.22), i.e. A can be evaluated by considering two cases as shown in Fig. 3.3. For the case that $r_o \leq R - d$, where the dash circle is inside the network area, the range of θ is from $-\pi$ to π, and thus $A = \pi$; while for the case that $r_o > R - d$, $\theta \in [-\theta_2, \theta_2]$, where θ_2 can be derived based on Cosine rule, and $A = \arccos\left(\frac{d^2 + r_o^2 - R^2}{2dr_o}\right)$. □

Therefore, based on the proposed TLbS mechanism, the ID ability of a MU is characterized by the following theorem in terms of ID success probability.

Theorem 3.1. *Based on the proposed* TLbS *mechanism, the ID success probability of a general MU, i.e.* $\mathcal{G}_{\mathrm{ID}}(\chi, d)$ *is given by*

$$\mathcal{G}_{\mathrm{ID}}(\chi, d) = \frac{1}{2} - \int_0^{R+d}\int_0^{\infty} \frac{\mathrm{Im}\{\mathcal{Z}(t, r_o)\psi(t, r_o)\}}{\pi t f_r^{-1}(r_o, d)}\mathrm{d}t\mathrm{d}r_o,$$

where

$$\mathcal{Z}(t, r_o) = \frac{\exp(jt(\sigma_N^2 + \sigma_C^2))\chi}{jr_o^{-\alpha}t + \chi},$$

$j = \sqrt{-1}$ *and* $\psi(\cdot)$ *is the characteristic function of interference* $\mathcal{I}$ *and* $f_r(r_o, d)$ *is the pdf of the distance* r_o *from a MU to its serving BS, which is given by*

$$f_r(r_o, d) = \begin{cases} -\dfrac{\mathrm{d}}{\mathrm{d}r_o}\exp(-\Lambda_1(r_o, d)),\ r_o \le R - d \\ -\dfrac{\mathrm{d}}{\mathrm{d}r_o}\exp(-\Lambda_2(r_o, d)),\ R - d < r_o \le R + d, \end{cases} \tag{3.23}$$

where

$$\Lambda_1(r_o, d) = \int_0^{r_o}\int_0^{2\pi} \tilde{\lambda}_b\left(\sqrt{\rho^2 + d^2 - 2\rho d\cos(\theta)}\right)\rho \mathrm{d}\rho\mathrm{d}\theta$$

$$\Lambda_2(r_o, d) = 2\int_0^{r_o}\int_0^{\theta_1} \tilde{\lambda}_b\left(\sqrt{\rho^2 + d^2 - 2\rho d\cos(\theta)}\right)\rho \mathrm{d}\rho\mathrm{d}\theta + 2\int_0^{r_o}\int_0^{\theta_2} \tilde{\lambda}_b(\rho)\,\rho \mathrm{d}\rho\mathrm{d}\theta$$
$$- 2\int_0^{\mathcal{Y}}\int_{\frac{y}{\tan(\theta_2)}}^{d + \frac{y}{\tan(\pi - \theta_1)}} \tilde{\lambda}_b(\sqrt{x^2 + y^2})\mathrm{d}x\mathrm{d}y$$

$\tilde{\lambda}_b(\cdot)$ *is the intensity function of the active BSs, which is given in Lemma 3.2;*

$$\theta_1 = \arccos\left(\frac{d^2 + r_o^2 - R^2}{2dr_o}\right),$$

$$\theta_2 = \arccos\left(\frac{R^2 + d^2 - r_o^2}{2Rd}\right),$$

and

$$\mathcal{Y} = \frac{\sqrt{(d + r_o + R)(d - r_o + R)(d + r_o - R)(r_o + R - d)}}{2d}.$$

Proof. The proof is basically based on the distribution of interference, i.e. the ID success probability of a general MU defined in (3.18) can be rewritten as

$$\begin{aligned}\mathcal{G}_{\mathrm{ID}}(\chi, d) =& \mathbb{P}\left[\mathcal{I} \le \frac{h_o r_o^{-\alpha}}{\chi} - \sigma_N^2 - \sigma_C^2\right] \\ =& \mathbb{E}_{h_o, r_o}\left[\mathrm{F}_{\mathcal{I}}\left(\frac{h_o r_o^{-\alpha}}{\chi} - \sigma_N^2 - \sigma_C^2\right)\right],\end{aligned}$$

where $\mathsf{F}_{\mathcal{I}}(\cdot)$ is the conditional cdf of aggregate interference, derived in Lemma 3.3. Then substitute the expression of $\mathsf{F}_{\mathcal{I}}(\cdot)$ and evaluate the expectation over the channel power gain h_o, i.e.

$$\mathcal{G}_{\mathrm{ID}}(\chi, d) = \mathbb{E}\left[\frac{1}{2} - \int_0^{\infty} \frac{\mathrm{Im}\left\{\int_0^{\infty}\exp(-jt(\frac{h_o r_o^{-\alpha}}{\chi} - \sigma_N^2 - \sigma_C^2))e^{-h}\psi(t, r_o)\mathrm{d}h\right\}}{\pi t}\mathrm{d}t\right].$$

Yuan Guo

Finally, by calculating the above integral as well as evaluating the expected value over distance r_o, the final expression in Theorem 3.1 is derived, where the pdf of r_o can be derived by calculating the derivative of its cdf, i.e.

$$F_r(r_o) = 1 - \mathbb{P}[r \geq r_o] = 1 - \exp(-\Lambda(d, r_o)),$$

where $\Lambda(r_o, d)$ represents the intensity measure function. As shown in Fig. 3.3, $\Lambda(r_o, d)$ can be calculated based on the two cases, i.e. the serving BS is close or far way from MUs. For both two cases, $\Lambda(r_o, d)$ is derived by integrating $\tilde{\lambda}_b(\cdot)$ over the intersection area of two circles using non-uniform measure. The angles θ_1 and θ_2 are used as integral limits in the calculation, which can be derived based on Cosine rule. □

Moreover, the ID success probability of the MUs located at the center of the considered finite region $\mathcal{A}$ can be further simplified due to the symmetrical properties of $\tilde{\lambda}_b(r)$, which is given in the following corollary.

Corollary 3.1. *Based on the proposed* TLbS *mechanism, the ID success probability of the MUs located at the origin, i.e.* $\mathcal{G}_{\mathrm{ID}}(\chi, 0)$ *is given by*

$$\mathcal{G}_{\mathrm{ID}}(\chi, 0) = \int_0^R f_r(r_o, 0) \exp\left(- \int_{r_o}^R \frac{2\pi v \tilde{\lambda}_b(v)}{1 + \chi^{-1}(v/r_o)^{\alpha}} \mathrm{d}v \right) \exp\left(- \chi r_o^{\alpha} (\sigma_N^2 + \sigma_{\mathrm{C}}^2) \right) \mathrm{d}r_o,$$

where $f_r(\cdot)$ *is the pdf of the distance from the MU located at the origin to its serving BS, which can be simplified as*

$$f_r(r_o, 0) = 2\pi \tilde{\lambda}_b(r_o) r_o \exp\left(-2\pi \int_0^{r_o} \tilde{\lambda}_b(v) v \mathrm{d}v \right).$$

3.4.3 Energy harvesting success probability with TLbS mechanism

In this section, we evaluate the ability of a general MU to harvest sufficient energy, i.e. the EH success probability, which is defined as

$$\mathcal{G}_{\mathrm{EH}}(\mathcal{Q}, d) = \mathbb{P}[\zeta \rho (\mathcal{S} + \mathcal{I}) \geq \mathcal{Q}], \tag{3.24}$$

where ζ accounts for conversion efficiency of the energy harvester and ρ is the power splitting factor. Therefore, by using the tools from stochastic geometry, the expression for the EH success probability of a MU is derived in the following theorem.

Yuan Guo

Theorem 3.2. *Based on the proposed* TLbS *mechanism, the EH success probability of a general MU, i.e.* $\mathcal{G}_{\mathrm{EH}}(\mathcal{Q}, d)$ *is given by*

$$\mathcal{G}_{\mathrm{EH}}(\mathcal{Q}, d) = \int_0^{R+d} f_r(r_o, d)\Big(\frac{1+\exp(-\bar{\mathcal{Q}} r_o^{\alpha})}{2} + \int_0^{\infty} \frac{\mathrm{Im}\left\{\mathcal{V}(t, r_o)\psi(t, r_o)\right\}}{\pi t}\mathrm{d}t\Big)\mathrm{d}r_o,$$

where

$$\mathcal{V}(t, r_o) = \frac{\exp(-\bar{\mathcal{Q}} r_o^{\alpha}) - \exp(-j\bar{\mathcal{Q}} t)}{j t r_o^{-\alpha} - 1},$$

and $\bar{\mathcal{Q}} = \mathcal{Q}/(\zeta\rho)$, $\psi(\cdot)$ *is the characteristic function given by* (3.20) *and* $f_r(\cdot)$ *is the pdf of the distance from a MU to its serving BS given by* (3.23).

Proof. The proof of the EH success probability is also based on the distribution of the interference $\mathcal{I}$. More specifically, the EH success probability can be rewritten as

$$\begin{aligned}\mathcal{G}_{\mathrm{EH}}(\mathcal{Q}, d) =& \mathbb{P}[\mathcal{S} \geq \bar{\mathcal{Q}}] + \mathbb{P}\left[\mathcal{I} \geq \bar{\mathcal{Q}} - \mathcal{S} | \mathcal{S} \leq \bar{\mathcal{Q}}\right] \\ =& \bar{\mathsf{F}}_{\mathcal{I}}(\bar{\mathcal{Q}} - \mathcal{S}) + \mathbb{P}[\mathcal{S} \geq \bar{\mathcal{Q}}],\end{aligned} \tag{3.25}$$

where $\bar{\mathcal{Q}} = \mathcal{Q}/(\rho\zeta)$ and $\bar{\mathsf{F}}_{\mathcal{I}}(\cdot) = 1 - \mathsf{F}_{\mathcal{I}}(\cdot)$. Therefore, we have,

$$\begin{aligned}&\mathcal{G}_{\mathrm{EH}}(\mathcal{Q}, d) \\ =&\mathbb{E}_{r_o}\left[\exp(-\bar{\mathcal{Q}} r_o^{\alpha}) + \int_0^{\bar{\mathcal{Q}} r_o^{\alpha}} \bar{\mathsf{F}}_{\mathcal{I}}(\bar{\mathcal{Q}} - h r_o^{-\alpha})\exp(-h)\mathrm{d}h\right] \\ =&\mathbb{E}_{r_o}\left[\frac{1+\exp(-\bar{\mathcal{Q}} r_o^{\alpha})}{2} + \int_0^{\infty} \frac{\mathrm{Im}\{\int_0^{\bar{\mathcal{Q}} r_o^{\alpha}} \exp(-jt(\bar{\mathcal{Q}} - h r_o^{-\alpha}))\exp(-h)\mathrm{d}h\phi(t, r_o)\}}{\pi t}\mathrm{d}t\right],\end{aligned}$$

where the integral over h can be computed in closed-form with the aid of the following notable results [19]:

$$\int_0^x \exp\big(-jt(A - B\xi)\big)\exp(-\xi)\mathrm{d}\xi = \frac{\exp(-Ajt) - \exp(Bjtx - Ajt - x)}{1 - Bjt}.$$

Finally, by evaluating the expectation over r_o, the final expression in Theorem 3.2 is derived. □

Since the harvested energy of a MU is mainly associated to its serving BS, especially for the case with a large number of traffic load threshold N, the interference power could be ignored for the simplification purpose. Hence, the EH success probability is approximated in the following corollary.

Corollary 3.2. *The EH success probability of a general MU derived in Theorem 3.2 can be approximated by ignoring the received interference power, and thus is given by*

$$\mathcal{G}_{\mathrm{EH}}(\mathcal{Q}, d) \approx \int_0^{R+d} \exp(-\bar{\mathcal{Q}} r_o^{\alpha}) f_r(r_o, d)\mathrm{d}r_o \tag{3.26}$$

Yuan Guo

3.4.4 Joint information decoding and energy harvesting success probability with TLbS mechanism

In this section, we focus the attention on the joint ID and EH performance of a general MU in the context of the joint ID and EH success probability, i.e. $\mathcal{G}_{\text{ID\&EH}}(\chi, \mathcal{Q}, d)$, which refers to the ability of a MU to accomplish both ID and EH constraints simultaneously. Hence, similar as before, the joint probability of the ID and EH is defined as

$$\mathcal{G}_{\text{ID\&EH}}(\chi, \mathcal{Q}, d) \triangleq \mathbb{P}\left[\frac{\mathcal{S}}{\mathcal{I}+\sigma_N^2+\sigma_C^2} \geq \chi \,\&\, \zeta\rho(\mathcal{S}+\mathcal{I}) \geq \mathcal{Q}\right], \tag{3.27}$$

where χ and $\mathcal{Q}$ represent the ID and EH thresholds, respectively.

Therefore, by following the similar approaches used before, the analytical expression of the joint ID and EH success probability is derived in the following theorem.

Theorem 3.3. *Based on the TLbS mechanism, the joint ID and EH success probability of a MU, i.e. $\mathcal{G}_{\text{ID\&EH}}(\chi, \mathcal{Q}, d)$ is given by*

$$\mathcal{G}_{\text{ID\&EH}}(\chi, \mathcal{Q}, d) = \int_0^{R+d} \left(\frac{1}{2}\exp(-\bar{\mathcal{Q}} r_o^{\alpha}) + \int_0^{\infty} \frac{\text{Im}\{\mathcal{X}(t, r_o)\psi(t, r_o)\}}{\pi t}\text{d}t\right) f_r(r_o, d)\text{d}r_o,$$

where

$$\begin{aligned}\mathcal{X}(t, r_o) =& \frac{\exp(-\bar{\mathcal{Q}} r_o^{\alpha}) - \exp\left(-\frac{r_o^{\alpha}(\bar{\mathcal{Q}}+\sigma_N^2+\sigma_C^2)+jt(\bar{\mathcal{Q}}\chi^{-1}-\sigma_N^2-\sigma_C^2)}{\chi^{-1}+1}\right)}{jtr_o^{-\alpha}-1} \\ &- \frac{\exp\left(-\frac{r_o^{\alpha}(\bar{\mathcal{Q}}+\sigma_N^2+\sigma_C^2)+jt(\bar{\mathcal{Q}}\chi^{-1}-\sigma_N^2-\sigma_C^2)}{\chi^{-1}+1}\right)}{jt\chi^{-1}r_o^{-\alpha}+1}.\end{aligned} \tag{3.28}$$

Proof. The proof follows the similar method in [19]. First, we rewrite the joint ID and EH success probability defined in (3.27) as

$$\begin{aligned}\mathcal{G}_{\text{ID\&EH}}(\chi, \mathcal{Q}, d) =& \mathbb{P}\left[\max\{0, \mathcal{Q}/(\zeta\rho) - \mathcal{S}\} \leq \mathcal{I} \leq \mathcal{S}/\chi - \sigma_N^2 - \sigma_C^2\right] \\ \overset{(a)}{=}& \mathbb{P}\left[\max\{0, \bar{\mathcal{Q}} - h_o r_o^{-\alpha}\} \leq \mathcal{I} \leq h_o r_o^{-\alpha}/\chi - \sigma_N^2 - \sigma_C^2\right],\end{aligned}$$

where $\bar{\mathcal{Q}} = \mathcal{Q}/(\zeta\rho)$, and (a) holds by introducing the inequality $h_o r_o^{-\alpha} \geq \chi/(1+\chi)(\bar{\mathcal{Q}} + \sigma_N^2 + \sigma_C^2)$. Hence, $\mathcal{G}_{\text{ID\&EH}}(\chi, \mathcal{Q}, d)$ can be evaluated by utilising the distribution of interference $\mathcal{I}$, and then by calculating the expected value over other random

Yuan Guo

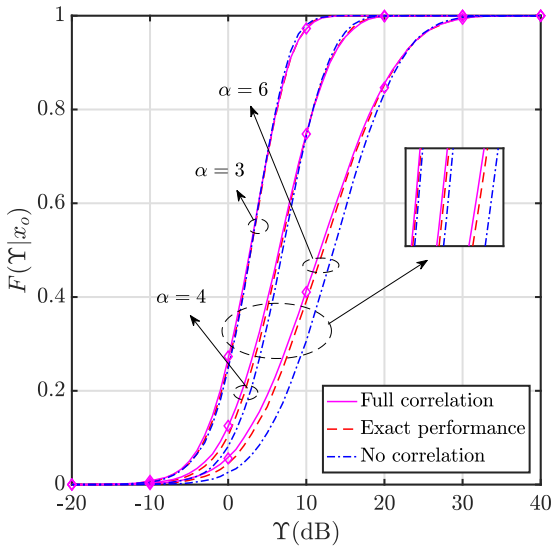

Figure 3.4: The conditional cdf of SIR_n for different $\alpha \in \{3, 4, 6\}$; $r_o = 30$ m.

variables, i.e. h_o and r_o, final expression can be derived. More specifically,

$$\begin{aligned}\mathcal{G}(\chi, \mathcal{Q}, d) =& \mathbb{E}\left[\mathsf{F}_{\mathcal{I}}\left(\frac{h_o r_o^{-\alpha}}{\chi} - \sigma_N^2 - \sigma_C^2\right) - \mathsf{F}_{\mathcal{I}}(\max\{0, \bar{\mathcal{Q}} - h_o r_o^{-\alpha}\})\right] \\ =& \mathbb{E}\left[\int_{\mathcal{A}(r_o)}^{\mathcal{B}(r_o)} \left(\mathsf{F}_{\mathcal{I}}\left(\frac{h r_o^{-\alpha}}{\chi} - \sigma_N^2 - \sigma_C^2\right) - \mathsf{F}_{\mathcal{I}}(\bar{\mathcal{Q}} - h r_o^{-\alpha})\right) e^{-h} \mathrm{d}h \right. \\ & \left. + \int_{\mathcal{B}(r_o)}^{\infty} \left(\mathsf{F}_{\mathcal{I}}\left(\frac{h r_o^{-\alpha}}{\chi} - \sigma_N^2 - \sigma_C^2\right) - \mathsf{F}_{\mathcal{I}}(0)\right) e^{-h} \mathrm{d}h\right],\end{aligned}$$

where $\mathcal{A}(r_o) = r_o^{\alpha} \frac{\chi}{1+\chi}(\bar{\mathcal{Q}} + \sigma_N^2 + \sigma_C^2)$ is obtained from the inequality $\bar{\mathcal{Q}} - h_o r_o^{-\alpha} \leq h_o r_o^{-\alpha}/\chi - \sigma_N^2 - \sigma_C^2$, and $\mathcal{B}(r_o) = \bar{\mathcal{Q}} r_o^{\alpha}$ is from $\bar{\mathcal{Q}} - h_o r_o^{-\alpha} \geq 0$.

Finally, by following the similar methodology in the Proof of Theorem 3.2, i.e. substitute the expression of $\mathsf{F}_{\mathcal{I}}(\cdot)$ and evaluate the above integrals, the final expression of joint ID and EH success probability is derived. □

3.5 Numerical results

In this section, we provide numerical and simulated results to validate the accuracy of our model and illustrate the performance of the proposed TbPS and TLbS schemes. In order to demonstrate the achieved gains of the network performance with our proposed techniques, the benchmark schemes are also numerically evaluated for the comparison purpose. Unless otherwise stated, in our results we con-

Yuan Guo

sider the following parameters: for large-scale networks, which encompass an infinite area, the radius of network area is considered infinite, $\lambda_b = \frac{1}{1600\pi}$, $\lambda_u = \frac{5}{1600\pi}$, path-loss exponent $\alpha = 3$, PS parameter $\rho = 0.5$, RF-to-DC efficiency $\zeta = 0.7$; for the small-scale networks, $R = 100$, $\lambda_b = \frac{2}{1600\pi}$, λ_u is the same as in large-scale networks, the small-scale networks also share the same α, ρ, and ζ values as the large-scale networks, $\sigma_N^2 - 85$ dBm and $\sigma_{cov}^2 = -35$ dBm.

Fig. 3.4 demonstrates the conditional cdf of the SIR_n for different path loss exponents. The solid lines represent the conditional cdf derived in Lemma 3.1 and the markers depict the analytical results. In order to demonstrate the impact of the interference correlation on the performance achieved by the TbPS scheme and validate the accuracy of the adopted assumptions, we numerically evaluate the scenario, where the interference power observed within each antenna pair is correlated but not equal (denoted as "Exact performance"), i.e. $\mathcal{I}_k \neq \mathcal{I}_{k+1}$, and the scenario where interference received at different antenna elements is independent with each other (denoted as "No correlation"). We can easily observe that the performance achieved by using the adopted assumptions provides a tight upper bound for the exact performance, with lower computational complexity. On the other hand, by ignoring the existence of spatial correlation between interference, it leads to a large deviation from the exact performance, especially, for higher path loss exponents. This was expected since, in dense urban areas, i.e. high path loss exponents, the aggregate interference is mainly composed by the interference caused by the closest interfering BS. Hence, if an antenna fails to decode the received signal, then the rest antennas will fail to decode the received signal with high probability, due to the existence of interference correlation.

Fig. 3.5 illustrates the effect of the threshold γ_{th} on the ability of a MU to successfully decode the received signal power. In particular, Fig. 3.5 plots the ID success probability with respect to the threshold γ_{th} for different decoding thresholds $\chi \in \{0, 5, 10\}$ dB. Both simulation and analytical results are presented in Fig. 3.5, denoted as "TbPS simulation" and "TbPS analysis", respectively. In addition, the scenario, where the interference power observed within each antenna pair is correlated but not equal, denoted as "Exact performance", is also presented here to validate the accuracy of the adopted assumption. It can be observed that there exists minimum gap between our analytical results and the exact performance. Moreover, we can easily observe that the ability of a MU to successfully decode the received signal

Yuan Guo

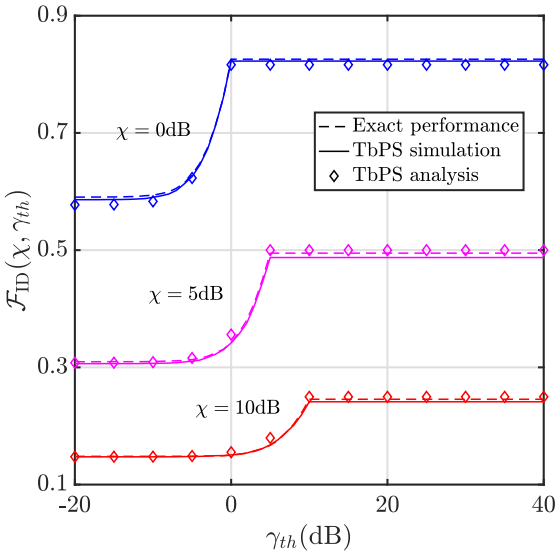

Figure 3.5: ID success probability of MUs with TbPS scheme versus the threshold γ_{th} for different $\chi \in \{0, 5, 10\}$ dB.

power increases with the increase of the predefined threshold γ_{th}. This was expected since, the increase of γ_{th} results in an increased number of antenna elements that perform ID, and consequently, the ability to successfully decode the received signal power is enhanced. However, beyond a critical value of γ_{th}, which is equal to $\gamma_{th} = \chi$, the ID success probability remains constant. This can be explained by the fact that, for large values of γ_{th}, a MU is unable to assign an additional pair of antennas for the ID due to the constrain of the existence of at least one pair of antennas for EH, i.e. the performance could be further boosted for the receiver with more pairs of antenna elements. Moreover, by increasing the decoding threshold χ, the ID performance drops, which is from fact that greater decoding threshold requires higher post-combiner SIR to achieve the same success probability.

Similarly, Fig. 3.6 illustrates the effect of γ_{th} on the EH success probability for different EH reliability thresholds $\mathcal{Q} \in \{-15, -10, -5\}$ dBm and different density of BSs $\lambda_b \in \{\frac{1}{1600\pi}, \frac{1}{2500\pi}\}$. Firstly it can be observed that denser BS deployments can boost the EH success probability based on the proposed TbPS technique. This is based on the fact that the increasing number of active BSs in the network results in a higher aggregated received signal power at the MUs, which can be harvested. Moreover, as expected, the harvested energy of MUs decreases as the predefined threshold γ_{th} increases, since the number of antenna elements allocated for energy harvesting reduces, and hence the EH success probability drops. Moreover, Fig. 3.6

Yuan Guo

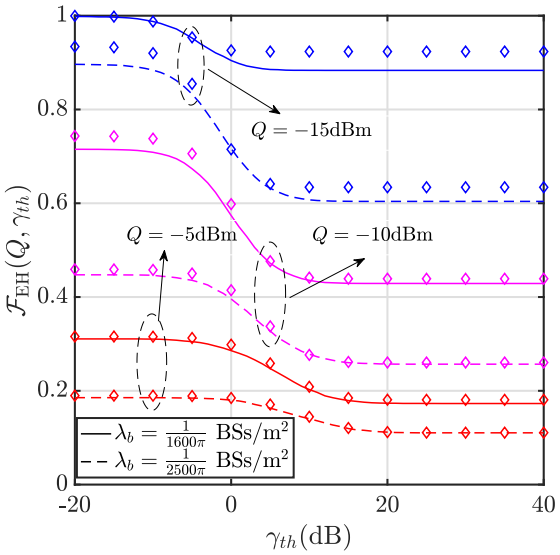

Figure 3.6: EH success probability of MUs with TbPS scheme versus the threshold γ_{th} for different $\mathcal{Q} \in \{-15, -10, -5\}$ dBm.

also demonstrates the impact of the considered approximation regarding the observed interference on the EH success probability. The small deviation from the simulation results shows that the overall network interference can be effectively approximated by the mean interference power, without being significantly deficient in accuracy. Moreover, we can conclude from Fig. 3.6 that, by changing network parameter (i.e.,density of BSs), a shifted EH performance is observed, while the curves' shape maintains constant. These observation holds for all figures presented in our results.

Fig. 3.7 shows the impact of the threshold γ_{th} on the ability of a MU to simultaneously satisfy the requirements for both ID and EH procedures. It is worth noting that, by increasing the threshold γ_{th}, the ability of a user to simultaneously satisfy the ID and EH constrains increases. This is because, as the value of the threshold γ_{th} increases, the proposed TbPS scheme allocates a higher number of antenna elements for the ID part. Hence, the ability of a MU to successfully decode the received signal is significantly improved, while its ability to harvest energy is slightly reduced. However, beyond the critical point $\gamma_{th} = \chi$, the ability of a user to simultaneously satisfy the ID and EH constrains decreases. As indicated in Fig. 3.5 and Fig. 3.6, the ability of a user to successfully decode the received signal beyond a threshold equal to χ, remains constant, while the ability to harvest energy is reducing, and hence the joint ID and EH success probability is decreasing. Finally, we numerically

Yuan Guo

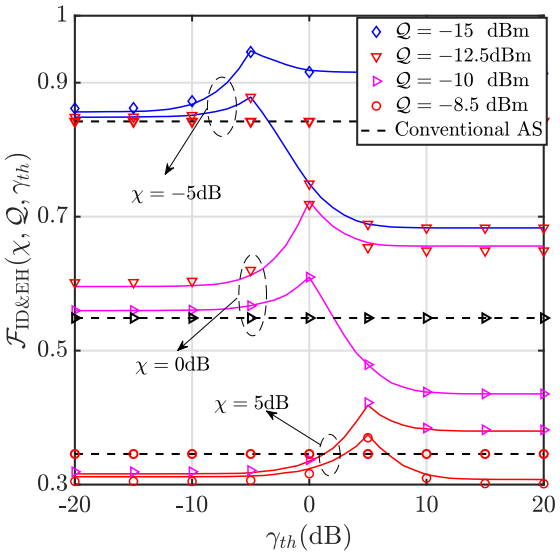

Figure 3.7: Joint ID and EH success probability versus the threshold γ_{th} for different $\chi \in \{-5, 0, 5\}$ dB and $\mathcal{Q} \in \{-15, -12.5, -10, -8.5\}$ dBm.

evaluate the conventional AS scheme, where half number of antennas are used for ID and half for EH [13]. It can be observed that, the performance achieved with our proposed technique outperforms that of the conventional scheme in terms of the optimal joint ID and EH success probability, where a maximum 5% gain over the conventional AS scheme can be achieved based on the considered network parameters. Moreover, the proposed TbPS scheme is able to satisfy various ID and EH requirements of practical applications, by adjusting the predefined threshold.

Fig. 3.8 shows the impact of our proposed TLbS mechanism on the ID performance of the MUs at different locations, i.e. $d = \{0, 70, 100\}$ m. We can firstly observe that, for low values of traffic load threshold, N, the ID success probability increases with the increase of the traffic load threshold. This was expected since, by increasing the value of N, more and more BSs are switched to sleeping mode, the inter-cell interference is reduced, and therefore, the ability of MUs to successfully decode the received signal is enhanced. However, beyond a critical value of N, the ID success probability decreases. This was expected since, by further increasing the traffic load threshold, the number of BSs that are in sleeping mode increases, resulting in the distances between the MU and its closest active BS to be greater, compromising the ability of a MU to successfully decode the received signal power. Moreover, we can observe that the ID success probability of the MUs located between the center and edge regions, i.e. $d = 70$ m, overcomes the performance

Yuan Guo

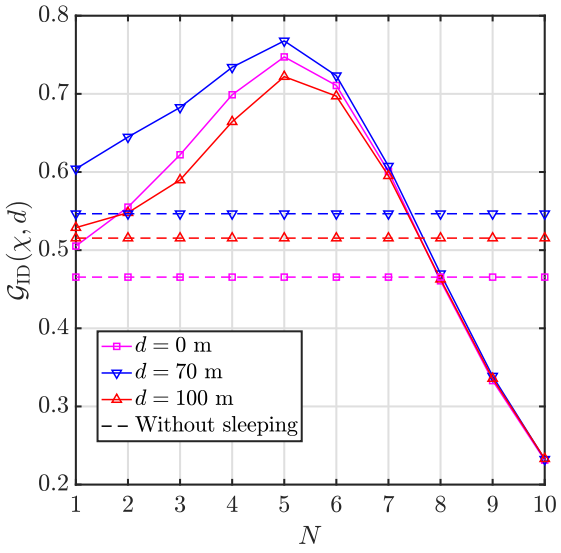

Figure 3.8: ID success probability of MUs with TLbS mechanism versus the minimum number of MUs constraint N for different $d \in \{0, 70, 100\}$ m; $\lambda_b = 2/(1600\pi)$, $R = 100$ m, and $\chi = 0$dB.

achieved by the MUs that are located at the center and edge regions. This can be explained by the fact that, the MUs which are located at the center experience severe inter-cell interference, while the MUs at the edge receive a weak signal power from their serving BSs due to the non-uniform distribution of BSs imposed by the proposed TLbS technique. Finally, Fig. 3.8 also plots the achieved performance without sleeping mechanism (dash lines) [90], i.e. all BSs are active. It can be observed that, by appropriately selecting the values of N, our proposed TLbS mechanism enables a higher ID success probability of MUs at different locations. This was expected since that, the inter-cell interference power is significantly reduced with TLbS mechanism, resulting in a higher SINR at MUs.

Fig. 3.9 demonstrates the impact of the traffic load threshold N on the EH success probability of the MUs at different locations, i.e. $d = \{0, 70, 100\}$ m. We can easily observe that the EH success probability of the MUs, regardless of the location, decreases with the increase of the traffic load threshold. We can easily observe, that the EH success probability of the MUs is reduced with the raise of the traffic load threshold, regardless of the MUs' locations. This is due to the fact that, by increasing the traffic load threshold, more and more BSs become inactive within the network, and consequently, the received RF ambient energy at the MUs' rectenna reduces. In addition, it can be easily observed that, the MUs located at center have the ability

Yuan Guo

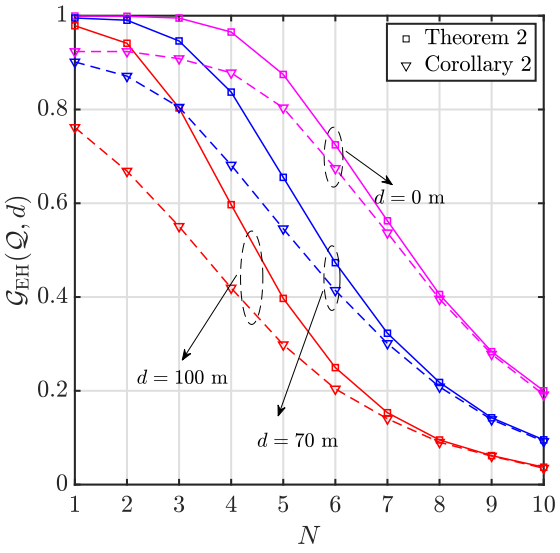

Figure 3.9: EH success probability of MUs with TLbS mechanism versus the minimum number of MUs constraint N for different $d \in \{0, 70, 100\}$ m; $\lambda_b = 2/(1600\pi)$, $R = 100$ m, and $\mathcal{Q} = -30$dBm.

to harvest significantly higher RF ambient energy compared with the MUs located elsewhere. This was expected, since the movement process of the MUs and the proposed TLbS technique lead to a larger number of active BSs around the network's center, and hence, the observed RF energy is significantly higher at the center region compared to that at the edge region of the network. Moreover, Fig. 3.9 demonstrates the impact of interference on the network performance. The small deviation from the theoretical curves at high traffic load thresholds indicates that, the aggregate interference power is negligible compared to the signal power from the serving BS for high values of N, providing a lower bound for the actual network performance.

Fig. 3.10 illustrates the impact of the traffic load threshold N on the ability of MUs to simultaneously satisfy ID and EH threshold. It is interesting to note that at low traffic load thresholds, the de-activation of BSs improves the network performance. However, by increasing the traffic load threshold beyond a critical point, the network performance decreases. As we previously mentioned, at low traffic load thresholds, the ability of MUs to successfully decode the received signal significantly increases with the increase of the traffic load threshold, while their ability to harvest energy is slightly reduces. In contrast, for high traffic load thresholds, both the ID and EH capabilities of the MUs are reduced, leading to a reduced joint ID and EH probability. Fig. 3.10 also highlights, that an optimal operating point,

Yuan Guo

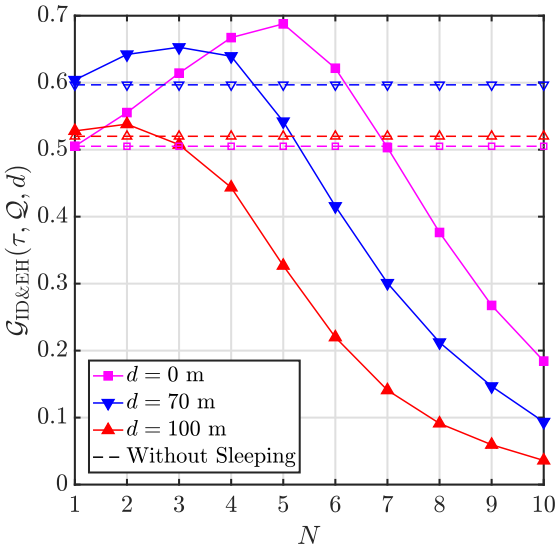

Figure 3.10: Joint ID and EH success probability of MUs with TLbS mechanism versus the minimum number of MUs constraint N for different $d \in \{0, 70, 100\}$ m; $\lambda_b = 2/(1600\pi)$, $R = 100$ m, $\chi = 0$dB and $\mathcal{Q} = -30$dBm.

as a function of N, exists, where the joint ID and EH probability attains its optimal value. The optimal value of N, in particular, decreases as the MU moves away from the center of the network area, i.e. d increases. Moreover, Fig. 3.10 also plots the conventional schemes where all BSs are active (dash lines) [90], i.e. the traffic load threshold $N = 0$, for the comparison purpose. It can be observed that the TLbS mechanism enables a higher joint ID and EH success probability of MUs at different locations, with appropriate values of traffic load threshold N, where a maximum 20% gain over the conventional scheme can be achieved by the TLbS mechanism. In addition, the TLbS mechanism enables the highest performance improvement for the MUs at the center, compared with the case where all BSs are active. It can be explained by the fact that, by properly selecting the traffic load threshold value N, the inter-cell interference power is reduced due to the de-activation of interfering BSs, while the MUs at center are still able to communicate with nearby serving BSs to maintain the acceptable signal strength.

Finally, Fig. 3.11 shows the impact of the power splitting factor on the SWIPT capabilities of the MUs located at the different locations. In particular, Fig. 3.11 plots the joint ID and EH success probabilities versus the power splitting factor, for $d \in \{0, 70, 100\}$ m . We can easily observe that, there exists an optimum power splitting factor for all MUs, which achieves the maximum joint ID and EH success

Yuan Guo

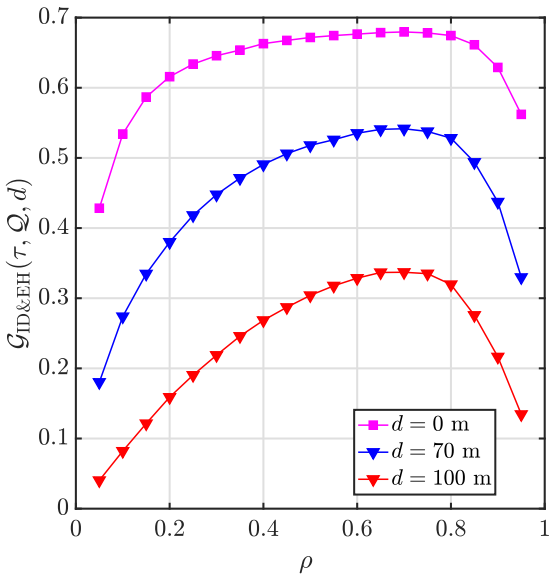

Figure 3.11: EH success probability of MUs with TLbS mechanism versus the power splitting factor ρ for different $d \in \{0, 70, 100\}$ m; $\lambda_b = 2/(1600\pi)$, $N = 5$, $\chi = 0$ dB and $\mathcal{Q} = -30$dBm.

probability. This was expected since, a trade-off exists between the ID and the EH performance of the MUs. Hence, for attaining the maximum performance for both MUs' abilities, a carefull selection of the power splitting factor has to be performed. Moreover, it is shown that, the MUs located at the center of the network area (i.e., $d = 0$ m) achieve the best SWIPT performance, while the edge MUs (i.e., $d = 100$ m) have the worst performance. This is expected since, based on the TLbS mechanism, the mobility of the MUs leads to a less number of active BSs around the network's edge area, and hence, the received RF signal power is much less at the edge region compared to that at the center region of the network. Finally, we can easily observe that, the power splitting factor can be adjusted based on the practical scenarios, to satisfy the various requirements of the information decoding and energy harvesting applications.

3.6 Summary

In this chapter, we investigated the SWIPT-enabled 6G mobile networks, where users' mobility is modelled based on RWP model. According to the areas of the considered networks, i.e. finite or infinite regions, we investigated the MUs' ability of ID and EH with two proposed novel techniques, i.e. TbPS scheme and TLbS mech-

Yuan Guo

anism. In particular, TbPS scheme was proposed to enhance the ID and EH performance for the SWIPT-enabled multi-antenna MUs in the infinite area networks, where the existence of interference correlation between nearby antennas was considered. Moreover, TLbS mechanism was proposed to dynamically determine the state of the BSs, i.e. either active or in sleeping mode, based on the traffic load, aiming the joint optimization of users' throughput and EH performance. By using the tools from stochastic geometry, the analytical expressions of ID, EH as well as joint ID and EH success probability were derived for MUs, based on TbPS or TLbS techniques. Finally, the optimal design parameters (i.e. antenna selection and traffic load threshold) of our proposed schemes were demonstrated, which could achieve the maximum joint ID and EH performance of MUs.

Yuan Guo

Chapter 4

SWIPT-enabled multi-antenna mobile users with a linear MMSE receiver

In this chapter, we evaluate the performance of a linear MMSE receiver in the context of SWIPT-enabled cellular networks. In contract to the existing works, where a single-antenna SWIPT architecture is mainly considered, we focus on the SWIPT performance of the multi-antenna receiver architecture, based on the AS and PS techniques. Aiming to further boost the network performance, we investigate a scenario where the receivers have the capability to employ a SIC scheme. By leveraging tools from stochastic geometry, we establish an analytical and tractable framework to evaluate the ID and the EH success probabilities of the considered network topologies.

4.1 Motivation and contribution

As we previously mentioned, for the SWIPT-enabled multi-antenna receivers, the interference observed across different antenna elements is spatially correlated [61] [67]. While it has been long recognized that the correlated fading reduces the performance gain of multi-antenna communication systems, the concept of interference correlation has been overlooked until recently. Due to the existence of interference correlation between different antennas, the MRC results in a suboptimal performance. Hence, in this chapter, we study the SWIPT performance for multi-antenna MUs in the context of a linear MMSE receiver. In particular, the MUs employ either a PS or an AS scheme to simultaneously extract information and harvest energy from

Kuan Guo

the received RF signals, where a MMSE receiver is employed for ID purpose. In order to further enhance the network performance, a SIC technique is investigated to improve the ID performance of the MUs, via mitigating the strongest multi-user interfering signals. By using stochastic geometry tools, we analytically derive the ID and the EH success probabilities, where closed-form expressions are obtained for the interference-limited scenarios. Our results show that the MMSE receiver achieves higher ID and EH success probabilities, compared with the conventional MRC. Moreover, it is demonstrated that, due to the MMSE receiver, the PS scheme outperforms the AS scheme in terms of both the ID and the EH performance. Finally, a significant gain of SWIPT performance can be achieved, by employing the SIC technique at the MUs.

4.2 System model

The network topology has been introduced in Section 2.2.2. In this chapter, we consider a single-input-multiple-output (SIMO) setup, where all BSs transmit unit-power signals with single omnidirectional antenna, while all MUs are equipped with L antenna elements [35, 36]. We assume that all MUs can decode information and harvest energy simultaneously by using the SWIPT technology, based on either PS (see Section 2.2.5) or AS schemes. For the scenario where the MU employs the AS scheme, ℓ antennas are used for ID, where $0 \leq \ell \leq L$, and the remaining $L - \ell$ antennas are used for EH [63]. A linear MMSE receiver is assumed to be equipped at each MU, where an optimal weight vector is determined, such that the output SINR is maximized [35, 36]. Hence, the output SINR can be expressed as

$$\gamma = \rho r_0^{-\alpha} \widehat{\mathbf{h}}_0^H \mathbf{R}^{-1} \widehat{\mathbf{h}}_0, \tag{4.1}$$

with

$$\mathbf{R} = \sum_{x_i \in \Phi \setminus x_0} \rho r_i^{\alpha} \widehat{\mathbf{h}}_i \widehat{\mathbf{h}}_i^H + \sigma^2 \mathrm{I}_\ell, \tag{4.2}$$

where $\widehat{\mathbf{h}}_i \subseteq \mathbf{h}_i$ is a ℓ dimensional vector representing the channel coefficients of the links between the i-th BS and the MU's antennas allocated for ID. Note that (4.1) holds for both the PS and AS scheme, i.e. $\ell = L$ and $0 \leq \rho \leq 1$ are adopted for the PS scheme, while $\rho = 1$ and $0 \leq \ell \leq L$ for the AS scheme. Regarding the energy transfer model, we adopt a non-linear EH model, and thus the harvested energy of

Yuan Guo

a MU is quantified as following [65]

$$\psi = \frac{\nu\rho\eta}{1+F}\sum_{x_i\in\Phi}\sum_{j=\ell+1}^{L} h_{ij} r_i^{-\alpha}. \tag{4.3}$$

4.3 SWIPT performance with a linear MMSE receiver

In this section, we investigate the ID and the EH performance for scenarios with a MMSE receiver [35]. Firstly, we analytically derive the exact expressions for the ID and the EH success probabilities, by using stochastic geometry tools. Moreover, closed-form expressions of the ID and the EH success probabilities are derived for the interference-limited regime.

4.3.1 Information decoding success probability

The ID success probability is defined as the probability that the output SINR of the MMSE receiver is greater than the decoding threshold β, i.e. $\mathbb{P}[\gamma \geq \beta]$. The achieved ID success probability of the typical MU that employs either the PS or the AS scheme is characterized by the following theorem.

Theorem 4.1. *By using a MMSE receiver, the ID success probability of the typical MU is given by*

$$\Pi^{\mathrm{I}}(\beta) = \int_0^\infty \frac{\Gamma\left(\ell, \sigma^2\rho^{-1}\beta r_0^\alpha + \lambda\delta(r_0,\beta)\right)}{\Gamma(\ell)} f(r_0)\mathrm{d}r_0, \tag{4.4}$$

where $\delta(r_0,\beta) = \frac{2\pi r_0^2 \beta_2 F_1\left(1, \frac{\alpha-2}{\alpha}; 2-\frac{2}{\alpha}; -\beta\right)}{\alpha-2}$, *and* $f(r_0)$ *is the pdf of the distance from the typical MU to its serving BS, which is given by* (3.23).

Proof. Firstly, by conditioning on the distance between the typical MU to all BSs, the conditional ID success probability could be formulated as [36]

$$\mathbb{P}[\gamma \geq \beta | r_0, r_1, \ldots, r_K] = \frac{\exp\left(-\sigma^2\beta r_0^\alpha\right)\sum_{i=0}^{\ell-1} a_i(\beta r_0)^i}{\prod_{j=1}^{K}\left(1 + r_j^{-\alpha}\beta r_0\right)},$$

where K is the number of BSs, and a_i are the first ℓ coefficient of the Taylor expansion of $\exp\left(-\sigma^2\beta r_0^\alpha\right)\prod_{j=1}^{N}(1+r_j^{-\alpha}\beta r_0)$.

Then, by un-conditioning over the distance from the typical MU to interfering BSs, i.e. $r_1, r_2, \cdots, r_K$, and following [35, Eq.(15)], the conditional ID success proba-

bility, i.e. $\mathbb{P}[\gamma \geq \beta | r_0]$ can be expressed as

$$\mathbb{P}[\gamma \geq \beta | r_0] = \exp\left(-\frac{\sigma^2 \beta r_0^\alpha}{\rho}\right) \sum_{j=0}^{\ell-1} \sum_{k=0}^{j} \frac{(\sigma^2 \rho^{-1} \beta r_0^\alpha)^{j-k}}{k!(j-k)!} \left(2\pi\lambda \int_{r_0}^{\infty} \frac{x^{1-\alpha} \beta r_0^\alpha}{1 + x^{-\alpha} \beta r_0^\alpha} \mathrm{d}x\right)^k$$
$$\times \exp\left(-2\pi\lambda \int_{r_0}^{\infty} \frac{x^{1-\alpha} \beta r_0^\alpha}{1 + x^{-\alpha} \beta r_0^\alpha} \mathrm{d}x\right).$$

The above integrals can be evaluated, by using the transformation $u \leftarrow x^2$ and by using the expression in [91, 3.24], such that we have

$$\mathbb{P}[\gamma \geq \beta | r_0] = \exp\left(-\frac{\sigma^2 \beta r_0^\alpha}{\rho}\right) \sum_{j=0}^{\ell-1} \sum_{k=0}^{j} \frac{(\sigma^2 \rho^{-1} \beta r_0^\alpha)^{j-k}}{k!(j-k)!} \big(\lambda \delta(r_0, \beta)\big)^k \exp\big(-\lambda \delta(r_0, \beta)\big),$$

where $\delta(r_0, \beta) = \frac{2\pi r_0^2 \beta {}_2F_1\left(1, \frac{\alpha-2}{\alpha}; 2 - \frac{2}{\alpha}; -\beta\right)}{\alpha - 2}$. Then, by using the binomial theorem [92], the above expression can be further reconstructed as

$$\mathbb{P}[\gamma \geq \beta | r_0] = \exp\left(-\frac{\rho\lambda\delta(r_0, \beta) + \beta r_0^\alpha \sigma^2}{\rho}\right) \times \sum_{j=0}^{\ell-1} \frac{(\sigma^2 \rho^{-1} \beta r_0^\alpha + \lambda \delta(r_0, \beta))^j}{j!}$$
$$= \frac{\Gamma\left(\ell, \sigma^2 \rho^{-1} \beta r_0^\alpha + \lambda \delta(r_0, \beta)\right)}{\Gamma(\ell)},$$

where the final step is based on the expression in [93, Eq(8.69)]. Finally, by unconditioning with respect to r_0, the result in Theorem 4.1 can be obtained. □

Even though the expression in Theorem 4.1 can be evaluated via numerical tools, this task could be cumbersome due to the complexity of the involved integral. Aiming to further simplify the analysis, we consider special cases with practical interests in the following propositions.

Proposition 4.1. *For the interference-limited scenario, where the noise is negligible in comparison to the multi-user interference, the ID success probability of the typical MU is given by*

$$\Pi^{\mathrm{I}}(\beta) = 1 - \left(\frac{\alpha - 2}{2\beta {}_2F_1\left(1, \frac{\alpha-2}{\alpha}; 2 - \frac{2}{\alpha}; -\beta\right)} + 1\right)^{-\ell}.$$

Proof. Based on the expression obtained in Theorem 4.1, the ID success probability for the interference-limited scenaro, where the additive noise is neglected, can be derived by utilizing the transformation $x \leftarrow \delta(r_0, \beta)$, which yields

$$\Pi^{\mathrm{I}}(\beta) = \int_0^{\infty} \frac{\Gamma(\ell, x)}{\Gamma(\ell)} \exp\left(-\frac{x(\alpha - 2)}{2\beta y}\right) \frac{\alpha - 2}{2\beta y} \mathrm{d}x,$$

where $y = {}_2F_1\left(1, \frac{\alpha-2}{\alpha}; 2 - \frac{2}{\alpha}; -\beta\right)$. Then, by using the resulting expression [91, 6.451], the desired expression can be obtained. □

Yuan Guo

Based on the expression in Proposition 1, we can observe that, for the interference-limited scenario, the density of the BSs, i.e. λ, has no effect on the ID success probability, when a MMSE receiver is employed. This can be indicated by the scale invariance property of the PPP [25]. In addition, the ID success probability only depends on the decoding threshold and the number of antennas that are assigned for ID, i.e. β and ℓ, respectively. For a certain decoding threshold β, as the number of antennas becomes large, i.e. $\ell \to \infty$, the ID success probability approaches one, i.e. $\lim_{\ell\to\infty} \Pi^{\mathrm{I}}(\beta) = 1$.

Proposition 4.2. *For the interference-limited scenario with a propagation exponent $\alpha = 4$, the ID success probability of the typical MU can be further simplified as*

$$\Pi^{\mathrm{I}}(\beta) = 1 - \left(\left(\sqrt{\beta} \tan^{-1}\left(\sqrt{\beta} \right) \right)^{-1} + 1 \right)^{-\ell},$$

where $\tan^{-1}(\cdot)$ *is the inverse tangent function.*

4.3.2 Energy harvesting success probability

We investigate the EH performance of the typical MU in the context of EH success probability, which is defined as the probability that, the harvested energy of the typical MU is higher than the EH threshold ϵ, i.e. $\mathbb{P}[\psi \geq \epsilon]$. The following theorem provides a closed-form expression for the EH success probability achieved by the typical MU.

Theorem 4.2. *The EH success probability of the typical MU is given by*

$$\Pi^{\mathrm{E}}(\epsilon) = 1 - \exp\left(\zeta + 2\pi\lambda \frac{\Gamma\left(-\frac{2}{\alpha}\right) s^{2/\alpha} \Gamma\left(L - \ell + \frac{2}{\alpha}\right)}{\alpha \Gamma(L-\ell)} \right), \tag{4.5}$$

where $s = \frac{\rho\nu\eta\zeta}{\epsilon}$.

Proof. The EH success probability can be re-written as

$$\mathbb{P}[\psi \geq \epsilon] = \mathbb{P}\left[F \leq \frac{\nu\eta\rho}{\epsilon} \sum\nolimits_{x_i \in \Phi} \sum\nolimits_{j=\ell+1}^{L} |h_{j,i}|^2 r_i^{-\alpha} - 1 \right].$$

Since F is an exponential random variable with mean ζ, the above equation can be expressed as

$$\mathbb{P}[\psi \geq \epsilon] = 1 - \mathbb{E}\left[\prod\nolimits_{x_i \in \Phi} \exp\left(-\frac{\rho\nu\eta\zeta c_i}{\epsilon r_i^{\alpha}} \right) \right] \exp(\zeta), \tag{4.6}$$

where $c_i = \sum_{j=\ell+1}^{L} |h_{j,i}|^2$. Since for the Rayleigh fading, the channel power gain is an exponential random variable, i.e. $|h_{j,i}|^2 \sim \exp(1)$, c_i is a Gamma distributed random variable with shape parameter $L-\ell$ and unit scale, i.e. $c_i \sim \mathcal{G}(L-\ell, 1)$ [68]. Therefore, the above expectations can be evaluated as following

$$\begin{aligned}
&\mathbb{E}\left[\prod\nolimits_{x_i\in\Phi}\int_0^{\infty}\exp\left(-\frac{\rho\nu\eta\zeta c}{\epsilon r_i^{\alpha}}\right)\frac{\exp(-c)c^{L-\ell-1}}{\Gamma(L-\ell)}\mathrm{d}c\right]\\
\overset{(a)}{=}&\mathbb{E}\left[\prod\nolimits_{x_i\in\Phi}\left(\frac{\epsilon r_i^{\alpha}}{\rho\nu\eta\zeta+\epsilon r_i^{\alpha}}\right)^{L-\ell}\right]\\
\overset{(b)}{=}&\exp\left(-2\pi\lambda\int_0^{\infty}\left(1-\left(\frac{\epsilon r^{\alpha}}{\rho\nu\eta\zeta+\epsilon r^{\alpha}}\right)^{L-\ell}\right)r\mathrm{d}r\right),
\end{aligned} \tag{4.7}$$

where (a) is derived based on the resulting expression [91, 3.351] and (b) follows from the probability generating functional of a PPP [25]. Finally, by evaluating the above integral and by substituting (4.7) into (4.6), the final result in Theorem 4.2 is derived. □

From the expression in Theorem 4.2, we can observe that, if the number of antennas used for EH purpose becomes large (i.e., $L-\ell \to \infty$), the EH success probability approaches one, i.e. $\lim_{L-\ell\to\infty}\Pi^{\mathrm{E}}(\epsilon) = 1$. Furthermore, a denser deployment of the BSs can improve EH performance. Specifically, in the ultra-dense networks with infinite BSs' density, the EH success probability is equal to one, i.e. $\lim_{\lambda\to\infty}\Pi^{\mathrm{E}}(\epsilon) = 1$.

Proposition 4.3. *For the special case with $\alpha = 4$, the EH success probability of the typical MU can be further simplified as*

$$\Pi^{\mathrm{E}}(\epsilon) = 1 - \exp\left(\zeta - \frac{\pi^2\lambda\sqrt{s}\big(2(L-\ell)\big)!}{4^{L-\ell}(L-\ell-1)!(L-\ell)!}\right).$$

Proof. Based on the expression given in Theorem 4.2 and the resulting expression $\Gamma\left(\frac{1}{2}+n\right) = \frac{(2n)!}{4^n n!}\sqrt{\pi}$, the simplified expression for the EH success probability can be obtained. □

4.4 Successive interference cancellation

In this section, a SIC technique is investigated to improve the ID performance of MUs, via mitigating the strongest interfering signals. The achieved additional gains of the ID performance, release the number of antennas required for ID purpose, which can be used to further enhance the EH performance. In particular, we assume

that each MU has the ability to implement an ideal SIC in accordance to [94]. More specifically, the SIC is utilized when the MU fails to decode the intended signal, and tries to decode and subtract the strongest interfering signal from the received signals. If it is successfully decoded, the received signals are re-combined by the MMSE receiver and the MU re-attempts to decode the intended signal. If it still fails to decode the intended signal, it proceeds to decode and subtract the next strongest interfering signal. We consider that the above procedure repeats up to N times, during which the MU will either successfully decode the intended signal or will be in outage. In addition, the order statistics of the received signal power are assumed to be determined by the distance. In what follows, the observed interference terms from different BSs are assumed to be mutually independent [94].

We start by calculating the probability of the typical MU to successfully decode and subtract the i-th strongest interfering signal, conditioned that the $i-1$ strongest interfering signal has been perfectly subtracted [94].

Lemma 4.1. *By using a MMSE receiver, the probability of the typical MU to successfully decode and subtract the i-th strongest interfering signal is given by*

$$\Pi^{\mathrm{D}}(\beta, i) = \int_0^{\infty} \frac{\Gamma\left(\ell, \sigma^2 \rho^{-1} \beta r_i^{\alpha} + \lambda \delta(r_i, \beta)\right)}{\Gamma\left(\ell\right)} f(r_i) \mathrm{d}r_i,$$

where $\delta(r_i, \beta) = \frac{2\pi r_i^2 \beta {}_2F_1\left(1, \frac{\alpha-2}{\alpha}; 2-\frac{2}{\alpha}; -\beta\right)}{\alpha-2}$ *and* $f(r_i)$ *is the pdf of the distance between the typical MU and the i-th closest interfering BS, which is given by* (3.23).

Proof. Since the $i-1$ interfering signals are assumed to be already subtracted, the remaining interferers set is $\widehat{\Phi} = \{x_{i+1}, x_{i+2}, \cdots\}$ and the i-th interfering signal is now treated as the intended signal to be decoded. Hence, the output SINR of the MMSE receiver is given by

$$\gamma_{\mathrm{i}} = \rho r_i^{-\alpha} \widehat{\mathbf{h}}_i^H \mathbf{R}^{-1} \widehat{\mathbf{h}}_i,$$

where $\mathbf{R} = \sum_{x_j \in \widehat{\Phi}} \rho r_i^{\alpha} \widehat{\mathbf{h}}_j \widehat{\mathbf{h}}_j^H + \sigma^2 \mathrm{I}_{\ell}$ denotes the covariance matrix of the interference plus noise. First conditioning on r_i and replacing the integral limits r_0 with r_i, then evaluating the expectation over r_i. □

Given that i strongest interfering signals have been successfully decoded and subtracted, the ID success probability of the typical MU is characterized in the following Lemma.

Lemma 4.2. *By using the MMSE receiver, the ID success probability of the typical MU, which has successfully subtracted i interfering signals is given by*

$$\Pi^{\mathrm{C}}(\beta,i)=\int_0^{\infty}\int_{r_0}^{\infty}\frac{\Gamma\left(\ell,\sigma^2\rho^{-1}\beta r_0^{\alpha}+\lambda\delta(r_i,\beta)\right)}{\Gamma(\ell)g^{-1}(r_0,r_i)}\mathrm{d}r_i\mathrm{d}r_0,$$

where $g(r_0,r_i)$ is the joint pdf of the distance from the typical MU to its serving BS and the i-th closest interfering BS, which is given by [95]

$$g\left(r_0,r_i\right)=\frac{4(\pi\lambda)^{i+1}r_0r_i\left(r_i^2-r_0^2\right)^{i-1}}{\exp\left(\pi\lambda r_i^2\right)(i-1)!}. \tag{4.8}$$

Proof. Since i strongest interfering signals have been subtracted, the remaining input of the MMSE receiver includes the intended received signal from serving BS at x_0 and other interfering signals. Then by conditioning on the distance from the typical MU to its serving BS and i-th interfering BS, i.e. r_0 and r_i, respectively, the conditional ID success probability can be obtained by using the similar steps in Lemma 4.1. Finally, by evaluating the expectation over r_0 and r_i, where the joint distribution is given by (4.8), the final result in Lemma 4.2 is derived. □

We now present the main theorem for the ID success probability of the typical MU, by taking into account both the MMSE receiver and the SIC technique.

Theorem 4.3. *By using a MMSE receiver, the ID success probability of the typical MU which attempts to cancel up to N interfering signals is given by*

$$\Pi^{\mathrm{SIC}}(\beta,N)=\Pi^{\mathrm{I}}(\beta)+\sum_{j=1}^{N}\left(\prod_{i=0}^{j-1}1-\Pi^{\mathrm{C}}(\beta,i)\right)\left(\prod_{i=1}^{j}\Pi^{\mathrm{D}}(\beta,i)\right)\Pi^{\mathrm{C}}(\beta,i). \tag{4.9}$$

Proof. For the sake of the analytical tractability, we assume that the interfering signals are independent. Therefore, the proof is directly given from the SIC procedure. □

4.5 Numerical results

In this section, we provide both simulation and theoretical results to validate the accuracy of our model, and to illustrate the performance and potential benefits of the considered system model. Unless otherwise stated, in our results we use the following parameters: $\lambda = 1/3600$, $\alpha = 4$, $L = 8$, $\zeta = 0.01$, $\eta = 0.7$, $N = 1$, $\beta = 10$ dB, $\epsilon = -30$ dBm and $\sigma^2 = -60$ dB.

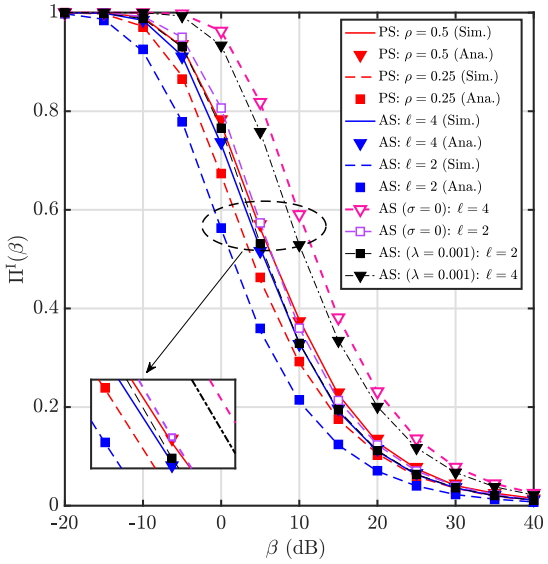

Figure 4.1: ID success probability versus the ID threshold (β), for the considered PS and AS schemes, where $\rho \in \{0.5, 0.25\}$ and $\ell \in \{4, 2\}$.

Fig. 4.1 illustrates the effect of the AS and the PS schemes on the ID performance of the typical MU with a MMSE receiver. In particular, Fig. 4.1 plots the ID success probability (given in Theorem 4.1) with respect to the decoding threshold for different AS and PS partitioning parameters, i.e. $\ell \in \{2, 4\}$ and $\rho \in \{0.25, 0.5\}$, respectively. Initially, the agreement between the theoretical results (markers) and the simulation results (solid and dash curves) validates our mathematical analysis. Firstly, it can be observed that a larger number of antennas or a larger power splitting ratio achieve a higher ID success probability. This was expected since, for the AS scheme, by allocating more antennas for ID purpose, a greater output SINR is achieved of the MMSE receiver. In addition, for the PS scheme, by allocating more signal power for ID purpose, noise effects are suppressed accordingly, thereby improving the ID performance of MUs. Another interesting observation is that, based on either the AS or the PS scheme, by allocating half number of the total antennas ($\ell = 4$) or half total received signal power ($\rho = 0.5$) for ID purpose, the PS scheme outperforms the AS scheme in terms of ID success probability. This observation is justified from the fact that the AS scheme randomly selects part of antennas for ID, which may have a poor signal quality (i.e. low SINR); while PS scheme utilizes all receiving antennas, which enables the best diversity branches to be combined, thus resulting in a better ID performance. Finally, we can observe that, with denser network deployments ($\lambda = 0.001$), the interference limited scenario (given in Propo-

Yuan Guo

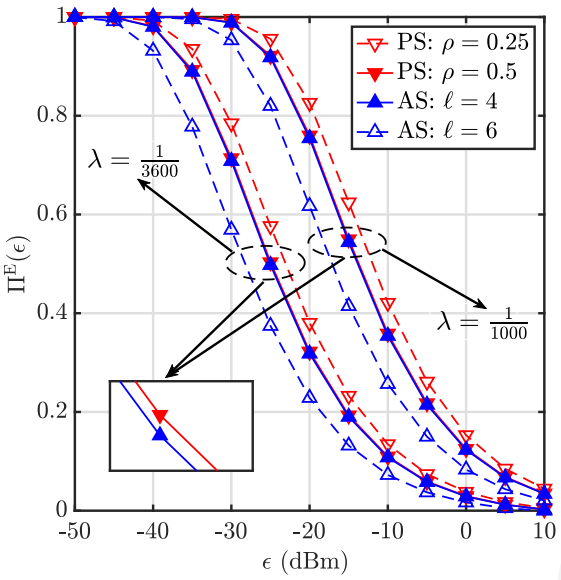

Figure 4.2: EH success probability versus the EH threshold for the considered PS and AS schemes, where $\rho \in \{0.5, 0.25\}$ and $\ell \in \{4, 6\}$.

sition 4.1 & 4.2) provides a tight approximation with the exact ID success probability.

Fig. 4.2 depicts the impact of the AS and the PS schemes on the EH success probability (given in Theorem 4.2 and Proposition 3) for different densities of the BSs, i.e. $\lambda \in \{1/3600, 1/1000\}$. Firstly, it can be observed that, a denser deployment of BSs achieves a higher EH success probability. This was expected since, a denser network provides more multi-user interference, which can be used for harvesting energy by the MUs. We can also observe that, by allocating more antennas or more signal power for EH purpose, the EH performance is improved. Finally, it is indicated that, for the case where the half received power or half number of antennas are allocated for EH based on the PS and AS scheme, respectively, the PS scheme achieves a slightly higher EH success probability than the AS scheme.

Fig. 4.3 shows the achieved ID and EH success probability regions, with different number of receiving antennas $L \in \{4, 8, 16\}$ and with different techniques, i.e. MRC receiver, MMSE receiver, and MMSE receiver with the SIC technique (denoted as MMSE-SIC), where the AS scheme is employed and the noise power is ignored. Firstly, a clear trade-off between the ID and the EH performance can be observed for any number of receiving antennas. This was expected since, by allocating more number of antennas for ID (or EH) purpose, the corresponding performance is improved, while on the other hand, the EH (or ID) success probability is decreased since less resources are allocated. Similarly, by increasing the total number of an-

Yuan Guo

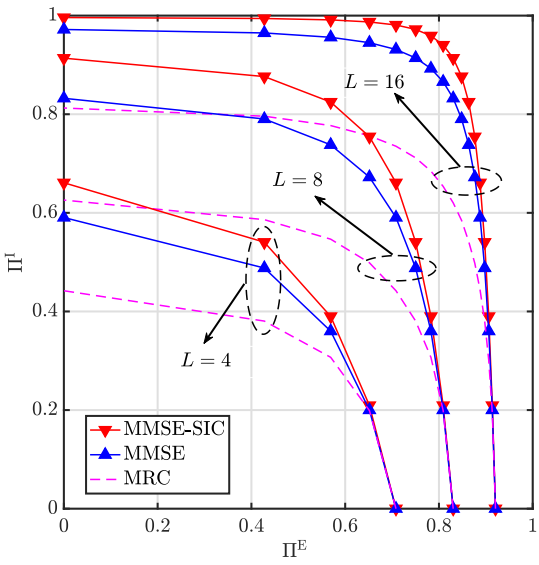

Figure 4.3: ID and EH success probability regions for the considered MMSE, MRC, and MMSE-SIC techniques, where $\beta = 10$ dB and $\epsilon = -30$ dBm.

tennas, both the ID and the EH performance is improved. Moreover, Fig. 4.3 plots the performance achieved by the MRC technique for comparison purpose [68]. We can observe that, the MMSE outperforms the MRC for any number of antennas. This is based on the fact that the MMSE receiver is an optimal combining approach, which yields a maximum output SINR, while the MRC receiver is a low-complexity approach and achieves a worse performance when the interference signals are correlated. Finally, an addition gain can be observed with the employment of the MMSE-SIC technique. In this case, the strongest interfering signals are decoded and subtracted, resulting in a higher SINR, thereby the ID success probability is increased.

4.6 Summary

In this chapter, we studied the SWIPT technology in the context of a linear MMSE receiver. By leveraging tools from stochastic geometry, we established a tractable mathematical framework to evaluate the SWIPT performance for multiple antennas MUs. Based on PS or AS schemes, exact analytical expressions for both the ID and the EH success probabilities were derived, while simple closed-form expressions were obtained for the interference-limited case. Moreover, a SIC technique was investigated to further improve the SWIPT performance, via mitigating the strongest interfering signals. Our results have shown that, the MMSE receiver outperforms

Yuan Guo

the conventional MRC in terms of SWIPT performance. By using a MMSE receiver and by allocating an equal fraction of resources for ID and EH, the PS scheme outperforms the AS in the context of both the ID and the EH performance. Finally, by employing the SIC technique, an additional gain on SWIPT performance was demonstrated in terms of both the ID and the EH success probabilities performance.

Yuan Guo

Chapter 5

SWIPT-enabled mobile networks with a coverage area-based CoMP technique

In this chapter, we propose a novel coverage area-based CoMP (CA-CoMP) scheme for SWIPT-enabled mobile networks, aiming at reducing the handover rate and enhancing the SWIPT performance. In particular, by taking into consideration the heterogeneity of BSs' footprints, the CA-CoMP scheme enables a MU to select and communicate with multiple BSs, whose coverage areas are greater than a pre-defined threshold. By leveraging stochastic geometry tools, we study the CA-CoMP scheme in terms of several key performance metrics, i.e. inter- and intra-cell handover rate, success probabilities, average spectral efficiency, average harvested energy as well as energy efficiency, of which the analytical expressions are derived.

5.1 Motivation and contributions

Although several CoMP techniques are developed for the mobile networks, which induce a higher network management complexity due to the multi-tier network topologies, low-complexity mobility management and energy-efficient CoMP techniques are missing from the literature. Moreover, the intra-cell handover analysis under a CoMP transmission scenario is overlooked from the current studies. Hence, the aim of this work is to fill these gaps by providing a novel CoMP scheme for SWIPT-enabled single-tier mobile networks, aiming at reducing the inter- and intra-

Yuan Guo

cell handover rate and enhancing the SWIPT performance. Specifically, the main contributions of this work are summarized as follows:

- We develop an analytical framework based on stochastic geometry, which comprises the co-design of SWIPT and CoMP techniques, shedding light on the analysis of SWIPT-enabled large-scale mobile networks. In particular, the developed framework takes into account the ability of MUs to jointly communicate with multiple BSs in a non-coherent manner and perform non-linear EH, where all MUs have arbitrary velocity and trajectory within the considered network area.

- We propose a novel low-complexity CoMP scheme, aiming to reduce the handover rate of the high mobility MUs and to enhance their SWIPT performance. More specifically, the CA-CoMP scheme enables the high mobility MUs to jointly communicate with multiple serving BSs, whose coverage areas are greater than a pre-defined threshold; thus frequent handovers associated with small-coverage area BSs are avoided.

- By leveraging tools from stochastic geometry, we derive closed-form expressions for both the inter- and intra-cell handover rate for the proposed CA-CoMP scheme. Analytical expressions for the ID and EH success probabilities, the average spectral efficiency, the harvested energy, as well as the energy efficiency are derived. Furthermore, under specific practical scenarios, closed-form expressions for the aforementioned metrics are derived. These closed-form expressions provide a quick and convenient method to evaluate the network performance and obtain insights into how key parameters affect the network.

- Our results reveal that with the employment of the proposed CA-CoMP scheme, MUs experience significantly fewer inter- and intra-cell handover processes compared to that observed with the employment of conventional CoMP schemes. In addition, by properly selecting the area threshold parameter, the numerical results exhibit considerable spectral efficiency increase by 41% compared to that achieved with the conventional schemes; the optimal area threshold that offers the highest SWIPT performance is also illustrated. Finally, we demonstrate that a higher average harvested energy and energy efficiency can be

Yuan Guo

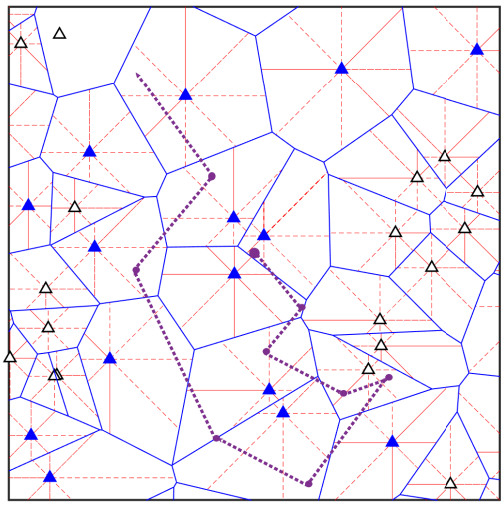

Figure 5.1: The Voronoi tessellation of a single-tier cellular network, where the BSs and the waypoints of a MU are represented by triangles and points, respectively. The candidate BSs are represented by solid triangles. The solid and dash lines represent the cell and beam boundaries, respectively, while the trajectory of the typical MU is illustrated by the dotted line.

achieved by the proposed CA-CoMP compared to conventional CoMP.

5.2 System model

We consider a single tier cellular network as illustrated in Fig. 5.1, and the spatial distribution is introduced in Section 2.2.2, while MUs are randomly moving within the network based on a RWP model. We assume that all BSs transmit signals with power P_t (dBm) and each BS serves only one MU at a time per resource block [25,38]. In the context of the proposed CA-CoMP scheme (detailed description in Section 5.3.1), each MU jointly communicates with N cooperating BSs in order to enhance the received signal power and mitigate the inter-cell interference.Based on the Slivnyak's theorem and without loss of generality, we perform our analysis for the typical MU, which is initially located at the origin, and our results are applicable to all MUs within the network area [19, 25, 96]. Moreover, we assume that all BSs are equipped with multiple antennas to generate directionality towards to the MUs, while all MUs are equipped with a single omnidirectional antenna. We consider that each BS has a codebook of $\mathcal{M}$ beamforming vectors with $\mathcal{M} = 2^m$ for $m \in \mathbb{N}$,

Yuan Guo

where the patterns of these beamforming vectors have non-overlapping main lobes and cover the full angular range, i.e. $[0, 2\pi)$ [38]. For simplicity, the beamwidth is considered as the central angle of a sector, i.e. $\theta = \frac{2\pi}{M}$ [19, 38]. Moreover, the main lobe is assumed to be restricted to the beamwidth and thus, the main lobe and the side lobe antenna gain are given by $G_m = \frac{2}{\left(1-\cos\left(\frac{\Theta}{2}\right)\right)+\xi\left(1+\cos\left(\frac{\Theta}{2}\right)\right)}$ and $G_s = \xi G_m$, respectively, where $\xi \in (0, 1)$ is the loss coefficient of the antenna directivity [97]. This antenna model approximates the actual beam pattern with sufficient accuracy and captures the directivity loss effect, while also providing tractability for the analytical process. Therefore, the antenna gain of the link between the typical MU and the i-th closest interfering BS, denoted as $G_{\mathcal{I},i}$, is given by $G_{\mathcal{I},i} = \{G_m, G_s\}$, with the corresponding probabilities $p_G = \{\frac{\theta}{2\pi}, \frac{2\pi-\theta}{2\pi}\}$; while the antenna gain of the link between the typical MU and its i-th closest serving BS, denoted as $G_{\mathcal{S},i}$, is evaluated in Section 5.3.1.

Regarding the downlink data transmission, we adopt a non-coherent joint transmission policy. Specifically, the non-coherent joint transmission allows multiple cooperative serving BSs transmit the same signal to their associated MU without prior phase-alignment and tight synchronization to that MU, which is thus suitable for the scenario where MUs exhibit high mobility [26, 28]. Then the MU combines the signals from multiple BSs using non-coherent combining techniques. In addition, a scheduling mechanism is employed in which each MU is scheduled for communicating with its serving BSs at different time-frequency resources. Therefore, no intra-cell interference exists since intra-cell users are served within orthogonal time-frequency resources, while only inter-cell interference is taken into consideration. Hence, the SINR observed at the typical MU can be formulated as

$$\text{SINR} = \frac{\left|\sum_{x_i \in \mathcal{S}} P_t^{1/2} G_{\mathcal{S},i}^{1/2} h_i^{1/2} \ell^{1/2}(r_i)\right|^2}{\sum_{x_i \in \Phi_b \setminus \mathcal{S}} P_t G_{\mathcal{I},i} h_i \ell(r_i) + \sigma_c^2 + \sigma_n^2}, \tag{5.1}$$

where $\mathcal{S}$ represent the set of serving BSs (Detailed in Section 5.3.1), σ_n^2 is the thermal noise, $\sigma_c^2 = \sigma_{cov}^2$ and $\sigma_c^2 = \sigma_{cov}^2/\rho$ for the TS and the PS scheme, respectively, σ_{cov}^2 is a constant that accounts for the noise induced by the signal conversion from RF to baseband [19].

Each MU is equipped with a rectifier circuit that is capable of converting a portion of the received RF signals into DC power to either charge its battery or power its circuits, while the RF signals may include the intended signal from the coordinated

Yuan Guo

serving BSs, as well as interfering signals from other BSs. We adopt a non-linear EH model, the amount of the instantaneous harvested energy of a MU is quantified as

$$\mathcal{Q} = \frac{\nu(1-\rho)\eta P_t}{1+F}\left(\sum_{x_i\in\mathcal{S}} G_{\mathcal{S},i}h_i\ell(r_i) + \sum_{x_i\in\Phi_b^{\setminus\mathcal{S}}} G_{\mathcal{I},i}h_i\ell(r_i)\right). \tag{5.2}$$

Note that (5.1) and (5.2) hold for both the TS and the PS scheme, i.e. $\rho = 1$ and $0 \leq \tau \leq 1$ are adopted for the TS scheme, while $\tau = 1$ and $0 \leq \rho \leq 1$ are adopted for the PS scheme.

5.3 Coverage area-based CoMP scheme and handover analysis

In this section, we introduce the proposed CA-CoMP technique in the context of SWIPT-enabled cooperative cellular networks. Our technique exploits the cooperation among randomly located BSs, that are selected according to their coverage areas, aiming at both enhancing the network performance and reducing the handover rate. In addition, we develop a tractable analytical framework to compute the handover rate associated with the CA-CoMP scheme, while closed-form expressions for the inter- and intra-cell handover rates and the misalignment probability are derived, which will be useful for evaluating the achieved ID and EH performance.

5.3.1 Coverage area-based CoMP scheme

The proposed CA-CoMP scheme is based on a two-stage procedure. In the first stage, a set of candidate BSs is selected based on their coverage areas. More specifically, due to the irregular shape of the cells, different BSs generally have various coverage areas, while the MUs only communicate with the BSs that have relative large coverage areas, named as candidate BSs. Hence, at the first stage the candidate BSs are determined, which consists of the BSs that their coverage areas are greater than a pre-defined area threshold $\mathcal{A}$ (m^2), i.e. $\tilde{\Phi}_b = \{x_i | \forall x_i \in \Phi_b, \mathcal{A}_i > \mathcal{A}\}$, where $\mathcal{A}_i$ is the coverage area of the i-th BS located at x_i. In the second stage, the set of serving BSs with which the MUs communicates, i.e. $\mathcal{S}$, is selected among the set of candidate BSs. In particular, in order to ensure high intended signal power, each

Yuan Guo

MU communicates with its N closest BSs among the set of candidate BSs. Hence, the final set of the serving BSs is formulated as, $\mathcal{S} = \{x_1, \cdots, x_N | r_i \leq r_{i+1}, \forall x_i \in \tilde{\Phi}_b\}$.

It is worth mentioning that, the proposed CA-CoMP scheme provides flexibility for the design of large-scale SWIPT-enabled communication networks, since according to the MUs' mobility within the network, the area threshold can be appropriately adjusted. Particularly, for high-velocity MUs, i.e. $v \to \infty$, the handover overhead is the dominant factor that jeopardizes the network performance. Therefore, a large area threshold is beneficial to be adopted in order to reduce the MUs' handover rate. On the other hand, for MUs with low velocity or static, i.e. $v \to 0$, the handover overhead is negligible, and hence, a small area threshold ensures that the MUs are associated with the N closest BSs in order to achieve the highest received signal strength. Moreover, it is worth emphasising that, the proposed CA-CoMP has low-complexity; more specifically, it only requires information about the coverage area of each BS, which is initially deterministic for a given network deployment and could be easily disseminated to MUs via the central network. In addition, compared to some other techniques, e.g. heterogeneous networks-based CoMP schemes [28, 29], that assign MUs with different network tiers based on their velocity for combating high handover rates, the proposed CA-CoMP is operated on a single-tier network topology with much lower complexity of the network structure and management.

5.3.2 Inter-cell handover analysis

We explore the inter-cell handover process of the typical MU, by considering that the typical MU is moving with an arbitrary trajectory. Along this trajectory, connections between the typical MU and its serving BSs change according to its location, such that the typical MU maintains the connectivity with the network. In addition, since each MU jointly communicates with N serving BSs according to the CA-CoMP scheme, the average inter-cell handover rate is defined as the total number of the triggered handovers with respect to the N serving BSs per unit time. More specifically, since the serving BSs of the typical MU are the N closest BSs among the set of candidate BSs, the inter-cell handover is triggered when the typical MU crosses the boundaries of an N-th order Voronoi cell [26, 28]. The inter-cell handover rate experienced by a MU in the considered network topology is evaluated in the following proposition.

Yuan Guo

Proposition 5.1. *Based on the CA-CoMP scheme, the inter-cell handover rate of the typical MU moving with velocity v, is given by*

$$\mu_c = \frac{8v\tilde{\lambda}_b^{\frac{1}{2}}\Gamma(\frac{1}{2}+N)}{\pi^{\frac{3}{2}}\Gamma(N)}, \tag{5.3}$$

where $\tilde{\lambda}_b = \frac{\Gamma(K,\mathcal{A}K\lambda_b)\lambda_b}{\Gamma(K)}$ *and* $K = 3.5$.

Proof. Since each MU only communicates and handovers with the BSs from the candidate BSs set, i.e. $\tilde{\Phi}_b$, we characterize the spatial distribution of $\tilde{\Phi}_b$. According to [89, 98], the area of an arbitrary Voronoi cell created by a homogeneous PPP is a random variable, of which the distribution could be accurately approximated by the Gamma distribution with a shape and a scale parameter K and $K\lambda_b$, respectively, i.e. $\mathcal{A}_i \sim \mathcal{G}[K, K\lambda_b]$ with $K = 3.5$. Let $\mathcal{P}_A$ denote the probability that the coverage area of a BS (i.e., $\mathcal{A}_i$) is larger than the pre-defined threshold $\mathcal{A}$. Hence, $\mathcal{P}_A$ can be derived as follows

$$\mathcal{P}_A = \mathbb{P}[\mathcal{A}_i \geq \mathcal{A}] = \int_{\mathcal{A}}^{\infty} \frac{(K\lambda_b)^K}{\Gamma(K)} \mathcal{A}_i^{K-1} \exp(-K\lambda_b\mathcal{A}_i) \mathrm{d}\mathcal{A}_i = \frac{\Gamma(K, \mathcal{A}K\lambda_b)}{\Gamma(K)}. \tag{5.4}$$

Moreover, since the original spatial distribution of the BSs follows a homogeneous PPP, and based on the thinning property, the distribution of the candidate BSs is still uniform, with a density $\tilde{\lambda}_b = \lambda_b\mathcal{P}_A$ [25]. Therefore, by associating a MU with its N closest BSs from the set of the candidate BSs $\tilde{\Phi}_b$, the Euclidean plane $\mathbb{R}^2$ is separated into regions, forming an N-th order Voronoi tessellation with PPP $\tilde{\Phi}_b$ and density $\tilde{\lambda}_b$ [28]. Then, by using the results in [28, Theorem 3], the inter-cell handover rate under the proposed CA-CoMP scheme can be derived. □

Although (5.3) can be easily evaluated by using numerical tools, intuitions on how key system parameters affect the inter-cell handover rate are difficult to derive. In the following corollary, we simplify the analysis by considering an extreme scenario, where the MUs are able to jointly communicate with a large number of serving BSs, i.e. $N \gg 0$.

Corollary 5.1. *For the special case with $N \gg 0$, the inter-cell handover rate, μ_c, is given by*

$$\mu_c \sim \frac{8v(\tilde{\lambda}_b N)^{\frac{1}{2}}}{\pi^{\frac{3}{2}}}. \tag{5.5}$$

Proof. According to [99], for $x \gg 0$, we have $\frac{\Gamma(x+a)}{\Gamma(x+b)} \sim x^{a-b}$. By associating $a = \frac{1}{2}$, $b = 0$ and $x = N$, the above expression is derived. □

From (5.5) we can easily observe that, for a certain density of candidate BSs, i.e. $\tilde{\lambda}_b$, when the number of cooperative serving BSs becomes large, i.e. $N \gg 0$, the inter-cell handover rate significantly increases. This is expected since, MUs experience more frequent handovers with multiple serving BSs than the scenario with a single serving BS. Moreover, we can observe that the inter-cell handover rate of the MUs increases with their velocity. This is based on the fact that a MU with higher velocity travels a longer distance along its trajectory, compared to a lower-velocity MU, resulting in a higher probability of crossing a cell boundary. We can also observe that the CA-CoMP scheme with $\tilde{\lambda}_b \leq \lambda_b$, achieves a lower inter-cell handover rate than the conventional CoMP scheme, corresponding to the special case of our proposed CA-CoMP scheme with $\mathcal{A} = 0$ [28]. The impact of the pre-defined area threshold, i.e. $\mathcal{A}$, on the inter-cell handover rate is evaluated in the following corollary.

Corollary 5.2. *By increasing the coverage area threshold of the CA-CoMP scheme, i.e. $\mathcal{A} \to \infty$, the inter-cell handover rate of the MUs reduces, i.e. $\mu_c \to 0$.*

Proof. By using the expression in [91, 8.356.4], the first order derivative of μ_c with respect to $\mathcal{A}$ can be derived, i.e.

$$\frac{\mathrm{d}\mu_c}{\mathrm{d}\mathcal{A}} = -\Omega \mathcal{A}^{K-1} \exp(-\mathcal{A} K \lambda_b), \tag{5.6}$$

where $\Omega = \frac{8v\lambda_b^{K+1} K^K N^{\frac{1}{2}} \Gamma(\frac{1}{2}+N)}{\pi^{\frac{3}{2}} \Gamma(N)\Gamma(K)} > 0$. Then, it is straightforward to conclude that, $\mathrm{d}\mu_c/\mathrm{d}\mathcal{A} < 0$ for any $\mathcal{A} \geq 0$. □

It is worth mentioning that the CA-CoMP enables MUs to ignore some nearby BSs, which have small coverage area, to mitigate the frequent handover; on the other hand, these nearby BSs could provide strong signal due to short propagation distances. Hence, we obtain a trade-off between the handover overhead and the received signal quality; the optimal area threshold for achieving the best network performance is discussed in Section 5.5.

5.3.3 Intra-cell handover analysis

We now focus our attention on the intra-cell handover process, where both geometry- and measurement-based handover procedures are considered. In particular, a geometry based intra-cell handover is triggered when a MU crosses the beam bound-

Yuan Guo

aries of the serving BSs, where a new beam is reselected for the downlink transmission. Nevertheless, there are various types of intra-cell handover in modern wireless communication systems, such as channel handover and sector handover; in our work, we mainly focus on the intra-cell handover caused by the beam alteration. [38]. Similarly to the inter-cell handover scenario, the geometry-based intra-cell handover rate equals to the average number of beam reselections with respect to the sum of N serving BSs per unit time. The following proposition evaluates the geometry-based intra-cell handover rate experienced by the typical MU with respect to its i-th closest serving BS, with $1 \leq i \leq N$.

Proposition 5.2. *Based on the CA-CoMP scheme, the geometry-based intra-cell handover rate of the typical MU with respect to its i-th closest serving BS, i.e. $\mu_{b,i}$, is given by*

$$\mu_{b,i} = \frac{\mathcal{M} v \tilde{\lambda}_b^{\frac{1}{2}} \Gamma(i - 0.5)}{\pi^{\frac{3}{2}} \Gamma(i)}. \tag{5.7}$$

Proof. The proof follows a similar approach as in [38]. Without loss of generality, we consider the movement of a typical MU at the origin, with trajectory from $(0,0)$ to $(1,0)$ along the x-axis. As shown in Fig. 5.2, the triangles denote the location of i-th and $(i-1)$-th closest serving BSs of the typical MU, i.e. BS_i and BS_{i-1}, the red circle ω_i denotes the location where the typical MU conducts the intra-cell handover with respect to BS_i, and θ_i is the angle of a beam boundary of BS_i with respect to the direction of the movement of the typical MU. Let Ψ_i denote the point process of intra-cell handover with BS_i. Hence, the average intra-cell handover rate with respect to BS_i is equivalent to the intensity of Ψ_i.

In order to compute the intensity of Ψ_i, we start considering the case where there is at most one intra-cell handover corresponding to BS_i, i.e. there are two beams of the same size for a BS. Thus, the event of the intra-cell handover corresponding to BS_i occurs when the following two events occur simultaneously, i.e.

1. the point of the intra-cell handover lies in the N-th order Voronoi cell of the N serving BSs, i.e. $\omega_i \in V_{\tilde{\Phi}_b}^{(N)}$, where BS_i is the i-th closest serving BSs of the typical MU.

2. the point of the intra-cell handover lies on the unit line connecting $(0,0)$ and $(1,0)$, i.e. $\omega_i \in [0,1]$.

Firstly, conditioning on θ_i, the location of BS_i should be located on the strip between the two lines passing through the origin and the point $(1,0)$. Moreover, the distance

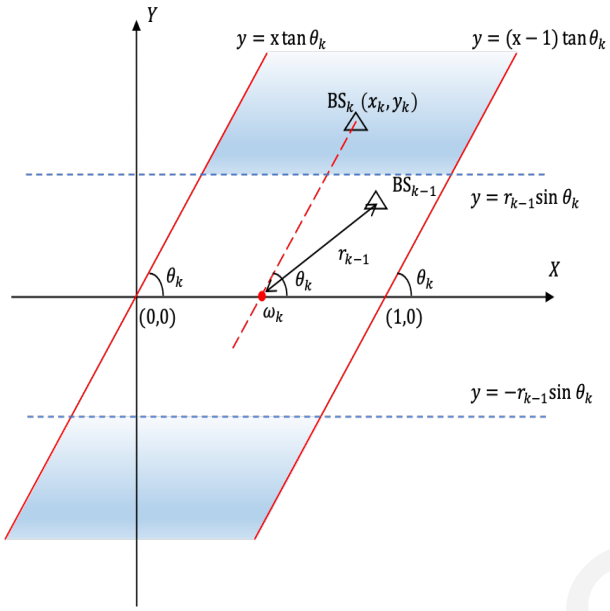

Figure 5.2: Triangles: BSs' location, red circles: intra-cell handover location, dashed lines: beam boundaries, and shaded area: possible locations of BS_k.

from the typical MU to the BS_i should not be less than the distance to BS_{i-1}, i.e. $r_i \geq r_{i-1}$, where $r_i = \frac{|y_i|}{|\sin\theta_i|}$. Hence, by conditioning on both θ_i and r_{i-1}, the possible locations of BS_i are displayed as the shaded area in the Fig. 5.2, and the average number of intra-cell handovers in $[0,1]$ can be formulated as

$$\begin{aligned}\mathbb{E}(\Psi_i[0,1]|\theta_i, r_{i-1}) =& \tilde{\lambda}_b \int_{-\infty}^{-r_{i-1}\sin\theta_i} \mathrm{d}y_i \int_{-\frac{y_i}{\tan\theta_i}}^{1-\frac{y_i}{\tan\theta_i}} \exp\left(-\tilde{\lambda}_b \pi \left(\frac{y_i^2}{\sin^2\theta_i} - r_{i-1}^2\right)\right) \mathrm{d}x_i \\ &+ \tilde{\lambda}_b \int_{r_{i-1}\sin\theta_i}^{\infty} \mathrm{d}y_k \int_{-\frac{y_i}{\tan\theta_i}}^{1-\frac{y_i}{\tan\theta_k}} \exp\left(-\tilde{\lambda}_b \pi \left(\frac{y_i^2}{\sin^2\theta_i} - r_{i-1}^2\right)\right) \mathrm{d}x_i \\ =& \exp\left(\pi\tilde{\lambda}_b r_{i-1}^2\right) \sqrt{\tilde{\lambda}_b} \left(\sqrt{\csc^2\theta_i}\sin^2\theta_i - \mathrm{erf}\left(\sqrt{\pi\tilde{\lambda}_b} r_{i-1}\right)\sin\theta_i\right),\end{aligned}$$

where $\mathrm{erf}(z) = \frac{2}{\pi}\int_0^z e^{-t^2}\mathrm{d}t$ is the Gauss error function. Then, by averaging over θ_i, which is uniformly distributed in $[0,\pi]$, we have

$$\mathbb{E}(\Psi_i[0,1]|r_{i-1}) = \frac{2\exp(-\pi r_{i-1}^2\tilde{\lambda}_b)\sqrt{\tilde{\lambda}_b}\left(1 - \mathrm{erf}(\sqrt{\pi\tilde{\lambda}_b} r_{i-1})\right)}{\pi}. \tag{5.8}$$

Subsequently, by averaging over r_{i-1}, we can derive the linear intensity of Ψ_i for the case of two beams as following

$$\mathbb{E}(\Psi_i[0,1]) = \int_0^{\infty} \mathbb{E}(\Psi_k[0,1]|r_{i-1}) f_{k-1}(r_{i-1}) \mathrm{d}r_{i-1} = \frac{2\sqrt{\tilde{\lambda}_b}\Gamma\left(i - \frac{1}{2}\right)}{\pi^{\frac{3}{2}}\Gamma(i)},$$

where

$$f_i(r_i) = 2(\pi\tilde{\lambda}_b)^i r_i^{2i-1} \frac{\exp(-\pi\tilde{\lambda}_b r_i^2)}{\Gamma(i)}, \tag{5.9}$$

Yuan Guo

is the PDF of distance from the typical MU to the i-th closest BS [89]. It should be noted that the above expressions also holds for the case with $i = 1$, where the proof is same as in [38] and hence is omitted. Then, for the case where each BS has $\mathcal{M}$ beams, there are $\frac{\mathcal{M}}{2}$ lines passing each BS to formate $\mathcal{M}$ beams. The intensity of the intersection points i.e. ω_i, is the summation of the intensity with respect to $\frac{\mathcal{M}}{2}$ lines, i.e. there are $\frac{\mathcal{M}}{2}$ possibilities of intra-cell handovers corresponding to the i-th closest serving BS. Finally, by also multiplying the velocity of the MU, i.e. v, the result in Proposition 5.2 is proven. □

From the expression in (5.7), we can easily observe that the intra-cell handover rate of the typical MU with respect to its i-th closest serving BS, i.e. $\mu_{b,i}$, is directly proportional to the number of beams and the velocity of the typical MU, i.e. $\mathcal{M}$ and v, respectively. Therefore, the downlink performance of high-velocity MUs is diminished by the frequent intra-cell handovers, especially for scenarios where large number of beams are employed at the BSs, e.g. 6G cellular networks. Note that the geometry-based intra-cell handover rate decreases with the increase of the distance from the typical MU to its serving BSs. This result can be theoretically justified by showing the ratio of $\mu_{b,i}$ with $\mu_{b,i+1}$, i.e. $\frac{\mu_{b,i+1}}{\mu_{b,i}} < 1$. In practice, a MU that is moving with a shorter distance to the serving BSs, is also close to the beam boundaries of these BSs, thereby resulting in a higher probability of crossing beam boundaries. Hence, although the closest serving BSs could provide the strongest intended signals due to the shortest propagation distances, the most frequent intra-cell handover occurs with the closest serving BSs, which jeopardizes the SWIPT performance of the MUs.

Note that the beam misalignment of the link between serving BSs and the typical MU may occur by taking into account the measurement-based intra-cell handover. More specifically, according to [38,100], the measurement-based intra-cell handover is operated based on measurements of the synchronization signal block (SSB) burst, which is transmitted periodically with a period T_{SSB} (ms). The beam misalignment occurs when a MU moves inside the side lobe area of the serving BSs before receiving the SSB burst, which results in a weak signal quality at the end-user devices. Hence, in the following proposition, we characterize the misalignment probability, which is useful for evaluating the distribution of the antenna gain and the corresponding ID and EH performance of the MUs.

Yuan Guo

Proposition 5.3. *The misalignment probability of the link between the typical MU and its i-th closest serving BS is given by*

$$\mathcal{P}_{\text{mis}}^{(i)} = 1 - \exp\big(-T_{\text{SSB}}\mu_{b,i}\big). \tag{5.10}$$

Proof. The beam misalignment occurs during the intra-cell handover process. Similar to the Proof of Proposition 5.2, we consider that the MU is moving from the original point (where a SSB burst is just received) to the point $(vT_{\text{SSB}}, 0)$ (where the next SSB burst will be arrived). Although the beam misalignment could be avoided when the intersection between the MUs' trajectory and beam boundary (i.e. ω_i) is coincident with point $(vT_{\text{SSB}}, 0)$, the probability is mathematically equal to zero. Moreover, during one period of SSB burst, the typical MU may cross more than one beam boundaries, e.g. MU moving with high velocity or close to the serving BSs, hence, we derive the probability of a non-misalignment. The linear intensity of the intersections between the typical MU's trajectory and the beam boundary of its i-th closest serving BS is $\mu_{b,i}/v$. By considering the process of intersections as a one-dimensional Poisson point process, the void probability of the intersections, i.e. non-misalignment probability, can be evaluated as [27]

$$\bar{\mathcal{P}}_{\text{ms}}^{(i)} = \mathbb{P}[\text{non-intersections within } (0,0) \text{ to } (v\tau, 0)] = \exp(-T_{\text{SSB}}\mu_{b,i}).$$

Then, the misalignment is derived as $\mathcal{P}_{\text{mis}}^{(i)} = 1 - \bar{\mathcal{P}}_{\text{ms}}^{(i)}$. □

Based on the above proposition, the misalignment probability depends on the MUs' velocity, the intra-cell handover rate as well as the period of the SSB burst, where high velocity of MUs results in a high probability of misalignment. Note that, for scenarios with extremely small or equal to zero period of the SSB burst, i.e. $T_{\text{SSB}} \to 0$, we have $\mathcal{P}_{\text{mis}}^{(i)} \to 0$, which indicates that, the geometry- and measurement-based intra-cell handovers are triggered at exact the same location, i.e. achieving perfect beam alignment [19]. Hence, the antenna gain of the link between the typical MU and its i-th closest serving BS can be modelled as a discrete random variable, i.e.

$$G_{\mathcal{S},i} = \begin{cases} G_m & \text{w.p.} \quad 1 - \mathcal{P}_{\text{mis}}^{(i)}, \\ G_s & \text{w.p.} \quad \mathcal{P}_{\text{mis}}^{(i)}. \end{cases} \tag{5.11}$$

Moreover, the joint probability mass function (PMF) of $G_{\mathcal{S},i}$ is given by

$$\mathcal{G}\left(G_{\mathcal{S},1},,\cdots,G_{\mathcal{S},N}\right) = \mathcal{P}_{\mathcal{S},1}(G_{\mathcal{S},1}) \cdot \cdots \cdot \mathcal{P}_{\mathcal{S},N}(G_{\mathcal{S},N}), \tag{5.12}$$

Yuan Guo

where $\mathcal{P}_{\mathcal{S},i}(G_m) = 1 - \mathcal{P}^{(i)}_{\text{mis}}$ and $\mathcal{P}_{\mathcal{S},i}(G_s) = \mathcal{P}^{(i)}_{\text{mis}}$. Then, based on the above discussion, the total intra-cell handover rate of the typical MU with respect to N serving BSs per unit time is evaluated in the following theorem.

Theorem 5.1. *The total average intra-cell handover rate of the typical MU, for the CA-CoMP scheme is given by*

$$\mu_b = \frac{2\mathcal{M}v\tilde{\lambda}_b^{\frac{1}{2}}\Gamma(\frac{1}{2}+N)}{\pi^{\frac{3}{2}}\Gamma(N)}. \tag{5.13}$$

Proof. Since each MU is jointly served by N serving BSs, where each BS has $\mathcal{M}$ beams, the total average intra-cell handover rate of the typical MU is the summation of the intra-cell handover rate with respect to N serving BSs, i.e.

$$\mu_b = \sum_{i=1}^{N} \mu_{b,i} = \sum_{i=1}^{N} \frac{\mathcal{M}v\sqrt{\tilde{\lambda}_b}\Gamma(i-0.5)}{\pi^{3/2}\Gamma(i)}. \tag{5.14}$$

Let $\mathcal{X} = \frac{\mathcal{M}v\sqrt{\tilde{\lambda}_b}}{\pi^{3/2}}$, we have

$$\begin{aligned}
\mu_b =& \mathcal{X}\sum_{i=1}^{N}\frac{\Gamma(i-\frac{1}{2})}{\Gamma(i)} = \mathcal{X}\sum_{i=0}^{N-1}\frac{\Gamma(i+\frac{1}{2})}{\Gamma(i+1)} \\
\overset{(a)}{=}& \mathcal{X}\sqrt{\pi}\sum_{i=0}^{N-1}\binom{i-\frac{1}{2}}{i} \overset{(b)}{=} \mathcal{X}\sqrt{\pi}\binom{N-\frac{1}{2}}{N-1} \\
\overset{(c)}{=}& 2N\mathcal{X}\sqrt{\pi}\binom{N-\frac{1}{2}}{N} = \mathcal{X}\frac{2}{\Gamma(N)}N!\binom{N-\frac{1}{2}}{N}\sqrt{\pi} = 2\mathcal{X}\frac{\Gamma(N+\frac{1}{2})}{\Gamma(N)},
\end{aligned} \tag{5.15}$$

where (a) is based on the property of Gamma function, i.e.

$$\Gamma\left(\frac{1}{2}+i\right) = \binom{i-\frac{1}{2}}{i} i!\sqrt{\pi},$$

(b) follows the Hockey-stick identity [101]; (c) is based on the identity of the binomial coefficients, and the final step follows the inverse process of step (a). Hence, the final expression for the intra-cell handover rate in Theorem 5.1 is proven. □

From (5.13) we can observe that, as the number of beams increases, i.e. $\mathcal{M} \to \infty$, the intra-cell handover rate increases, i.e. $\mu_b \to \infty$. This is based on the fact that, by increasing the number of beams, the spatial density of the beam boundaries increases, thus resulting in a higher probability of beam boundary crosses by the MUs. Moreover, since the density of the candidate BSs is smaller than the complete BSs set, i.e. $\tilde{\lambda}_b \leq \lambda_b$, the CA-CoMP achieves a lower intra-cell handover rate compared

Yuan Guo

to conventional CoMP schemes. Finally, it is easily to observe that the intra-cell handover rate is generally greater than the inter-cell handover rate, and is directly proportional to the inter-cell handover rate, i.e. $\mu_b = \frac{\mathcal{M}}{4}\mu_c$.

5.4 SWIPT performance with CA-CoMP scheme

In this section, we study the information and energy transfer performance of the SWIPT-enabled mobile cellular networks achieved by the proposed CA-CoMP scheme. We start by evaluating the information transfer performance via computing the ID success probability as well as the average spectral efficiency. Subsequently, we assess the EH ability of the MUs in terms of the EH success probability and the average harvested energy. Finally, the energy efficiency of the SWIPT-enabled MUs is evaluated for the CA-CoMP scheme. The analytical expressions for the aforementioned performance metrics are presented.

5.4.1 Interference characterization

We first characterize the interference observed at the typical MU, by calculating the Laplace transform, i.e. $\mathcal{L}_{\mathbf{I}}(s) = \mathbb{E}\{\exp(-s\mathbf{I})\}$, where a closed-form expression is derived in the following lemma.

Lemma 5.1. *The Laplace transform of the received interference at the typical MU is given by*

$$\mathcal{L}_{\mathbf{I}}(s) = \prod_{G=\{G_m,G_s\}} \exp\left(sGp_G P_t \pi \left(\frac{(\tilde{\lambda}_b - \lambda_b) r_N^2 \, {}_2F_1\left[1, \frac{2}{\alpha}; \frac{\alpha+2}{\alpha}; \frac{-r_N^\alpha}{1+P_tGs}\right]}{1+P_tGs} - \frac{2\lambda_b r_N^{2-\alpha} \, {}_2F_1\left[1, \frac{\alpha-2}{\alpha}; 2-\frac{2}{\alpha}; -\frac{1+P_tGs}{r_N^\alpha}\right]}{\alpha-2}\right)\right). \tag{5.16}$$

Proof. The proof directly follows from the definition of the Laplace transform, i.e.

$$\begin{aligned}
\mathcal{L}_{\mathbf{I}}(s) =& \mathbb{E}\left\{ \exp\left(\sum\nolimits_{x_i \in \Phi_b^{\setminus s}} -sP_tG_{\mathcal{I},i}h_i\ell(r_i)\right)\right\} \\
=& \mathbb{E}\left\{ \prod\nolimits_{x_i \in \Phi_b^{\setminus s}} \mathbb{E}_h\left\{\exp\left(-sP_tG_{\mathcal{I},i}h\ell(r_i)\right)\right\}\right\} \\
=& \mathbb{E}\left\{ \exp\left(2\pi(\lambda_b - \tilde{\lambda}_b)\int_0^{r_N}\left(\frac{1}{1+sP_tG_{\mathcal{I},i}\ell(r)} - 1\right) r\mathrm{d}r \right.\right. \\
& \left.\left. + 2\pi\lambda_b \int_{r_N}^{\infty}\left(\frac{1}{1+sP_tG_{\mathcal{I},i}\ell(r)} - 1\right) r\mathrm{d}r\right)\right\},
\end{aligned} \tag{5.17}$$

where the second step is based on the fact that the channel power gain h_i is an i.i.d. exponential random variable, and the last step follows from the PGFL of the PPP and the moment generating function (MGF) of an exponential random variable. Then by using [91, 3.194.5], the above integrals in could be solved. □

It can be observed from (5.16) that the Laplace transform of the interference consists of two terms inside the exponential function. The first term is related to the interference generated by the nearby interfering BSs, that their distance to the typical MU is less than r_N (i.e. the distance from the N-th serving BS to the typical MU). The second term refers to the interference from other distant interfering BSs. For simplicity and due to the high directionality of the transmitter's antennas, the second term could be neglected [102].

5.4.2 Information transfer analysis

By applying the Laplace transform of the interference, we now evaluate the ID success probability, which is defined as the probability that a MU is able to achieve a certain SINR threshold β (dB), i.e. $\mathcal{P}^{\mathrm{ID}}(\beta) = \mathbb{P}\{\mathrm{SINR} \geq \beta\}$. The analytical expression for the ID success probability is provided in the following theorem.

Theorem 5.2. *The ID success probability of the typical MU for the CA-CoMP scheme, i.e. $\mathcal{P}^{\mathrm{ID}}(\beta)$ is given by*

$$\mathcal{P}^{\mathrm{ID}}(\beta) = \sum_{i=1}^{N} \sum_{G_{\mathcal{S},i}} \mathcal{X}\left(G_{\mathcal{S},1}, \cdots, G_{\mathcal{S},N}\right) \mathcal{G}\left(G_{\mathcal{S},1},, \cdots, G_{\mathcal{S},N}\right), \tag{5.18}$$

where

$$\mathcal{X}\left(G_{\mathcal{S},1}, \cdots, G_{\mathcal{S},N}\right) \triangleq \int\limits_{0 \leq r_1 \leq \cdots \leq r_N \leq \infty} \mathcal{L}_{\mathbf{I}}(s) \exp\left(-(\sigma_c^2 + \sigma_n^2)s\right) f_r(r_1, \cdots, r_N) \mathrm{d}r_1 \cdots \mathrm{d}r_N, \tag{5.19}$$

$s = \frac{\beta}{P_t(G_{\mathcal{S},1}\ell(r_1) + \cdots + G_{\mathcal{S},N}\ell(r_N))}$, *and $f_r(r_1, \cdots, r_N)$ is the joint probability density function (PDF) of the distance from the typical MU to the serving BSs, which is given by* [89]

$$f_r(r_1, \cdots, r_N) = (2\tilde{\lambda}_b \pi)^N \exp(-\tilde{\lambda}_b \pi r_N^2) \prod_{i=1}^{N} r_i. \tag{5.20}$$

Yuan Guo

Proof. The ID success probability can be re-written as

$$\begin{aligned}\mathcal{P}^{\mathrm{ID}}(\beta) =& \mathbb{P}\left\{\left|\sum_{x_i\in\mathcal{S}} P_t^{\frac{1}{2}} G_{\mathcal{S},i}^{\frac{1}{2}} h_i^{\frac{1}{2}} \ell^{\frac{1}{2}}(r_i)\right|^2 \geq \beta\left(\sum_{x_i\in\Phi_b^{\setminus\mathcal{S}}} P_t G_{\mathcal{I},i} h_i \ell(r_i) + \sigma_c^2 + \sigma_n^2\right)\right\} \\ \overset{(a)}{=}& \mathbb{E}\left\{\exp\left(-(\mathbf{I}+\sigma_c^2+\sigma_n^2)\frac{\beta}{P_t(G_{\mathcal{S},1}\ell(r_1)+\cdots+G_{\mathcal{S},N}\ell(r_N))}\right)\right\} \\ =& \mathbb{E}\left\{\mathcal{L}_{\mathbf{I}}(s)\exp\left(-(\sigma_c^2+\sigma_n^2)s\right)\right\}, \end{aligned} \tag{5.21}$$

where $\mathcal{L}_{\mathbf{I}}(s)$ is the Laplace transform given in Lemma 5.1, $s = \frac{\beta}{P_t(G_{\mathcal{S},1}\ell(r_1)+\cdots+G_{\mathcal{S},N}\ell(r_N))}$, and (a) is based on the fact that for the Rayleigh fading, $h_i^{\frac{1}{2}} \sim \mathcal{CN}(0,1)$, thus $\left|\sum_{x_i\in\mathcal{S}} P_t^{\frac{1}{2}} G_{\mathcal{S},i}^{\frac{1}{2}} h_i^{\frac{1}{2}} \ell^{\frac{1}{2}}(r_i)\right|^2$ is an exponential random variable with mean $\sum_{x_i\in\mathcal{S}} P_t G_{\mathcal{S},i}\ell(r_i)$. Then, by evaluating the expectation over distance $r_1, ..., r_N$, we have

$$\begin{aligned}&\mathcal{P}^{\mathrm{ID}}(\beta) \\ =&\mathbb{E}_{G_{\mathcal{S},1},\ldots,G_{\mathcal{S},N}}\left\{\int\limits_{0\leq r_1\leq\cdots\leq r_N\leq\infty} \mathcal{L}_{\mathrm{I}}(s)\exp\big(-(\sigma_c^2+\sigma_n^2)s\big) f_r(r_1,\cdots,r_N)\mathrm{d}r_1\cdots\mathrm{d}r_N\right\}.\end{aligned}$$

Finally, by evaluating the expectations over $G_{\mathcal{S},i}$ for $1 \leq i \leq N$, where the joint PMF is given by (5.12), the final results are derived. □

Remark 5.1. *In the interference-limited region, i.e. $\sigma_n = \sigma_c = 0$, the TS and the PS schemes achieve the same ID success probability.*

It should be noted that the ID success probability only provides the statistics of the instantaneous SINR observed at the typical MU. Therefore, in order to show the impact of the handover overhead on the information transfer performance, we further investigate the average spectral efficiency, denoted as η_{SE}, achieved by the proposed CA-CoMP scheme. In particular, the average spectral efficiency is defined as the ergodic Shannon rate achieved by the typical MU per unit bandwidth, i.e. $\eta_{\mathrm{SE}} = \mathbb{E}\{\mathcal{T}_{\mathrm{eff}}^{\mathrm{ID}}\log(1+\mathrm{SINR})\}$, which is evaluated in the following proposition.

Proposition 5.4. *The average spectral efficiency achieved at the typical MU for the CA-CoMP scheme, is given by*

$$\eta_{\mathrm{SE}} = \mathcal{T}_{\mathrm{eff}}^{\mathrm{ID}}(\mu_c,\mu_b)\int_0^\infty \frac{\mathcal{P}^{\mathrm{ID}}(\beta)}{\beta+1}\mathrm{d}\beta, \tag{5.22}$$

where $\mathcal{T}_{\mathrm{eff}}^{\mathrm{ID}}(\mu_c,\mu_b)$ is the average effective time allocated for ID purpose per unit time with

$$\mathcal{T}_{\mathrm{eff}}^{\mathrm{ID}}(\mu_c,\mu_b) = \begin{cases}\max\{0,\tau(1-T_b\mu_b-T_c\mu_c)\}, & \text{TS scheme}\\ \max\{0,1-T_b\mu_b-T_c\mu_c\}, & \text{PS scheme,}\end{cases}$$

Yuan Guo

and T_c and T_b are the signalling overhead delay of the inter- and intra-cell handovers, respectively.

Proof. The proof is directly from the definition of the ergodic Shannon rate and the average spectral efficiency [38]. □

Based on the expression derived in Proposition 5.4, we can observe that the handover overhead degrades the average spectral efficiency. In particular, the effective time of the information transfer depends on the handover rate, i.e. a higher handover rate results in a shorter time interval for information transfer. Note that due to the heavy signalling overhead, a large handover rate may result in an outage for the information transfer, i.e. $\eta_{\text{SE}} = 0$, which is discussed in the following two corollaries.

Corollary 5.3. *An information transfer outage (i.e. $\eta_{\text{SE}} = 0$) occurs, when the velocity of a MU exceeds $\hat{v} = \frac{\pi^{\frac{3}{2}}\Gamma(N)}{2\sqrt{\tilde{\lambda}_b}\Gamma(0.5+N)(\mathcal{M}T_b+4T_c)}$, i.e. $v \geq \hat{v}$.*

Proof. According to the definition of the information transfer outage, i.e. $\eta_{\text{SE}} = 0$, we have $1 - T_b\mu_b - T_c\mu_c = 0$. Then by applying the result $\mu_b = \frac{\mathcal{M}}{4}\mu_c$ and by substituting the expression of μ_c given in Proposition 5.1, we have

$$\frac{4}{T_b\mathcal{M} + 4T_c} = \frac{8\hat{v}\tilde{\lambda}_b^{\frac{1}{2}}\Gamma(\frac{1}{2}+N)}{\pi^{\frac{3}{2}}\Gamma(N)}. \tag{5.23}$$

Finally, by solving the above equation in respect of $\hat{v}$, the final result is derived. □

Note that, for the high mobility MUs, a relatively large coverage area threshold should be selected to ensure the communication of the MUs. The minimum area threshold for the CA-CoMP scheme to avoid the information transfer outage is derived in the following corollary.

Corollary 5.4. *In order to avoid an information transfer outage, when a MU is moving with a velocity v, the minimum area threshold is given by*

$$\mathcal{A}_{\min} = Q^{-1}(K, Z)(K\lambda_b)^{-1}, \tag{5.24}$$

where $Q(a,b) = \frac{\Gamma(a,b)}{\Gamma(a)}$ is the regularized incomplete Gamma functions, $b = Q^{-1}\left(a, \frac{\Gamma(a,b)}{\Gamma(a)}\right)$ is the inverse regularized incomplete Gamma function and $Z = \frac{\pi^3}{4\lambda_b v^2}\left(\frac{\Gamma(N)}{(\mathcal{M}T_b+4T_c)\Gamma(0.5+N)}\right)^2$.

Yuan Guo

Proof. The proof follows a similar methodology with Corollary 5.3. By substituting the expression of $\tilde{\lambda}_b$, which is given in Proposition 5.1, and by solving equation (5.23) in respect of $\mathcal{A}$, the final expression is derived. □

The results provided in the above corollaries can be easily utilized for the network designing under the CA-CoMP scheme, to avoid the potential information transfer outage and provide stable downlink services for the MUs. In addition, these results hold for the energy transfer process, which will be discussed in the next subsection.

5.4.3 Energy transfer analysis

We now focus our attention on the achieved energy transfer performance of the CA-CoMP scheme. We evaluate the EH success probability, which is defined as the probability that the harvested energy of the typical MU is higher than the EH threshold ϵ (dBm), i.e. $\mathbb{P}\{\mathcal{Q} \geq \epsilon\}$. The analytical expression for the EH success probability is presented in the following theorem.

Theorem 5.3. *The EH success probability of the typical MU for the CA-CoMP scheme is given by*

$$\mathcal{P}^{\mathrm{EH}}(\epsilon) \approx 1 - \sum_{i=1}^{N} \sum_{G_{\mathcal{S},i}} \mathcal{Y}(G_{\mathcal{S},1}, \cdots, G_{\mathcal{S},N}) \mathcal{G}\left(G_{\mathcal{S},1}, \cdots, G_{\mathcal{S},N}\right) \quad - \int_0^{\infty} f_N(r_N) \mathcal{L}_{\mathbf{I}}(\psi) \mathrm{d}r_N, \tag{5.25}$$

where

$$\mathcal{Y}(G_{\mathcal{S},1}, \cdots, G_{\mathcal{S},N}) \triangleq \int_0^{\infty} \cdots \int_0^{r_2} \prod_{i=1}^{N} \frac{1}{1 + \psi P_t G_{\mathcal{S},i} \ell(r_i)} f_r(r_1, \cdots, r_N) \mathrm{d}r_1 \cdots \mathrm{d}r_N, \tag{5.26}$$

$\psi = \frac{\nu\eta(1-\rho)\zeta}{\epsilon}$ *and* $\mathcal{L}_{\mathbf{I}}(\cdot)$ *is the Laplace transform of the interference, which is given in Lemma 5.1.*

Proof. Since F is an exponential random variable with mean ζ, i.e. $F \sim \exp(\zeta)$, the EH success probability can be re-written as

$$\begin{aligned}
\mathcal{P}^{\mathrm{EH}}(\epsilon) =& \mathbb{P}[\mathcal{Q} \geq \epsilon] \\
=& \mathbb{P}\left\{ F \leq \frac{\nu\eta(1-\rho)}{\epsilon} \left(\sum\nolimits_{x_i \in \mathcal{S}} P_t G_{\mathcal{S},i} h_i \ell(r_i) + \sum\nolimits_{x_i \in \Phi \setminus \mathcal{S}} P_t G_{\mathcal{I},i} h_i \ell(r_i) \right) - 1 \right\} \\
\approx& 1 - \mathbb{E}\left\{ \exp\left(- \frac{\nu\eta(1-\rho)\zeta}{\epsilon} \mathbf{S} \right) \right\} - \mathbb{E}\left\{ \exp\left(- \frac{\nu\eta(1-\rho)\zeta}{\epsilon} \mathbf{I} \right) \right\},
\end{aligned} \tag{5.27}$$

where $\mathbf{S}$ and $\mathbf{I}$ are the intended and interfering signals, respectively; the last step is derived based on the cdf of an exponential random variable and by ignoring the term $\exp(\zeta)$, which approaches to one for small ζ [65]. Note that the second expectation in (5.27) includes the Laplace transform of the interference, i.e.,

$$\mathbb{E}\Big\{ \exp\Big(-\frac{\nu\eta(1-\rho)\zeta}{\epsilon}\mathbf{I}\Big)\Big\} = \mathbb{E}_{r_N}\Big\{ \mathcal{L}_{\mathbf{I}}\Big(\frac{\nu\eta(1-\rho)\zeta}{\epsilon}\Big)\Big\}. \tag{5.28}$$

By averaging over the distance from the typical MU to its N-th closest serving BS, i.e. r_N, of which the PDF is given by (5.9), the expectation in (5.28) can be evaluated. Then, let $\psi = \frac{\nu\eta(1-\rho)\zeta}{\epsilon}$, the first term of (5.27) can be solved as following

$$\begin{aligned}
&\mathbb{E}\Big\{ \exp\Big(-\psi\mathbf{S}\Big)\Big\} \\
=&\mathbb{E}\left\{ \mathbb{E}_{h_i}\left\{ \prod_{x_i\in\mathcal{S}} \exp\Big(-\psi P_t G_{\mathcal{S},i} h_i \ell(r_i)\Big)\right\}\right\} \\
=&\mathbb{E}\left\{ \prod_{x_i\in\mathcal{S}} \frac{1}{1+\psi P_t G_{\mathcal{S},i}\ell(r_i)}\right\} \\
=&\mathbb{E}_{G_{\mathcal{S},i}}\Big\{ \int_0^{\infty}\int_0^{r_N}\cdots\int_0^{r_2}\prod_{i=1}^{N}\frac{1}{1+\psi P_t G_{\mathcal{S},i}\ell(r_i)} f_r(r_1,\cdots,r_N)\mathrm{d}r_1,\cdots,\mathrm{d}r_{N-1},\mathrm{d}r_N\Big\}.
\end{aligned} \tag{5.29}$$

Then, by evaluating the expectations over $G_{\mathcal{S},i}$, of which the joint PMF is given by (5.12), the final results in Theorem 5.3 are proven. □

From (5.25) we can observe that the expression of the EH success probability consists of two main terms, i.e. the intended signal part and the interference signal part. Motivated by the high directionality of the antennas, the interference power can be ignored. Moreover, for the MUs moving with low-velocity, the misalignment probability approaches zero, and thus a perfect beam alignment is achieved, i.e. $\mathcal{G}(G_m,\cdots,G_m) = 1$. Therefore, based on the aforementioned observations, we provide an approximated expression for the EH success probability in the following remark.

Remark 5.2. *By ignoring the interference power, the EH success probability of the low-velocity MU is given by*

$$\mathcal{P}^{\mathrm{EH}}(\epsilon) \approx 1 - \int_0^{\infty}\cdots\int_0^{r_2}\prod_{i=1}^{N}\frac{1}{1+\phi\ell(r_i)} f_r(r_1,\cdots,r_N)\mathrm{d}r_1\cdots\mathrm{d}r_N, \tag{5.30}$$

where $\phi = \frac{P_t G_m \nu\eta(1-\rho)\zeta}{\epsilon}$.

Note that, the EH success probability reveals the statistics of the instantaneous harvested energy, while by taking into account the handover signalling cost, we can assess the EH performance in terms of the average harvested energy. More specifically, the average harvested energy is defined as the average amount of energy harvested by the typical MU per unit time; the analytical expression is provided in the following theorem.

Theorem 5.4. *The average harvested energy per unit time of the typical MU for the CA-CoMP scheme is given by*

$$\bar{\mathcal{Q}} = \bar{\mathcal{Q}}_{\mathbf{S}} + \bar{\mathcal{Q}}_{\mathbf{I}}, \tag{5.31}$$

where $\bar{\mathcal{Q}}_{\mathbf{S}}$ *and* $\bar{\mathcal{Q}}_{\mathbf{I}}$ *are given by*

$$\bar{\mathcal{Q}}_{\mathbf{S}} = \sum_{i=1}^{N} \sum_{G_{\mathcal{S},i}} \int_0^{\infty} \cdots \int_0^{r_2} \left(G_{\mathcal{S},1}\ell(r_1) + \cdots + G_{\mathcal{S},N}\ell(r_N)\right) \mathcal{B}\mathcal{Y}\left(G_{\mathcal{S},1}, \cdots, G_{\mathcal{S},N}\right) \times f_r(r_1, \cdots, r_N) \mathrm{d}r_1 \cdots r_N, \tag{5.32}$$

and

$$\bar{\mathcal{Q}}_{\mathbf{I}} = \int_0^{\infty} \sum_{G} 2\pi\mathcal{B}G p_G \left(\frac{(\lambda_b - \tilde{\lambda}_b) r_N^2 {}_2F_1\left[1, \frac{2}{\alpha}, \frac{2+\alpha}{\alpha}, -r_N^2\right]}{2} + \frac{\lambda_b r_N^{2-\alpha} {}_2F_1\left[1, \frac{\alpha-2}{\alpha}, \frac{2\alpha-2}{\alpha}, -r_N^2\right]}{\alpha - 2} \right) f_N(r_N) \mathrm{d}r_N, \tag{5.33}$$

respectively; $\mathcal{B} = 2\pi\eta P_t(1-\rho)\mathcal{T}_{\text{eff}}^{\text{EH}}$ *and* $\mathcal{T}_{\text{eff}}^{\text{EH}}$ *is the effective time for the EH procedure, with*

$$\mathcal{T}_{\text{eff}}^{\text{EH}} = \begin{cases} \max\left\{0, (1-\tau)(1 - T_b\mu_b - T_c\mu_c)\right\}, & \text{TS scheme} \\ \max\left\{0, 1 - T_b\mu_b - T_c\mu_c\right\}, & \text{PS scheme.} \end{cases} \tag{5.34}$$

Proof. The average harvested energy per unit time can be calculated by averaging the instantaneous harvested energy over the random channel, path loss components and the antenna gains, i.e.

$$\begin{aligned} \bar{\mathcal{Q}} =& \mathbb{E}\left\{ \frac{\mathcal{T}_{\text{eff}}^{\text{EH}} \nu (1-\rho)\eta}{1+F} \left(\mathbf{S} + \mathbf{I}\right) \right\} = \underbrace{\mathbb{E}\left\{ \frac{\nu}{1+F} \right\}}_{=1} \mathbb{E}\left\{ \mathcal{T}_{\text{eff}}^{\text{EH}}(1-\rho)\eta\mathbf{S} + \mathcal{T}_{\text{eff}}^{\text{EH}}(1-\rho)\eta\mathbf{I} \right\} \\ =& \bar{\mathcal{Q}}_{\mathbf{S}} + \bar{\mathcal{Q}}_{\mathbf{I}}, \end{aligned} \tag{5.35}$$

where $\bar{\mathcal{Q}}_{\mathbf{S}}$ and $\bar{\mathcal{Q}}_{\mathbf{I}}$ represent the average harvested energy from intended and interfering signals, respectively. We evaluate $\bar{\mathcal{Q}}_{\mathbf{S}}$ as

$$\bar{\mathcal{Q}}_{\mathbf{S}} = \mathbb{E}\left\{ \mathcal{B} \textstyle\sum_{x_i \in \mathcal{S}} h_i G_{\mathcal{S},i} \ell(r_i) \right\} \overset{(a)}{=} \mathbb{E}\left\{ \mathcal{B} \textstyle\sum_{x_i \in \mathcal{S}} G_{\mathcal{S},i} \ell(r_i) \right\}, \tag{5.36}$$

where $\mathcal{B} = \mathcal{T}_{\text{eff}}^{\text{EH}}(1-\rho)\eta P_t$, and (a) follows from the fact that the channel power gain h_i are i.i.d. exponential random variables with mean one. Then, the above expectation can be evaluated by averaging over the antenna gains and distance from the typical MU to the serving BSs, of which the joint PMF and the joint PDF are given by (5.12) and (5.20), respectively. In addition, $\bar{\mathcal{Q}}_{\mathbf{I}}$ can be calculated based on the Campbell's Theorem [25], i.e.

$$\begin{aligned}\bar{\mathcal{Q}}_{\mathbf{I}} &= \sum_{x_i \in \Phi \setminus \mathcal{S}} \mathcal{B} h_i G_{\mathcal{I},i} \ell(r_i) \\ &= \mathbb{E}_{r_N}\left\{ 2\pi\mathcal{B} \sum\nolimits_G G p_G \left(\int_0^{r_N} (\lambda_b - \tilde{\lambda}_b) \frac{r}{1-r^{\alpha}} \mathrm{d}r + \int_{r_N}^{\infty} \lambda_b \frac{r}{1-r^{\alpha}} \mathrm{d}r \right) \right\}, \quad (5.37)\end{aligned}$$

where the integrals can be easily evaluated based on the resulting expression [91, 3.194.5]. Finally, by evaluating the expectation over r_N, of which the PDF is given by (5.9), the results in Theorem 5.4 could be derived. □

The above theorem reveals the negative impact of the handover process on the average harvested energy, i.e. a higher handover rate leads to less harvested energy per unit time. Moreover, for scenarios with high velocities, energy transfer outage may occur, i.e. $\bar{\mathcal{Q}} \to 0$. In order to avoid such energy transfer outage, the area threshold of the CA-CoMP scheme should be greater than $\mathcal{A}_{\min}$, which is provided in Corollary 5.4. Finally, by adjusting the PS or TS parameters, i.e. ρ or τ, the proposed CA-CoMP scheme can satisfy different requirements for various mIoT applications.

5.4.4 Energy efficiency analysis

In order to provide a comprehensive evaluation for the performance of CA-CoMP scheme, we investigate another equally important metric, namely, the energy efficiency, which refers to the ability of a MU to receive and process data with the minimum possible energy. Since a SWIPT-enabled MU is capable of converting part of the received RF signal into DC power, which is then used to power its circuitry, the total energy consumed by a MU is calculated by subtracting the amount of harvested energy from the total energy used for data receiving and processing. Hence, the energy efficiency of a SWIPT-enabled MU is defined as the ratio of the average downlink data rate to the amount of energy consumed at MU's battery [103]. For the sake of simplicity, we only consider communication-related energy consumption at

Yuan Guo

the MUs. In particular, for a certain input data rate, i.e. $\mathcal{R}$, the energy consumed at the MU for processing the downlink input signal is given by [104]

$$\psi(\mathcal{R}) = \mathcal{R} K_{BB} F_0 a G_a k_{\mathrm{B}} T_{\mathrm{env}} \ln 2 + C_{\mathrm{cir}}, \tag{5.38}$$

where $\mathcal{R} = B_w \eta_{\mathrm{SE}}$ is the downlink rate, B_w is the bandwidth, K_{BB} is the logic operations per bit in the baseband processor, F_0 is the fanout, i.e., the number of loading logic gates, a is the activity factor of transistors for the chip in MUs' devices, k_{B} is the Boltzmann constant, and T_{env} is the temperature of the environment, $G_a \approx 454.2$ is the gap between the switch energy consumption for the transistor and the Landauer limit, and C_{cir} represents the constant power consumption of the baseband processor. Then, based on the ID and EH performance metrics derived in the previous section, we provide the energy efficiency of the typical MU in the following proposition.

Proposition 5.5. *The energy efficiency of the typical MU with the CoMP scheme is given by*

$$\mathcal{E} = \frac{\mathcal{R}}{\psi(\mathcal{R}) - \bar{\mathcal{Q}}}, \tag{5.39}$$

where $\bar{\mathcal{Q}}$ is the average harvested energy by the typical MU.

5.5 Numerical results

In this section, we present analytical and simulation results to validate the accuracy of our model and illustrate the performance of the proposed CA-CoMP scheme. Unless otherwise stated, we consider the following parameters: the BS density is $\lambda_b = 1/3600$, the number of cooperative BSs is $N = 3$, the transmitted power of BSs is $P_t = 43$ dBm, the path-loss exponent is $\alpha = 3$, thermal noise is $\sigma_n^2 = -94$ dBm, conversion noise is $\sigma_c^2 = -74$ dBm, power splitting ratio is $\rho = 0.5$, time switching ratio is $\tau = 0.5$, the number of beams is $\mathcal{M} = 128$, RF-to-DC conversion efficiency is $\eta = 0.7$, SSB periodicity is $T_{\mathrm{SSB}} = 20$ ms, velocity of MUs is $v = 25, 30, 40$ m/s, inter-cell handover delay is $T_c = 43$ ms, intra-cell handover delay is $T_b = 23$ ms, bandwidth is $B_w = 100$ MHz, logic operations per bit is $K_{BB} = 10^8$, fanout is $F_0 = 4$, activity factor of transistors is $a = 0.2$, environment temperature is $T_{\mathrm{env}} = 303$ K, constant power consumption is $C_{\mathrm{cir}} = 1.5$ W, loss coefficient of antenna directivity is $\xi = 0.1$, and the parameter for random effect of EH is $\zeta = 0.01$. It is worth

Yuan Guo

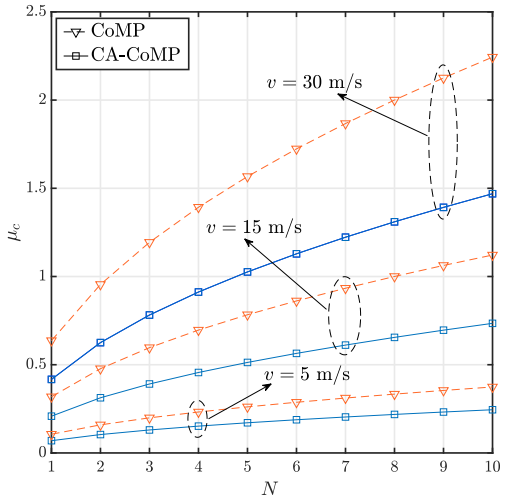

(a) Inter-cell handover rate (μ_c) versus the number of serving BSs (N).

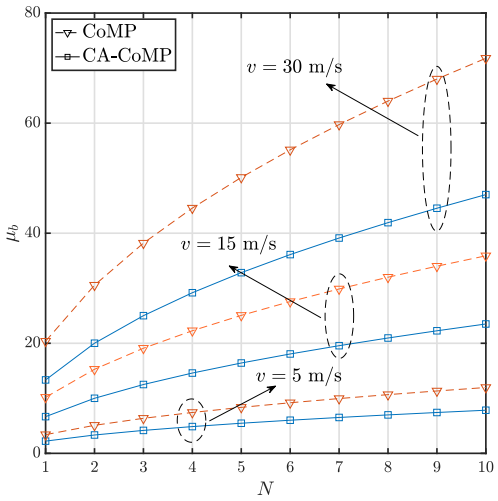

(b) Intra-cell handover rate (μ_b) versus the number of serving BSs (N).

Figure 5.3: Inter- and intra-cell handover rate for MUs with different velocities, where $\lambda_b = \frac{1}{3600}$, $\mathcal{A} = \frac{1}{\lambda_b}$, and $v \in \{5, 15, 30\}$ m/s.

mentioning that, the proposed analytical framework is generic, and the selection for these parameter values is for the purpose of illustration.

Fig. 5.3 demonstrates the impact of the number of serving BSs and the MUs' velocity on the handover rate achieved by the proposed CA-CoMP scheme. In particular, Fig. 5.3a plots the inter-cell handover rate, i.e. μ_c, versus the number of serving BSs, i.e. N, for MUs that move with different velocities, i.e. $v \in \{5, 15, 30\}$ m/s. For comparison purposes, we also present the inter-cell handover rate obtained based on the conventional CoMP scheme [28], where each MU jointly communicates with N closest BSs, denoted as "CoMP". Firstly, we can observe that the proposed CA-CoMP scheme achieves a much lower inter-cell handover rate compared to the conventional CoMP. This was expected since, by employing the proposed CA-CoMP scheme, the communication of MUs with small area cells that induce frequent handover processes is avoided, thereby achieving a significantly lower inter-cell handover rate. Hence, the proposed scheme alleviates the signalling overhead and thus is promising for practical and low-complexity implementations. Moreover, we can observe that, the inter-cell handover rate increases with the increase of the number of serving BSs as well as the velocity of the MUs. This can be justified by the fact that, for the joint communication of a MU with multiple BSs as well as for the

Yuan Guo

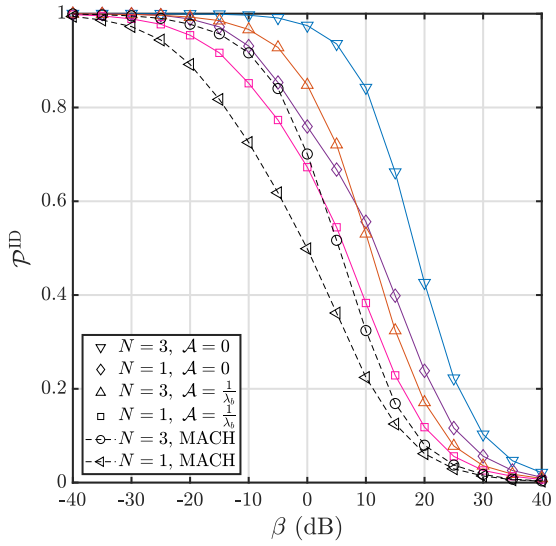

Figure 5.4: ID success probability $\left(\mathcal{P}^{\mathrm{ID}}\right)$ versus the decoding threshold (β), for different area threshold ($\mathcal{A}$) and number of serving BSs (N), where $\lambda_b = \frac{1}{3600}$.

communication of a high-velocity MU, frequent handover operations are required to ensure high QoS. Moreover, another interesting observation is that a higher gain is achieved by the CA-CoMP scheme over the conventional CoMP, when the MU is connecting with more serving BSs or moving with a higher velocity. This result is in line with the expression in (5.3), where for a certain given area threshold, the achieved gain by the CA-CoMP scheme is directly proportional to the number of serving BSs and the velocity of the MUs.

Similar results can be observed in Fig. 5.3b, which plots the intra-cell handover rate versus the number of serving BSs. Initially, the comparison of inter- and intra-handover rates that are depicted in Fig. 1(a) and Fig1(b), respectively, reveals that the intra-handover rate is the dominant limiting factor compared to the inter-handover rate. This was expected since, each BS has multiple beams (hundreds of beams in 6G networks), which could result in a much more frequent intra-cell handover compared with the inter-cell handover. Finally, the agreement between the theoretical curves (solid and dash lines) and the simulation result (markers) validates our theoretical analysis.

Fig. 5.4 illustrates the effect of the area threshold and the number of serving BSs on the ID success probability. In particular, Fig. 5.4 plots the ID success probability (Theorem 3.1) with respect to the SINR threshold for different area threshold, i.e. $\mathcal{A} = \{0, \frac{1}{\lambda_b}\}$, and different number of serving BSs, i.e. $N = \{1, 3\}$. Firstly, it

Yuan Guo

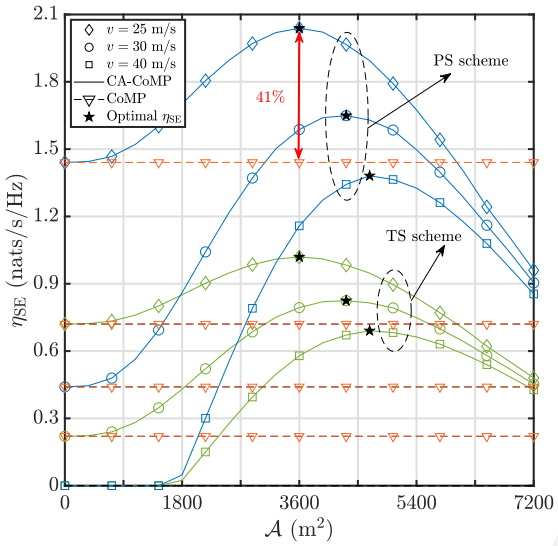

Figure 5.5: Average spectral efficiency (η_{SE}) versus the area threshold ($\mathcal{A}$), for different velocities of MUs, where $\lambda_b = \frac{1}{3600}$, $\mathcal{M} = 128$, $\tau = 0.5$ and $\rho = 0.5$.

can be easily observed that, for a fixed area threshold, the ID success probability increases with the increase of the number of serving BSs. This could be explained by the fact that the increased number of serving BSs leads to an improved power of the intended received signal and to the reduction of the number of interfering BSs, and thus the overall observed interference is reduced, which results in an enhanced SINR. We can further observe that, by increasing the area threshold $\mathcal{A}$, the success probability drops. This is based on the fact that, the density of the BSs that satisfy the coverage area condition (i.e. the candidate BSs) decreases with the increase of the area threshold, resulting in a longer distance between the MU and its serving BSs, thereby reducing the received signal strength. Note that, the interference experienced by a MU is significantly stronger compared to the noise power, and thus, the ID success probability achieved with the employment of the PS scheme is approximately identical to the performance achieved with the TS scheme. Hence, due to space limitation, only the TS scheme is presented in Fig. 5.4. Finally, we can clearly observe from Fig. 5.4 that the CA-CoMP scheme achieves a higher coverage probability than the MACH scheme [29] for any number of serving BSs. It was expected since the employment of the MACH scheme associates the MU with multiple BSs which are in the direction of MU's movement, while several nearby BSs that do not belong in the set of cooperative BSs cause severe inter-cell interference, compromising the performance of the MU.

Yuan Guo

Fig. 5.5 reveals the impact of the area threshold on the downlink spectral efficiency for the proposed CA-CoMP scheme. In particular, Fig. 5.5 plots the spectral efficiency, i.e. η_{SE}, versus the area threshold, i.e. $\mathcal{A}$, where the MUs employ either the PS or the TS scheme. We can observe from the figure that the network performance is enhanced for low area threshold values by increasing the area threshold. However, by increasing the area threshold beyond a critical point, i.e. the optimal spectral efficiency, the spectral efficiency decreases. This observation is based on the fact that at low area threshold constants, the MUs experience less intra- and inter-cell handover operations, while the MUs are still able to communicate with their serving BSs. In contrast, for large area threshold values, the distances between a MU and its serving BSs increase, and thus the spectral efficiency significantly decreases. Furthermore, it can be observed that, the spectral efficiency achieved with the employment of the PS scheme outperforms the TS scheme, independently of the MUs' velocity. This can be explained by the fact that, by employing the TS scheme, the MUs assign a fraction of the time slot for ID, while the PS scheme enables the MUs to allocate more effective time for ID, resulting in a higher achieved data rate. Furthermore, as expected, for the MUs moving with a high velocity, the information transfer outage occurs (i.e. $\eta_{\text{SE}} = 0$) due to severe handover overhead, which could be avoided with the employment of the CA-CoMP scheme by increasing the area threshold. Finally, the performance achieved with the conventional CoMP is also illustrated in Fig. 5.5 for comparison purposes. Note that CoMP does not depend on the area threshold, thus the achieved spectral efficiency remains constant. We can easily observe that the CA-CoMP scheme outperforms the CoMP for both the PS and TS schemes. In particular, by selecting the area threshold equal to $\mathcal{A} = \frac{1}{\lambda_b}$, a 41% gain is achieved by the CA-CoMP scheme over the conventional CoMP for a velocity of $v = 25$ m/s.

Fig. 5.6 depicts the impact of the area threshold on the EH success probability achieved by the employment of the proposed CA-CoMP scheme. More specifically, Fig. 5.6 plots the achieved EH success probability (Theorem 5.3) versus the EH threshold, for $\mathcal{A} \in \{0, \frac{1}{\lambda_b}, \frac{2}{\lambda_b}\}$. It can be observed that, the EH success probability increases with the decrease of the area threshold. This is based on the fact that, a smaller area threshold enables the communication of the MUs with their closest BSs, even if their coverage areas are small, enhancing the harvesting power, and thus improving the EH success probability. Moreover, Fig. 5.6 presents the approxi-

Yuan Guo

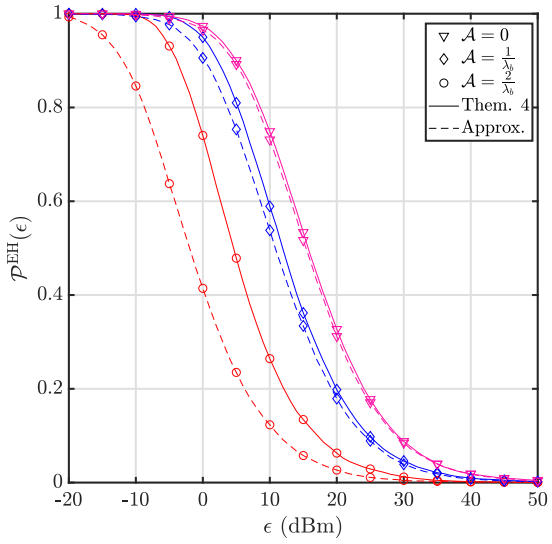

Figure 5.6: EH success probability $\left(\mathcal{P}^{\mathrm{EH}}\right)$ versus the decoding threshold (ϵ), for different area threshold ($\mathcal{A}$), where $\lambda_b = \frac{1}{3600}$.

mated EH success probability (provided in Remark 5.2), which is represented by the dash lines. We can observe that, by ignoring the interfering signal power, i.e. only the intended signals are harvested by the MUs, it achieves a tight lower bound for the actual performance. This was expected since the BSs employ high gain directional antennas that can transmit strong signals to specific directions to enhance the intended signal power at the MUs, while the observed interference signal power at the MUs is much lower and thus it can be neglected.

Fig. 5.7 shows the effect of the area threshold on the MUs' EH performance in terms of the average harvested energy. In particular, Fig. 5.7 plots the average harvested energy of MUs versus the area threshold $\mathcal{A}$, for different velocities of MUs, i.e. $v \in \{25, 30, 40\}$ m/s. In correspondence to the observations obtained in Fig. 5.5, Fig. 5.7 illustrates that the amount of the average harvested energy initially increases and then decreases by increasing the area threshold. Hence, for a MU moving with a certain velocity, we can find an optimal area threshold to achieve the highest EH performance for the CA-CoMP scheme. Moreover, it can be observed that the MUs with a lower velocity are able to achieve a better energy harvesting performance, since smaller handover rates provide more effective time for EH process. Finally, we observe that our proposed CA-CoMP scheme enhances the EH performance of MUs for different velocities, which achieves a better EH performance compared to conventional CoMP scheme. This was expected since the CA-CoMP scheme reduces

Yuan Guo

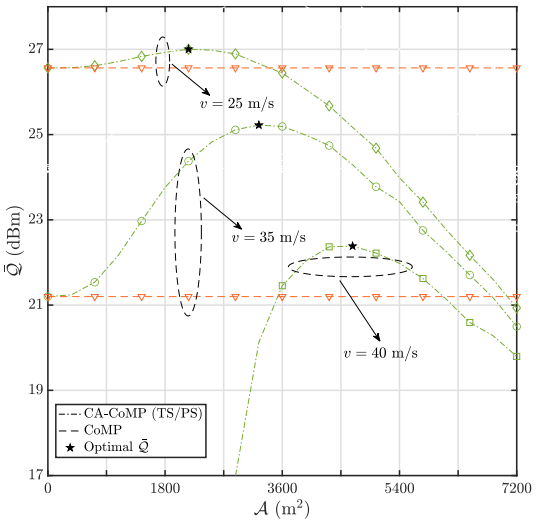

Figure 5.7: Average harvested energy ($\bar{\mathcal{Q}}$) versus area threshold ($\mathcal{A}$) for MUs with different velocity, where $\lambda_b = \frac{1}{3600}$ and $\mathcal{M} = 128$.

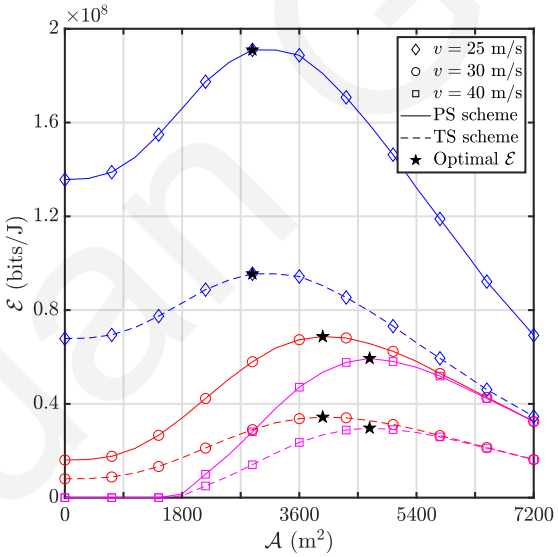

Figure 5.8: Energy efficiency ($\mathcal{E}$) versus the area threshold ($\mathcal{A}$) for MUs with different velocities.

the handover rate, and thus MUs can dedicate more time for EH.

Fig. 5.8 presents the achieved energy efficiency of the CA-CoMP scheme. We can easily observe that the mobility has a negative impact on the energy efficiency, i.e. MUs with lower velocity can achieve a higher energy efficiency. This is based on the fact that, MUs moving with higher velocity need to allocate more time to ensure connection with multiple BSs, which results in less effective time for data

Yuan Guo

and energy transfer for the network. We can also observe that, by employing the CA-CoMP scheme, there is an optimal area threshold to achieve the highest energy efficiency. Moreover, it can be observed that the optimal area threshold increases with the increase of MUs' velocities. This was expected since, the frequent handover becomes a dominant factor that reduces the ID and EH performance, and thus the area threshold for the CA-CoMP scheme should be increased to mitigate the handover rate. Finally, based on the results illustrated in Fig. 5.5, 5.7 and 5.8, we can observe that the CA-CoMP scheme can satisfy different requirements of ID, EH or energy efficiency for diverse applications at MUs by properly selecting the area threshold.

5.6 Summary

In this chapter, we have studied a novel CA-CoMP scheme in the context of SWIPT-enabled mobile networks. By exploring the different cell areas caused by the irregular network deployment, our proposed CA-CoMP scheme enables high-mobility MUs to jointly communicate with multiple nearby serving BSs, whose coverage areas satisfy a pre-defined threshold. In order to provide a comprehensive interpretation of the mobility effect on the network performance, we have investigated both the inter- and intra-cell handover operations, where the handover rates were derived in closed form. Moreover, by using tools from stochastic geometry, we have studied the ID and EH performance achieved with the employment of CA-CoMP scheme and the performance metrics are derived in analytical expressions. Our results have shown that the proposed CA-CoMP can greatly reduce the handover rate, and by properly selecting the area threshold, the CA-CoMP scheme can avoid the information and power transfer outage for the high-velocity MUs. Furthermore, we have shown that compared to conventional CoMP schemes, our proposed technique offers a much better SWIPT performance in terms of the spectral efficiency and the average harvested energy, while the optimal area threshold of the CA-CoMP scheme to achieve the highest SWIPT performance has been numerically demonstrated. Finally, our results have revealed that the PS scheme outperforms the TS scheme in terms of SWIPT performance for high-velocity MUs under the CoMP scenario.

Yuan Guo

Chapter 6

SWIPT-assisted vehicular networks

In this chapter, we investigate a SWIPT-assisted vehicular network. Utilizing SWIPT technology, battery-operated road-side sensors simultaneously receive control information and harvest energy from cellular BSs, subsequently using the harvested energy to spread data to vehicles. By leveraging stochastic geometry tools, we establish a tractable framework, where the load of BSs and sensors are taken into account. The analytical expressions for the active probability and average harvested energy of sensors, as well as the ID success probability of vehicles are derived. Our results reveal the significant impact of system parameters, such as sensor density, time splitting factor, and information threshold on vehicular network performance. The optimal sensor density and time splitting factor that maximize ID success probability are illustrated. Additionally, the optimal sensor density within vehicular networks dynamically adjusts in response to varying traffic congestion levels. Our results offer invaluable insights for vehicular network design, highlighting the need for adaptive strategies that seamlessly respond to evolving network conditions and traffic patterns.

6.1 Motivation and contributions

Benefiting from the advancements in wireless network technologies, vehicular networks are emerging as a cornerstone of technological progress in transportation, significantly enhancing road safety, improving traffic flow, and increasing overall convenience for drivers [105]. To fully harness the potential benefits of vehicular networks, an extensive deployment of road-side sensors for gathering and dissem-

Yuan Guo

inating vital information, is of paramount importance [106]. However, the majority of sensors are battery-operated, presenting a significant challenge in terms of power sustainability. To this end, SWIPT technology becomes a promising solution, offering a dual benefit: continuous power supply and seamless data communication [11, 13].

Recently, stochastic geometry tools have been leveraged for modeling and analyzing the vehicular networks [105, 107, 108]. Specifically, the authors in [108] presents an in-depth introduction to the Poisson line Cox process, which captures the randomness of road layouts and vehicle positions, demonstrating its utility in enhancing system-level performance analysis for modern vehicular networks. Moreover, by adopting the Poisson Line Cox Process model, the authors in [105] investigate the downlink coverage and rate of a cellular vehicle-to-everything network and derive the coverage probability with the consideration of shadowing effects. Although significant research has been conducted on vehicular communication networks, the incorporation of SWIPT technology offers both enhanced sustainability and communication efficiency, which has been overlooked from the literature.

Motivated by above considerations, in this work, we investigate the advanced capabilities of SWIPT-assisted vehicular networks. Specifically, we consider that each unit time is divided into two parts: initially, road-side sensors employ SWIPT technology to receive control information and harvest energy from cellular BSs, then activate to transmit data to vehicles. By leveraging stochastic geometry tools, we establish a tractable analytical framework to assess the downlink performance. The analytical expressions for the active probability, the average harvested energy of sensors, and the ID success probability of vehicles are derived, by taking into account the number of sensors and vehicles associated with each BS and sensor, respectively. Our results show that the ID performance of vehicles depends on multiple system parameters, such as the density of sensors and vehicles, as well as the time-splitting factor, etc. The optimal density of sensors and the time-splitting factor that maximize the ID success probability of vehicles are illustrated. Finally, it is shown that the these optimal system parameters dynamically shift according to the varying traffic situations, and a higher density of vehicles results in a lower ID success probability achieved by each vehicle.

Yuan Guo

6.2 System model

We consider a large-scale downlink communications networks, consisting of traditional cellular BSs, road-side sensors and vehicles, which are randomly located. In specific, cellular BSs are modeled according to a homogeneous PPP Φ_b with intensity λ_b [19, 25]. Additionally, sensors and vehicles are distributed based on two independent one-dimensional (1D) PPPs on each roadway, i.e. Φ_s and Φ_v with intensity λ_s and λ_v, respectively. Further, the roadways are modeled by a homogeneous Poisson line process (PLP) Φ_l with line intensity μ_l [105, 107]. Regarding the association policy, we consider that each sensor communicates with its closest BS, and each vehicle receives information from its nearest sensor on the same roadway.

We assume that all wireless signals experience both small-scale fading and large-scale path-loss effects. Specifically, the small-scale fading is modeled as Rayleigh fading, where different links are assumed to be independent and identically distributed. We denote the channel power gain of the link between BSs and sensors by h, and the channel power gain between sensors and vehicles by g. Therefore, h and g are exponential random variables with unit mean [19]. Moreover, the large-scale path-loss between a transmitter and a receiver with distance r is modeled by an unbounded singular model, i.e.

$$\ell(r) = \begin{cases} r^{-\alpha_c}, & \text{path-loss between BSs and sensors,} \\ r^{-\alpha_v}, & \text{path-loss between sensors and vehicles,} \end{cases}$$

where α_c & $\alpha_v > 2$ are the path-loss exponents.

Furthermore, we consider that sensors and vehicles have single omnidirectional antennas, and all BSs are equipped with multiple antennas, of which the actual antenna pattern is approximated by a widely-adopted sectorized model [19, 109]. More specifically, the antenna array gain of the link between a BS and a sensor is modeled by two discrete values, i.e. $G = \{G_m, G_s\}$ with corresponding probability $p_G = \left\{\frac{\omega}{2\pi}, \frac{2\pi-\omega}{2\pi}\right\}$, where G_m and G_s are the main- and side-lobe gains, respectively, and ω is the beamwidth of the main-lobe [97]. We assume a perfect beam-alignment achieved between each sensor and its serving BS [110].

We assume that each unit time period is split into two parts with a time splitting factor τ, as illustrated in Fig. 6.1. During the first fraction τ of time, cellular BSs transmit central control information and power to sensors; while sensors send data

Yuan Guo

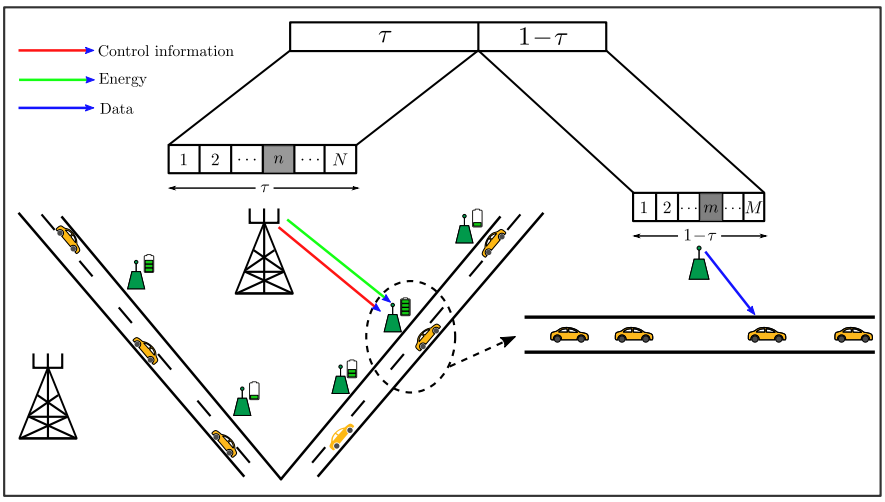

Figure 6.1: System diagram of the SWIPT-assisted vehicular networks.

to vehicles during the rest $(1-\tau)$ of time. Additionally, we consider that the communication between BSs and sensors occurs on distinct frequency bands from those used for communication between sensors and vehicles. Furthermore, we assume a time division multiple access scheme for the downlink networks, based on which, each BS and sensor evenly divide the allocated transmission time into multiple time-slots according to the number of associated sensors and vehicles, respectively. More specifically, the transmission time dedicated to each sensor by a BS is precisely $\frac{\tau}{N}$, where N is the number of sensors served by this BS; while the duration of each time-slot allocated to a vehicle is $\frac{1-\tau}{M}$, where M is the number of vehicles associated with a sensor.

Finally, we consider that all sensors are battery-operated and have SWIPT capability to decode information and harvest energy simultaneously by adopting a PS scheme. In specific, a fraction ρ of the received signal power is allocated for ID purpose, and the rest is directed to the EH circuit. If the decoded information by a sensor during a time slot satisfies a pre-defined threshold, it transmits information to the associated vehicles by using the harvested energy.

6.3 Performance analysis of the SWIPT-assisted vehicular networks

In this section, we study the performance of the considered SWIPT-assisted vehicular networks. We initially assess the ID and EH performance achieved by each

Yuan Guo

sensor, in terms of the active probability and the average harvested energy, receptively. Further, the distribution of the number of sensors associated with each BS is evaluated. Finally, we analyze the ID success probability for vehicles, by taking into consideration of the number of vehicles served by each sensor.

6.3.1 SWIPT performance achieved by sensors

Considering that N sensors are associated with a BS, the conditional active probability of a sensor is defined as the probability that the decoded information during a time-slot exceeds a pre-defined threshold, β bits, i.e.

$$\mathcal{A}(\beta, N) \triangleq \mathbb{P}\left\{\frac{\tau}{N} B_c \log_2(1+\mathrm{SINR}) \geq \beta \mid N\right\}. \tag{6.1}$$

The analytical expression of $\mathcal{A}(\beta, N)$ is presented in the following lemma.

Lemma 6.1. *Conditioning on the case where N sensors are associated with a BS, the active probability of the sensor served by this BS is given by*

$$\mathcal{A}(\beta, N) = \int_0^\infty \mathcal{L}(\varrho) \exp\left(-\frac{s\sigma_c^2}{\rho} - \pi\lambda_b r^2\right) 2\pi\lambda_b r \mathrm{d}r, \tag{6.2}$$

where

$$\mathcal{L}(\varrho) = \prod_{G\in\{G_m, G_s\}} \exp\left(-\frac{2\pi\varrho\lambda_b P_b r^{2-\alpha_c}}{\alpha_c - 2} G p_G \, {}_2F_1\left[1, \frac{\alpha_c-2}{\alpha_c}; \frac{2\alpha_c-2}{\alpha_c}; -\frac{G p_G P_b \varrho}{r^{\alpha_c}}\right]\right), \tag{6.3}$$

$\varrho = \left(2^{\frac{N\beta}{B_c\tau}} - 1\right) \frac{r^{\alpha_c}}{P_b G_m}$ *and P_b is the transmit power of a BS.*

Proof. The conditional active probability is computed as

$$\begin{aligned}
\mathcal{A}(\beta, N) =& \mathbb{P}\left\{\frac{\rho P_b G_m r_o^{-\alpha_c} h_o}{\sum_{x_i\in\Phi_b^{\setminus x_o}} \rho P_b G_i r_i^{-\alpha_c} h_i + \sigma_s^2} \geq 2^{\frac{N\beta}{B_c\tau}} - 1\right\} \\
=& \mathbb{P}\left\{h_o \geq s\left(\sum\nolimits_{x_i\in\Phi_b^{\setminus x_o}} P_b G_i r_i^{-\alpha_c} h_i + \sigma_s^2/\rho\right)\right\} \\
=& \mathbb{E}\left\{\exp\left(-s\sum\nolimits_{x_i\in\Phi_b^{\setminus x_o}} P_b G_i r_i^{-\alpha_c} h_i\right) \exp\left(-\frac{\sigma_s^2}{\rho}\right)\right\} \\
=& \mathbb{E}\left\{\mathcal{L}(s)\exp\left(-\frac{\sigma_s^2}{\rho}\right)\right\},
\end{aligned} \tag{6.4}$$

where r_o and r_i represent the distance from a sensor to its serving BS and the i-th interfering BS, respectively, $\mathcal{L}(s)$ is the Laplace transform of the interference and $s = \left(2^{\frac{N\beta}{B_c\tau}} - 1\right) \frac{r^{\alpha_c}}{P_b G_m}$. The rest of the proof follows the similar steps as the proof of Theorem 5.2, and thus is omitted due to the limited space. □

Yuan Guo

It can be easily observed from the expression in Lemma 6.1 that, the active probability of a sensor depends on the number of sensors associated with a BS, the PS factor, and the density of cellular BSs. In specific, a greater number of sensors served by the same BS results in a shorter transmission time-slot for each sensor and thus decreases the active probability. Moreover, reducing the PS factor amplifies the impact of noise on the signal, consequently causing a decrease in active probability. Finally, the density of base stations presents a noteworthy trade-off. While higher density can enhance the intended signal strength by reducing the distance between a sensor and serving its BS, it also leads to increased interference from neighboring BSs.

We now study the EH performance achieved by a sensor. By conditioning the scenario where N sensors served by a BS, the average amount of harvested energy by a sensor per unit time, is evaluated in the following lemma.

Lemma 6.2. *Conditioning on the case where N sensors are associated with a BS, the average harvested energy of a sensor served by this BS per unit time is given by*

$$\mathcal{E}(N) = \frac{\pi^{\frac{\alpha_c}{2}} \tau P_b \lambda_b^{\frac{\alpha_c}{2}} \mathcal{Q}(N)}{(\alpha_c - 2)N}, \tag{6.5}$$

where

$$\begin{aligned}
&\mathcal{Q}(N) \\
=&G_m \Bigg(2p_m(N-\rho)\Gamma\left(2 - \frac{\alpha_c}{2}, \pi r_{\min}^2 \lambda_b\right) + (\alpha_c - 2)(1-\rho)\Gamma\left(1 - \frac{\alpha_c}{2}, \pi r_{\min}^2 \lambda_b\right) \Bigg) \\
+&G_s \Bigg(2(N-\rho)p_s\Gamma\left(2 - \frac{\alpha_c}{2}, \pi r_{\min}^2 \lambda_b\right) + (\alpha_c - 2)(N-1)\Gamma\left(1 - \frac{\alpha_c}{2}, \pi r_{\min}^2 \lambda_b\right) \Bigg) \Bigg),
\end{aligned} \tag{6.6}$$

η is the efficiency of the EH circuit and $r_{\min} = 1$ represents the minimum distance between a BS and a sensor.

Proof. Note that the received signal power is split during one time slot, i.e. τ/N, which is dedicated to downlink communication between a sensor and its serving BS; while during the remaining time, it harvests energy from the interference, and thus there is no need to perform power splitting. Therefore, the average harvested

YuanGuo

energy by a sensor per unit time is computed as

$$\mathcal{E}(N) = \mathbb{E}\Bigg\{ \underbrace{\frac{\tau(1-\rho)}{N}\eta\left(P_b G_m r_o^{-\alpha_c} + \sum_{x_i \in \Phi_b^{\setminus x_o}} P_b G_i r_i^{-\alpha_c}\right)}_{\text{power-splitting is applied}} + \underbrace{\frac{(N-1)\tau}{N}\eta\left(P_b G_s r_o^{-\alpha_c} + \sum_{x_i \in \Phi_b^{\setminus x_o}} P_b G_i r_i^{-\alpha_c}\right)}_{\text{all received power is dedicated for energy harvesting}} \Bigg\}, \tag{6.7}$$

where channel power gain is canceled due to the fact that $\mathbb{E}\{h\} = 1$. Then, by applying the Campbell's theorem [25], we have

$$\begin{aligned} &\mathbb{E}\left\{\textstyle\sum_{x_i \in \Phi_b^{\setminus x_o}} \frac{P_b G_i}{r_i^{\alpha_c}}\right\} \\ &= \int_{r_o}^{\infty} \mathbb{E}_{G_i}\{P_b G_i r^{-\alpha_c}\} 2\pi\lambda_b r \mathrm{d}r = \frac{2P_b G_m p_m \pi \lambda_b r_o^{2-\alpha_c}}{\alpha_c - 2} + \frac{2P_b G_s p_s \pi \lambda_b r_o^{2-\alpha_c}}{\alpha_c - 2}. \end{aligned} \tag{6.8}$$

Then, by substituting (6.8) into (6.7) and by evaluating the expectation over r_o, the final results in Lemma 6.2 is derived. □

Based on the closed-form expressions obtained in Lemma 6.2, we can observe that the EH performance of the sensors depends on multiple factors, such as the density of BSs, and the number of sensors associated with single BS, etc. In specific, the increase of BSs' density leads to improved EH performance. This can be explained by the fact that the increased density of BSs offers a dual advantage. Firstly, it provides more access points for energy harvesting, allowing sensors to maintain stronger connections and harvest more energy from the signals they receive; while secondly, it leads to the increase of interference which can be harvested by each sensor.

Given that the number of sensors served by a BS, i.e. N, significantly impacts the performance of the sensors, we delve into the distribution of N. The analytical expression for the probability mass function (PMF) of N is presented in the following lemma.

Lemma 6.3. *The PMF of the number of sensors served by a BS, i.e. N, is given by*

$$\begin{aligned} \mathbb{P}\{N = n\} \approx &\int_0^{\infty} \frac{\Gamma(n+\kappa(z))\lambda_s^n}{n!\theta(z)^{\kappa(z)}\Gamma(\kappa(z))} \left(\frac{\theta(z)}{1+\lambda_s\theta(z)}\right)^{\kappa(z)+n} \\ &\times \frac{K^K z^{K-1}\lambda_b^K \exp(-Kz\lambda_b)}{\Gamma(K)}\mathrm{d}z, \end{aligned} \tag{6.9}$$

where $n = 0, 1, 2, ...$, $\kappa(z) = \frac{3\pi^{3/2}\mu_l\sqrt{z}}{16}$, $\theta(z) = \frac{16\sqrt{z}}{3\pi^{3/2}}$ and $K = 3.5$.

Yuan Guo

Proof. Without loss of generality, we focus on the PMF of the number of sensors associated with the typical BS, which is located at the origin. Since all sensors are deployed on roadways, the number of sensors served by the typical BS is directly related to the total length of roadways within the typical cell, denoted by L. Although the exact and approximated distributions of L were presented in [111], those expressions lead to high-complexity analysis and low computationally efficient. In what follows, we apply a moment-matching approach, offering a tight approximation that substantially lowers the computational complexity.

Note that the locations of cellular BSs are independent of the road networks. Therefore, by conditioning on that the area of typical cell is Z, we initially evaluate the conditional expectation and variance of L, i.e. $\mathbb{E}\{L_{|Z}\}$ and $\mathbb{V}\{L_{|Z}\}$, respectively. Since that μ_l represents the length of roads per unit area, it follows that $\mathbb{E}\{L_{|Z}\} = \mu_l Z$. Further, applying the Eve's law [112], we obtain the following:

$$\mathbb{V}\{L_{|Z}\} = \mathbb{E}\big\{\mathbb{V}\{L_{|Z} \mid N_{|Z}\}\big\} + \mathbb{V}\big\{\mathbb{E}\{L_{|Z} \mid N_{|Z}\}\big\}, \tag{6.10}$$

where $N_{|Z}$ is the number of roads intersecting the typical cell. Let L_i denote the length of intersection for the i-th road. By replacing $L_{|Z}$ with $L_{|Z} = \sum_{i=1}^{N_{|Z}} L_i$, the equation for variance transforms as follows:

$$\mathbb{V}\{L_{|Z}\} = \underbrace{\mathbb{E}\left\{\mathbb{V}\left\{\sum_{i=1}^{N_{|Z}} L_i \mid N_{|Z}\right\}\right\}}_{V_1} + \underbrace{\mathbb{V}\left\{\mathbb{E}\left\{\sum_{i=1}^{N_{|Z}} L_i \mid N_{|Z}\right\}\right\}}_{V_2}. \tag{6.11}$$

Note that this formulation segregates the variance into two parts: V_1, the expected variance of the sum of intersection lengths given the number of intersecting roads, and V_2, the variance of the expected sum of intersection lengths for a given number of intersecting roads. Since L_i and L_j for $i \neq j$ are independent, we have

$$V_1 = \mathbb{E}\left\{N_{|Z}\right\} \mathbb{V}\left\{L_i\right\}. \tag{6.12}$$

Furthermore, $\mathbb{E}\left\{\sum_{i=1}^{N_{|Z}} L_i \mid N_{|Z}\right\}$ is simply $N_{|Z}\mathbb{E}\left\{L_i\right\}$ and thus,

$$V_2 = \mathbb{V}\left\{N_{|Z}\right\} \mathbb{E}\left\{L_i\right\}^2. \tag{6.13}$$

Since $N_{|Z}$ follows the Poisson distribution for a given Z, this implies $\mathbb{E}\{N_{|Z}\} = \mathbb{V}\{N_{|Z}\} = 2\mu_l\sqrt{\frac{Z}{\pi}}$ [25]. Then, by substituting V_1 and V_2 into (6.11), we have

$$\mathbb{V}\{L_{|Z}\} = 2\mu_l\sqrt{\frac{Z}{\pi}}\left(\mathbb{V}\left\{L_i\right\} + \mathbb{E}\left\{L_i\right\}^2\right) = 2\mu_l\sqrt{\frac{Z}{\pi}}\mathbb{E}\left\{L_i^2\right\}, \tag{6.14}$$

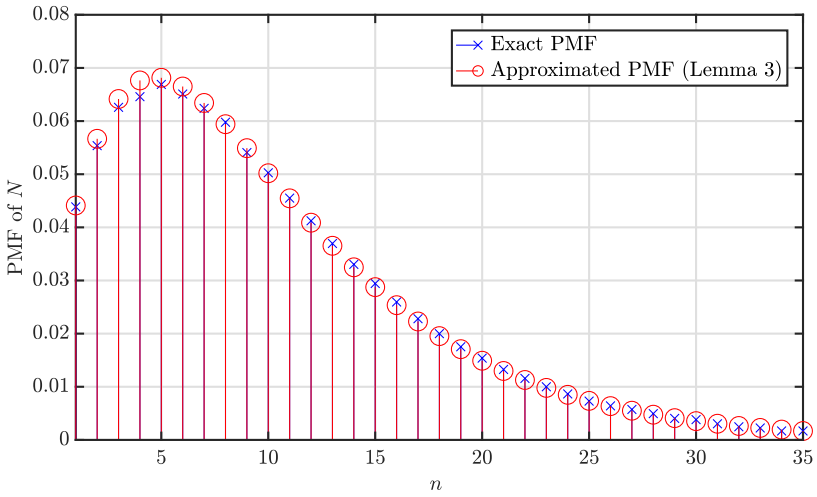

Figure 6.2: The exact and approximated PMF for the number of sensors associated with a BS.

where the second moment of L_i is calculated as

$$\mathbb{E}\left\{L_i^2\right\} = \int_0^{\sqrt{Z/\pi}} 4(Z/\pi - x^2)\frac{1}{\sqrt{Z/\pi}}\mathrm{d}x = \frac{8Z}{3\pi}. \tag{6.15}$$

Then, utilizing the moment-matching technique, we approximate the distribution of $L_{|Z}$ with a gamma distribution. The shape and scale parameters of this distribution are given by

$$\kappa(Z) = \frac{\mathbb{E}\{L_{|Z}\}^2}{\mathbb{V}\{L_{|Z}\}}, \quad \text{and} \quad \theta(Z) = \frac{\mathbb{V}\{L_{|Z}\}}{\mathbb{E}\{L_{|Z}\}}. \tag{6.16}$$

Further, given that the distribution of sensors on each roadway follows a 1D PPP, the PMF of the number of sensors associated with the typical BS is computed as

$$\mathbb{P}\{N = n\} = E_Z\left\{\int_0^{\infty} (\lambda_s L)^n \frac{\exp(-\lambda_s L)}{n!} f_{L_{|Z}}(L)\mathrm{d}L\right\}, \tag{6.17}$$

where

$$f_{L_{|Z}}(L) = \frac{L^{\kappa(Z)-1}}{\theta(Z)^{\kappa(Z)}\Gamma(\kappa(Z))}\exp\left(-\frac{L}{\theta(Z)}\right). \tag{6.18}$$

Finally, by evaluating the expectation over Z, of which the PDF is given by [89]

$$f_Z(z) = \frac{K^K z^{K-1}\lambda_b^K \exp(-Kz\lambda_b)}{\Gamma(K)}, \tag{6.19}$$

the results in Lemma 6.3 is obtained. □

It is worth highlighting that the PMF of N presented in Lemma 6.3 offers significantly lower computational complexity compared to the approach adopted in [111].

Yuan Guo

This simplification, involving a single integral that can be easily evaluated using numerical methods, enables the analytical tractability of sophisticated performance metrics. The accuracy of the approximation is illustrated in Fig. 6.2, which achieves a good match with exact PMF. Leveraging the results of Lemmas 6.3, two valuable insights are provided in the following remarks.

Remark 6.1. *The average number of sensors associated with a BS is given by* $\mathbb{E}\{N\} = \lambda_s \mu_l / \lambda_b$.

Remark 6.1 indicates that the average number of sensors is a function of three system parameters, i.e. the density of sensors, roadways and the BSs. This can be used for quickly estimating the average duration of the transmission time-slot, which are crucial for overall performance achieved in the considered vehicular networks. In following remark, we evaluate the transmit power of a sensor.

Remark 6.2. *Conditioning on the scenario where N sensors are associated with a BS, the transmit power of the sensor is given by*

$$P_s(N) = \frac{\mathcal{E}(N)}{\mathcal{A}(\beta, N)(1-\tau)}. \tag{6.20}$$

Proof. Given that each sensor utilizes harvested energy for signal transmission, the transmitter power is adjusted such that the average energy transmitted equates to the average harvested energy. Additionally, the active probability of a sensor is given by $\mathcal{A}(\beta, N)$, and thus we have

$$\mathcal{E}(N) - P_s(N)(1-\tau)\mathcal{A}(\beta, N) = 0. \tag{6.21}$$

By solving above equation for $P_s(N)$, the result in Remark 6.2 is obtained. □

6.3.2 Downlink performance achieved by vehicles

In order to assess the achievable performance of individual vehicles, we commence by examining the distribution of the number of vehicles associated with each sensor, i.e. M. Specifically, the closed-form expression for the PMF of M is provided in the following lemma.

Lemma 6.4. *The PMF of the number of vehicles associated with a sensor, i.e. M, is given by*

$$\mathbb{P}\{M = m\} = \frac{4\lambda_v^m \lambda_s^2 (m+1)}{(2\lambda_s + \lambda_v)^{m+2}}, \tag{6.22}$$

where $m = 0, 1, 2, 3, \ldots$.

Proof. We initially assess the conditional probability that m vehicles are associated with a sensor, given that the sensor's coverage range is W. Since the locations of vehicles follow an 1-D PPP, the probability of m vehicles located within the length W is given by

$$\mathbb{P}\{M = m|W\} = \frac{(W\lambda_v)^m \exp(-W\lambda_v)}{m!}. \tag{6.23}$$

Recall that each vehicle is associated with its closest sensor on the same road. Therefore, the coverage area of a sensor can be defined as the mid-point between its adjacent sensors. Specifically, the coverage length of a sensor is calculated as the sum of the distances to its immediate left and right neighboring sensors, divided by two. Hence, the CDF of W is computed as

$$\begin{aligned} F_W(w) =& \mathbb{P}\{W \leq w\} = 1 - \mathbb{P}\{2W > 2w\} \\ =& 1 - \exp(-2w\lambda_s) - 2w\lambda_s \exp(-2w\lambda_s). \end{aligned} \tag{6.24}$$

By taking the first-order derivative with respect to w, the PDF of W is obtained, i.e.

$$f_W(w) = 4\lambda_s^2 w \exp(-2\lambda_s w). \tag{6.25}$$

Then, by taking the expectation of (6.23) over W, we have

$$\mathbb{P}\{M = m\} = \int_0^\infty \frac{(W\lambda_v)^m \exp(-W\lambda_v)}{m!} f_W(W)\mathrm{d}W. \tag{6.26}$$

Finally, by solving the above integral with the assistance of the expression in [91, 3.326], the final result in Lemma 6.4 is derived. □

Based on (6.22), it can be observed that the probability of a sensor being associated with a large number of vehicles decreases with increasing vehicle density. The expectation of M is provided in following remark.

Remark 6.3. *The average number of vehicles associated with a sensor is given by* $\mathbb{E}\{M\} = \lambda_v/\lambda_s$

We now state the main result of this work, namely, the ID success probability achieved by a vehicle, which is defined as the probability that the decoded information by a vehicle per unit time exceeds a pre-defined threshold, γ bits. The analytical expression for the ID success probability is presented in the following theorem.

Theorem 6.1. *The ID success probability achieved by a vehicle is given by*

$$\mathcal{P}_{\mathrm{ID}}(\gamma) = \sum_{n=1}^{\infty} \sum_{m=1}^{\infty} \mathbb{P}\{N = n-1\}\mathbb{P}\{M = m-1\}\mathcal{A}(\beta, n)\varphi(n, m, \gamma), \tag{6.27}$$

Table 6.1: Simulation Parameters.

Parameters	**Values**
Intensity of Φ_b	$\lambda_b = 1\ \text{km}^{-2}$
Intensity of Φ_s	$\lambda_s = 2\ \text{km}^{-1}$
Intensity of Φ_v	$\lambda_v = \{10, 30, 50\}\ \text{km}^{-1}$
Intensity of Φ_l	$\mu_l = 5\ \text{km}^{-1}$
Transmit power of BS	$P_b = 45$ dB
Beamwidth of cellular BSs	45^o
Main-lobe array gain of BS	$G_m = 13.217$ dBm
Side-lobe array gain of BS	$G_s = -6.783$ dB
Bandwidth of cellular networks	$B_c = 25$ MHz
Bandwidth of the vehicular networks	$B_v = 15$ kHZ
Power splitting parameter	$\rho = 0.5$
Time splitting parameter	$\tau = 0.8$
Thermal noise power	$\sigma_c^2 = -70$ dBm, $\sigma_v^2 = -94$ dBm
Energy harvesting efficiency	$\eta = 0.7$
Path-loss exponent	$\alpha_c = 4$, $\alpha_v = 4$
Threshold of control information	$\beta = 10$ bits

where

$$\varphi(n, m, \gamma) = \int_0^\infty \exp\left(-\frac{\sigma_v^2 r^{\alpha_v}(2^{\frac{m\gamma}{B_v(1-\tau)}} - 1)}{P_s(n)} - 2r\lambda_s\right) 2\lambda_s \mathrm{d}r \tag{6.28}$$

B_v is the communication bandwidth.

Proof. By conditioning on N, M, and the serving sensor is active, the ID success

Yuan Guo

probability achieved by a vehicle is computed as

$$\begin{aligned}
&\mathcal{P}_{\mathrm{ID}}(\gamma \mid N=n \,\&\, M=m \,\&\, \text{the nearest sensor is active}) \\
=&\mathbb{P}\left\{\frac{B_v(1-\tau)}{m}\log_2\left(1+\frac{P_s(n)gr^{-\alpha_v}}{\sigma_v^2}\right)\geq\gamma\right\} \\
=&\mathbb{P}\left\{g\geq\frac{\sigma_v^2 r^{\alpha_v}}{P_s(n)}\left(2^{\frac{m\gamma}{B_v(1-\tau)}}-1\right)\right\} \\
=&\int_0^\infty \exp\left(-\frac{\sigma_v^2 r^{\alpha_v}}{P_s(n)}\left(2^{\frac{m\gamma}{B_v(1-\tau)}}-1\right)\right)2\lambda_s\exp(-2r\lambda_s)\mathrm{d}r.
\end{aligned} \tag{6.29}$$

Then, by multiplying the active probability of the sensor and by applying the law of total probability, the final result in Theorem 6.1 is proven. □

From the results presented in Theorem 6.1, we can observe that several critical system parameters effect the ID success probability achieved by a vehicle. It is significant to carefully design and adjust the system parameters to achieve the high performance, while the optimal sensors' density and time-splitting factor that maximize the ID success probability is illustrated in Section

6.4 Numerical results

We present analytical and simulation results to illustrate the impact of system parameters on the key performance metrics, and to find the optimal values to maximize the performance of the considered vehicular networks. Unless otherwise stated, we use the parameters given in Table 6.1. It is worth mentioning that, the proposed analytical framework is generic, and the selection for these parameter values is for the purpose of illustration.

Fig. 6.3 illustrates the impact of the number of sensors and the time splitting factor on the active probability achieved by the sensor. In specific, Fig. 6.3 plots the active probability versus the number of sensors associated with a BS, for different information threshold, i.e. β, and under varying time splitting factors, i.e. $\tau \in \{0.2, 0.4, 0.8\}$. We can observe that the active probability increases with a higher τ for a given N. This is because a larger proportion of time is allocated for information transferring from the BS to sensors, thus enhancing the active probability. Moreover, it can be observed that as the number of sensors associated with a BS rises, the active probability for each sensor diminishes, which is due to the increased competition for limited time resources. Further, we can also observe that this decrease in

Yuan Guo

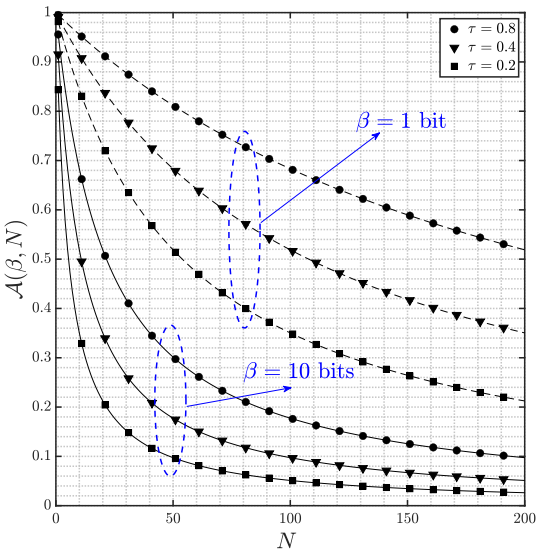

Figure 6.3: Active probability versus the number of sensor served by a BS.

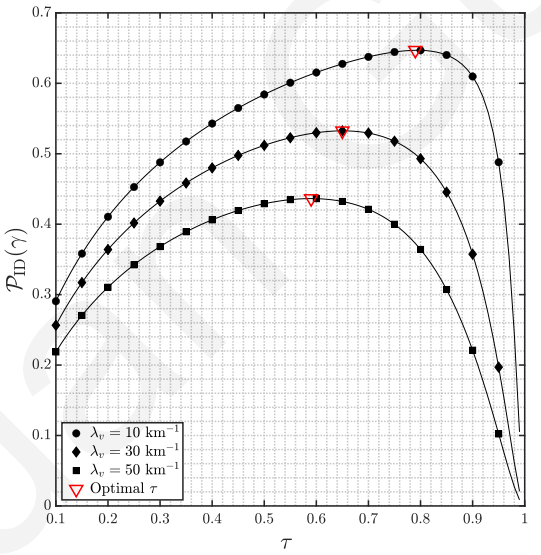

Figure 6.4: ID success probability versus the time splitting parameter, where $\gamma = 1$k bits.

active probability with more sensors is mitigated by a higher τ. Finally, a higher information threshold (β) corresponds to lower overall active probabilities, implying that more stringent data requirements exacerbate the challenges of maintaining sensor activity.

Fig. 6.4 shows the impact of time splitting parameter on the network performance, under various vehicle densities. Specifically, Fig. 6.4 plots the ID success probability versus the time splitting parameter, with vehicles density $\lambda_v \in$

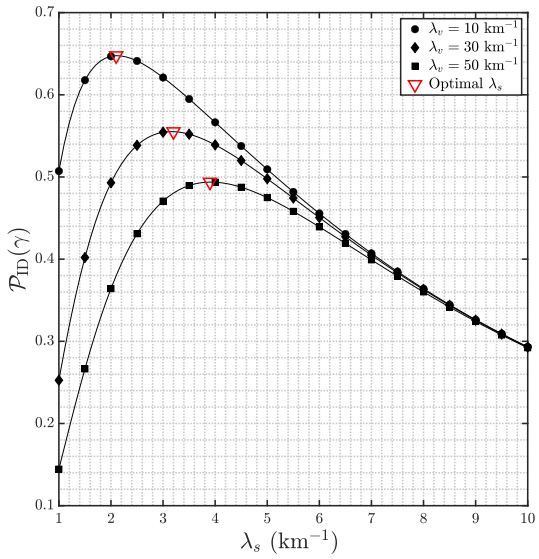

Figure 6.5: ID success probability versus the density of sensors, where $\gamma = 1$k bits.

$\{10, 30, 50\}$ /km. We can easily observe that the ID success probability initially ascends with an increase in τ, and subsequently descends across all vehicle densities. The ascent reflects the enhanced reception of power and control information by the sensors from the BS during the first fraction of the time, thereby improving their ability to communicate with vehicles. However, beyond the optimal τ, an excessive allocation of time to the BSs leaves inadequate time for sensors to effectively transmit data to vehicles. The shift of the optimal τ towards lower values as vehicle density increases. This can be explained based on the fact that, in more congested traffic conditions, it is more beneficial to allocate a greater portion of time for sensor-to-vehicle communication to ensure that the increased number of vehicles can be adequately served.

Fig. 6.5 illustrates the impact of sensors' density on the ID performance achieved by vehicles, with different traffic situations. In specific, Fig. 6.5 plots the ID success probability versus the density of sensors, for different density of vehicles, i.e. $\lambda_v \in \{10, 30, 50\}$ /km. We can observe that as sensor density increases, the ID success probability initially increases, reaches an optimal point, and then decreases, for any density of vehicles. This can be explained by the fact that, a higher density of sensors leads to shorter time-slot dedicated to each sensor, due to the increased number of sensors served by each BS, limiting the efficiency of information and power transfer from BSs to sensors. However, an increased density of sensors is beneficial for the information transfer from each sensor to vehicles, i.e. vehicles is likely

Yuan Guo

to be closer to a sensor, receiving stronger signals. Therefore, the initial increase in ID success probability reflects the improved sensor-to-vehicle communication, while the subsequent decline beyond the peak points to the constraints in the BS-to-sensor communication phase, highlighting a critical trade-off in the network design. Another interesting observation is that, in crowded traffic scenarios, as indicated by higher vehicle densities, i.e. λ_v, the optimal sensor density shifts to a higher value, which suggests that in more congested environments, the network benefits from a greater number of sensors. This is because, with more vehicles present, having additional sensors improves the probability of each vehicle being in closer proximity to a sensor, thus enhancing the efficacy of sensor-to-vehicle communication.

6.5 Summary

In this chapter, we present a novel analytical framework for investigating the performance of SWIPT-assisted vehicular networks. More specifically, by applying the SWIPT technology, battery-operated sensors simultaneously receive control information and harvest energy from the cellular networks, and then transmit data to vehicles by using the harvested energy. By leveraging stochastic geometry tools, we derive the analytical expressions for several key performance metrics, such as the active probability and the average harvested energy of sensors, as well as the ID coverage probability achieved by vehicles, etc. Our comprehensive analysis has demonstrated the significant impact of system parameters such as the density of sensors, the time splitting factor, and the information threshold in optimizing the performance of vehicular networks. Moreover, the optimal density of sensors and time splitting factor, that maximize ID success probability across various vehicle densities have been illustrated. Notably, the optimal sensor density is found to be dynamic, shifting in response to traffic congestion levels. These insights contribute to the design of more efficient and reliable vehicular networks, ensuring robust sensor-to-vehicle communication in increasingly complex and demanding traffic scenarios.

The integration of SWIPT technology in vehicular networks not only enhances the sustainability of roadside sensors by ensuring a continuous power supply but also facilitates reliable data communication crucial for advanced vehicular applications. This system shows promise for a wide range of applications, from real-

Yuan Guo

time traffic management and autonomous driving to emergency vehicle notification systems and dynamic road condition monitoring. The ability to sustain sensor operations without the need for frequent battery replacements or wired power sources significantly increases the feasibility of deploying a dense network of sensors, thereby supporting the high granularity of data required for these applications. Furthermore, the adaptability of sensor density and time splitting factors in response to varying traffic conditions underscores the system's capability to meet the demands of dynamic vehicular environments, ensuring that the network remains robust and efficient under different traffic scenarios. This adaptability, combined with the demonstrated impact of system parameters on network performance, highlights the practicality of implementing SWIPT-assisted vehicular networks in real-world settings, paving the way for safer, more efficient, and intelligent transportation systems.

Yuan Guo

Chapter 7

LEO satellite-based non-terrestrial heterogeneous networks

In this chapter, we investigate the large-scale heterogeneous LEO satellite networks in the context of three association schemes. In contrast to existing studies, which typically assume a single-tier LEO satellite-based network, the developed framework captures the heterogeneous nature of real-world satellite network deployments. More specifically, we investigate a multi-tier LEO satellite-based network, where different tiers of LEO satellites are modelled by multiple independent Poisson point processes, and each tier differs in density, transmit power and altitude. We propose three association schemes for the considered network topology based on: 1) the Euclidean distance, 2) the averaged received power, and 3) a random selection. We establish a tractable framework for evaluating the performance of the considered network deployments in the context of the proposed association schemes, in terms of the association probability, downlink coverage probability and spectral efficiency.

7.1 Motivation and contributions

Recently, stochastic geometry has been leveraged to analyse the performance of large-scale LEO satellite-based communication systems, highlighting its effectiveness as a powerful and tractable mathematical tool for assessing the impact of key parameters on network performance [51, 55, 57, 82, 83]. Nevertheless, these studies highlight the potential of stochastic geometry in modelling large-scale LEO satellite-based networks, which typically focus on the assumption that all LEO satellites are

Yuan Guo

deployed at the same altitude. In contrast, real-world LEO satellite-based networks exhibit significant heterogeneity, featuring satellites deployed at varying altitudes, transmitting signals with different power levels, and possessing diverse spatial densities [51, 52, 81]. In light of the heterogeneity present in large-scale LEO satellite-based networks, the association scheme is of paramount importance, as it directly influences key aspects of network performance, such as coverage probability and data rate. Various association schemes for the conventional terrestrial networks have been extensively explored in the literature, which typically focus on connecting users to the most suitable BSs based on the contact distance, cell area, received signal strength, or other quality of service metrics [58, 113]. However, the efficient association schemes for the large-scale heterogeneous LEO satellite networks are overlooked in the current literature, while the majority of works that investigate the massive LEO satellite networks either ignore the heterogeneity or assume a simplistic distance-based association scheme [54, 55, 57, 82, 83]. This is mainly due to the challenges arising from varying altitudes of multi-tier LEO satellites [114]. More specifically, unlike conventional terrestrial networks, where the height of BSs' antennas is typically ignored in the analysis, the altitude difference between multi-tier LEO satellites is a critical factor that has to be considered, since the varying altitudes directly impact the coverage area and signal strength. Such diverse altitudes of LEO satellite networks lead to much higher complexity in designing association schemes and analysing the corresponding network performance.

Motivated by the above discussion, in this chapter, we focus on modelling the heterogeneity of LEO satellite-based networks. The main contributions are summarized as follows:

- We develop an analytical framework based on stochastic geometry, which sheds light on the modelling and analysing large-scale heterogeneous LEO satellite networks. In particular, the developed framework takes into account the heterogeneity of large-scale LEO satellite networks, which involves deploying different tiers of satellites at various altitudes with varying transmit power and density. Moreover, we adopt multiple independent random point processes for modelling the spatial deployments of multi-tier LEO satellites and study the performance of the considered networks from a macroscopic point-of-view.

Yuan Guo

- We propose two association schemes for the considered LEO satellite networks. Specifically, the proposed schemes are designed based on the Euclidean distance and the average received power, respectively; while a random tier selection-based association is also introduced as a benchmark scheme. The achieved performance by each association scheme is evaluated in terms of association probability, coverage probability and spectral efficiency.

- By leveraging tools from stochastic geometry, we derive the analytical expressions for the association probability, coverage probability and spectral efficiency, by taking into account the existence of inter-cell interference. Moreover, in order to reveal the fading impact on the network performance, we further assess the downlink performance in two distinct scenarios, namely, Rayleigh fading and non-fading environments, while expressions for the corresponding performance metrics are analytically derived.

- Our results show that the fading channel, the altitude, the number of satellites, and the transmit power of LEO satellites significantly affect the coverage probability and spectral efficiency. In specific, we demonstrate that the existence of multipath fading channels results in a degraded coverage probability in low SINR regimes, while surpassing non-fading scenarios in high SINR situations. Moreover, the average power-based association scheme consistently outperforms the distance- and random selection-based schemes across various scenarios. Furthermore, as the number of LEO satellites increases, the random selection-based scheme surpasses the distance-based scheme due to the efficient utilization of LEO satellites from higher altitude tiers that typically have larger transmit power. Finally, we demonstrate that greater path-loss results in reduced spectral efficiency, and increasing transmit power initially elevates spectral efficiency, but levels off due to the increased interference from neighbouring satellites.

7.2 System model

We consider a multi-tier constellation setup described in Section 2.2.2. Let $x_{i,k}$ denote the location of the i-th LEO satellite that belongs to the k-th tier constellation, and $r_{i,k}$ represent the Euclidean distance from this LEO satellite to the typical gUE.

Yuan Guo

Additionally, let $x_{0,k}$ with $1 \leq k \leq K$ depict the locations of the closest LEO satellites to the typical gUE from each tier constellation. Since the communication between the LEO satellites and the gUEs mainly refers to the LoS transmission, i.e. a gUE can only receives signals from the LEO satellites above its local horizon, the maximum distance between a gUE and a visible LEO satellite that belongs to the k-th tier constellation is given by $R_{\max_k} = \sqrt{H_k^2 + 2H_k R_{\oplus}}$. Regarding the antenna directionality of LEO satellites and gUEs, we adopt a sectorized antenna model. This approach provides a suitable approximation of the actual beam pattern while maintaining adequate accuracy for analysis purposes. Specifically, the antenna array gain of the LEO satellites that belongs in the k-th tier is given by $G_k^L = \{G_{m,k}^L, G_{s,k}^L\}$, where $G_{m,k}^L$ and $G_{s,k}^L$ represent the main- and the side-lobe gains of LEO satellites' antenna, respectively. Similarly, the antenna array gain of a gUE is characterized by the two discrete values, i.e. the main-lobe gain G_m^U and the side-lobe gain G_s^U. Furthermore, we assume that the receiving beam is perfectly aligned with the antenna boresight of the serving satellite, while being misaligned with those of interfering satellites [115]. It is worth mentioning that, although interfering satellites may also be aligned with the received antenna's boresight with a small probability, the employment of such assumption offers a tractable analysis for the considered large-scale LEO satellite networks. Therefore, the antenna array gain of the intended link between the typical gUE and its serving LEO satellite is maximized to $G_{m,k}^L G_m^U$; while the antenna array gain for the interfering links can be expressed as $G_{s,j}^L G_s^U$.

The altitudes of LEO satellites have a significant impact on the downlink network performance, e.g. higher altitudes of LEO satellites typically result in longer propagation distances of wireless signals, degrading the received signal quality at the gUEs. Hence, a power adjusting mechanism is assumed to be employed by the LEO satellites, such that the LEO satellites located at higher altitudes can achieve a larger effective isotropic radiated power to compensate for the sever path-loss effect [116]. More specifically, we assume that by properly adjusting the transmit power of the LEO satellites according to their altitudes, the maximum achievable received signal power at the typical gUE from each tier LEO satellites are identical, i.e.

$$\frac{P_k G_{m,k}^L}{H_k^{\alpha}} = \frac{P_j G_{m,j}^L}{H_j^{\alpha}}, \ \forall\, 1 \leq j,k \leq K, \tag{7.1}$$

where P_k is the transmit power of the k-th tier LEO satellites. It is worth mentioning

that the adopted power adjusting mechanism not only captures the heterogeneity of multi-tier LEO satellite networks but also facilitates the analytical tractability of the developed framework for evaluating the performance of large-scale LEO satellite-based networks.

7.3 Association schemes LEO satellite networks

The proposed association schemes for the considered large-scale heterogeneous LEO satellite networks are executed through a two-stage process. The first stage is the same for all association schemes. More specifically, in the first stage process, K LEO satellites are selected into the set of candidate LEO satellites; while in the second stage, the serving LEO satellite is selected from the set of candidate LEO satellites, based on the Euclidean distance, the average received power, or the random selection. In what follows, we describe the detailed procedures of each proposed association scheme.

7.3.1 The distance-based association (DbA) scheme

The first association scheme is designed based on the Euclidean distance between the typical gUE and the LEO satellites. In specific, by aiming to minimize the path-loss between a gUE and its serving LEO satellite, the proposed DbA scheme enables each gUE to select and communicate with its nearest LEO satellite to maintain an acceptable received signal quality. Therefore, in the first stage of the DbA scheme, the nearest LEO satellites to the typical gUE from each tier are selected into the set of candidate LEO satellites, i.e. $\mathcal{C} = \{x_{0,1}, \cdots, x_{0,k}, \cdots, x_{0,K}\}$. Then in the second stage, the typical gUE selects the closest LEO satellite from the set of candidate LEO satellites as the serving satellite, e.g. $x_{0,k} = \arg\min_{x_{0,j} \in \mathcal{C}} \|x_{0,j}\|$, that denotes the case where the typical gUE is associated with the k-th tier LEO satellite. It is worth mentioning that the proposed DbA scheme is a low-complexity scheme, since the gUEs only requires the information about the relative position of the LEO satellites in order to make the selection, which can be easily obtained via the global positioning system (GPS) [117].

Yuan Guo

7.3.2 The power-based association (PbA) scheme

The second proposed association scheme, namely PbA scheme, takes into consideration of the average received signal power at the gUEs. In specific, the PbA scheme associates a gUE with the LEO satellite that provides the highest average signal power observed at the gUE. Note that LEO satellites which belong in the same tier have identical transmit power and antenna array gain, and thus the nearest one to the gUE provides the strongest average signal received by the gUE. Hence, the candidate LEO satellites are same as that of the DbA scheme, i.e. $\mathcal{C} = \{x_{0,1}, \cdots, x_{0,k}, \cdots, x_{0,K}\}$. Then, in the second stage, the serving LEO satellite is selected among the set of candidate LEO satellites, which provides the highest average received signal power observed at the gUE, e.g. $x_{0,k} = \arg\max_{x_{0,j} \in \mathcal{C}} \mathbb{E}\left\{h_{0,j} P_j G^L_{m,j} G^U_m r^{-\alpha}_{0,j}\right\}$, that denotes the case where the typical gUE is associated with the k-th tier LEO satellite.

7.3.3 The random selection-based association (RbA) scheme

The third association scheme, namely RbA scheme, is based on a random tier selection. More specifically, the RbA scheme enables a gUE to randomly associate with one tier network and to communicate with the closest LEO satellite that belongs to this tier. In specific, the first stage process of the RbA scheme is same as that of the DbA and PbA schemes, i.e. the set of candidate LEO satellites which contains the closest LEO satellites to the typical gUE from each tier, are pre-selected from all LEO satellites. In the second stage, the typical gUE randomly selects one serving LEO satellite among the set of candidate LEO satellites. It should be noted that the RbA scheme does not requires any operations of comparing the distance and/or received power of the candidate LEO satellites, and thus corresponds to a low implementation complexity. Therefore, it is appropriate for the various IoT devices which typically have limited power/computation constraints.

7.4 Association probability analysis

In this section, we present a detailed analysis of the association probability for each scheme introduced in Section 7.3. More specifically, the association probability denotes the probability of a gUE being associated with each tier of LEO satellites,

Yuan Guo

which is essential for analysing the performance of large-scale heterogeneous LEO satellite networks. By leveraging tools from stochastic geometry, the expressions of the association probability for all proposed association schemes are analytically in the following sections.

7.4.1 Association probability for the DbA scheme

We first evaluate the association probability of the DbA scheme. As the DbA scheme relies on the Euclidean distance, we begin by analysing the statistical properties of the distance between the typical gUE and the candidate LEO satellites. Specifically, we assess the distribution of the distance between the typical gUE and its nearest LEO satellite from each tier (i.e. candidate LEO satellites), while the pdf of $r_{0,k}$ for $1 \leq k \leq K$, is evaluated in the following lemma.

Lemma 7.1. *The pdf of the distance between the typical gUE and its k-th candidate LEO satellite is given by*

$$f_D(r, \lambda_k, H_k) = \frac{2\pi\lambda_k r(R_\oplus + H_k)}{R_\oplus} \exp\left(-\frac{\pi\lambda_k(R_\oplus + H_k)(r^2 - H_k^2)}{R_\oplus}\right), \tag{7.2}$$

where $H_k \leq r < R_{\max_k}$.

Proof. The proof follows a similar approach as [55]. We first compute the cdf of $r_{0,k}$ based on the null probability of PPP [25], i.e.

$$F_D(r, \lambda_k, H_k) = \mathbb{P}\{r_{0,k} \leq r\} = 1 - \mathbb{P}\{r_{0,k} > r\} = 1 - \exp\left(-\lambda_k R(r, H_k)\right), \tag{7.3}$$

where $R(r, H_k)$ represents the area of the spherical dome as shown in Fig. 7.1, which is given by

$$R(r, H_k) = \frac{\pi(r^2 - H_k^2)(R_\oplus + H_k)}{R_\oplus}.$$

Finally, by taking the derivative of $F_D(r, \lambda_k, H_k)$ with respect to r, i.e. $f_D(r, \lambda_k, H_k) = \frac{\partial}{\partial r} F_D(r, \lambda_k, H_k)$, the final expression in Lemma 7.1 is derived. □

It is worth emphasizing that while several previous studies have focused on deriving the Earth-centered zenith angle distribution for investigating single-tier LEO satellite-based networks[1], the distance distribution presented in Lemma 7.1 is

[1]For a single-tier LEO satellite network, the distance between a gUE and a LEO satellite can be uniquely determined by the Earth-centered zenith angle [51, 52, 55, 57].

Yuan Guo

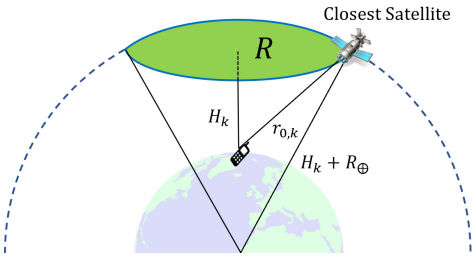

Figure 7.1: The closest LEO satellite of the k-th tier constellation.

a more general result that can be applied for analysing both single- and multi-tier LEO satellite networks. Then, based on the above results, we further examine the availability of LEO satellites for the considered large-scale LEO satellite networks in the following proposition.

Proposition 7.1. *For the considered large-scale LEO satellite networks, the probability of existing at least one k-th tier LEO satellite above the local horizon of the typical gUE is approximately equal to one, i.e.* $P^{\circ}(N_k, H_k) \approx 1$.

Proof. The probability that at least one k-th tier LEO satellite above the local horizon of the typical gUE is computed as

$$\begin{aligned} P^{\circ}(N_k, H_k) =& \int_{H_k}^{R_{\max_k}} f_D(r, \lambda_k, H_k) \mathrm{d}r \\ =& 1 - \exp\left(-\frac{\pi \lambda_k (R_\oplus + H_k)(R_{\max_k}^2 - H_k^2)}{R_\oplus} \right) \\ =& 1 - \exp\left(-\frac{N_k}{2\left(\frac{R_\oplus}{H_k} + 1\right)} \right). \end{aligned} \tag{7.4}$$

Note that $R_\oplus \approx 6371$ km, and the altitude of the LEO satellites, i.e. H_k, is typically from 500 km to 2000 km. Moreover, for the considered large-scale LEO satellite networks, each tier consists of several hundreds of LEO satellites, i.e. $N_k \gg 100$. Hence, the exponential term approaches to zero, i.e. $\exp\left(-\frac{N_k}{2\left(\frac{R_\oplus}{H_k}+1\right)} \right) \to 0$, and $P^{\circ}(N_k, H_k) \to 1$; while an intuitive evaluation of availability is illustrated in Figure. 7.2. □

Based on the discussion in Proposition 7.1, we exclude the extreme scenario where no LEO satellite exists above the local horizons of the gUEs throughout our analysis [55]. The accuracy of the adopted assumption is validated by our numerical and simulation results presented in Section 7.6. Then, by applying the result from

Yuan Guo

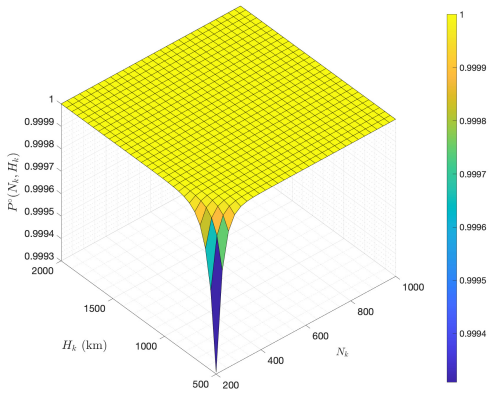

Figure 7.2: The available probability of LEO satellites versus the number and the altitudes of LEO satellites.

Lemma 7.1, we present the association probability for the DbA scheme, denoted as $\mathcal{A}_{D,k}$ in the following lemma.

Lemma 7.2. *When the DbA scheme is employed, the probability that the typical gUE is associated with the k-th tier is given by*

$$\mathcal{A}_{D,k} = \sum_{i=k}^{K} \int_{H_i}^{H_{i+1}} \frac{2\pi\lambda_k r(R_\oplus + H_k)}{R_\oplus} \prod_{j=1}^{i} \exp\left(-\frac{\pi\lambda_j (R_\oplus + H_j)(r^2 - H_j^2)}{R_\oplus}\right) \mathrm{d}r, \quad (7.5)$$

where $H_{K+1} = r_{\max_K}$.

Proof. By employing the DbA scheme, the probability that the typical gUE is associated with the k-th tier LEO satellite can be expressed as

$$\mathcal{A}_{D,k} = \mathbb{P}\left\{r_{0,k} < \min_{j,j\neq k} r_{0,j}\right\}. \quad (7.6)$$

Note that for the considered heterogeneous LEO satellites networks, $H_k \ll R_\oplus$, and thus it is easy to verify that $H_1 \leq H_2 \leq \cdots \leq H_K \leq R_{\max_1} \leq R_{\max_2} \leq \cdots \leq R_{\max_K}$. Hence, by applying the law of total probability and by denoting $R_{\max_K}$ by H_{K+1}, we can rewrite (7.6) as following

$$\mathcal{A}_{D,k} = \sum_{i=k}^{K} \mathbb{P}\left\{\min_{1\leq j\leq K, j\neq k} r_{0,j} > r_{0,k} \;\&\; H_i \leq r_{0,k} \leq H_{i+1}\right\}. \quad (7.7)$$

Upon observing that $r_{0,k} \leq \min_{1\leq j\leq K-i} r_{0,i+j}$ is valid for $H_i \leq r_{0,k} \leq H_{i+1}$, we can further simplify (7.7) as

$$\mathcal{A}_{D,k} = \sum_{i=k}^{K} \mathbb{P}\left\{\min_{1\leq j\leq i, j\neq k} r_{0,j} > r_{0,k} \;\&\; H_i \leq r_{0,k} \leq H_{i+1}\right\}. \quad (7.8)$$

Yuan Guo

Then, by noticing that $r_{0,j}$ and $r_{0,k}$, $\forall\ j \neq k$ are mutually independent, each term of the probability within (7.8) can be evaluated as

$$\begin{aligned}
&\mathbb{P}\left\{\min_{1\leq j\leq i, j\neq k} r_{0,j} > r_{0,k}\ \&\ H_i \leq r_{0,k} \leq H_{i+1}\right\} \\
&= \int_{H_i}^{H_{i+1}} \frac{\prod_{j=1}^{i} \exp\left(-\frac{\pi\lambda_j(R_\oplus+H_j)(r^2-H_j^2)}{R_\oplus}\right)}{\exp\left(-\frac{\pi\lambda_k(R_\oplus+H_k)(r^2-H_k^2)}{R_\oplus}\right)} f_D(r,\lambda_k,H_k)\mathrm{d}r \\
&= \int_{H_i}^{H_{i+1}} \prod_{j=1}^{i} \exp\left(-\frac{\pi\lambda_j(R_\oplus+H_j)(r^2-H_j^2)}{R_\oplus}\right) \frac{2\pi\lambda_k r(R_\oplus+H_k)}{R_\oplus}\mathrm{d}r,
\end{aligned} \tag{7.9}$$

where the last step is obtained by substituting the expression of $f_D(r,\lambda_k,H_k)$ and by cancelling out the common factors of the numerator and denominator. Hence, by substituting (7.9) into (7.8), the final result in Lemma 7.2 is derived. □

The results derived above provide valuable insights into the association probability of the DbA scheme and the complex interplay between various parameters that affect the network performance. More specifically, based on the analytical expression presented in Lemma 7.2, the association probability can be immediately determined for any given network parameters, including the number of tiers, the height of each LEO satellite tier, and the density of LEO satellites, while the exponential product term in (7.5) underscores the interdependence of each LEO satellite tier.

7.4.2 Association probability for the PbA scheme

We now focus on the association probability for the PbA scheme. Since the PbA scheme is a power-based scheme, our initial step is to evaluate the statistical properties of the average signal power received at the typical gUE from its nearest LEO satellite that belongs in the k-th tier, i.e. the k-th candidate LEO satellite. Let $\xi_{0,k}$ represent the average received signal power from the LEO satellite located at $x_{0,k}$. Note that $\xi_{0,k}$ is computed by taking the expectation over the channel power gain, i.e. $\xi_{0,k} = \bar{h}P_k G_{m,k}^L r_{0,k}^{-\alpha} G_m^U$, where $\bar{h}$ is the first-order moment of the channel power gain, i.e. $\bar{h} = (2b+\Omega)$ for the SR fading model [84]. In the following lemma, we provide the pdf of $\xi_{0,k}$, which is instrumental in assessing the association probability for the PbA scheme.

Lemma 7.3. *The pdf of the average received signal power at the typical gUE from its k-th candidate LEO satellite is given by*

$$\begin{aligned} &f_P(\xi, \lambda_k, H_k) \\ =&\frac{2\pi\lambda_k(R_\oplus + H_k)}{\xi\alpha R_\oplus}\left(\frac{\varrho_k}{\xi}\right)^{\frac{2}{\alpha}} \exp\left(-\frac{\pi\lambda_k(R_\oplus + H_k)}{R_\oplus}\left(\left(\frac{\varrho_k}{\xi}\right)^{\frac{2}{\alpha}} - H_k^2\right)\right), \end{aligned} \tag{7.10}$$

where $\varrho_k = \bar{h}P_k G_{m,k}^L G_m^U$, $\xi_{\min_k} < \xi \leq \xi_{\max_k}$, $\xi_{\min_k} = \varrho_k R_{\max_k}^{-\alpha}$ *and* $\xi_{\max_k} = \varrho_k H_k^{-\alpha}$.

Proof. To begin with, we evaluate the cdf of $\xi_{0,k}$ as following

$$\begin{aligned} F_P(\xi, \lambda_k, H_k) =&\mathbb{P}\{\xi_{0,k} \leq \xi\} = \mathbb{P}\{\bar{h}P_k G_{m,k}^L r_{0,k}^{-\alpha} G_m^U \leq \xi\} \\ =&1 - \mathbb{P}\left\{r_{0,k} < \left(\frac{\bar{h}P_k G_{m,k}^L G_m^U}{\xi}\right)^{\frac{1}{\alpha}}\right\}. \end{aligned} \tag{7.11}$$

Then by applying the cdf of $r_{0,k}$, which is given by (7.3), we have

$$F_P(\xi, \lambda_k, H_k) = 1 - \exp\left(-\pi\lambda_k \frac{R_\oplus + H_k}{R_\oplus}\left(\left(\frac{\bar{h}P_k G_{m,k}^L G_m^U}{\xi}\right)^{\frac{2}{\alpha}} - H_k^2\right)\right). \tag{7.12}$$

Finally, the pdf of $\xi_{0,k}$ is obtained by taking the derivative of $F_P(\xi, \lambda_k, H_k)$ with respect to ξ, i.e. $f_P(\xi, \lambda_k, H_k) = \frac{\partial}{\partial\xi} F_P(\xi, \lambda_k, H_k)$. □

It is worth emphasising that, while the distance distribution was utilized to analyze the performance of the DbA scheme in Section 7.4.1, the power distribution presented in Lemma 7.3 offers a more appropriate method for assessing the performance achieved by the PbA scheme. In particular, the average received signal power from candidate LEO satellites exhibits identical lower and upper bounds. More specifically, the minimum value of the average received signal power from any candidate LEO satellites approaches zero due to the extremely long communication distance, i.e., $\xi_{\min_k} \approx 0, \forall\, 1 \leq k \leq K$; whereas the maximum average received signal power from all candidate LEO satellites is also identical, i.e., $\xi_{\max_k} = \xi_{\max_j}$, $\forall\, 1 \leq j, k \leq K$, owing to the power adjusting mechanism. As a result, by applying the aforementioned lemma, the association probability for the PbA scheme is assessed in the subsequent lemma.

Lemma 7.4. *When the PbA scheme is employed, the probability that the typical gUE is*

associated with the k-th tier is given by

$$\begin{aligned}\mathcal{A}_{P,k} =& \frac{2\pi\lambda_k \varrho_k^{\frac{2}{\alpha}}(R_\oplus + H_k)}{\alpha R_\oplus} \times \\ & \int_{\xi_{\min_k}}^{\xi_{\max_k}} \left(\frac{1}{\xi}\right)^{\frac{2}{\alpha}+1} \prod_{j=1}^{K} \exp\left(-\frac{\pi\lambda_j(R_\oplus + H_j)}{R_\oplus}\left(\left(\frac{\varrho_k}{\xi}\right)^{\frac{2}{\alpha}} - H_j^2\right)\right) \mathrm{d}\xi.\end{aligned} \tag{7.13}$$

Proof. According to the procedure of the PbA scheme, the probability that the typical gUE is associated with the k-th tier LEO satellite is formulated as

$$\mathcal{A}_{P,k} = \mathbb{P}\left\{\xi_{0,k} > \max_{1\le j\le K, j\neq k} \xi_{0,j}\right\}. \tag{7.14}$$

The deployments of K tiers of LEO satellites follow K independent PPPs, which indicates that $\xi_{0,j}$ for $1 \le j \le K$ are mutually independent between each other. Hence, based on the order statistics [118], we can rewrite (7.14) as

$$\begin{aligned}\mathcal{A}_{P,k} =& \prod_{j=1, j\neq k}^{K} \mathbb{P}\left\{\xi_{0,k} > \xi_{0,j}\right\} \\ =& \mathbb{E}_{\xi_{0,k}}\left\{\prod_{j=1, j\neq k}^{K}\left(1 - F_P\left(\xi_{0,k}, \lambda_j, H_j\right)\right)\right\} \\ =& \mathbb{E}_{\xi_{0,k}}\left\{\prod_{j=1, j\neq k}^{K} \exp\left(-\pi\lambda_j \frac{R_\oplus + H_j}{R_\oplus}\left(\left(\frac{\bar{h}P_j G_{m,j}^L G_m^U}{\xi_{0,k}}\right)^{\frac{2}{\alpha}} - H_j^2\right)\right)\right\}.\end{aligned} \tag{7.15}$$

Finally, by evaluating the expectation over $\xi_{0,k}$, the result in Lemma 7.4 is derived. □

From the expression derived in above lemma, we can observe that the PbA scheme considers one extra parameter compared to the DbA scheme, i.e. the received signal power. Despite this, the analytical expression for the association probability of the PbA scheme has a more concise form than that of the DbA scheme, due to the employment of the power adjusting mechanism.

7.4.3 Association probability for the RbA scheme

Recall that the RbA enables a gUE to randomly select one LEO satellite among K candidate LEO satellites, following a uniform distribution. Hence, the probability of a gUE being associated with each tier is equal, i.e.

$$\mathcal{A}_{R,k} = \mathcal{A}_{R,j} = \frac{1}{K}, \ \forall\, 1 \le k, j \le K. \tag{7.16}$$

Yuan Guo

Till now we have evaluated the association probability for each proposed scheme. As we move forward, our focus will shit to the downlink performance achieved by employing these association schemes in next section.

7.5 Downlink performance of large-scale heterogeneous LEO satellite networks

In this section, we investigate the downlink performance of the large-scale heterogeneous LEO satellite networks in the context of proposed association schemes. Specifically, the downlink performance is initially evaluated in terms of the coverage probability, which indicates the probability that the instantaneous SINR exceeds a predefined threshold, denoted as β (dB), i.e. $\mathbb{P}\left\{\frac{\mathcal{S}}{\mathcal{I}+\sigma^2} \geq \beta\right\}$, where S and $\mathcal{I}$ are the intended and interfering signals, respectively. By leveraging tools from stochastic geometry, we formulate a tractable mathematical framework, while analytical expressions for the coverage probability are derived for with the employment of each association scheme. Furthermore, we discuss the performance of the proposed association schemes under another two distinct extreme scenarios, namely, Rayleigh fading and non-fading environments, which correspond to the most demanding and idealized communication situations, respectively. Finally, we investigate the spectral efficiency achieved at typical gUEs with the employment of each association scheme, a critical metric for 6G networks that reflects how effectively bandwidth is utilized to support efficient data transmission and meet diverse communication demands.

7.5.1 Coverage probability for the DbA scheme

In order to facilitate the analysis of the coverage probability achieved by the DbA scheme, we initially evaluate the distribution of the contact distance for the DbA scheme, which is the distance between the typical gUE and its serving LEO satellite. This distribution is crucial for evaluating the network performance, as it directly impacts the received signal strength and interference levels at the typical gUE. To this end, we present the pdf of the contact distance for the DbA scheme in the following lemma, which considers the case where the typical gUE is associated with the k-th tier network for $1 \leq k \leq K$.

Yuan Guo

Lemma 7.5. *When the DbA scheme is employed, the pdf of the contact distance is given by*

$$f_{D,k}(r|\mathcal{A}_{D,k}) = \frac{2\pi\lambda_k(R_\oplus + H_k)}{R_\oplus \mathcal{A}_{D,k}} \times \sum_{i=k}^{K} \mathbb{I}(H_i \leq r < H_{i+1}) \exp\left(-\sum_{j=1}^{i} \frac{\pi\lambda_j(R_\oplus + H_j)(r^2 - H_j^2)}{R_\oplus}\right) r, \quad (7.17)$$

where $\mathbb{I}(H_i \leq r < H_{i+1})$ *is the indicator function that is given by*

$$\mathbb{I}(H_i \leq r < H_{i+1}) = \begin{cases} 1, & H_i \leq r < H_{i+1}, \\ 0, & \textit{otherwise}. \end{cases} \quad (7.18)$$

Proof. Without loss of generality, we consider that the typical gUE is associated with the k-th tier network for $1 \leq k \leq K$. Then, the cdf of the contact distance is computed as

$$\begin{aligned} F_{D,k}(r|\mathcal{A}_{D,k}) =& \mathbb{P}\left\{ r_{0,k} \leq r \;\middle|\; r_{0,k} < \min_{1\leq j\leq K, j\neq k} r_{0,j} \right\} \\ =& 1 - \frac{\mathbb{P}\left\{ r_{0,k} > r \;\&\; r_{0,k} < \min_{1\leq j\leq K, j\neq k} r_{0,j} \right\}}{\mathbb{P}\left\{ r_{0,k} < \min_{1\leq j\leq K, j\neq k} r_{0,j} \right\}}. \end{aligned} \quad (7.19)$$

Note that $\mathbb{P}\left\{ r_{0,k} < \min_{1\leq j\leq K, j\neq k} r_{0,j} \right\} = \mathcal{A}_{D,k}$. Then, for the case where $H_i \leq r < H_{i+1}$, the probability term in (7.19) is computed as

$$\begin{aligned} &\mathbb{P}\left\{ r < r_{0,k} < \min_{1\leq j\leq K, j\neq k} r_{0,j} \;\&\; H_i \leq r < H_{i+1} \right\} \\ &= \int_r^{H_{i+1}} \prod_{j=1}^{i} \exp\left(-\frac{\pi\lambda_j(R_\oplus + H_j)(r^2 - H_j^2)}{R_\oplus}\right) \frac{2\pi\lambda_k r(R_\oplus + H_k)}{R_\oplus} \mathrm{d}r. \end{aligned} \quad (7.20)$$

By taking into account all possible ranges of r within $H_k \leq r \leq R_{\max_k}$ and by substituting (7.20) into (7.19), we obtain the final expression of $F_D(r|\mathcal{A}_{D,k})$, i.e.

$$F_{D,k}(r|\mathcal{A}_{D,k}) = 1 - \frac{\sum_{i=k}^{K} \mathbb{I}(H_i \leq r < H_{i+1}) \int_r^{H_{i+1}} \prod_{j=1}^{i} \exp\left(-\frac{\pi\lambda_j(R_\oplus + H_j)(r^2 - H_j^2)}{R_\oplus}\right) \frac{2\pi\lambda_k r(R_\oplus + H_k)}{R_\oplus} \mathrm{d}r}{\mathcal{A}_{D,k}}, \quad (7.21)$$

where $\mathbb{I}(H_i \leq r < H_{i+1})$ is the indicator function, which takes a value of 1 if the condition $H_i \leq r < H_{i+1}$ is met, and 0 otherwise. Finally, the pdf of the contact distance, i.e. $f_{D,k}(r|\mathcal{A}_k)$, can be derived by taking the derivative of $F_{D,k}(r|\mathcal{A}_{D,k})$ with respect to r, i.e. $f_{D,k}(r|\mathcal{A}_k) = \frac{\partial}{\partial r} F_{D,k}(r|\mathcal{A}_{D,k})$. □

Yan Gao

It is worth emphasising that the results presented in Lemma 7.5 are applicable to a variety of LEO satellite network topologies and can be adapted to different network parameters. For instance, by setting $H_k = H$, $G^L_{m,k} = G^L_m$, $P_k = P$ and $\lambda_k = \lambda \; \forall \; 1 \leq k \leq K$, we can obtain the corresponding results for single-tier LEO satellite networks as investigated in previous studies [55, 57, 82]. Additionally, by setting $H_k = H \; \forall \; 1 \leq k \leq K$, we can obtain the conventional topology of heterogeneous networks for the LEO satellite communication scenario [113]. These examples demonstrate the versatility and adaptability of our derived results in analysing various LEO satellite network topologies and settings.

By applying the results obtained in the Lemma 7.1 and Lemma 7.2 and by approximating the power of the aggregate interference signals with its mean, we derive the expression for the coverage probability achieved by the DbA scheme in the following theorem.

Theorem 7.1. *The coverage probability achieved by the DbA scheme is given by*

$$\mathcal{P}_D(\beta) = \sum_{k=1}^{K} \mathcal{A}_{D,k} \mathcal{P}_{D,k}(\beta), \tag{7.22}$$

where

$$\mathcal{P}_{D,k}(\beta) \approx \int_{H_k}^{R_{\max_k}} \left(1 - F_h\left(\frac{\beta r^{\alpha}(\widetilde{\mathcal{I}}_D(r) + \sigma^2)}{P_k G^L_{m,k} G^U_m}\right)\right) f_{D,k}(r|\mathcal{A}_{D,k}) \mathrm{d}r, \tag{7.23}$$

$$\widetilde{\mathcal{I}}_D(r) = \sum_{j=1}^{K} \frac{2\pi\lambda_j \bar{h} P_j G^L_{s,j} G^U_s (R_{\oplus} + H_j) \left(\max\left\{\min\{r^{2-\alpha}, H_j^{2-\alpha}\} - R^{2-\alpha}_{\max_j}, 0\right\}\right)}{(\alpha - 2) R_{\oplus}}. \tag{7.24}$$

Proof. By the law of the total probability and according to the definition of the coverage probability, we have

$$\mathcal{P}_D(\beta) = \sum_{k=1}^{K} \mathcal{P}_{D,k}(\beta) \mathcal{A}_{D,k}, \tag{7.25}$$

where $\mathcal{P}_{D,k}(\beta)$ represents the coverage probability when the typical gUE is associ-

Yuan Guo

ated with the k-th tier, which is given by

$$\begin{aligned}\mathcal{P}_{D,k}(\beta) =&\mathbb{P}\left\{\frac{P_k h_{0,k} G_{m,k}^L G_m^U r_{0,k}^{-\alpha}}{\sum_{x_{i,j}\in\cup_{j=1}^K \Phi_j^{\setminus x_{0,k}}} P_j h_{i,j} r_{i,j}^{-\alpha} G_{s,j}^L G_s^U + \sigma^2} \geq \beta\right\}\\ =&\mathbb{E}_{r_{0,k},h_{i,j}}\left\{\mathbb{P}\left\{h_{0,k} \geq \frac{\beta\left(\sum_{x_{i,j}\in\cup_{j=1}^K \Phi_j^{\setminus x_{0,k}}} P_j h_{i,j} r_{i,j}^{-\alpha} G_{s,j}^L G_s^U + \sigma^2\right)}{P_k G_{m,k}^L G_m^U r_{0,k}^{-\alpha}}\right\}\right\}\\ \approx&\mathbb{E}_{r_{0,k}}\left\{\mathbb{P}\left\{h_{0,k} \geq \frac{\beta\left(\widetilde{\mathcal{I}}_D(r_{0,k}) + \sigma^2\right)}{P_k G_{m,k}^L G_m^U r_{0,k}^{-\alpha}}\right\}\right\}\\ =&\mathbb{E}_{r_{0,k}}\left\{1 - F_h\left(\frac{\beta\left(\widetilde{\mathcal{I}}_D(r_{0,k}) + \sigma^2\right)}{P_k G_{m,k}^L G_m^U r_{0,k}^{-\alpha}}\right)\right\},\end{aligned} \tag{7.26}$$

where $F_h(\cdot)$ is the cdf of channel power gain; $\widetilde{\mathcal{I}}_D(r_{0,k})$ is the mean of the aggregate interference power, and is computed as following

$$\begin{aligned}\widetilde{\mathcal{I}}_D(r_{0,k}) =&\mathbb{E}\left\{\sum\nolimits_{x_{i,j}\in\cup_{j=1}^K \Phi_j^{\setminus x_{0,k}}} P_j G_{s,j}^L h_{i,j} r_{i,j}^{-\alpha} G_s^U\right\}\\ =&\mathbb{E}\left\{\sum\nolimits_{x_{i,j}\in\cup_{j=1}^K \Phi_j^{\setminus x_{0,k}}} \int_0^\infty P_j G_{s,j}^L h r_{i,j}^{-\alpha} G_s^U f_h(r)\mathrm{d}h\right\}\\ =&\mathbb{E}\left\{\sum\nolimits_{x_{i,j}\in\cup_{j=1}^K \Phi_j^{\setminus x_{0,k}}} \bar{h} P_j G_{s,j}^L r_{i,j}^{-\alpha} G_s^U\right\}\\ \overset{(a)}{=}&\sum_{j=1}^K \int_0^{2\pi}\int_\theta \bar{h}\lambda_j P_j G_{s,j}^L r_{i,j}^{-\alpha} G_s^U (R_\oplus + H_j)^2 \sin\theta \mathrm{d}\theta\mathrm{d}\phi\\ =&\sum_{j=1}^K \int_\theta 2\pi\bar{h}\lambda_j P_j G_{s,j}^L r_{i,j}^{-\alpha} G_s^U (R_\oplus + H_j)^2 \sin\theta\mathrm{d}\theta,\end{aligned} \tag{7.27}$$

where (a) follows from the Campbell's Theorem of PPP with the spherical coordinates [31, 55]. Then, by replacing θ with a function of r based on the law of cosines, i.e. $\theta = \arccos\left(\frac{R_\oplus^2 + (R_\oplus + H_j)^2 - r^2}{2R_\oplus(R_\oplus + H_j)}\right)$, we have

$$\begin{aligned}\mathrm{d}\theta =&\frac{r}{R_\oplus(H_j + R_\oplus)\sqrt{1 - \frac{\left((H_j+R_\oplus)^2 - r^2 + R_\oplus^2\right)^2}{4R_\oplus^2(H_j+R_\oplus)^2}}}\mathrm{d}r,\\ \sin\theta =&\sqrt{1 - \frac{\left((H_j + R_\oplus)^2 - r^2 + R_\oplus^2\right)^2}{4R_\oplus^2(H_j + R_\oplus)^2}}.\end{aligned} \tag{7.28}$$

Hence, by substituting (7.28) into (7.27), we can further compute $\widetilde{\mathcal{I}}_D(r_{0,k})$ as following

$$\widetilde{\mathcal{I}}_D(r_{0,k}) = \sum_{j=1}^K \int_{\max\{r_{0,k},H_j\}}^{R_{\max_j}} 2\pi\bar{h}\lambda_j \frac{R_\oplus + H_j}{R_\oplus} P_j G_{s,j}^L r^{1-\alpha} G_s^U \mathrm{d}r. \tag{7.29}$$

Finally, by solving the above integral and by evaluating the expectation over $r_{0,k}$, the final results in Theorem 7.1 are derived. □

Note that the term $\widetilde{\mathcal{I}}_D(r)$ represents the conditional mean of the aggregate interference. By approximating the instantaneous interference power with its mean, we facilitate the analytical framework and avoid the intractability that typically arises when performing system-level analysis with the SR fading model. Moreover, the closed-form expression of $\widetilde{\mathcal{I}}_D(r)$ provides a convenient approach for analysing the average interference levels in the large-scale LEO satellite networks. In specific, we can easily observe that the average interference received by the typical gUE is directly proportional to the density and transmit power of LEO satellites, while a greater path-loss exponent can mitigate the interference power.

7.5.2 Coverage probability for the PbA scheme

We initially evaluate the distribution of the average received signal power at the typical gUE from its serving LEO satellite. In specific, upon conditioning for the scenario in which the typical gUE is associated with the k-th tier, the conditional pdf of $\xi_{0,k}$ is evaluated in the following lemma.

Lemma 7.6. *When the PbA scheme is employed, the pdf of the average signal power received by the typical gUE from its serving LEO satellite is given by*

$$\begin{aligned} &f_{P,k}(\xi|\mathcal{A}_{P,k}) \\ =&\frac{2\pi\lambda_k \varrho_k^{\frac{2}{\alpha}}(R_\oplus + H_k)}{\alpha R_\oplus \mathcal{A}_{P,k}} \left(\frac{1}{\xi}\right)^{\frac{2}{\alpha}+1} \prod_{j=1}^{K} \exp\left(-\frac{\pi\lambda_j(R_\oplus + H_j)}{R_\oplus}\left(\left(\frac{\varrho_k}{\xi}\right)^{\frac{2}{\alpha}} - H_j^2\right)\right). \end{aligned} \tag{7.30}$$

Proof. Consider that the typical gUE is associated with the k-th tier, the cdf of $\xi_{0,k}$ is computed as

$$\begin{aligned} F_P(\xi|\mathcal{A}_{P,k}) =& \mathbb{P}\left\{\xi_{0,k} \le \xi \middle| \xi_{0,k} > \max_{1\le j\le K, j\neq k} \xi_{0,j}\right\} \\ =& \frac{\mathbb{P}\left\{\max\limits_{1\le j\le K, j\neq k} \xi_{0,j} < \xi_{0,k} \le \xi\right\}}{\mathbb{P}\left\{\xi_{0,k} > \max\limits_{1\le j\le K, j\neq k} \xi_{0,j}\right\}}. \end{aligned} \tag{7.31}$$

Note that the denominator of (7.31) is exactly the association probability presented in Lemma 7.4, i.e. $\mathbb{P}\left\{\xi_{0,k} > \max\limits_{1\le j\le K,\, j\neq k} \xi_{0,j}\right\} = \mathcal{A}_{P,k}$; while the numerator can be

further computed as

$$
\begin{aligned}
&\mathbb{P}\left\{\max_{\substack{1\le j\le K\\ j\neq k}} \xi_{0,j} < \xi_{0,k} \le \xi\right\} \\
&= \int_{\xi_{\min_k}}^{\xi} \prod_{j=1, j\neq k}^{K} \mathbb{P}\left\{\xi_{0,k} > \xi_{0,j}\right\} f_P(\xi_{0,k}, \lambda_k, H_k) \mathrm{d}\xi_{0,k} \\
&= \int_{\xi_{\min_k}}^{\xi} \prod_{j=1, j\neq k}^{K} \left(1 - F_P(\xi_{0,k}, \lambda_j, H_j)\right) f_P(\xi_{0,k}, \lambda_k, H_k) \mathrm{d}\xi_{0,k} \qquad (7.32) \\
&= \int_{\xi_{\min_k}}^{\xi} \prod_{j=1, j\neq k}^{K} \exp\left(-\pi\lambda_j \frac{R_\oplus + H_j}{R_\oplus} \left(\left(\frac{\bar{h} P_j G_{m,j}^L G_m^U}{\xi_{0,k}}\right)^{\frac{2}{\alpha}} - H_j^2\right)\right) f_P(\xi_{0,k}, \lambda_k, H_k) \mathrm{d}\xi_{0,k}.
\end{aligned}
$$

Then by substituting (7.32) into (7.31) and by taking the partial derivative of $F_P(\xi|\mathcal{A}_{P,k})$ with respect to ξ, the conditional pdf of $\xi_{0,k}$ is derived. □

Then, by utilizing the aforementioned results, we provide the analytical expression for the coverage probability achieved by the PbA scheme, in the following theorem.

Theorem 7.2. *The coverage probability achieved by the PbA scheme is given by*

$$\mathcal{P}_P(\beta) = \sum_{k=1}^{K} \mathcal{A}_{P,k} \mathcal{P}_{P,k}(\beta), \qquad (7.33)$$

where

$$\mathcal{P}_{P,k}(\beta) \approx \int_{\xi_{\min_k}}^{\xi_{\max_k}} \left(1 - F_h\left(\frac{\beta\bar{h}\left(\widetilde{\mathcal{I}}_P(\xi_{0,k}) + \sigma^2\right)}{\xi_{0,k}}\right)\right) f_{P,k}(\xi_{0,k}|\mathcal{A}_{P,k}) \mathrm{d}\xi_{0,k}, \qquad (7.34)$$

$$\widetilde{\mathcal{I}}_P(\xi_{0,k}) = \sum_{j=1}^{K} \frac{2\pi\lambda_j P_j G_{s,j}^L G_s^U \bar{h}(R_\oplus + H_j)\left(\min\left\{\left(\frac{\varrho_k}{\xi_{0,k}}\right)^{\frac{2-\alpha}{\alpha}}, H_j^{2-\alpha}\right\} - R_{\max_j}^{2-\alpha}\right)}{(\alpha-2)R_\oplus}. \qquad (7.35)$$

Proof. Based on the definition of the PbA scheme and by the law of the total probability, the coverage probability is formulated as

$$\mathcal{P}_P(\beta) = \sum_{k=1}^{K} \mathcal{P}_{P,k}(\beta) \mathcal{A}_{P,k}, \qquad (7.36)$$

where $\mathcal{P}_{P,k}(\beta)$ is given by

$$
\begin{aligned}
\mathcal{P}_{P,k}(\beta) =& \mathbb{P}\left\{\frac{P_k h_{0,k} G_{m,k}^L G_m^U r_{0,k}^{-\alpha}}{\sum_{x_{i,j}\in\cup_{j=1}^{K}\Phi_j^{\setminus x_{0,k}}} P_j h_{i,j} r_{i,j}^{-\alpha} G_{s,j}^L G_s^U + \sigma^2} \ge \beta\right\} \\
\approx& \mathbb{E}_{\xi_{0,k}}\left\{\mathbb{P}\left\{h_{0,k} \ge \frac{\beta\bar{h}\left(\widetilde{\mathcal{I}}_P(\xi_{0,k}) + \sigma^2\right)}{\xi_{0,k}}\right\}\right\},
\end{aligned} \qquad (7.37)
$$

where $\widetilde{\mathcal{I}}_P(\xi_{0,k})$ is the mean of the aggregate interference signal power observed at the gUE with the employment of the PbA scheme, which is computed as

$$\begin{aligned}\widetilde{\mathcal{I}}_P(\xi_{0,k}) =& \mathbb{E}\left\{\sum_{x_{i,j}\in\cup_{j=1}^{K}\Phi_j^{\setminus x_{0,k}}} P_j h_{i,j} r_{i,j}^{-\alpha} G_{s,j}^{L} G_s^{U}\right\} = \bar{h}\mathbb{E}\left\{\sum_{x_{i,j}\in\cup_{j=1}^{K}\Phi_j^{\setminus x_{0,k}}} P_j r_{i,j}^{-\alpha} G_{s,j}^{L} G_s^{U}\right\} \\ =& \sum_{j=1}^{K}\int_0^{2\pi}\int_\theta \bar{h}\lambda_j P_j G_{s,j}^{L} r_{i,j}^{-\alpha} G_s^{U}(R_\oplus + H_j)^2 \sin\theta \mathrm{d}\theta\mathrm{d}\phi \\ =& \sum_{j=1}^{K}\int_{\max\left\{\left(\varrho_k/\xi_{0,k}\right)^{1/\alpha}, H_j\right\}}^{R_{\max_j}} 2\pi\bar{h}\lambda_j \frac{R_\oplus + H_j}{R_\oplus} P_j G_{s,j}^{L} r^{1-\alpha} G_s^{U} \mathrm{d}r.\end{aligned}$$

Finally, by applying the cdf of $h_{0,k}$, and by evaluating the average over $\xi_{0,k}$, the results in Theorem 7.2 are proven. □

Note that the derivation of $\mathcal{P}_P(\beta)$ follows a similar analytical framework as that of the $\mathcal{P}_D(\beta)$, i.e. the coverage probability achieved by the DbA scheme. As the process of the PbA scheme incorporates a comparison of received signal power among candidate LEO satellites, it results in an enhanced intended signal power received by the typical gUE compared to the DbA scheme. Moreover, the interference level experienced by the typical gUE using the PbA scheme is lower compared to the interference level with the DbA scheme. This observation can be explained by the fact that the PbA scheme prioritizes the selection of LEO satellites based on the received signal power. As a result, the gUE is more likely to connect to a satellite with a stronger signal, which in turn reduces the impact of interference from other LEO satellites in the network.

7.5.3 Coverage probability for the RbA scheme

While the PbA scheme effectively enhances the coverage performance of the considered LEO satellite networks, it is important to explore other options to meet various requirements in different network scenarios. As a result, the RbA scheme emerges as a promising alternative, offering low-complexity association capabilities particularly suited for heterogeneous LEO satellite-based networks with a large number of tiers. A detailed coverage performance analysis of the RbA scheme is presented in the this subsection, showcasing its potential in addressing the challenges faced by these complex networks.

Yuan Guo

The derivation of the coverage probability for the RbA scheme follows the similar steps as that utilized for the DbA scheme. More specifically, we first evaluate the distribution of the contact distance. By considering that the typical gUE is associated with the k-th tier, the pdf of the contact distance with the employment of the RbA scheme is presented in the following lemma.

Lemma 7.7. *When the RbA scheme is employed, the pdf of contact distance is given by*

$$f_{R,k}(r|\mathcal{A}_{R,k}) = \frac{2\pi\lambda_k r(R_\oplus + H_k)}{R_\oplus} \exp\left(-\frac{\pi\lambda_k(R_\oplus + H_k)(r^2 - H_k^2)}{R_\oplus}\right). \tag{7.38}$$

Proof. The cdf of the contact distance by conditioning on the case that the typical gUE is associated with the k-th tier LEO satellite is given by

$$\begin{aligned} &F_{R,k}(r|\mathcal{A}_{R,k}) \\ =&1 - \mathbb{P}\left\{r_{0,k} \geq r | \text{ the typical gUE is associated with the } k\text{-th tier}\right\}. \end{aligned} \tag{7.39}$$

Since the tier selection is based on a random operation, i.e. it is independent with $r_{0,k}$, thus we have $F_{R,k}(r|\mathcal{A}_{R,k}) = 1 - \mathbb{P}\left\{r_{0,k} \geq r\right\}$. Then by directly following the results presented in Lemma 7.1, the final expression of $f_{R,k}(r|\mathcal{A}_{R,k})$ is derived. □

From the above results, it is evident that when the RbA scheme is employed, the distribution of the contact distance depends solely on the deployment of the selected tier LEO satellites due to its random tier selection. This is in contrast to the PbA and DbA schemes, where these factors are influenced by the deployment of the entire set of tiers. Then, based on the above discussion and result, we now evaluate the coverage probability attained by the RbA scheme, with its analytical expression provided in the following theorem.

Theorem 7.3. *The coverage probability achieved by the RbA scheme is given by*

$$\mathcal{P}_R(\beta) = \sum_{k=1}^{K} \mathcal{A}_{R,k}\mathcal{P}_{R,k}(\beta), \tag{7.40}$$

where

$$\mathcal{P}_{R,k}(\beta) \approx \int_{H_k}^{R_{\max_k}} \left(1 - F_h\left(\frac{\beta r_{0,k}^{\alpha}(\widetilde{\mathcal{I}}_R(r_{0,k}) + \sigma^2)}{P_k G_{m,k}^L G_m^U}\right)\right) f_{R,k}(r_{0,k}|\mathcal{A}_{R,k})\mathrm{d}r_{0,k}, \tag{7.41}$$

$$\begin{aligned} \widetilde{\mathcal{I}}_R(r_{0,k}) = \frac{1}{(\alpha-2)R_\oplus}\Bigg(&2\pi\lambda_k P_k G_{s,k}^L G_s^U \bar{h}(R_\oplus + H_k)(r_{0,k}^{2-\alpha} - R_{\max_k}^{2-\alpha}) \\ &+ \sum_{j=1, j\neq k}^{K} 2\pi\lambda_j P_j G_{s,j}^L G_s^U \bar{h}(R_\oplus + H_j)(H_j^{2-\alpha} - R_{\max_j}^{2-\alpha})\Bigg). \end{aligned} \tag{7.42}$$

Yuan Guo

Proof. The proof follows the similar steps presented in Proof of Theorem 7.1, but with the average interference power and association probability that correspond to the RbA scheme. □

Some key insights can be obtained from the expression presented in the above theorem. Although the RbA scheme has a low-complexity implementation, it results in a higher level of interference experienced by the gUEs compared to the other two schemes. Specifically, the random tier selection results in some nearby LEO satellites from other tiers contributing significant interference to the typical gUE.

7.5.4 Coverage probability in Rayleigh fading and non-fading scenarios

Although the adopted SR model captures the fact that communication between gUEs and LEO satellites typically involves a LoS connection [51], the Rayleigh fading model can still be used to provide a conservative lower bound for system performance, especially when considering indoor communications, i.e. the receiver is located indoors. In such scenarios, multipath effects from indoor structures can significantly impact the signal. Therefore, by focusing on these multipath effects and assuming a weak or obstructed LoS, we examine the scenario with Rayleigh fading, i.e. $h \sim \exp(1)$, in the following proposition, where the exact analytical expressions for the coverage probability achieved by the each association scheme is obtained.

Proposition 7.2. *In the Rayleigh fading scenario, the coverage probabilities achieved by the DbA, PbA and RbA schemes are given by*

$$\mathcal{P}^{\dagger}_{\Delta}(\beta) = \sum_{k=1}^{K} \mathcal{A}_{\Delta,k} \mathcal{P}^{\dagger}_{\Delta,k}(\beta), \tag{7.43}$$

where $\Delta \in \{D, P, R\}$ stands for the DbA, PbA and RbA schemes, $\mathcal{P}^{\dagger}_{\Delta,k}(\beta)$ is given by

$$\mathcal{P}^{\dagger}_{\Delta,k}(\beta) = \begin{cases} \int_{H_k}^{R_{\max_k}} \mathcal{L}^{\dagger}_{\mathcal{I}_D}(\varkappa_D) \exp(-\varkappa_D \sigma^2) f_{D,k}(r_{0,k}|\mathcal{A}_{D,k}) \mathrm{d}r_{0,k}, & \textit{DbA scheme}, \\ \int_{\xi_{\min_k}}^{\xi_{\max_k}} \mathcal{L}^{\dagger}_{\mathcal{I}_P}(\varkappa_P) \exp(-\varkappa_P \sigma^2) f_{P,k}(\xi_{0,k}|\mathcal{A}_{P,k}) \mathrm{d}\xi_{0,k}, & \textit{PbA scheme}, \\ \int_{H_k}^{R_{\max_k}} \mathcal{L}^{\dagger}_{\mathcal{I}_R}(\varkappa_R) \exp(-\varkappa_R \sigma^2) f_{R,k}(r_{0,k}|\mathcal{A}_{R,k}) \mathrm{d}r_{0,k}, & \textit{RbA scheme}, \end{cases} \tag{7.44}$$

$\mathcal{L}^{\dagger}_{\mathcal{I}_\Delta}(\varkappa_\Delta)$ is the Laplace transform of the aggregate interference power with each association

scheme, which is given by

$$\mathcal{L}^{\dagger}_{\mathcal{I}_\Delta}(\varkappa_\Delta)=\begin{cases}\prod\limits_{j=1}^{K}\exp\left(-\frac{2\pi\lambda_j P_j G^L_{s,j} G^U_s \varkappa_D (R_\oplus+H_j)\left(\varpi_j(\max\{r_{0,k},H_j\},\varkappa_D)-\varpi_j(R_{\max_j},\varkappa_D)\right)}{R_\oplus(\alpha-2)}\right), \\ \qquad\qquad\qquad\qquad\qquad\qquad\qquad\qquad\qquad\qquad \textbf{for } \Delta=D; \\ \prod\limits_{j=1}^{K}\exp\left(-\frac{2\pi\lambda_j P_j G^L_{s,j} G^U_s \varkappa_P (R_\oplus+H_j)\left(\varpi_j\left(\max\left\{\left(\varrho_k/\xi_{0,k}\right)^{1/\alpha},H_j\right\},\varkappa_P\right)-\varpi_j(R_{\max_j},\varkappa_P)\right)}{R_\oplus(\alpha-2)}\right), \\ \qquad\qquad\qquad\qquad\qquad\qquad\qquad\qquad\qquad\qquad \textbf{for } \Delta=P; \\ \exp\left(-\frac{2\pi\lambda_k P_k G^L_{s,k} G^U_s \varkappa_R (R_\oplus+H_k)\left(\varpi_k(r_{0,k},\varkappa_R)-\varpi_k(R_{\max_k},\varkappa_R)\right)}{R_\oplus(\alpha-2)}\right)\times \\ \qquad \prod\limits_{j=1,j\neq k}^{K}\exp\left(-\frac{2\pi\lambda_j P_j G^L_{s,j} G^U_s \varkappa_R (R_\oplus+H_j)\left(\varpi_j(H_j,\varkappa_R)-\varpi_j(R_{\max_j},\varkappa_R)\right)}{R_\oplus(\alpha-2)}\right), \\ \qquad\qquad\qquad\qquad\qquad\qquad\qquad\qquad\qquad\qquad \textbf{for } \Delta=R.\end{cases} \tag{7.45}$$

$\varpi_j(r,\varkappa)$ is given by

$$\varpi_j(r,\varkappa)=r^{2-\alpha}\,{}_2F_1\left[1,\frac{\alpha-2}{\alpha};2-\frac{2}{\alpha};-P_j G^L_{s,j} G^U_s r^{-\alpha}\varkappa\right];$$

$\varkappa_D=\frac{\beta}{P_k G^L_{m,k} G^U_m r^{-\alpha}_{0,k}}$, $\varkappa_P=\frac{\beta}{\xi_{0,k}}$, $\varkappa_R=\varkappa_D$.

Proof. We initially evaluate the coverage probability for DbA scheme under the Rayleigh fading. Considering that the typical gUE is associated with the k-th tier, then the coverage probability achieved by the DbA scheme is computed as

$$\begin{aligned}&\mathcal{P}^{\dagger}_{D,k}(\beta)\\ =&\mathbb{E}\left\{\mathbb{P}\left\{h_{0,k}\geq\frac{\beta\left(\sum_{x_{i,j}\in\cup_{j=1}^{K}\Phi_j^{\setminus x_{0,k}}}P_j h_{i,j} r_{i,j}^{-\alpha} G^L_{s,j} G^U_s+\sigma^2\right)}{P_k G^L_{m,k} G^U_m r^{-\alpha}_{0,k}}\right\}\right\}\\ =&\mathbb{E}\left\{\exp\left(-\frac{\beta\left(\sum_{x_{i,j}\in\cup_{j=1}^{K}\Phi_j^{\setminus x_{0,k}}}P_j h_{i,j} r_{i,j}^{-\alpha} G^L_{s,j} G^U_s+\sigma^2\right)}{P_k G^L_{m,k} G^U_m r^{-\alpha}_{0,k}}\right)\right\}\\ =&\mathbb{E}_{r_{0,k}}\left\{\mathbb{E}\left\{\exp\left(-\varkappa_D\sum_{x_{i,j}\in\cup_{j=1}^{K}\Phi_j^{\setminus x_{0,k}}}P_j h_{i,j} r_{i,j}^{-\alpha} G^L_{s,j} G^U_s\right)\right\}\exp(-\varkappa_D\sigma^2)\right\}\\ =&\int_{H_k}^{R_{\max_k}}\mathcal{L}^{\dagger}_{\mathcal{I}_D}(\varkappa_D)\exp(-\varkappa_D\sigma^2) f_{D,k}(r_{0,k}|\mathcal{A}_{D,k})\mathrm{d}r_{0,k},\end{aligned} \tag{7.46}$$

where the first step is based on the fact that for the Rayleigh fading model, the channel power gain is an exponential random variable with mean one, i.e. $h\sim\exp(1)$; $\varkappa_D=\frac{\beta}{P_k G^L_{m,k} G^U_m r^{-\alpha}_{0,k}}$ and $\mathcal{L}^{\dagger}_{\mathcal{I}_D}(z)$ is the Laplace transform of the interference,

which is evaluated as following, i.e.

$$\begin{aligned}
&\mathcal{L}^{\dagger}_{\mathcal{I}_D}(\varkappa_D)\\
=&\mathbb{E}\left\{\prod_{x_{i,j}\in\cup_{j=1}^{K}\Phi_j^{\setminus x_{0,k}}}\mathbb{E}_{h_{i,j}}\left\{\exp\left(-\varkappa_D P_j h_{i,j} r_{i,j}^{-\alpha} G_{s,j}^{L} G_s^{U}\right)\right\}\right\}\\
=&\mathbb{E}\left\{\prod_{x_{i,j}\in\cup_{j=1}^{K}\Phi_j^{\setminus x_{0,k}}}\exp\left(\frac{1}{1+\varkappa_D P_j r_{i,j}^{-\alpha} G_{s,j}^{L} G_s^{U}}\right)\right\} \qquad (7.47)\\
=&\mathbb{E}\left\{\prod_{j=1}^{K}\exp\left(-2\pi\lambda_j\frac{R_{\oplus}+H_j}{R_{\oplus}}\int_{\max\{r_{0,k},H_j\}}^{R_{\max_j}}\left(1-\frac{1}{1+\varkappa_D P_j r^{-\alpha} G_{s,j}^{L} G_s^{U}}\right) r\mathrm{d}r\right)\right\}.
\end{aligned}$$

where the last step is obtained by using the probability generating function of the PPP [31], where the above integral can be solved based on [91, 3.194.5]. Finally, by applying the law of total probability, the coverage probability of DbA scheme in the Rayleigh fading scenario is derived. Note that the proof of the coverage probability of PbA and RbA schemes in the Rayleigh fading scenario, follows a similar methodology and thus is omitted. □

In contrast to the previous discussion with the Rayleigh fading channel, in the following proposition, we investigate another extreme case, i.e. non-fading scenario. More specifically, in this scenario, the effects of fading channels are absent, and the channel remains constant, i.e. $h = 1$. This idealized situation provides a useful benchmark for comparison to evaluate how significant the fading effect is on the performance of LEO satellites networks.

Proposition 7.3. *In the non-fading scenario, the coverage probabilities achieved by the DbA, PbA and RbA schemes are given by*

$$\mathcal{P}^{\ddagger}_{\Delta}(\beta) = \sum_{k=1}^{K}\mathcal{A}_{\Delta,k}\mathcal{P}^{\ddagger}_{\Delta,k}(\beta), \qquad (7.48)$$

Yuan Guo

respectively, where $\mathcal{P}^{\ddagger}_{\Delta,k}(\beta)$ *for* $\Delta \in \{D, P, R\}$ *are given by*

$$\mathcal{P}^{\ddagger}_{\Delta,k}(\beta) = \begin{cases} \int_{H_k}^{R_{\max_k}} \left(\frac{1}{2} - \frac{1}{\pi} \int_0^{\infty} \frac{\Im\left\{ \exp\left(jt\left(\beta\sigma^2 - P_k G^L_{m,k} G^U_m r_{0,k}^{-\alpha} \right) \right) \mathcal{L}^{\ddagger}_{\mathcal{I}_D}(-jt\beta) \right\}}{t} \mathrm{d}t \right) f_{D,k}(r_{0,k}|\mathcal{A}_{D,k}) \mathrm{d}r_{0,k}, \\ \qquad\qquad \textbf{for } \Delta = D; \\ \int_{\xi_{\min_k}}^{\xi_{\max_k}} \left(\frac{1}{2} - \frac{1}{\pi} \int_0^{\infty} \frac{\Im\left\{ \exp\left(jt(\beta\sigma^2 - \xi_{0,k}) \right) \mathcal{L}^{\ddagger}_{\mathcal{I}_P}(-jt\beta) \right\}}{t} \mathrm{d}t \right) f_{P,k}(\xi_{0,k}|\mathcal{A}_{P,k}) \mathrm{d}\xi_{0,k}, \\ \qquad\qquad \textbf{for } \Delta = P; \\ \int_{H_k}^{R_{\max_k}} \left(\frac{1}{2} - \frac{1}{\pi} \int_0^{\infty} \frac{\Im\left\{ \exp\left(jt\left(\beta\sigma^2 - P_k G^L_{m,k} G^U_m r_{0,k}^{-\alpha} \right) \right) \mathcal{L}^{\ddagger}_{\mathcal{I}_D}(-jt\beta) \right\}}{t} \mathrm{d}t \right) f_{R,k}(r_{0,k}|\mathcal{A}_{R,k}) \mathrm{d}r_{0,k}, \\ \qquad\qquad \textbf{for } \Delta = R. \end{cases} \tag{7.49}$$

$\mathcal{L}^{\ddagger}_{\mathcal{I}_\Delta}(z)$ *is given by*

$$\mathcal{L}^{\ddagger}_{\mathcal{I}_\Delta}(z) = \begin{cases} \prod_{j=1}^{K} \exp\left(\frac{\pi\lambda_j (R_\oplus + H_j) \left(\vartheta_j(\max\{r_{0,k}, H_j\}, z) - \vartheta_j(R_{\max_j}, z) \right)}{R_\oplus \alpha} \right), & \textbf{for } \Delta = D; \\ \prod_{j=1}^{K} \exp\left(\frac{\pi\lambda_j (R_\oplus + H_j) \left(\vartheta_j\left(\max\left\{ \left(\varrho_k / \xi_{0,k} \right)^{1/\alpha}, H_j \right\}, z \right) - \vartheta_j(R_{\max_j}, z) \right)}{R_\oplus \alpha} \right), & \textbf{for } \Delta = P; \\ \exp\left(\frac{\pi\lambda_k (R_\oplus + H_k) \left(\vartheta_k(r_{0,k}, z) - \vartheta_k(R_{\max_k}, z) \right)}{R_\oplus \alpha} \right) \times \\ \qquad \prod_{\substack{j=1 \\ j \neq k}}^{K} \exp\left(\frac{\pi\lambda_j (R_\oplus + H_j) \left(\vartheta_j(H_j, z) - \vartheta_j(R_{\max_j}, z) \right)}{R_\oplus \alpha} \right), & \textbf{for } \Delta = R. \end{cases} \tag{7.50}$$

$\vartheta_j(r, z)$ *is given by*

$$\vartheta_j(r, z) = P_j G^L_{s,j} G^U_s \left(r^2 \left(\alpha - 2\mathcal{E}\left(\frac{2+\alpha}{\alpha}, r^{-\alpha} z \right) \right) + 2 z^{\frac{2}{\alpha}} \Gamma\left[-\frac{2}{\alpha} \right] \right),$$

$\Im\{\cdot\}$ *is the imaginary operator, and* $\mathcal{E}(a, b) = \int_1^{\infty} \frac{e^{-bx}}{x^a} \mathrm{d}x$.

Proof. We provide the detailed proof of the coverage probability for the DbA scheme in the non-fading scenario, while the similar approach can be easily applied to the PbA and RbA scheme. Hence, considering that the DbA scheme is employed and the typical gUE is associated with the k-th tier, the coverage probability is formu-

Yuan Guo

lated as

$$\begin{aligned}\mathcal{P}_{D,k}^{\ddagger}(\beta) =&\mathbb{P}\left\{\frac{P_k G_{m,k}^L G_m^U r_{0,k}^{-\alpha}}{\sum_{x_{i,j}\in\cup_{j=1}^K \Phi_j^{\setminus x_{0,k}}} P_j r_{i,j}^{-\alpha} G_{s,j}^L G_s^U + \sigma^2} \geq \beta\right\}\\ =&\mathbb{P}\left\{P_k G_{m,k}^L G_m^U r_{0,k}^{-\alpha} - \beta \sum_{x_{i,j}\in\cup_{j=1}^K \Phi_j^{\setminus x_{0,k}}} P_j r_{i,j}^{-\alpha} G_{s,j}^L G_s^U \geq \beta\sigma^2\right\}\\ =&\int_{H_k}^{R_{\max_k}} \mathbb{P}\left\{\chi(r_{0,k}) \geq \beta\sigma^2\right\} f_{D,k}(r_{0,k}|\mathcal{A}_{D,k})\mathrm{d}r_{0,k}, \end{aligned} \tag{7.51}$$

where $\chi(r_{0,k}) = \mathcal{S}(r_{0,k}) - \beta\mathcal{I}_D(r_{0,k})$, $\mathcal{S}(r_{0,k}) = P_k G_{m,k}^L G_m^U r_{0,k}^{-\alpha}$, and

$$\mathcal{I}_D(r_{0,k}) = \sum_{x_{i,j}\in\cup_{j=1}^K \Phi_j^{\setminus x_{0,k}}} P_j r_{i,j}^{-\alpha} G_{s,j}^L G_s^U.$$

Then, by applying the Gil-Pelaez inversion theorem [119–121], the probability term in (7.51) can be further computed as

$$\mathbb{P}\left\{\chi(r_{0,k}) \geq \beta\sigma^2\right\} = \frac{1}{2} - \frac{1}{\pi}\int_0^{\infty} \frac{\Im\left\{\psi_{\chi(r_{0,k})}(t)\exp(jt\beta\sigma^2)\right\}}{t}\mathrm{d}t, \tag{7.52}$$

where $\Im\{\cdot\}$ is the imaginary operator and $\psi_{\chi(r_{0,k})}$ is the characteristic function of $\chi(r_{0,k})$ which is given by

$$\begin{aligned}\psi_{\chi(r_{0,k})}(t) =&\mathbb{E}\left\{\exp\Big(-jt\big(\mathcal{S}(r_{0,k}) - \beta\mathcal{I}_D(r_{0,k})\big)\Big)\right\}\\ =&e^{-jt\mathcal{S}(r_{0,k})}\mathbb{E}\left\{e^{jt\beta\mathcal{I}_D(r_{0,k})}\right\}\\ =&e^{-jt\mathcal{S}(r_{0,k})}\mathcal{L}_{\mathcal{I}_D}^{\ddagger}(-jt\beta),\end{aligned} \tag{7.53}$$

where $\mathcal{L}_{\mathcal{I}_D}^{\ddagger}(z) = \mathbb{E}\left\{e^{-z\mathcal{I}_D(r_{0,k})}\right\}$ is the Laplace transform of the interference, which can be evaluated as following

$$\begin{aligned}&\mathcal{L}_{\mathcal{I}_D}^{\ddagger}(z)\\ =&\mathbb{E}\left\{\prod_{x_{i,j}\in\cup_{j=1}^K \Phi_j^{\setminus x_{0,k}}} \exp\left(-zP_j r_{i,j}^{-\alpha} G_{s,j}^L G_s^U\right)\right\}\\ =&\mathbb{E}\left\{\prod_{j=1}^K \exp\left(-2\pi\lambda_j \frac{R_\oplus + H_j}{R_\oplus}\int_{\max\{r_{0,k},H_j\}}^{R_{\max_j}} \left(1 - \exp\left(-zP_j r^{-\alpha} G_{s,j}^L G_s^U\right)\right) r\mathrm{d}r\right)\right\}.\end{aligned} \tag{7.54}$$

Hence, by solving the above integral and by substituting (7.52)-(7.54) into (7.51), the final expression of $\mathcal{P}_{D,k}^{\ddagger}(\beta)$ is obtained. Finally, by the law of total probability, the coverage probability of DbA scheme in the non-fading scenario is derived. □

Yuan Guo

7.5.5 Spectral efficiency

We now assess the spectral efficiency of the considered large-scale heterogeneous LEO satellite networks. In specific, the spectral efficiency is measured in terms of the average ergodic rate per unit bandwidth [109, 113]. For simplicity, the average ergodic rate is computed in unit of nats/s/Hz. By following the similar approach of the derivation for the coverage probability, the average ergodic rate achieved at the typical gUE is given by

$$\mathcal{R}_{\Delta} = \sum_{k=1}^{K} \mathcal{R}_{\Delta,k} \mathcal{A}_{\Delta,k}, \tag{7.55}$$

where $\mathcal{R}_{\Delta,k}$ denotes the average ergodic rate per unit bandwidth of a typical gUE associated with the k-tier, and $\mathcal{A}_{\Delta,k}$ is the association probability for each scheme derived in Section 7.4. Consider that the typical gUE is associated with the k-th tier, we provide the analytical expression for $\mathcal{R}_{\Delta,k}$ in the following proposition.

Proposition 7.4. *The average ergodic rate per unit bandwidth of the typical gUE associated with the k-th tier is given by*

$$\mathcal{R}_{\Delta,k} = \int_{0}^{\infty} \frac{\mathcal{P}_{\Delta,k}(\beta)}{1+\beta} \mathrm{d}\beta, \tag{7.56}$$

where $\Delta \in \{D, P, R\}$ *and* $\mathcal{P}_{\Delta,k}(\beta)$ *is given in Theorem 7.1, 7.2 & 7.3.*

Proof. The proof directly follows from the definition of average ergodic rate and the spectra efficiency [109, 113]. □

Hence, by combining (7.55) and (7.56), the spectral efficiency of the network under each association scheme is obtained. Additionally, by replacing $\mathcal{P}_{\Delta,k}(\beta)$ with $\mathcal{P}^{\dagger}_{\Delta,k}(\beta)$ and $\mathcal{P}^{\ddagger}_{\Delta,k}(\beta)$ in (7.56), we can obtain the spectral efficiency of the network under the Rayleigh fading and non-fading scenarios, respectively.

7.6 Numerical results

In this section, we present analytical and simulation results to validate the accuracy of our model and illustrate the performance of the proposed association schemes. Unless otherwise stated, the simulation parameters are set as follows: the network consists of three tiers with $K = 3$, and the LEO satellites are placed at altitudes of $H_1 = 500$km, $H_2 = 600$km, and $H_3 = 700$km. The path-loss exponent, α, is set

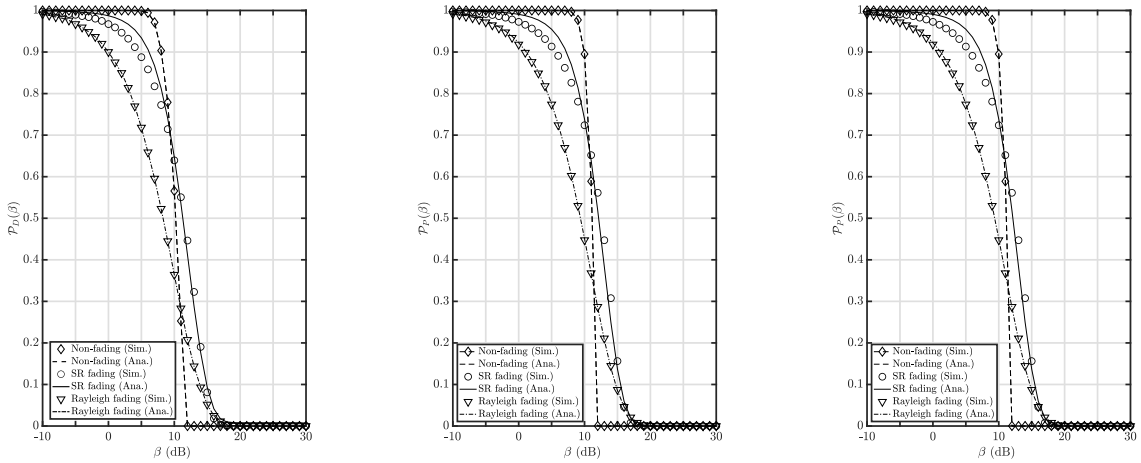

(a) Coverage probability for DbA scheme versus the SINR threshold.

(b) Coverage probability for PbA scheme versus the SINR threshold.

(c) Coverage probability for RbA scheme versus the SINR threshold.

Figure 7.3: Coverage probability achieved by each association scheme, in the SR, the Rayleigh and the non-fading scenarios.

to 3. The number of LEO satellites in each tier, N_1, N_2, and N_3, are 500, 1000, and 1500, respectively. The Earth's radius, $R_{\oplus}$, is considered to be 6371, km, while the transmit power of LEO satellites in each tier, P_1, P_2, and P_3, are 32W, 55.3W, and 87.8W. The thermal noise power, σ^2, is set to -81.4, dBm, and the main-lobe gain of LEO satellites and gUEs, are 47dBi and 10dBi, respectively. The side-lobe gain of LEO satellites and gUEs, are 27dBi and 0dBi, respectively. Lastly, the parameters of the SR fading model, b, Ω, and m, are set to 0.158, 19.4, and 1.59 [52].

Fig. 7.3 illustrates the impact of fading channels on the performance of LEO satellite networks. In specific, Fig. 7.3 plots the coverage probability achieved by the three association schemes (DbA, PbA, and RbA) in SR, Rayleigh and non-fading scenarios. Initially, in low SINR thresholds region, the non-fading scenario results in a higher coverage probability than other two fading scenarios, for all association schemes. However, as the SINR threshold increases, the non-fading scenario demonstrates the poorest performance, whereas the SR fading scenario consistently outperforms the Rayleigh fading scenario across all SINR regions. This can be explained by the fact that, fading can lead to random attenuation of signals, including interference, which can consequently enhance the SINR in certain scenarios. Taking this into account, the observed performance differences can be attributed to the

Yuan Guo

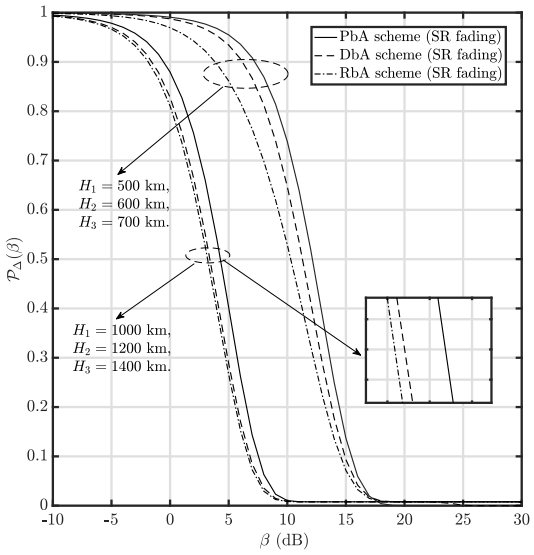

Figure 7.4: Coverage probability achieved by each association scheme versus the SINR threshold for different LEO satellites' altitudes.

distinct characteristics of each fading scenario. More specifically, the non-fading scenario excels at low SINR thresholds due to its stable signal strength; however, at higher SINR thresholds, its performance suffers from the lack of signal diversity arising from the absence of fading effects. In contrast, the SR fading, with its strong LoS component, consistently delivers more stable and robust signal quality than the Rayleigh fading scenario, which lacks such a component, across the entire range of SINR thresholds. Finally, we can observe that for each association scheme, the Rayleigh and non-fading scenarios demonstrate a perfect match between simulation (denoted by "Sim.") and analysis (denoted by "Ana.") results; while there are minor gaps between the simulation and analytical results for the SR fading scenario at low SINR thresholds due to the approximations used in the analysis.

Fig. 7.4 depicts the effect of LEO satellites' altitudes on the coverage performance. Specifically, Fig. 7.4 plots the coverage probability versus the SINR threshold for different association schemes and different altitudes. Initially, it can be observed that the coverage probability decreases with the increase of the LEO satellites' altitudes. This was expected since higher altitudes of LEO satellites lead to a longer propagation distance between the gUEs and its serving satellites, which results in a lower intended signal strength received by the gUEs that decreases the SINR. Moreover, we observe that the PbA scheme surpasses both the DbA and RbA schemes in terms of coverage probability. This can be explained by the fact that

Yuan Guo

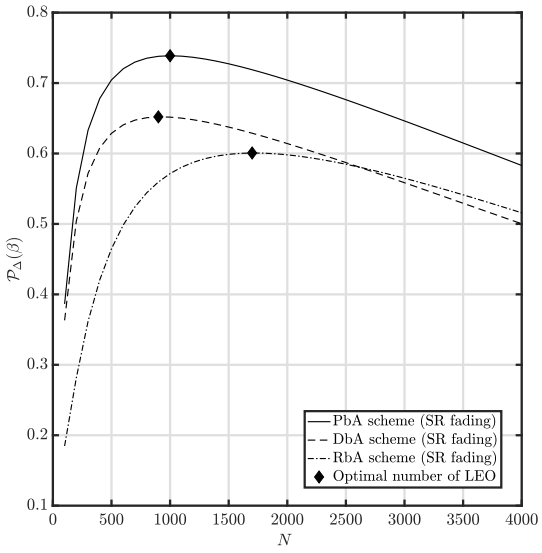

Figure 7.5: The coverage probability achieved by each association schemes versus the number of LEO satellites, where $\beta = 10$ dB and $N_1 = N_2 = N_3 = N$.

the PbA scheme associates the gUE with the LEO satellite that delivers the highest average signal power, thereby boosting the SINR. In contrast, the DbA scheme associates the gUE with the nearest LEO satellite, while other candidate LEO satellites with larger transmit power than the serving satellite generate strong interference, leading to a degraded SINR at the gUE. Moreover, the RbA scheme randomly associates the gUE with one of the candidate LEO satellites, which does not guarantee an optimal selection for achieving the highest SINR, leading to the lowest coverage probability. Finally, the difference in coverage probability between the DbA and RbA schemes diminishes as the satellites' altitude increases. This is due to the fact that as the altitude of the satellites increases, the difference in path loss between the nearest and other candidate LEO satellites becomes less significant, and thus the advantage of associating the gUE with the nearest LEO satellite in the DbA scheme diminishes.

Fig. 7.5 demonstrates the effect of the number of LEO satellites on the coverage performance. For the sake of simplicity, we consider that each tier comprises an equal number of LEO satellites, i.e. $N_1 = N_2 = N_3 = N$. Accordingly, Fig. 7.5 plots the coverage probability versus the the number of LEO satellites within each tier, i.e. N, for different association schemes, with the SINR threshold set to $\beta = 10$ dB. We can clearly observe that for all association schemes, namely DbA, PbA, and RbA, there is an initial increase in coverage probability as the number of LEO satel-

Yuan Guo

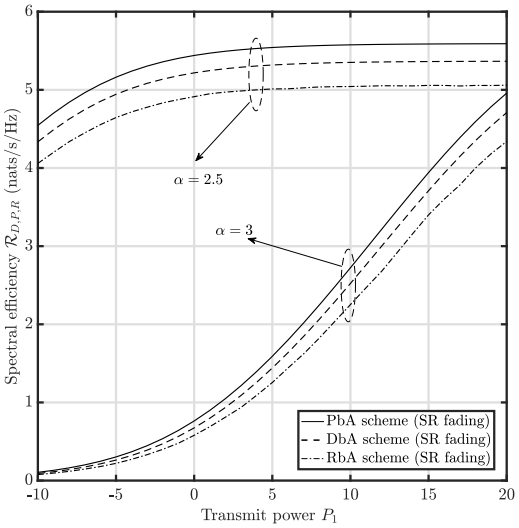

Figure 7.6: The spectral efficiency versus the transmit power of LEO satellites.

lites rises, followed by a decline after surpassing a particular threshold (denoted as “Optimal number of LEO"). The observed enhancement in coverage probability can be explained by the diminishing distance between the serving LEO satellite and the gUE as more LEO satellites are added, which results in decreased path-loss and subsequently leads to an elevated SINR at the gUE. However, when the number of LEO satellites exceeds a certain limit, the coverage probability experiences a downward trend. This decline is attributed to the increased presence of interfering satellites, which significantly increase the interference and adversely affect the overall SINR, ultimately reducing the coverage probability. Another notable observation is that the PbA scheme consistently achieves the highest coverage probability among the three association schemes. Additionally, the DbA scheme outperforms the RbA scheme when the number of LEO satellites is relatively small, while as the number of LEO satellites increases, the RbA scheme surpasses the DbA scheme in terms of coverage probability. This observation can explained by the fact that, as the number of LEO satellites increases, the RbA scheme’s random association with satellites across all tiers allows for better utilization of higher transmit power from higher altitude tiers, resulting in improved performance compared to the distance-based DbA scheme.

Finally, Fig. 7.6 shows the impact of LEO satellites’ transmit power and the large-scale fading on the spectral efficiency of the considered networks. More specifically, Fig. 7.6 plots the spectral efficiency versus the transmit power of the first tier

Yuan Guo

LEO satellites for different path-loss exponent. It should be noted that according to the power adjusting mechanism, the corresponding transmit power of the second and the third tier LEO satellites are given by $P_2 = \frac{H_2^{\alpha} G_{m,1}^{L}}{H_1^{\alpha} G_{m,2}^{L}} P_1$ and $P_3 = \frac{H_3^{\alpha} G_{m,1}^{L}}{H_1^{\alpha} G_{m,3}^{L}} P_1$, respectively. Firstly, for all association schemes, i.e. the DbA, the PbA, and the RbA schemes, a higher path-loss corresponds to a lower spectral efficiency, which can be attributed to the reduced signal strength at the receiver. Secondly, the PbA scheme consistently outperforms the DbA and RbA schemes, as it focuses on maximizing the received signal power, a crucial aspect that directly influences the achievable data rate. Finally, when the path-loss exponent is small (e.g., $\alpha = 2.5$), increasing the transmit power initially leads to a higher data rate. However, the gUE experiences strong interference from neighbouring satellites as a result of the reduced signal attenuation, which ultimately counterbalances the benefits of higher transmit power, causing the data rate to plateau and remain constant at a saturation point.

7.7 Summary

In this chapter,we present a comprehensive analysis of large-scale heterogeneous LEO satellite networks based on stochastic geometry. The proposed framework captures the heterogeneity of real-world LEO satellite network deployments, featuring various tiers of satellites with different altitudes, transmit powers, and densities. We introduce three association schemes and evaluate their performance in terms of association probability, coverage probability, and spectral efficiency, while the analytical expressions are derived by leveraging tools from stochastic geometry. Moreover, by aiming to reveal the impact of fading channels on network performance, we evaluate the coverage probability in different fading scenarios, i.e. SR, Rayleigh and non-fading scenarios with the employment of each association scheme. Our results highlight the critical impact of fading channels, altitude, the number of satellites, and transmit power on the coverage probability and spectral efficiency. Specifically, we demonstrate that multipath fading channels reduce coverage probability in low SINR regimes, while outperforming non-fading scenarios in high SINR situations. Additionally, the PbA scheme consistently outperforms the other two schemes, while the RbA scheme surpasses the DbA scheme as the number of satellites increases; and the optimal number of LEO satellites for achieving the highest coverage probability is numerically demonstrated. Furthermore,

Yuan Guo

we show that higher path-loss results in reduced spectral efficiency, and increasing transmit power initially enhances spectral efficiency and then remains constant due to interference from neighbouring satellites. Our work offers valuable insights and guidance for the design and optimization of future large-scale heterogeneous LEO satellite networks.

Yuan Guo

Chapter 8

LEO satellite-based space solar power systems

In this chapter, we explore the feasibility of a LEO satellite-based SSP system, where LEO satellites use large photovoltaic (PV) panels to collect solar power and then transmits it to a ground receiver. We establish a theoretical framework to analyze the performance of the considered LEO satellite-based SSP system. Specifically, by taking into account the satellite's rotation angle with respect to sunlight and the mobility of the LEO satellites, we analytically evaluate the solar energy collection through PV panels and quantify the amount of harvested energy by the ground receiver. Our results demonstrate that increasing transmit power of LEO satellites can boost the energy harvesting performance at the ground receiver. Furthermore, by deploying around 100 LEO satellites, a LEO satellite-based SSP system achieves comparable performance to that of a single geostationary orbit satellite-based SSP system.

8.1 Motivation and contributions

The concept of SSP systems was first proposed in [122]. Inspired by this, several SSP architectures have been proposed in the literature [45–47]. For instance, the National Aeronautics and Space Administration (NASA) conducted a study involving a large satellite deployed in geostationary orbit (GEO) equipped with PV panels for collecting solar energy [45]. The satellite uses a radio-frequency (RF) microwave to transmit many gigawatts of electricity, which is then collected by a large ground rec-

Yuan Guo

tifying antenna. More recently, the SunTower was conceptually studied by NASA, which employs an array of concentrator PV elements [46]. One of the key advantages of this design is its flexibility in terms of deployment options. The proposed SunTower satellite system can be deployed in middle Earth orbit, GEO altitudes, or LEO in a sun-synchronous orbit, depending on the specific application requirements. Moreover, the SPS 2000 Japanese model was proposed by the Institute of Space and Astronautical Science, which utilizes a LEO satellite equipped with large solar panels to transmit megawatts of power to the ground [47].

LEO satellites are already widely used for a variety of purposes, including communication, remote sensing, and Earth observation [123]. One of the main advantages of using LEO satellites for SSP systems is their closer proximity to Earth compared to other orbiting satellites, such as GEO satellites or lunar bases. This means that the energy transmitted to Earth experiences less transmission loss, thereby making the system more efficient [124]. Despite these advantages of LEO satellites, their high mobility introduces additional challenges on the system implementation. Motivated by this, in this paper, we investigate the feasibility of an SSP system utilizing LEO satellites. More specifically, the main contributions of this work are as follows. First, we analyze the satellite solar energy collection through the PV panels by taking into account the satellite rotation angle with the sunlight. Then, the energy harvested by the ground receiver is quantified by considering the mobility of LEO satellites. Our results indicate that increasing the transmit power of LEO satellites can significantly improve the energy harvesting performance of the ground receiver. Additionally, a LEO satellite-based SSP system can achieve comparable performance to a GEO satellite-based SSP system by deploying around one hundred LEO satellites.

8.2 System model

We consider a LEO satellite-based SSP system, which consists of N identical LEO satellites evenly deployed on a sun-synchronous orbit as illustrated in Fig. 8.1. Particularly, the sun-synchronous orbit is characterized by the altitude of LEO satellites, as well as the angle between the orbital plane of the satellite and the sunlight, which are denoted by H and φ, respectively. Each LEO satellite is equipped with a large PV cell array to collect solar energy, while the collected energy is stored in large-

Yuan Guo

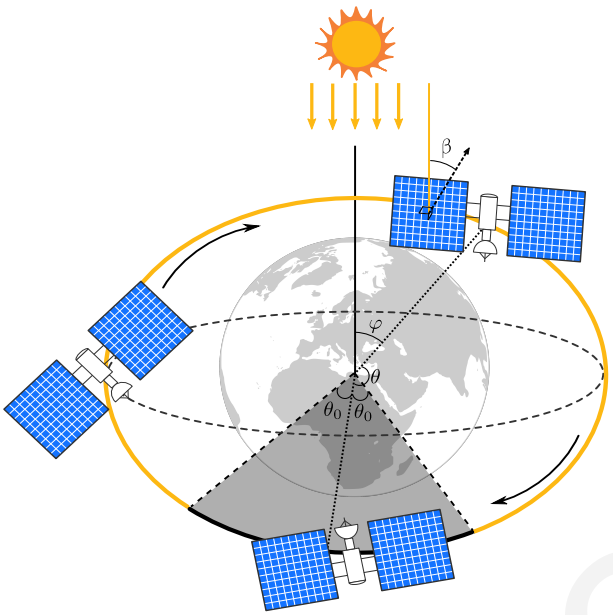

Figure 8.1: Illustration of the LEO satellite's orbit.

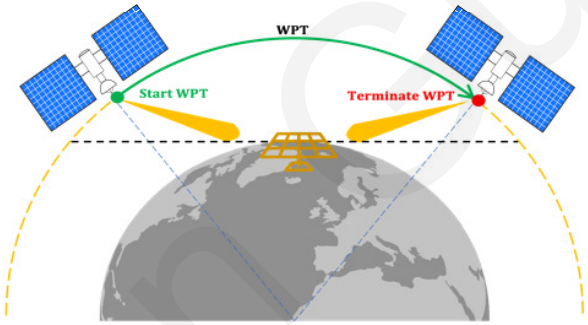

Figure 8.2: Illustration of the WPT process.

capacity rechargeable batteries [125]. Moreover, we consider that multiple large ground rectennas (gRAs) are deployed according to the ground track of LEO satellites' orbits, such that each LEO satellite pass over a gRA every orbit period. Once a LEO satellite pass over a gRA, denoted as *transmission window*, it transmits the collected energy to the gRA via microwave radiation, as illustrated in Fig. 8.2, which is referred to as the wireless power transfer (WPT) process.

8.3 Satellite energy collection

In this section, we focus on modeling the output energy of the solar PV panels. We note that the output power of the solar panels is not constant and is affected by the area of the PV cell array, $\mathcal{A}_s$, the efficiency of energy conversion, η_{PV}, and the angle between the sunlight and the normal line of the solar panels. Typically, the

satellite's solar panels adopt single-axis solar tracking, which adjusts the angle of the solar panels with the sun as the satellite orbits the Earth, thereby maximizing the amount of solar energy that can be harvested [125]. More specifically, let θ denote the satellite rotation angle from the midpoint of the shaded area, as depicted in Fig. 8.1. Let β denote the angle between the sunlight and the normal of the solar panels. By adopting the single-axis solar tracking, the minimum achievable β can be expressed as [125, 126]

$$\beta(\theta) = \arccos \sqrt{1 - \cos^2 \varphi \cos^2 \theta}. \tag{8.1}$$

Furthermore, during each orbit of a LEO satellite, its solar panels collect energy as the satellite moves through areas of direct sunlight. We define $\mathcal{G}_0$ as the solar irradiance per unit area. In the following lemma, we evaluate the total energy collected by each LEO satellite during one orbit period.

Lemma 8.1. *The energy collected by the solar panels of a LEO satellite for one orbit period is given by*

$$\mathcal{E}_{\text{Solar}} = \int_{\frac{\theta_0}{\omega}}^{\frac{2\pi-2\theta_0}{\omega}} \mathcal{G}_0 \eta_{\text{PV}} \mathcal{A}_{\text{s}} \beta(\omega t) \mathrm{d}t, \tag{8.2}$$

where

$$\theta_0 = \begin{cases} 0, \varphi > \arcsin \frac{R_\oplus}{R_\oplus + H} \\ \arcsin \frac{\sqrt{R_\oplus^2 \cos^2 \varphi - (2R_\oplus H + H^2) \sin^2 \varphi}}{(R_\oplus + H) \cos \varphi}, \end{cases} \tag{8.3}$$

represents the half-angle of the shaded area as shown in Fig. 8.1, $\omega = \sqrt{\frac{GM}{(R_\oplus + H)^3}}$ *is the angular velocity of the LEO satellite, G is the gravitational constant, and M is the mass of Earth and* $R_\oplus$ *is the Earth radius.*

Proof. We consider that the LEO satellite is initially located at the midpoint of the shaded area. At time t, the satellite has passed an angle $\theta = \omega t$, where $0 < t < \frac{2\pi}{\omega}$ and the output power of the PV solar panels can be formulated as

$$\mathcal{E}(t) = \begin{cases} 0, & t \leq \frac{\theta_0}{\omega} \\ \mathcal{G}_0 \eta_{\text{PV}} \mathcal{A}_{\text{s}} \beta(\omega t), & \frac{\theta_0}{\omega} \leq t \leq \frac{\pi}{\omega} \\ \mathcal{G}_0 \eta_{\text{PV}} \mathcal{A}_{\text{s}} \beta(2\pi - \omega t), & \frac{\pi}{\omega} \leq t \leq \frac{2\pi - 2\theta_0}{\omega} \\ 0, & t \geq \frac{2\pi - 2\theta_0}{\omega} \end{cases} \tag{8.4}$$

Then, by noting that $\beta(2\pi - \omega t) = \beta(\omega t)$ due to the periodicity of the cosine function, and by integrating the output power over one orbit period, the final expression in Lemma 8.1 is derived. □

Yuan Guo

8.4 Wireless power transfer

In this section, we analyze the WPT operation from the satellite to the gRA. Typically, the solar energy harvested by the PV panels is stored by the rechargeable batteries and then passes through a direct current to RF (DC-to-RF) converter to generate a microwave of suitable frequency, i.e. f_{RF}. Then, the output power is beamed down to the considered gRA, where it is converted into a usable form. Subsequently, we discuss the RF link efficiency between the transmitting satellite and the gRA, before analyzing the harvested energy by the gRA.

8.4.1 Microwave link efficiency

The size of the transmit and receive antenna apertures plays a crucial role in the design of the microwave link efficiency. In general, microwave links are modeled using the Friis transmission equation. However, for microwave power transmission applications, a huge antenna system is required. As a result, the Friis transmission equation is no longer valid [48]. In addition, the relationship between the antenna apertures, wavelength, and distance has only been analyzed empirically [48, 127]. Therefore, based on these experimental results, we provide a closed-form expression for the energy collection efficiency of the RF link from the satellite to the gRA, by using curve fitting, as depicted in Fig. 8.3. More specifically, it is modeled as

$$\eta_{\mathrm{RF}}(r) = \frac{c_1}{c_2 + \exp(-c_3\tau(r))}, \tag{8.5}$$

where $\tau(r) = \frac{\sqrt{\mathcal{A}_{\mathrm{t}}\mathcal{A}_{\mathrm{r}}}}{\lambda r}$ represents the normalized antenna apertures, $\mathcal{A}_{\mathrm{t}}$ and $\mathcal{A}_{\mathrm{r}}$ denote the transmit and receive antenna apertures, respectively. Moreover, $\lambda = \frac{c}{f_{\mathrm{RF}}}$ is the wavelength, c is the speed of the light, and r is the distance between the satellite and the gRA. Finally, $c_1 = 0.04417$, $c_2 = 0.0445$, and $c_3 = 3.643$ represent the constants for the fitting function.

8.4.2 Energy harvesting analysis

We consider that each LEO satellite intends to transmit all the collected energy during the *transmission window*. Each LEO satellite transmits energy with a constant transmit power P_t. More specifically, the WPT process starts at the location with the Earth-centered zenith angle $-\phi$ and terminates at the location with the zenith

Yuan Guo

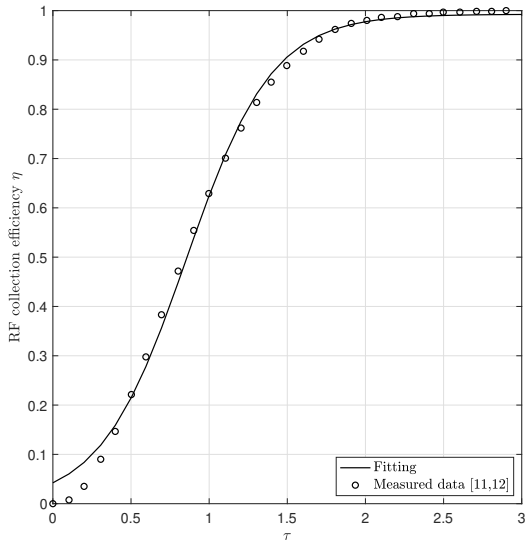

Figure 8.3: RF collection efficiency as function of τ.

Table 8.1: System parameters.

Parameter	**LEO** [47]	**GEO** [48]
Altitude (H)	500 km	36000 km
Solar panel size ($\mathcal{A}_\mathrm{s}$)	1000×1000 m^2	6700×2500 m^2
Satellite transmit antenna aperture ($\mathcal{A}_\mathrm{t}$)	132×132 m^2	$750^2\pi$ m^2
RF collection efficiency (η_RF)	(8.5)	75%
Orbit angle (φ)	$\pi/4$	-
Solar irradiance ($\mathcal{G}_0$)	1370 W/m^2	
Gravitational constant (G)	6.67259×10^{-11} m^{3}kg^{-1}s^{-2}	
Mass of Earth (M)	5.9736×10^{24} kg	
Radius of Earth ($R_\oplus$)	6371 km	
Operating frequency (f_RF)	2.45 GHz	
Ground antenna aperture ($\mathcal{A}_\mathrm{r}$)	$2500^2\pi$ m^2	
PV energy conversion efficiency (η_PV)	30%	
DC-to-RF conversion efficiency ($\eta_{\mathrm{DC-RF}}$)	76%	
RF-to-DC conversion efficiency ($\eta_{\mathrm{RF-DC}}$)	70%	

angle ϕ, which are denoted by the green and red points in Fig. 8.2, respectively. It is worth mentioning that during the WPT process, the satellite's solar panels continue to capture and store energy that can be utilized for energy transmission during sub-

Yuan Guo

sequent orbital period. Moreover, a LEO satellite can perform WPT only when it is visible from the gRA's position, i.e. the LEO satellite is located above the horizon of the gRA. Hence, the zenith angle ϕ is upper-bounded, i.e. $|\phi| \leq \arccos\left(\frac{R_\oplus}{R_\oplus+H}\right)$. Therefore, the time for the WPT process of each LEO satellite for one orbit period is given by

$$T_s = \min\left\{\frac{\eta_{\mathrm{DC-RF}}\mathcal{E}_{\mathrm{Solar}}}{P_{\mathrm{t}}}, \frac{2}{\omega}\arccos\left(\frac{R_\oplus}{R_\oplus+H}\right)\right\}, \tag{8.6}$$

where $\eta_{\mathrm{DC-RF}}$ denotes the overall efficiency of the DC-to-RF converter. Based on the discussion above, we are now able to provide our main result, i.e. the amount of harvested energy at the gRA during one orbit period, in the following proposition.

Proposition 8.1. *The amount of harvested energy by the gRA during one orbit period is given by*

$$\mathcal{E}_{\mathrm{gRA}} = 2N\int_0^{\frac{T_s}{2}} P_t\eta_{\mathrm{RF}}\big(r(t)\big)\eta_{\mathrm{RF-DC}}\mathrm{d}t, \tag{8.7}$$

where

$$r(t) = \sqrt{(R_\oplus+H)^2 + R_\oplus^2 - 2(R_\oplus+H)R_\oplus\cos(\omega t)},$$

and $\eta_{\mathrm{RF-DC}}$ is the RF-to-DC energy conversion efficiency of the gRA.

Proof. Consider that at time $t = 0$, the LEO satellite starts to transmit power to the gRA. After a period of time Δt ($\Delta t \leq T_s$), the Euclidean distance between the LEO satellite and the gRA can be calculated by using the Law of cosines, which is given by

$$r(\Delta t) = \begin{cases} \sqrt{(R_\oplus+H)^2 + R_\oplus^2 - 2(R_\oplus+H)R_\oplus\cos(\phi-\omega\Delta t)}, & 0 \leq t \leq \frac{T_s}{2} \\ \sqrt{(R_\oplus+H)^2 + R_\oplus^2 - 2(R_\oplus+H)R_\oplus\cos(\omega\Delta t-\phi)}, & \frac{T_s}{2} \leq t \leq T_s. \end{cases} \tag{8.8}$$

Then, the instantaneous harvested power at the gRA is given by

$$P_{\mathrm{gRA}}(\Delta t) = P_t\eta_{\mathrm{RF}}(r(\Delta t))\eta_{\mathrm{RF-DC}}. \tag{8.9}$$

Hence, the total harvested energy by the gRA from N LEO satellite during one orbit period can be evaluated by integrating the received power $P_{\mathrm{gRA}}(\Delta t)$ over the time period $t \in [0, T_s]$ and then multiplying by N, i.e.

$$\mathcal{E}_{\mathrm{gRA}} = N\int_0^{T_s} P_t\eta_{\mathrm{RF}}\big(r(\Delta t)\big)\eta_{\mathrm{RF-DC}}\mathrm{d}\Delta t. \tag{8.10}$$

In addition, by noting that $\phi = \frac{\omega T_s}{2}$ and $\cos(\phi-\omega\Delta t) = \cos(\omega\Delta t-\phi)$, the integral range of (8.10) can be adjusted to $[0, \frac{T_s}{2}]$. Ultimately, the final result in Proposition 8.1 is obtained. □

Yuan Guo

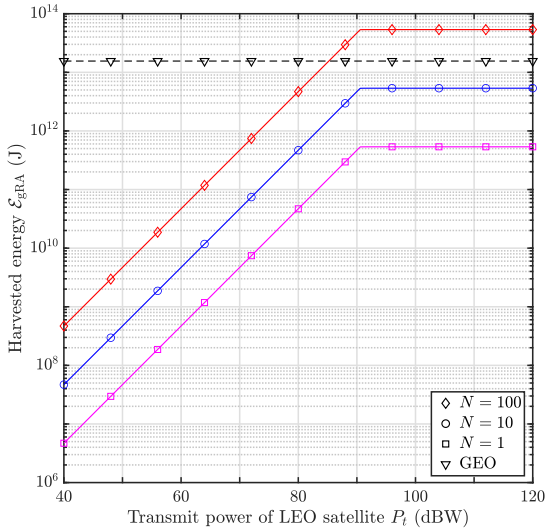

Figure 8.4: Harvested energy by the gRA vs. the transmit power of LEO satellites.

8.5 Numerical results

We now present the numerical results of the considered LEO satellite-based SSP system. The system parameters are summarized in Table 1. The effect of the transmit power of LEO satellites on the harvested energy by the gRA is shown in Fig. 8.4. Specifically, we plot the amount of the harvested energy by the gRA for one orbit period, i.e. $\mathcal{E}_{\mathrm{gRA}}$ (J), versus the transmit power of LEO satellites, i.e. P_t (dBW), for various number of LEO satellites, i.e. $N \in \{1, 10, 100\}$. We first notice that the harvested energy by the gRA first increases with an increase in the transmit power of the LEO satellites and then reaches a constant value. This is expected since increasing the transmit power allows each LEO satellite to transmit all of its stored energy to the gRA in a shorter amount of time. Therefore, the LEO satellite begins transmitting when it is close to the gRA, resulting in a shorter distance between the satellite and the gRA during the WPT process, thus a higher collection efficiency can be achieved. In addition, for scenarios with extremely high transmit power, the LEO satellite transmits all energy immediately, which leads to a constant harvested energy by the gRA. Finally, we numerically evaluate the performance achieved by the GEO-based SSP system [48] for the comparison purpose (denoted by dash lines). It can be observed that increasing the number of LEO satellites can lead to a greater amount of energy harvested by the gRA, resulting in comparable performance to that of a single GEO satellite-based SSP system. This is due to the fact that by having

Yuan Guo

multiple LEO satellites during one orbit period, the gRA can harvest energy from each of them, resulting in a higher overall harvested energy.

8.6 Summary

In this chapter, we investigate a LEO satellite-based SSP system for harvesting solar energy and wirelessly transmitting it to a gRA. We analyze the satellite solar energy collection through PV panels and provide WPT analysis to quantify the performance of the SSP system, where the expression for the harvested energy by the gRA during one orbit period is analytically derived. Our results show that the transmit power of LEO satellites has a significant effect on the harvested energy by the gRA. In specific, increasing the transmit power of LEO satellites boosts the energy harvested by the gRA. Finally, we conclude that deploying a larger number of LEO satellites achieves comparable performance to that of a GEO satellite-based SSP system.

Yuan Guo

Chapter 9

Conclusion and future work

In the upcoming era of 6G, SWIPT has a critical role to play in fostering highly reliable, ultra-dense, and energy-efficient networks. Unlike previous generations of wireless technology, 6G envisions ubiquitous connectivity with a heavy emphasis on IoT devices and AI-driven applications, demanding a seamless, high-rate, and continuous supply of power. SWIPT, with its transformative capability to wirelessly transmit both data and energy simultaneously, offers a robust solution to this challenge. By harnessing the dual functionality of electromagnetic waves, SWIPT can empower a new generation of self-sustaining devices, alleviating concerns around battery life, frequent recharging, and environmental impact, thus leading to a truly connected and sustainable future.

In this thesis, we addressed some of the challenges brought by the integration of SWIPT in cellular networks, by taking into account the unique features of next-generation networks. We primarily focus on the system-level analysis of SWIPT-enabled 6G cellular networks, by proposing novel advanced antenna selection, cell sleeping, mobility management and user association techniques, etc. By employing stochastic geometry tools, we established a tractable analytical frameworks to evaluate the achieved performance of the aforementioned techniques from a large-scale point-of-view. Additionally, the performance of LEO satellite-based networks was assessed, highlighting the potential of space-based information and energy transfer systems. Tractable closed-form expressions for fundamental network performance metrics, such as the coverage probability, association probability and handover probability, etc., are derived. These closed-form expressions, provide valuable engineering insights to help network operators in the deployment of SWIPT-

Yuan Guo

enabled networks, and how key system parameters affect the network performance.

Furthermore, the practical deployment of the models and techniques proposed in this thesis necessitates a nuanced understanding of their real-world applicability. The advanced antenna selection, cell sleeping, mobility management, and user association techniques developed herein are not only theoretically robust but are also designed with practical implementation scenarios in mind. For instance, the proposed solutions are highly relevant for urban environments where the density of IoT devices and the demand for AI-driven applications are rapidly increasing. These environments, characterized by dynamic user mobility patterns and varying energy demands, stand to benefit significantly from the energy efficiency and enhanced connectivity provided by SWIPT. Additionally, the exploration of LEO satellite-based networks opens new avenues for extending connectivity to remote and underserved areas, showcasing the feasibility of employing SWIPT in diverse operational contexts. By facilitating a seamless integration of SWIPT into existing and future cellular infrastructures, this research paves the way for network operators to harness the benefits of 6G technologies effectively. Pilot programs and real-world trials will be instrumental in validating the efficacy of these proposed models, offering a clear pathway for transitioning from theoretical insights to practical implementations. Such empirical validations are crucial for optimizing model parameters in accordance with real-world complexities, thereby ensuring the scalability and sustainability of SWIPT-enabled 6G networks. This thesis underscores the importance of bridging the gap between theoretical research and practical applications, highlighting the critical role of SWIPT in achieving the ambitious goals of next-generation wireless networks.

9.1 Future work

In advancing the exploration of next-generation wireless networks, future work will integrate novel concepts poised to significantly enhance network functionalities and efficiencies. This includes pioneering efforts to leverage base stations in sleep mode for energy harvesting, which opens up new avenues for energy efficiency across network infrastructures. Moreover, the exploration of hybrid antenna structures will be pivotal in optimizing energy harvesting and communication capabilities simultaneously, marking a strategic evolution in network component design. Additionally,

Yuan Guo

within the vehicular network dimension, the research focus will refine the criteria for sensor deployment, prioritizing the 'best' sensor selection based on performance metrics rather than proximity alone, which promises to elevate the accuracy and reliability of vehicular communications and sensing capabilities. These forward-looking initiatives are designed to seamlessly integrate with my existing research directions, enriching comprehensive strategy to advance wireless communication networks' performance, sustainability, and adaptability. Some other possible future directions are summarized as the following:

1. **SWIPT-assisted ISAC systems for vehicular networks**: The integration of sensing functionality is emerging as a key feature of the 6G networks, allowing for the exploitation of dense cell infrastructures to construct a perceptive network [128–131]. ISAC's implementation in vehicular systems is critical for enhancing road safety and traffic management. By leveraging the capabilities of 6G networks for real-time environmental sensing and robust data communication, ISAC facilitates adaptive and intelligent interactions among vehicles, infrastructure, and pedestrians [132, 133]. This adaptability is crucial in dynamic traffic conditions, where rapid responses to changing scenarios can prevent accidents and improve traffic flow. The integration of SWIPT into ISAC systems marks a trans-formative step in wireless technology. SWIPT addresses a fundamental challenge in environments where a consistent power supply and efficient communication are essential but difficult to maintain. This is particularly pertinent in remote or autonomous sensors used in vehicular networks. By allowing these sensors to receive power and transmit data simultaneously, SWIPT significantly enhances the sustainability and reliability of vehicular communication systems. Despite all the above advancements, several challenges still arise when applying SWIPT-assisted ISAC systems to vehicular networks, which as summarized as following:

    - Accurate spatial model of vehicular networks: Developing a precise spatial model for vehicular networks is crucial. This involves understanding and accurately predicting the movement and distribution of vehicles within a network. The model must account for dynamic factors such as vehicle speed, density, and direction, as well as the urban landscape which can include varying building densities and road layouts [108]. The

model discussed in Chapter 6, while comprehensive, can benefit from further refinement to encompass a broader range of environments. Extending it to accurately represent different settings, such as large-scale and small-scale cities, urban centers, remote areas, typical roads, and highways, will enhance its applicability and effectiveness. Such an expanded model would be invaluable in optimizing the deployment and performance of SWIPT-assisted ISAC systems in various vehicular scenarios. By accounting for the diverse characteristics of these environments, the model can facilitate more precise planning and implementation, ensuring that the technological solutions are tailored to meet the specific demands and challenges of each unique setting.

- Interference management: In SWIPT-assisted ISAC systems, managing interference is a complex yet opportunistic task. The superimposition of data transmission and power transfer signals often leads to interference, which, in the context of ultra-dense mobile device deployments, can be significantly magnified. This interference, however, presents an opportunity for energy harvesting. Advanced signal processing is key, separating data signals for clear communication while capturing energy from ambient interference. This requires innovative approaches in signal processing that dynamically adapt to varying interference levels [11].
- Mobility management: Mobility management in SWIPT-assisted ISAC systems within vehicular networks presents multifaceted challenges. In vehicular networks, vehicles are constantly moving, which leads to frequent changes in network topology [134–136]. Maintaining stable connectivity and seamless communication in such a highly mobile environment is challenging. SWIPT-assisted ISAC systems must be capable of dynamically adjusting to these changes to ensure continuous and reliable communication. As vehicles move, they often need to switch between different network cells or access points. This process, known as handover, must be managed efficiently to avoid communication disruptions. The challenge is to minimize the latency and potential data loss during these handovers, which is particularly crucial for time-sensitive applications like autonomous driving.

Yuan Guo

2. **SWIPT-enabled satellite communication networks**: Satellite communication systems, particularly those based on LEO satellites, are increasingly recognized for their potential to drive advanced applications such as high-speed internet, ultra-low latency communication, and extensive IoT deployments. These systems are integral in empowering diverse sectors like smart cities, agriculture, and transportation. As the global communication infrastructure evolves from 5G to 6G, the role of satellite communication networks becomes even more crucial in achieving the vision of a fully connected and intelligent world. The integration of SWIPT into these satellite networks represents an exciting frontier. While LEO satellite-based communication and energy transfer systems have been discussed in this thesis, the co-design of information and power transfer in satellite networks through SWIPT remains a largely unexplored area, which presents several design challenges:

    - Energy efficiency and harvesting: In satellite networks, energy efficiency is paramount. SWIPT technology must be designed to optimize power transfer without compromising the efficiency of information transmission. The challenge lies in developing energy harvesting mechanisms that can effectively capture and utilize solar and other forms of energy in space, such as the LEO satellites-based SSP system.
    - Signal propagation and attenuation: The vast distances and atmospheric conditions in satellite communication result in significant signal attenuation. Designing SWIPT systems that can effectively transmit power and data over long distances while overcoming these losses is a major challenge.
    - Cost and complexity: Finally, the cost and complexity of implementing SWIPT in satellite networks are significant. Balancing the technological advancements with practical, cost-effective solutions is crucial for the viability of these systems.

Yuan Guo

Bibliography

[1] Ericsson. (2022) Ericsson mobility report. [Online]. Available: https://www.ericsson.com/en/reports-and-papers/mobility-report/reports

[2] IoT Analytics. (2020) State of the iot 2020: 12 billion iot connections, surpassing non-iot for the first time. [Online]. Available: https://iot-analytics.com/state-of-the-iot-2020-12-billion-iot-connections-surpassing-non-iot-for-the-first-time/

[3] J. G. Andrews, S. Buzzi, W. Choi, S. V. Hanly, A. Lozano, A. C. K. Soong, and J. C. Zhang, "What will 5G be?" *IEEE J. Sel. Areas Commun.*, vol. 32, no. 6, pp. 1065–1082, Jun. 2014.

[4] T. Huang, W. Yang, J. Wu, J. Ma, X. Zhang, and D. Zhang, "A survey on green 6G network: Architecture and technologies," *IEEE Access*, vol. 7, pp. 175 758–175 768, Dec. 2019.

[5] Z. Zhang, Y. Xiao, Z. Ma, M. Xiao, Z. Ding, X. Lei, G. K. Karagiannidis, and P. Fan, "6G wireless networks: Vision, requirements, architecture, and key technologies," *IEEE Veh. Technol. Mag.*, vol. 14, no. 3, pp. 28–41, Sep. 2019.

[6] H. Viswanathan and P. E. Mogensen, "Communications in the 6G era," *IEEE Access*, vol. 8, pp. 57 063–57 074, Mar. 2020.

[7] M. Vaezi, A. Azari, S. R. Khosravirad, M. Shirvanimoghaddam, M. M. Azari, D. Chasaki, and P. Popovski, "Cellular, wide-area, and non-terrestrial IoT: A survey on 5G advances and the road toward 6G," *IEEE Commun. Surv. Tutor.*, vol. 24, no. 2, pp. 1117–1174, Feb. 2022.

[8] Y. Hui, N. Cheng, Z. Su, Y. Huang, P. Zhao, T. H. Luan, and C. Li, "Secure and personalized edge computing services in 6G heterogeneous vehicular networks," *IEEE Internet Things J.*, vol. 9, no. 8, pp. 5920–5931, Apr. 2022.

[9] J. Angjo, I. Shayea, M. Ergen, H. Mohamad, A. Alhammadi, and Y. I. Daradkeh, "Handover management of drones in future mobile networks: 6G technologies," *IEEE Access*, vol. 9, pp. 12 803–12 823, Jan. 2021.

[10] S. Özyurt, A. F. Coşkun, S. Büyükçorak, G. Karabulut Kurt, and O. Kucur, "A survey on multiuser SWIPT communications for 5G+," *IEEE Access*, vol. 10, pp. 109 814–109 849, Oct. 2022.

[11] I. Krikidis and C. Psomas, "Wireless information and power transfer: A bottom-up multi-layer design framework," *IEEE Internet Things Mag.*, vol. 6, no. 1, pp. 142–147, Mar. 2023.

Yuan Guo

[12] Q. Qi, X. Chen, C. Zhong, and Z. Zhang, "Integration of energy, computation and communication in 6G cellular internet of things," *IEEE Commun. Lett.*, vol. 24, no. 6, pp. 1333–1337, Jun. 2020.

[13] I. Krikidis, S. Timotheou, S. Nikolaou, G. Zheng, D. W. K. Ng, and R. Schober, "Simultaneous wireless information and power transfer in modern communication systems," *IEEE Commun. Mag.*, vol. 52, no. 11, pp. 104–110, Nov. 2014.

[14] R. Zhang and C. K. Ho, "MIMO broadcasting for simultaneous wireless information and power transfer," *IEEE Trans. Wireless Commun.*, vol. 12, no. 5, pp. 1989–2001, May 2013.

[15] J. Wang, K. Zhu, and E. Hossain, "Green internet of vehicles (IoV) in the 6G era: Toward sustainable vehicular communications and networking," *IEEE Trans. Green Communi. Netw.*, vol. 6, no. 1, pp. 391–423, Mar. 2022.

[16] A. Kurs, A. Karalis, R. Moffatt, J. D. Joannopoulos, P. Fisher, and M. Soljačić, "Wireless power transfer via strongly coupled magnetic resonances," *Science*, vol. 317, no. 5834, pp. 83–86, Jul. 2007.

[17] V. Liu, A. Parks, V. Talla, S. Gollakota, D. Wetherall, and J. R. Smith, "Ambient backscatter: Wireless communication out of thin air," *ACM SIGCOMM Comput. Commun. Rev.*, vol. 43, no. 4, pp. 39–50, Aug. 2013.

[18] Y. Alsaba, S. K. A. Rahim, and C. Y. Leow, "Beamforming in wireless energy harvesting communications systems: A survey," *IEEE Commun. Surv. Tutor.*, vol. 20, no. 2, pp. 1329–1360, Jan. 2018.

[19] M. Di Renzo and W. Lu, "System-level analysis and optimization of cellular networks with simultaneous wireless information and power transfer: Stochastic geometry modeling," *IEEE Trans. Veh. Technol.*, vol. 66, no. 3, pp. 2251–2275, Mar. 2017.

[20] A. I. Akin, I. Stupia, and L. Vandendorpe, "On the effect of blockage objects in dense mimo swipt networks," *IEEE Trans. Commun.*, vol. 67, no. 2, pp. 1059–1069, Feb. 2019.

[21] A. S. Parihar, P. Swami, and V. Bhatia, "On performance of swipt enabled PPP distributed cooperative noma networks using stochastic geometry," *IEEE Trans. Veh. Technol.*, vol. 71, no. 5, pp. 5639–5644, May 2022.

[22] S. Kusaladharma, W.-P. Zhu, W. Ajib, and G. A. A. Baduge, "Stochastic geometry based performance characterization of SWIPT in cell-free massive MIMO," *IEEE Trans. Veh. Technol.*, vol. 69, no. 11, pp. 13 357–13 370, Nov. 2020.

[23] C. Psomas and I. Krikidis, "Successive interference cancellation in bipolar ad hoc networks with SWIPT," *IEEE Wireless Commun. Lett.*, vol. 5, no. 4, pp. 364–367, Aug. 2016.

[24] Z. Popovic, "Cut the cord: Low-power far-field wireless powering," *IEEE Microwave Mag.*, vol. 14, no. 2, pp. 55–62, Mar. 2013.

[25] M. Haenggi, *Stochastic Geometry for Wireless Networks.* Cambridge University Press, 2012.

[26] E. Demarchou, C. Psomas, and I. Krikidis, "Mobility management in ultra-dense networks: Handover skipping techniques," *IEEE Access*, vol. 6, pp. 11 921–11 930, Feb. 2018.

[27] S. S. Kalamkar, F. M. Abinader, F. Baccelli, A. S. M. Fani, and L. G. U. Garcia, "Stochastic geometry-based modeling and analysis of beam management in 5G," in *IEEE Global Commun. Conf.*, Taipei, Dec. 2020, pp. 1–6.

[28] W. Bao and B. Liang, "Stochastic geometric analysis of handoffs in user-centric cooperative wireless networks," in *Proc. IEEE Int. Conf. Comput. Commun.*, San Francisco, CA, USA, Apr. 2016, pp. 1–9.

[29] W. Sun, L. Wang, J. Liu, N. Kato, and Y. Zhang, "Movement aware CoMP handover in heterogeneous ultra-dense networks," *IEEE Trans. Commun.*, vol. 69, no. 1, pp. 340–352, Jan. 2021.

[30] J. G. Andrews, F. Baccelli, and R. K. Ganti, "A tractable approach to coverage and rate in cellular networks," *IEEE Trans. Commun.*, vol. 59, no. 11, pp. 3122–3134, Nov. 2011.

[31] M. Haenggi, J. G. Andrews, F. Baccelli, O. Dousse, and M. Franceschetti, "Stochastic geometry and random graphs for the analysis and design of wireless networks," *IEEE J. Sel. Areas Commun.*, vol. 27, no. 7, pp. 1029–1046, Sep. 2009.

[32] E. G. Larsson, O. Edfors, F. Tufvesson, and T. L. Marzetta, "Massive MIMO for next generation wireless systems," *IEEE Commun. Mag.*, vol. 52, no. 2, pp. 186–195, Feb. 2014.

[33] L. Zheng and D. Tse, "Diversity and multiplexing: a fundamental tradeoff in multiple-antenna channels," *IEEE Trans. Inf. Theory*, vol. 49, no. 5, pp. 1073–1096, May 2003.

[34] F. Rusek, D. Persson, B. K. Lau, E. G. Larsson, T. L. Marzetta, O. Edfors, and F. Tufvesson, "Scaling up MIMO: Opportunities and challenges with very large arrays," *IEEE Signal Process. Mag.*, vol. 30, no. 1, pp. 40–60, Jan. 2013.

[35] O. B. S. Ali, C. Cardinal, and F. Gagnon, "Performance of optimum combining in a Poisson field of interferers and Rayleigh fading channels," *IEEE Trans. Wireless Commun.*, vol. 9, no. 8, pp. 2461–2467, Aug. 2010.

[36] H. Gao, P. Smith, and M. Clark, "Theoretical reliability of MMSE linear diversity combining in Rayleigh-fading additive interference channels," *IEEE Trans. Commun.*, vol. 46, no. 5, pp. 666–672, May 1998.

[37] X. Yu, J. Zhang, M. Haenggi, and K. B. Letaief, "Coverage analysis for millimeter wave networks: The impact of directional antenna arrays," *IEEE J. Sel. Areas Commun.*, vol. 35, no. 7, pp. 1498–1512, Jul. 2017.

[38] S. S. Kalamkar, F. Baccelli, F. M. Abinader, A. S. M. Fani, and L. G. U. Garcia, "Beam management in 5G: A stochastic geometry analysis," *IEEE Trans. Wireless Commun.*, vol. 21, no. 4, pp. 2275–2290, Apr. 2022.

Yuan Guo

[39] S. Aghashahi, S. Aghashahi, Z. Zeinalpour-Yazdi, A. Tadaion, and A. Asadi, "Stochastic modeling of beam management in mmWave vehicular networks," *IEEE Trans. Mob. Comput.*, vol. 22, no. 6, pp. 3665–3676, Jun. 2023.

[40] P. Popineau, S. S. Kalamkar, and F. Baccelli, "On velocity-based association policies for multi-tier 5G wireless networks," in *IEEE Global Commun. Conf.*, Dec. 2021, pp. 1–6.

[41] X. Fang, W. Feng, T. Wei, Y. Chen, N. Ge, and C.-X. Wang, "5G embraces satellites for 6G ubiquitous IoT: Basic models for integrated satellite terrestrial networks," *IEEE Internet Things J.*, vol. 8, no. 18, pp. 14 399–14 417, Sep. 2021.

[42] E. Yaacoub and M.-S. Alouini, "A key 6G challenge and opportunity—connecting the base of the pyramid: A survey on rural connectivity," *Proc. IEEE*, vol. 108, no. 4, pp. 533–582, Apr. 2020.

[43] X. Zhu and C. Jiang, "Integrated satellite-terrestrial networks toward 6G: Architectures, applications, and challenges," *IEEE Internet Things J.*, vol. 9, no. 1, pp. 437–461, Jan. 2022.

[44] S. Sasaki, K. Tanaka, and K.-i. Maki, "Microwave power transmission technologies for solar power satellites," *Proc. IEEE*, vol. 101, no. 6, pp. 1438–1447, Jun. 2013.

[45] R. Dietz, G. Arndt, J. Seyl, L. Leopold, and J. Kelley, "Satellite power system: Concept development and evaluation program. volume 3: Power transmission and reception. technical summary and assessment," Tech. Rep., Jul. 1981.

[46] J. C. Mankins, "A technical overview of the "suntower" solar power satellite concept," *Acta Astronaut.*, vol. 50, no. 6, pp. 369–377, 2002.

[47] M. Nagatomo, "Conceptual study of a solar power satellite SPS 2000," in *19th International Symp. on Space Technology and Science*, 1994.

[48] P. Jaffe and J. McSpadden, "Energy conversion and transmission modules for space solar power," *Proc. IEEE*, vol. 101, no. 6, pp. 1424–1437, Jun. 2013.

[49] W. Seboldt, M. Klimke, M. Leipold, and N. Hanowski, "European sail tower sps concept," *Acta Astronautica*, vol. 48, no. 5-12, pp. 785–792, 2001.

[50] J. McSpadden and J. Mankins, "Space solar power programs and microwave wireless power transmission technology," *IEEE Microw. Mag.*, vol. 3, no. 4, pp. 46–57, Dec. 2002.

[51] R. Wang, M. A. Kishk, and M.-S. Alouini, "Ultra-dense LEO satellite-based communication systems: A novel modeling technique," *IEEE Commun. Mag.*, vol. 60, no. 4, pp. 25–31, Apr. 2022.

[52] A. Talgat, M. A. Kishk, and M.-S. Alouini, "Stochastic geometry-based analysis of LEO satellite communication systems," *IEEE Commun. Lett.*, vol. 25, no. 8, pp. 2458–2462, Aug. 2021.

[53] A. Al-Hourani, "Session duration between handovers in dense LEO satellite networks," *IEEE Wireless Commun. Lett.*, vol. 10, no. 12, pp. 2810–2814, Dec. 2021.

Yuan Guo

[54] N. Okati and T. Riihonen, "Nonhomogeneous stochastic geometry analysis of massive LEO communication constellations," *IEEE Trans. Commun.*, vol. 70, no. 3, pp. 1848–1860, Mar. 2022.

[55] A. Al-Hourani, "An analytic approach for modeling the coverage performance of dense satellite networks," *IEEE Wireless Commun. Lett.*, vol. 10, no. 4, pp. 897–901, Apr. 2021.

[56] N. Okati, T. Riihonen, D. Korpi, I. Angervuori, and R. Wichman, "Downlink coverage and rate analysis of low earth orbit satellite constellations using stochastic geometry," *IEEE Trans. Commun.*, vol. 68, no. 8, pp. 5120–5134, Aug. 2020.

[57] A. Al-Hourani, "Optimal satellite constellation altitude for maximal coverage," *IEEE Wireless Commun. Lett.*, vol. 10, no. 7, pp. 1444–1448, Jul. 2021.

[58] W. Lu and M. D. Renzo, "Stochastic geometry modeling of cellular networks: Analysis, simulation and experimental validation," in *Proc. ACM Int. Conf. Modeling, Anal. Simulation Wireless Mobile Syst.*, Cancun, Nov. 2015, pp. 179–188.

[59] J. Huang, J. Cui, C.-C. Xing, and H. Gharavi, "Energy-efficient SWIPT-empowered D2D mode selection," *IEEE Trans. Veh. Technol.*, vol. 69, no. 4, pp. 3903–3915, Apr. 2020.

[60] O. Georgiou, "Simultaneous wireless information and power transfer in cellular networks with directional antennas," *IEEE Commun. Lett.*, vol. 21, no. 4, pp. 885–888, Apr. 2017.

[61] T. Tu Lam, M. Di Renzo, and J. P. Coon, "System-level analysis of SWIPT MIMO cellular networks," *IEEE Commun. Lett.*, vol. 20, no. 10, pp. 2011–2014, Oct. 2016.

[62] Q. Wu and R. Zhang, "Weighted sum power maximization for intelligent reflecting surface aided SWIPT," *IEEE Wireless Commun. Lett.*, vol. 9, no. 5, pp. 586–590, May 2020.

[63] I. Krikidis, S. Sasaki, S. Timotheou, and Z. Ding, "A low complexity antenna switching for joint wireless information and energy transfer in MIMO relay channels," *IEEE Trans. Commun.*, vol. 62, no. 5, pp. 1577–1587, May 2014.

[64] E. Boshkovska, D. W. K. Ng, N. Zlatanov, and R. Schober, "Practical non-linear energy harvesting model and resource allocation for SWIPT systems," *IEEE Commun. Lett.*, vol. 19, no. 12, pp. 2082–2085, Sep. 2015.

[65] N. Deng and M. Haenggi, "The energy and rate meta distributions in wirelessly powered D2D networks," *IEEE J. Sel. Areas Commun.*, vol. 37, no. 2, pp. 269–282, Sep. 2019.

[66] X. Lu, I. Flint, D. Niyato, N. Privault, and P. Wang, "Self-sustainable communications with RF energy harvesting: Ginibre point process modeling and analysis," *IEEE J. Sel. Areas Commun.*, vol. 34, no. 5, pp. 1518–1535, Apr. 2016.

[67] M. Haenggi, "Diversity loss due to interference correlation," *IEEE Commun. Lett.*, vol. 16, no. 10, pp. 1600–1603, Oct. 2012.

[68] R. Tanbourgi, H. S. Dhillon, J. G. Andrews, and F. K. Jondral, "Effect of spatial interference correlation on the performance of maximum ratio combining," *IEEE Trans. Commun.*, vol. 13, no. 6, pp. 3307–3316, Jun. 2014.

[69] S. Krishnan and H. S. Dhillon, "Spatio-temporal interference correlation and joint coverage in cellular networks," *IEEE Trans. Wireless Commun.*, vol. 16, no. 9, pp. 5659–5672, Sep. 2017.

[70] C. Skouroumounis and I. Krikidis, "An evolutionary game for mobile user access mode selection in sub-6 GHz/mmWave cellular networks," *IEEE Trans. Wireless Commun.*, pp. 1–1, Jan. 2022.

[71] S. Bandyopadhyay, E. J. Coyle, and T. Falck, "Stochastic properties of mobility models in mobile Ad Hoc networks," *IEEE Trans. Mobile Comput.*, vol. 6, no. 11, pp. 1218–1229, Nov. 2007.

[72] Z. Kong and E. M. Yeh, "On the latency for information dissemination in mobile wireless networks," in *Proc. ACM MobiHoc*, May 2008, pp. 139–148.

[73] C. Bettstetter, G. Resta, and P. Santi, "The node distribution of the random waypoint mobility model for wireless ad hoc networks," *IEEE Trans. Mobile Comput.*, vol. 2, no. 3, pp. 257–269, Sep. 2003.

[74] X. Lin, R. K. Ganti, P. J. Fleming, and J. G. Andrews, "Towards understanding the fundamentals of mobility in cellular networks," *IEEE Trans. Wireless Commun.*, vol. 12, no. 4, pp. 1686–1698, Apr. 2013.

[75] M. Banagar and H. S. Dhillon, "Performance characterization of canonical mobility models in drone cellular networks," *IEEE Trans. Wireless Commun.*, vol. 19, no. 7, pp. 4994–5009, Jul. 2020.

[76] K. Koufos and C. P. Dettmann, "Temporal correlation of interference and outage in mobile networks over one-dimensional finite regions," *IEEE Trans. Mobile Comput.*, vol. 17, no. 2, pp. 475–487, Feb. 2018.

[77] E. Hyytia, P. Lassila, and J. Virtamo, "Spatial node distribution of the random waypoint mobility model with applications," *IEEE Trans. Mobile Comput.*, vol. 5, no. 6, pp. 680–694, Apr. 2006.

[78] Z. Gong and M. Haenggi, "Interference and outage in mobile random networks: Expectation, distribution, and correlation," *IEEE Trans. Mobile Comput*, vol. 13, no. 2, pp. 337–349, Feb. 2014.

[79] G. Nigam, P. Minero, and M. Haenggi, "Coordinated multipoint joint transmission in heterogeneous networks," *IEEE Trans. Commun.*, vol. 62, no. 11, pp. 4134–4146, Oct. 2014.

[80] S. Liu, Z. Gao, Y. Wu, D. W. Kwan Ng, X. Gao, K.-K. Wong, S. Chatzinotas, and B. Ottersten, "LEO satellite constellations for 5G and beyond: How will they reshape vertical domains?" *IEEE Commun. Mag.*, vol. 59, no. 7, pp. 30–36, Jul. 2021.

[81] H. Xie, Y. Zhan, G. Zeng, and X. Pan, "LEO mega-constellations for 6G global coverage: Challenges and opportunities," *IEEE Access*, vol. 9, pp. 164 223–164 244, Dec. 2021.

[82] D.-H. Jung, J.-G. Ryu, W.-J. Byun, and J. Choi, "Performance analysis of satellite communication system under the shadowed-rician fading: A stochastic geometry approach," *IEEE Trans. Commun.*, vol. 70, no. 4, pp. 2707–2721, Apr. 2022.

[83] H. Jia, C. Jiang, L. Kuang, and J. Lu, "An analytic approach for modeling uplink performance of mega constellations," *IEEE Trans. Veh. Technol.*, vol. 72, no. 2, pp. 2258–2268, Feb. 2023.

[84] A. Abdi, W. Lau, M.-S. Alouini, and M. Kaveh, "A new simple model for land mobile satellite channels: first- and second-order statistics," *IEEE Trans. Wireless Commun.*, vol. 2, no. 3, pp. 519–528, May 2003.

[85] F. Benkhelifa and M. Alouini, "Prioritizing data/energy thresholding-based antenna switching for SWIPT-enabled secondary receiver in cognitive radio networks," *IEEE Trans. Cogn. Commun.*, vol. 3, no. 4, pp. 782–800, Dec. 2017.

[86] O. L. A. López, H. Alves, R. D. Souza, and S. Montejo-Sánchez, "Statistical analysis of multiple antenna strategies for wireless energy transfer," *IEEE Trans. Commun.*, vol. 67, no. 10, pp. 7245–7262, Oct. 2019.

[87] P. N. Alevizos and A. Bletsas, "Sensitive and nonlinear far-field RF energy harvesting in wireless communications," *IEEE Trans. Wireless Commun.*, vol. 17, no. 6, pp. 3670–3685, Jun. 2018.

[88] X. Lin, J. Bergman, F. Gunnarsson, O. Liberg, S. M. Razavi, H. S. Razaghi, H. Rydn, and Y. Sui, "Positioning for the Internet of Things: A 3GPP perspective," *IEEE Commun. Mag.*, vol. 55, no. 12, pp. 179–185, Dec. 2017.

[89] S. Singh, X. Zhang, and J. G. Andrews, "Joint rate and SINR coverage analysis for decoupled uplink-downlink biased cell associations in HetNets," *IEEE Trans. Wireless Commun.*, vol. 14, no. 10, pp. 5360–5373, Oct. 2015.

[90] P. Pratt, C. P. Dettmann, and O. Georgiou, "Optimal non-uniform deployments in ultra-dense finite-area cellular networks," *IEEE Commun. Lett.*, vol. 21, no. 5, pp. 1139–1142, May 2017.

[91] I. S. Gradshteyn and I. M. Ryzhik, *Table of integrals, series, and products*. Elsevier, 2007.

[92] G. Upton and I. Cook, *A Dictionary of Statistics*. OUP Oxford, 2008.

[93] G. B. Arfken and H. J. Weber, *Mathematical methods for physicists*, 6th ed. Elsevier, 2005.

[94] M. Wildemeersch, T. Q. S. Quek, M. Kountouris, A. Rabbachin, and C. H. Slump, "Successive interference cancellation in heterogeneous networks," *IEEE Trans. Commun.*, vol. 62, no. 12, pp. 4440–4453, Jun. 2014.

[95] S. T. Veetil, K. Kuchi, and R. K. Ganti, "Performance of PZF and MMSE receivers in cellular networks with multi-user spatial multiplexing," *IEEE Trans. Wireless Commun.*, vol. 14, no. 9, pp. 4867–4878, Sep. 2015.

[96] C. Skouroumounis, C. Psomas, and I. Krikidis, "Heterogeneous FD-mm-Wave cellular networks with cell center/edge users," *IEEE Trans. Commun.*, vol. 67, no. 1, pp. 791–806, Jan. 2019.

[97] V. Petrov, M. Komarov, D. Moltchanov, J. M. Jornet, and Y. Koucheryavy, "Interference and SINR in millimeter wave and terahertz communication systems with blocking and directional antennas," *IEEE Trans. Wireless Commun.*, vol. 16, no. 3, pp. 1791–1808, Mar. 2017.

[98] J.-S. Ferenc and Z. Néda, "On the size distribution of poisson voronoi cells," *Phys. A, Stat. Mech. Appl.*, vol. 385, no. 2, pp. 518–526, Nov. 2007.

[99] J. Frame, "An approximation to the quotient of gamma functions," *The American Mathematical Monthly*, vol. 56, no. 8, pp. 529–535, 1949.

[100] M. Giordani, M. Polese, A. Roy, D. Castor, and M. Zorzi, "A tutorial on beam management for 3GPP NR at mmWave frequencies," *IEEE Commun. Surveys Tuts.*, vol. 21, no. 1, pp. 173–196, Sep. 2019.

[101] P. Ross, "Generalized hockey stick identities and n-dimensional blockwalking," *The College Mathematics Journal*, vol. 28, no. 4, p. 325, 1997.

[102] S. M. Razavizadeh, M. Ahn, and I. Lee, "Three-dimensional beamforming: A new enabling technology for 5G wireless networks," *IEEE Signal Process. Mag.*, vol. 31, no. 6, pp. 94–101, Nov. 2014.

[103] J. Tang, A. Shojaeifard, D. K. C. So, K.-K. Wong, and N. Zhao, "Energy efficiency optimization for CoMP-SWIPT heterogeneous networks," *IEEE Trans. Commun.*, vol. 66, no. 12, pp. 6368–6383, Aug. 2018.

[104] J. Yang, X. Ge, J. Thompson, and H. Gharavi, "Power-consumption outage in beyond fifth generation mobile communication systems," *IEEE Trans. Wireless Commun.*, vol. 20, no. 2, pp. 897–910, Oct. 2021.

[105] V. V. Chetlur and H. S. Dhillon, "Coverage and rate analysis of downlink cellular vehicle-to-everything (C-V2X) communication," *IEEE Trans. Wireless Commun.*, vol. 19, no. 3, pp. 1738–1753, Mar. 2020.

[106] F. Zhu, Y. Lv, Y. Chen, X. Wang, G. Xiong, and F.-Y. Wang, "Parallel transportation systems: Toward IoT-enabled smart urban traffic control and management," *IEEE Trans. Intell. Transp. Syst.*, vol. 21, no. 10, pp. 4063–4071, Oct. 2020.

[107] V. V. Chetlur and H. S. Dhillon, "Coverage analysis of a vehicular network modeled as Cox process driven by Poisson line process," *IEEE Trans. Wireless Commun.*, vol. 17, no. 7, pp. 4401–4416, Jul. 2018.

[108] ——, "Spatial models for networks on roads: Bridging the gap between industry and academia," *IEEE Netw.*, vol. 36, no. 1, pp. 26–31, Feb. 2022.

[109] S. S. Kalamkar, F. Baccelli, F. M. Abinader, A. S. M. Fani, and L. G. U. Garcia, "Beam management in 5G: A stochastic geometry analysis," *IEEE Trans. Wireless Commun.*, vol. 21, no. 4, pp. 2275–2290, Apr. 2022.

[110] A. M. Haimovich, R. S. Blum, and L. J. Cimini, "MIMO radar with widely separated antennas," *IEEE Signal Processing Magazine*, vol. 25, no. 1, pp. 116–129, Dec. 2007.

[111] V. V. Chetlur and H. S. Dhillon, "On the load distribution of vehicular users modeled by a poisson line cox process," *IEEE Wireless Communications Letters*, vol. 9, no. 12, pp. 2121–2125, 2020.

[112] D. Bertsekas and J. N. Tsitsiklis, *Introduction to probability*. Athena Scientific, 2008, vol. 1.

[113] H.-S. Jo, Y. J. Sang, P. Xia, and J. G. Andrews, "Heterogeneous cellular networks with flexible cell association: A comprehensive downlink SINR analysis," *IEEE Trans. Wireless Commun.*, vol. 11, no. 10, pp. 3484–3495, Oct. 2012.

[114] Y. Guo, C. Skouroumounis, and I. Krikidis, "Large-scale heterogeneous ultra-dense leo satellite-based cellular networks," in *Proc. IEEE Int. Conf. Commun. (ICC)*, Rome, Italy, May. 2023.

[115] J. Park, J. Choi, and N. Lee, "A tractable approach to coverage analysis in downlink satellite networks," *IEEE Trans. Wireless Commun.*, vol. 22, no. 2, pp. 793–807, Feb. 2023.

[116] B. R. Elbert, *The satellite communication applications handbook*. Artech House, 2004.

[117] L. M. B. Winternitz, W. A. Bamford, and G. W. Heckler, "A GPS receiver for high-altitude satellite navigation," *IEEE J. Sel. Top. Signal Process.*, vol. 3, no. 4, pp. 541–556, Aug. 2009.

[118] H.-C. Yang and M.-S. Alouini, *Order statistics in wireless communications: diversity, adaptation, and scheduling in MIMO and OFDM systems*. Cambridge University Press, 2011.

[119] J. Gil-Pelaez, "Note on the inversion theorem," *Biometrika*, vol. 38, no. 3-4, pp. 481–482, Dec. 1951.

[120] J. Sayehvand and H. Tabassum, "Interference and coverage analysis in co-existing RF and dense TeraHertz wireless networks," *IEEE Wireless Commun. Lett.*, vol. 9, no. 10, pp. 1738–1742, Oct. 2020.

[121] Y. Guo, C. Skouroumounis, and I. Krikidis, "Joint information and energy transfer of SWIPT-enabled mobile users in wireless networks," *IEEE Trans. Green Commun. Netw.*, vol. 6, no. 2, pp. 1141–1156, Jun. 2022.

[122] P. E. Glaser, "Power from the sun: Its future," *Science*, vol. 162, no. 3856, pp. 857–861, Nov. 1968.

[123] S. Liu, Z. Gao, Y. Wu, D. W. K. Ng, X. Gao, K.-K. Wong, S. Chatzinotas, and B. Ottersten, "LEO satellite constellations for 5G and beyond: How will they reshape vertical domains?" *IEEE Commun. Mag.*, vol. 59, no. 7, pp. 30–36, Jul. 2021.

[124] S. T. Goh, S. A. Zekavat, and O. Abdelkhalik, "LEO satellite formation for SSP: energy and doppler analysis," *IEEE Trans. Aerosp. Electron. Syst.*, vol. 51, no. 1, pp. 18–30, Jan. 2015.

[125] Y. Yang, M. Xu, D. Wang, and Y. Wang, "Towards energy-efficient routing in satellite networks," *IEEE J. Sel. Areas Commun.*, vol. 34, no. 12, pp. 3869–3886, Dec. 2016.

Yuan Guo

[126] Y. Song, X. Li, H. Ji, and H. Zhang, "Energy-aware task offloading and resource allocation in the intelligent LEO satellite network," in *2022 IEEE 33rd Annual International Symposium on Personal, Indoor and Mobile Radio Communications (PIMRC)*. IEEE, 2022, pp. 481–486.

[127] W. C. Brown and E. E. Eves, "Beamed microwave power transmission and its application to space," *IEEE Trans. Microw. Theory Tech.*, vol. 40, no. 6, pp. 1239–1250, Jun. 1992.

[128] F. Liu, Y. Cui, C. Masouros, J. Xu, T. X. Han, Y. C. Eldar, and S. Buzzi, "Integrated sensing and communications: Toward dual-functional wireless networks for 6G and beyond," *IEEE J. Sel. Areas Commun.*, vol. 40, no. 6, pp. 1728–1767, Jun. 2022.

[129] F. Liu, C. Masouros, A. P. Petropulu, H. Griffiths, and L. Hanzo, "Joint radar and communication design: Applications, state-of-the-art, and the road ahead," *IEEE Tran. Commun.*, vol. 68, no. 6, pp. 3834–3862, Jun. 2020.

[130] Y. Cui, F. Liu, X. Jing, and J. Mu, "Integrating sensing and communications for ubiquitous iot: Applications, trends, and challenges," *IEEE Network*, vol. 35, no. 5, pp. 158–167, Oct. 2021.

[131] A. Hassanien, M. G. Amin, E. Aboutanios, and B. Himed, "Dual-function radar communication systems: A solution to the spectrum congestion problem," *IEEE Signal Process. Mag.*, vol. 36, no. 5, pp. 115–126, Sep. 2019.

[132] X. Cheng, D. Duan, S. Gao, and L. Yang, "Integrated sensing and communications (ISAC) for vehicular communication networks (VCN)," *IEEE Internet Things J.*, vol. 9, no. 23, pp. 23 441–23 451, Dec. 2022.

[133] W. Yuan, Z. Wei, S. Li, J. Yuan, and D. W. K. Ng, "Integrated sensing and communication-assisted orthogonal time frequency space transmission for vehicular networks," *EEE J. Sel. Top. Signal Process.*, vol. 15, no. 6, pp. 1515–1528, Nov. 2021.

[134] Y. Lin, Z. Zhang, Y. Huang, J. Li, F. Shu, and L. Hanzo, "Heterogeneous user-centric cluster migration improves the connectivity-handover trade-off in vehicular networks," *IEEE Trans. Veh. Technol.*, vol. 69, no. 12, pp. 16 027–16 043, Dec. 2020.

[135] V. V. Paranthaman, Y. Kirsal, G. Mapp, P. Shah, and H. X. Nguyen, "Exploiting resource contention in highly mobile environments and its application to vehicular ad-hoc networks," *IEEE Trans. Veh. Technol.*, vol. 68, no. 4, pp. 3805–3819, Apr. 2019.

[136] P. Sun, N. AlJeri, and A. Boukerche, "An energy-efficient proactive handover scheme for vehicular networks based on passive rsu detection," *IEEE Trans. Sustain. Comput.*, vol. 5, no. 1, pp. 37–47, Mar. 2020.

Yuan Guo